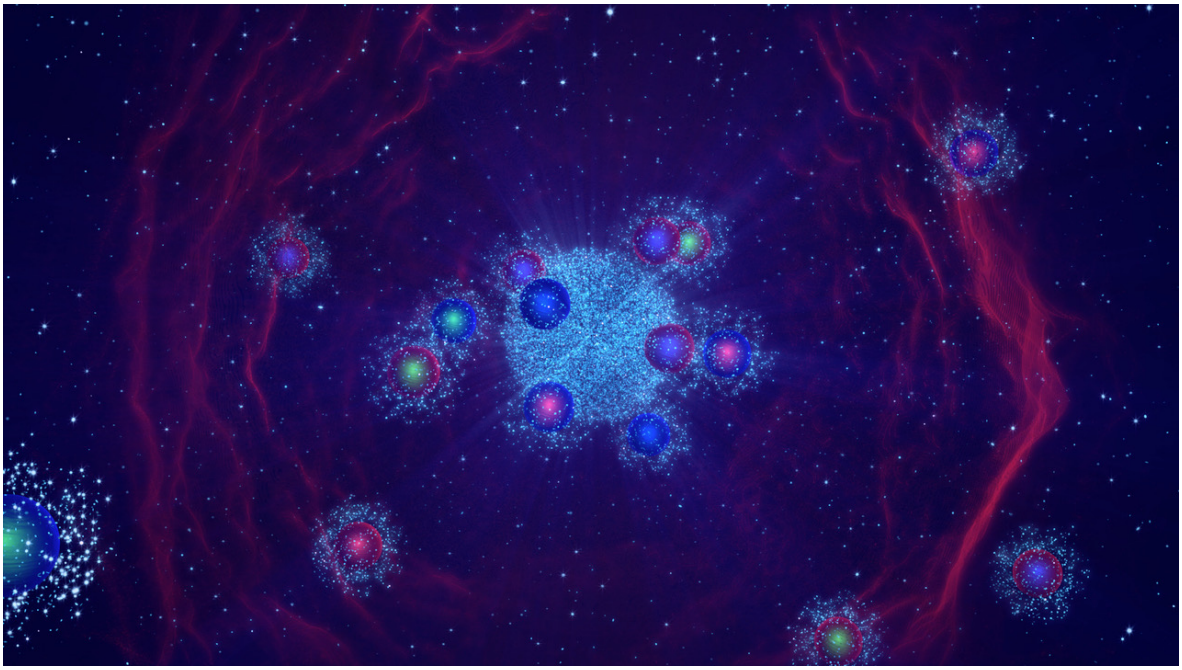

Particle Physics

New York Lectures

Jesse Liu

Department of Physics, New York University,
726 Broadway, New York, NY 10003, USA

These lecture notes accompany the NYU graduate introduction to particle physics (PHYS-GA 2027) in Spring 2025. This course presents the phenomenological and experimental discoveries leading to the Standard Model. After introducing the historical foundations, the class surveys the empirical evidence underpinning quantum electrodynamics, the strong force, and electroweak interactions. The level is for graduate students exposed to special relativity, quantum mechanics, and electromagnetism.

0 Syllabus

Course: NYU PHYS-GA 2027 Particle Physics
Semester: Spring 2025
Instructor: Jesse Liu
Lectures: Tuesday and Thursdays, 11:00–12:15, 726 Broadway, Room 1025
Office hours: Wednesdays, 11:00–12:00, Room 852 or by appointment

0.1 Course overview

This is the New York University graduate introduction to the Standard Model of particle physics (PHYS-GA 2027). The semester comprises 14 weeks of classes with two 75-minute lectures per week, totalling 27 planned lectures slots. Like previous versions of this class, the finals week is devoted to student presentations. Below is a lecture plan, which is subject to change based on the pace of delivery (sections of lecture notes in parentheses):

Historical origins

1. Course overview, motivation and introduction to the Standard Model (1.1–1.3).
2. Radioactivity, evidence for neutrinos, ionisation and cloud chambers (2.1).
3. Proton and neutron, cosmic rays for positron and muon discoveries (2.2–2.3).
4. Relativity and quantum mechanics review, constructing Dirac equation (3.1–3.2).
5. Weyl equations, helicity and chirality, Dirac mass, antimatter (3.3).
6. Spinor rotation, non-relativistic limit to Pauli equation: gyromagnetic factor (3.4).

Quantum electrodynamics

7. Feynman diagrams, electromagnetic scattering, virtual particles, propagators (4.1–4.3).
8. Gauge theory of forces, local symmetry, gauge fixing, Feynman rules (4.4).
9. Accelerators, cross-sections, Fermi's golden rule, density of states (5.1–5.4).
10. Electron–positron annihilation, spinor–helicity analysis, resonances (6.1–6.3).
11. Loop effects: Lamb shift, anomalous magnetic moment, running coupling (7.1–7.3).

Strong force

12. Particle zoo: nuclear moments, emulsions, cyclotrons, bubble chambers (8.1–8.4).
13. Quark model, strangeness, meson and baryon multiplets, colour charge (9.1–9.4).
14. Nuclear form factors, deep inelastic scattering and evidence for partons (10.1–10.2).
15. Evidence for quarks and their quantum properties, charmonium J/ψ (10.3–10.4).

16. Yang–Mills theory, evidence for colour, gluons, asymptotic freedom (11.1–11.4).

Electroweak interactions

17. Low-energy beta decay: Fermi theory, neutrino detection, parity violation (12–12.3).
18. Helicity suppression, flavour mixing, charge-parity violation in kaons (12.3–12.5).
19. Collider experiments, particle–matter interactions, terascale detectors (13.1–13.3).
20. Collider kinematics and event reconstruction, particle identification (13.4–13.5).
21. Abelian Higgs model, Glashow–Salam–Weinberg model (14.1–14.2).
22. Generating gauge boson masses, electroweak unification (14.3).
23. W and Z boson discovery, evidence for three light neutrinos (14.4–14.5).
24. Higgs boson discovery, ATLAS and CMS measurements (15.1–15.2).
25. Higgs–Yukawa couplings, Cabbibo–Kobayashi–Maskawa matrix (15.3–15.4).
26. Evidence for massive neutrinos, solar and atmospheric oscillations (16.1–16.4).

Outlook

27. Open questions, motivation for physics beyond the Standard Model.

Structure and approach

This graduate class has been taught by many esteemed colleagues at NYU with various levels and approaches. In recent years, the class required Quantum Field Theory I (PHYS-GA 2058), but this version does not. I instead return to more conventional introductory particle physics textbooks for advanced undergraduates and beginning graduates. This course develops relativistic quantum mechanics and emphasises experimental discoveries, assuming a standard US undergraduate physics curriculum as pre-requisites. This enables the course to complement rather than overlap too much with the theoretical QFT classes.

Given the breadth of particle physics, the choice of topics can neither be an exhaustive nor encyclopedic list of all particles, processes, calculations, and experiments. The aim instead is to convey the foundations and build intuition using illustrative examples as a springboard for more specialised study. This includes the literature review presentations in this class and the start of your graduate careers.

The course is organised into four parts covering how the Standard Model was discovered: (i) historical origins discussing motivation alongside foundational discoveries, (ii) quantum electrodynamics as the prototypical gauge theory, (iii) strong force showing how quarks and gluons emerged from the particle zoo, (iv) electroweak interactions from parity violation in low-energy beta decay to the Higgs boson and neutrino oscillations. The ordering may appear superficially historical, but worry not, the structure largely charts increasing energy

scales and decreasing interaction strengths. This unsurprisingly coincides with technological advances, with more powerful machines simply taking longer to develop.

The lectures endeavour to weave selected historical, phenomenological, and experimental perspectives that make particle physics such a fascinating subject. Indeed understanding the *process* of discovery is as interesting as the discovery itself, especially for aspiring researchers learning how to uncover new knowledge themselves. I anticipate a mix of board work for mathematical derivations supplemented by slides to show more detailed figures and data. As time permits, the last lecture(s) may introduce the motivation for physics beyond the Standard Model and/or special research topics.

Pre-requisites

Mathematics: linear algebra (matrix multiplication, eigenvalues), complex numbers, vector calculus (integration in spherical coordinates). Physics: special relativity (space-time metric, Lorentz boosts), electromagnetism (Maxwell's equations, electromagnetic waves), quantum mechanics (Schrödinger equation, Pauli matrices, perturbation theory).

Recommended but not required: Quantum Field Theory I (PHYS-GA 2058) and II (PHYS-GA 2077) covers similar topics with more theoretical emphasis.

Assessment

- Grade: 60%. Homework. There are 5 problem sets planned based on lecture content.
- Grade: 40%. Research review. 10–15 minute presentation with slides. Attendance is required. Usual class location and time during finals week.

Presentation topics

In lieu of a final exam, each student selects a historical discovery or ongoing experiment related to particle physics and prepares a 10–15 minute talk; I recommend 10 slides of content. The presentation comprises a research literature review using slides during the regular class times of finals week. The topic is mutually agreed upon with me in advance (to ensure breadth by not too many people choosing the same topic). Suggested topics include:

1. Discovery of tau-lepton and/or tau-neutrino.
2. Discovery of top quark at Tevatron, Fermilab.
3. Higgs potential shape and Higgs self-coupling probes at LHC.
4. Tetraquarks and pentaquarks at LHCb Experiment.

5. Charge-parity violation in B-mesons.
6. Laboratory neutrino oscillations and charge-parity violation e.g. MicroBOONE, DUNE.
7. Majorana vs. Dirac neutrinos and neutrinoless double beta decay e.g. SNO+.
8. Measuring the muon anomalous magnetic moment $(g-2)$ at Fermilab.
9. Physics of High-Luminosity LHC and detector upgrades.
10. Future high-energy colliders (e.g. FCC, Muon Collider) and their physics goals.
11. Searches for weak-scale dark matter at colliders and direct detection experiments.
12. Searches for axion dark matter and axion-like particles.
13. Cosmic-ray observatories in space and terrestrial e.g. AMS, IceCube, Auger.
14. Accelerators and detectors in medical physics for imaging and radiotherapy.
15. Cosmic-ray muography for imaging volcanoes and archaeology sites.

0.2 Literature

There is no required textbook and I encourage you to browse your library to find your preferred text. This list also represents a bibliography I consulted (or studied as a student) in preparing the lecture notes.

Open access books. It is a truth universally acknowledged that textbooks are expensive. So I was happy to see certain texts recently made open access funded by the SCOAP[3] initiative coordinated by CERN, which is worth supporting:

- Giles Barr, Robin Devenish, Roman Walczak, Tony Weidberg, *Particle Physics in the LHC era* [1] (OUP 2016, Open Access Library[1]). Based on Oxford Part C master's level course; I myself took the graduate lectures in particle physics as a PhD student.
- Alessandro Bettini, *Introduction to Elementary Particle Physics* (3rd Edition, CUP 2024, open access on Cambridge Core[2]. This recently-updated textbook has particularly lucid accounts of the history behind experimental discoveries of particle physics.

Online lecture materials. A quick Internet search of "particle physics lectures" reveals many high-quality materials online. I list some from my academic heritage:

- **Advanced undergraduate level**
  Tina Potter teaches the Cambridge *Part II Nuclear and Particle Physics*[3] course for

[1] https://library.oapen.org/handle/20.500.12657/59108
[2] https://doi.org/10.1017/9781009440745
[3] https://www.hep.phy.cam.ac.uk/~chpotter/particleandnuclearphysics/mainpage.html

final (third) year undergraduates, which also covers nuclear physics. This is a standard introductory course for third-year British undergraduates, where I myself took the analogous lectures at Oxford taught by Alan Barr in 2014. I still possess some notes from my studies that I recycle here.

- **Graduate level**
  Chris Lester has over 600 slides for the Cambridge Natural Sciences *Part III Particle Physics*[4] master's level course with an experimental emphasis and complements the Thomson textbook. Theory counterparts are written up by David Tong[5], alongside Fernando Quevedo and Andreas Schachner[6].

  My education followed the *Standard Model* course at the Perimeter Institute, taught by Stefania Gori and Gordan Krnjaic with Daniel Wohns and Gang Xu in 2015; video recordings remain online[7] and the most recent 2025 edition is lectured by Sydek Ipek[8]. I also took an advanced PSI classes by David Morrissey who has clear SM notes[9] and Brian Shuve who has SM lectures recorded[10].

Canonical textbooks. Here are a few much-loved particle physics textbooks that do not assume quantum field theory, where the publication year is suggestive of whether post-LHC updates are included:

- David Griffiths, *Introduction to Elementary Particles* (2nd Edition, Wiley 2004). An old favourite with good coverage of history and Feynman rule calculations.
- Andrew J. Larkoski. *Elementary Particle Physics: An Intuitive Introduction* (CUP 2019). This recent textbook provides pedagogical coverage of LHC-era analysis topics.
- Brian R. Martin and Graham Shaw, *Particle Physics* (4th Edition, Manchester Physics Series 2017). Discussions on the quark model and interactions are especially clear, with good introductory chapters about accelerator and detector techniques.
- Donald Perkins, *Introduction to High Energy Physics* (4th Edition, CUP 2000). Old but classic with good balance of experiment and phenomenology, which trained many generations of professionals before the Higgs discovery.

[4] https://www.hep.phy.cam.ac.uk/~lester/teaching/partIIIparticles/welcome.html
[5] https://www.damtp.cam.ac.uk/user/tong/standardmodel.html
[6] https://arxiv.org/abs/2409.09211
[7] https://pirsa.org/c15001
[8] https://pirsa.org/c25003
[9] https://particletheory.triumf.ca/PHYS528/
[10] https://brianshuvephysics.com/materials

- Mark Thomson, *Modern Particle Physics* (CUP 2013)[11]. Modern classic written for the Cambridge Natural Sciences Part III course by the new CERN Director General.

Further reading. More specialised reading and summer school materials for the aspiring particle physics researcher:

- Particle Data Group, *Review of Particle Physics* (PRD 2024)[12]. *The* standard reference compiling up-to-date values and reviews, regularly updated by the group.
- Theoretical Advanced Study Institute (2024)[13]. Colorado summer school lectures providing advanced training for aspiring theorists and phenomenologists.
- Fermilab–CERN Hadron Collider Physics School (2024)[14]. The summer school alternates between Fermilab and CERN with slides available for advanced training aimed at aspiring collider physicists.
- Robert Cahn and Gerson Goldhaber, *The Experimental Foundations of Particle Physics* (CUP 2009). Nice account of the experimental evidence with prints of original discovery papers that led to the Standard Model.
- Howard Georgi, *Lie Algebras In Particle Physics: from Isospin To Unified Theories* (CRC Press 2000). For those who want to study the more mathematical aspects of group and representation theory underpinning particle physics.
- Glenn Knoll, *Radiation Detection and Measurement* (Wiley 2010). The standard reference for instrumentation underpinning detector physics.
- Tom Lancaster and Stephen Blundell, *Quantum Field Theory for the Gifted Amateur*[15] (OUP 2014). An accessible and lucid quantum field theory text written by condensed matter experimentalists that I found very helpful as a student.

[11] https://www.hep.phy.cam.ac.uk/~thomson/MPP/ModernParticlePhysics.html
[12] https://pdg.lbl.gov/, https://doi.org/10.1103/PhysRevD.110.030001
[13] https://sites.google.com/colorado.edu/tasi-2024-hub/home
[14] https://indico.fnal.gov/event/63696/
[15] https://academic.oup.com/book/36442

0.3 About these notes

For my own organisation, I have typeset lecture notes for this course, which grew from preparing for the class I first taught in Spring 2025. It comprises a synthesis of standard textbooks, journal articles, and online material with guided explanations for education purposes. I sketch numerous figures myself and endeavour to provide the sources for other figures in the captions.

These notes are intended to help you navigate the subject and certainly do not replace the wealth of excellent literature listed. Nonetheless this first version will inevitably have some rough edges. As a work-in-progress document created by a fallible human, feel free to send corrections to typographical errors. Presentational clarity and discussions will hopefully improve as future iterations of this class arise. Hopefully you may find them useful.

Miscellaneous

I typeset these notes using LaTeX adapting the JHEP template[16]. I draw various diagrams using `figma`, `feynmp-auto`, `tikz.net`. My typing hands and spellcheck dictionary are set to 'British English' e.g. aluminium, anti-clockwise, centre, colour, flavour, fulfil, labelled, metre, normalise, parametrise vs aluminum, counter-clockwise, center, color, flavor, fulfill, labeled, meter, normalize, parameterize. The title page image shows an artist's impression of Higgs field interactions from CERN[17]. These notes were initially prepared while generously supported by a Junior Research Fellowship at Trinity College, University of Cambridge.

Version history

0.1: preliminary draft 20th January 2025

[16] https://jhep.sissa.it/jhep/help/JHEP_TeXclass.jsp
[17] https://home.cern/science/physics/

Contents

I Historical origins

1 Introduction

Why study nature at the smallest scales? Why understand the fundamental forces of the universe? Why do we invest resources operating vast collider experiments? You are probably reading these notes because you think particle physics is interesting enough to enrol in a graduate class. So *you* likely need no convincing and can merrily skip this motivational introduction. But outside the classroom, your friends, family and acquaintances may ask why you picked this class or why the basic sciences are worth prioritising, especially when other pressing problems exist in our world. These are fair and timeless questions. So for completeness, let us summarise the canonical reasons to study particle physics.

1.1 Why study particle physics?

Particle physics aims to understand the fundamental building blocks of nature, simply put:

> "What is the world made of?"

The idea that we can divide what we see around us into indivisible constituents dates back to ancient philosophies and cultures. By identifying these parts and how they interact, we can not only explain natural phenomena with deeper principles but also engineer solutions to problems in our society. Scientific discovery follows an uneven but familiar cadence:

Discovery phase		**Empirical structure**		**Predictive theory**
Observations surprise and even seem chaotic	$\rightarrow$	Systematic characterisation reveals unexplained patterns	$\rightarrow$	Simple principles dynamically generate rich phenomena

We will see this process play out throughout the Standard Model, such as the particle zoo to quark model to flavour physics. Chemistry is the first success story that betrays an uncanny resemblance to particle physics, so let us start there.

The principled structure of chemistry

In the early nineteenth century, scientists noticed that chemical reactions proceed with integer ratios of elements. Water combined two parts hydrogen with one part oxygen and ammonia

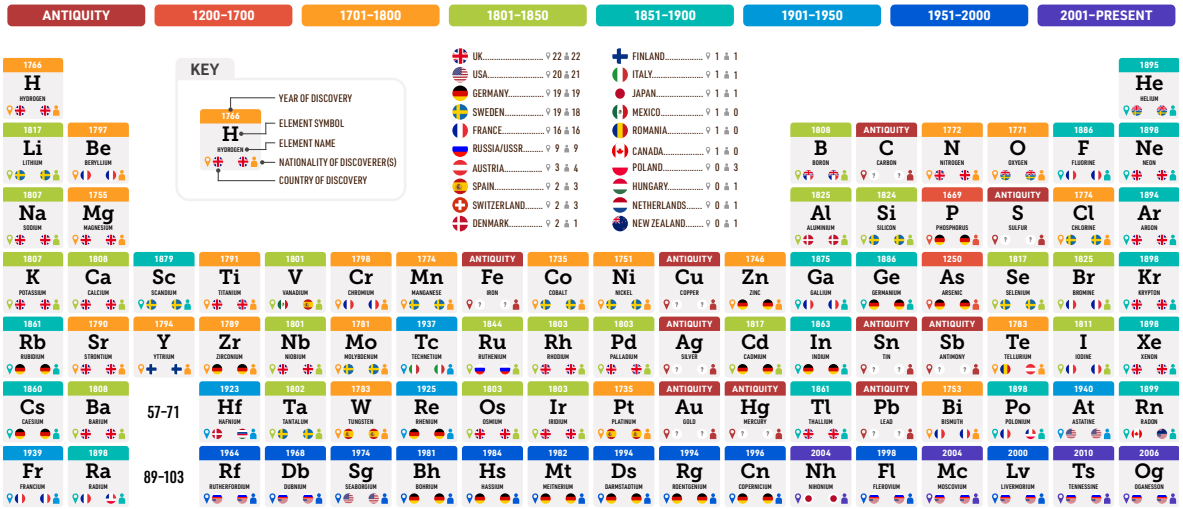

Figure 1: **Periodic table by discovery year**. This illustrates how empirical structure emerges much later than experimental discovery and detailed empirical characterisation. Image: Andy Brunning/Compound Interest (2019).

comprised three parts hydrogen to one part nitrogen. This led to John Dalton's "Law of Multiple Proportions" and 1807 proposal of atomic theory. The former appeared empirically successful but the reality of tiny unseeable atoms remained controversial for a century. By 1864, around fifty chemical elements were known with scientists such as John Newlands observing a mysterious eight-fold periodicity in a "Law of Octaves".

In 1869, Dmitri Mendeleev famously arranged the chemical elements into an organised table (figure 1). He used it to predict three new elements: gallium, germanium, and scandium. Elements are grouped by their empirical attributes: silvery solid alkalis and gaseous halogens react vigorously, while neighbouring noble gases stay inert. This pattern repeats with a mass periodicity of eight then eighteen for heavier elements. Structure was emerging after centuries of disjointed discoveries. But it was natural to ask why? How many more elements await discovery? Are deeper dynamics behind this structure?

In 1905, Albert Einstein applied statistical physics to Brownian motion to show atoms exist. Abridging the ensuing decades of revolutionary quantum mechanics and semesters of undergraduate physics to one sentence revealed just three subatomic building blocks:

$$\text{Atoms} : \{\, \text{protons}\,,\ \text{neutrons}\,,\ \text{electrons}\,\}\,. \tag{1.1}$$

From this mere handful of parts, we can build the hundreds of elements and their isotopes. How very elegant. Quantum mechanics and electromagnetism govern wavefunction orbitals

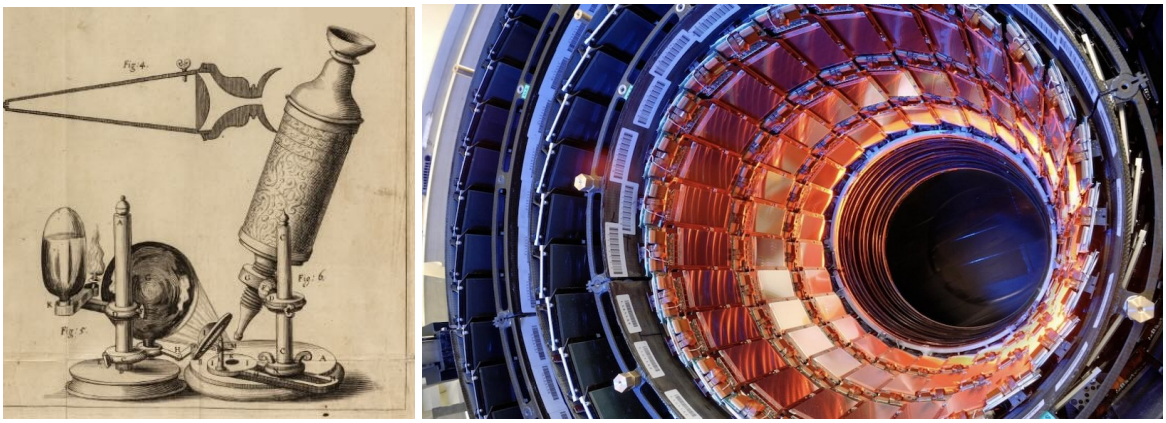

(a) Hooke's microscope c. 1665 (b) Compact Muon Solenoid (CMS) Experiment c. 2010

Figure 2: **Discovery instruments: microscopes four centuries apart**. Optical microscopes discovered biological cells in the seventeenth century, opening the field of microbiology. Today, detectors such as Compact Muon Solenoid at CERN comprise the most powerful microscopes probing 10^{-18} m. Images: Royal Society and CERN.

and ionisation energies, explaining why halogens are so reactive but not noble gases next door. This is the principled structure of chemistry. It endows the richness of molecular biology to material science and semiconductor electronics. It answers "how many more elements exist?": thankfully finite, just over hundred! Pack too many protons and neutrons into a nucleus, they become unstable and radioactively decay. This is a triumph for empirical reductionism. Just after the neutron discovery, the alluring "what is the world made of?" picture of (1.1) led Paul Dirac to reflect at the 1933 Solvay Conference:

> "If we consider protons and neutrons as elementary particles, we would have [with electrons] three kinds of elementary particles... This number may seem large but, from that point of view, two is already a large number."

We now know that this is far from the end of the story. It is the birth of particle physics.

Microscopes illuminate the microcosm

How do we know subatomic particles even exist? What instruments do we need to unveil the microcosm? Nature under microscopes is truly surprising (figure 2). Antonie van Leeuwenhoek and Robert Hooke peered through their microscopes bending light in the seventeenth century to unveil objects 100 times smaller than what the eye can resolve of around 0.1 mm. They revealed the building blocks of life: the existence of cells. Today, we overcome the

diffraction limit of optical microscopes using wave-particle duality to probe ever smaller scales via higher energies. We build city-sized particle colliders and their cathedral-sized detectors as the most powerful microscopes probing 10^{-18} m length scales. Even with hindsight, it is unclear if or how pure philosophical or mathematical contemplation in a cave could have revealed the Standard Model without empirical guidance. Studying the experimental instruments revealing subatomic degrees of freedom is utterly worthwhile.

Stunning empirical verification

Why do we celebrate the Standard Model as a theory of nature? How well does it stand up to experimental scrutiny? Perturbation theory allows quantum field theory to predict observables that pass diverse experimental tests. The epitome of such empirical success is the electron gyromagnetic factor g_e from intrinsic spin. Its recent measurements and predictions agree to parts per trillion precision [2, 3]

$$g_e^{\text{meas}} = 2.002\,319\,304\,361, \tag{1.2}$$

$$g_e^{\text{pred}} = 2.002\,319\,304\,364. \tag{1.3}$$

This is among the most precisely tested quantities in nature. Few other empirical fields manage such feats. It is spectacular.

Yet a single observable alone is not what makes the Standard Model so successful. Its range of empirical validity extends to the highest laboratory energies. Electroweak theory and data predicted the existence of the top quark and Higgs boson. The Standard Model is a particular quantum field theory, and the fact it describes reality so well is why we trust its most peculiar predictions from anti-matter to vacuum polarisation.

Profound explanatory power

How does the Standard Model deepen our understanding of reality? What is its explanatory power? The Schrödinger equation cannot describe relativistic electrons or photons. Amazingly, making quantum mechanics consistent with special relativity explains many mysteries of undergraduate physics while revealing plenty more surprises. It tells us why the electron has spin half and its gyromagnetic factor is (nearly) two. We learn how two electrons can even be exactly identical. We find out nature gives us left and right handed electrons but we barely noticed until we realised the weak force cares. We upend our view of what inertial mass is: a scalar field gains a non-zero value to pair left with right handed electrons.

We reveal the uncertainty principle and mass–energy equivalence means the quantum vacuum is neither static nor empty. It is actually dynamical, a teeming sea of virtual particles

and anti-particles popping in and out of existence. We learn that matter and charge are conserved due to symmetries in nature. While electromagnetism, the strong and weak nuclear forces could not behave more differently on first glance, we uncover that they actually share the same theoretical structure called gauge theories. These surprising but principled pictures of reality are radical departures from classical physics. It is why many find particle physics profound. Some might say beautiful.

Particle astrophysics and cosmology

How did the universe create all the matter we see? How do they propagate and interact in the cosmos? Particle physics is the study of our primordial origins (figure 3a). Big Bang cosmology (see the Cosmology course PHYS-GA 2052 for further details) implies the early universe saw far higher temperatures than today:

Electroweak transition: quarks & leptons gain mass	10^{-12} s	10^{15} K	100 GeV
Quark–hadron transition: quarks confine into protons	10^{-6} s	10^{12} K	100 MeV
Nucleosynthesis: protons & neutrons fuse into nuclei	3 mins	10^{9} K	100 keV

When the universe was about 10^{-12} s old, the temperature cooled to a balmy $k_B T \approx 100$ GeV, triggering electroweak symmetry breaking and giving gauge bosons, quarks and leptons finite mass. At 10^{-6} s, free quarks and gluons confine into protons and neutrons as the universe cools to $k_B T \approx 100$ MeV. Particle physics tells these phase transitions must have happened. For the first time in 13.8 billion years, we now have colliders that can recreate these extreme conditions of the early universe in the relative comforts of our laboratory.

Big Bang nucleosynthesis started fusing protons and neutrons in the first few minutes. It would take another 300 000 years before these nuclei bound to electrons to create atoms. The Standard Model particle content and interactions are now imprinted in the cosmic microwave background. This allows cosmology to measure the total Standard Model contribution (dominated by baryons) Ω_{SM} to the energy budget of the universe [6]

$$\Omega_{\text{SM}} \simeq 0.049, \quad \Omega_{\text{DM}} \simeq 0.26, \quad \Omega_{\text{DE}} \simeq 0.69. \tag{1.4}$$

The remainder is enigmatically named dark matter Ω_{DM} and dark energy Ω_{DE}, whose microscopic properties remain major research questions (figure 3b).

Astronomy historically relied on observing light using telescopes. These "messengers" now extend photons to other electrons, positrons, protons, neutrinos, and gravitational waves (figure 3c). Crucially, particle interactions at colliders behave the same as those inhabiting

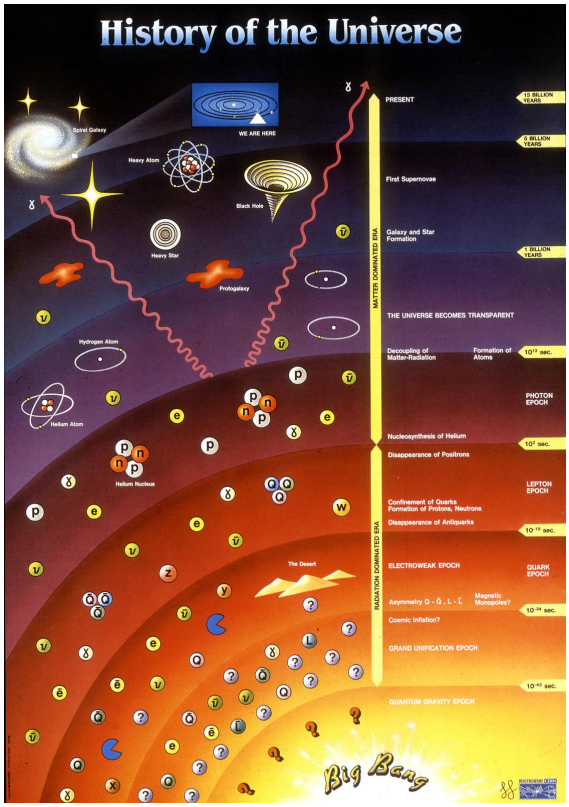

(a) Early universe cosmology

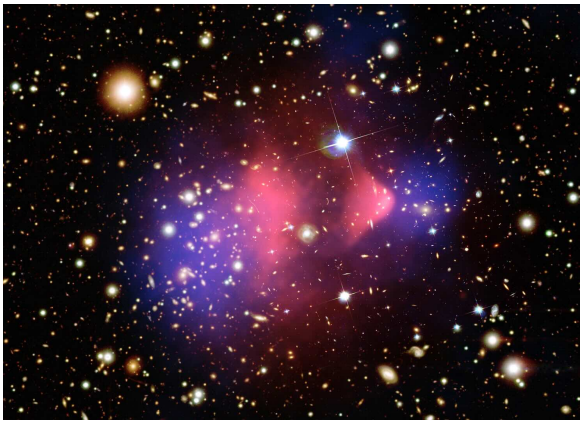

(b) Dark matter

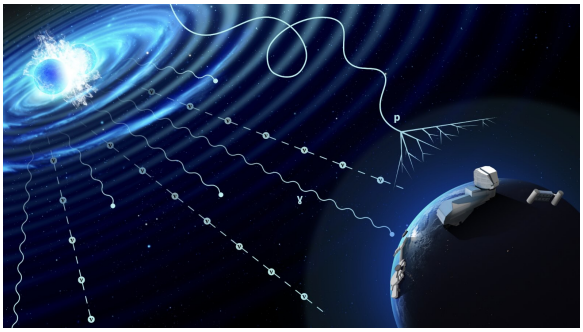

(c) Multi-messenger astronomy

Figure 3: **Particle physics connections with astrophysics and cosmology**. (a) History of the universe connecting particle physics with the hot Big Bang. (b) The Bullet Cluster provides evidence for dark matter via gravitational lensing (purple) displaced from the hot gas via X-rays (pink) [4]. (c) Artist's impression of an astrophysical multi-messenger event producing gravitational waves, photons, neutrinos, and protons. Images: CERN [5], NOIRLab, ESA/NASA/CXC/CfA/M.Markevitch/STScI, Magellan/U.Arizona/D.Clowe/ESO WFI.

distant galaxies and the early universe. This central fact arises because particles are excitations of the same quantum fields. This opens connections applying particle physics to exciting contemporary research areas in multi-messenger astrophysics.

The strong and weak nuclear forces also underpin stellar astrophysics. The solar proton–proton chain burns hydrogen into helium $2p + 2e^- \to {}^4_2\mathrm{He} + 2\nu_e$, overcoming proton electrostatic repulsion. A key process fuses two protons (hydrogen nuclei) into a deuterium nucleus of one proton and neutron:

$$p + p \to {}^2_1\mathrm{D} + e^+ + \nu_e. \tag{1.5}$$

This weak force mediates this crucial step and is the dominant factor limiting it rate in the

Sun. Its weakness compared to the strong force binding nucleons prevents the Sun burning out faster than giga-years. This enables planets to form and life to get started on Earth.

1.2 Applications and society

How does fundamental physics benefit other disciplines and wider society? Often overlooked in textbooks, particle physics finds widespread applications from neighbouring scientific fields to the humanities. Let us briefly survey some examples. Perhaps you will be inspired to find breakthrough applications using Higgs bosons for the betterment of humanity.

Big computing and the Web

In 1989, Tim Berners-Lee presented an innocuous-sounding document entitled "Information Management: A Proposal" to CERN [7]. He sought to answer a frequently asked question of project management:

> "Yes, but how will we ever keep track of such a large project?"

The document was to convince CERN of the value of the World Wide Web. This serves to distribute information around the globe, which CERN adopted (figure 4a) and still uses today. This has had a truly transformative impact on society, to say the least, notably in the ubiquity of "`www`" prefixing website addresses. The development of an international Grid of high-performance computing was necessary for "big data", processing vast volumes of data and simulation for particle physics experiments.

Medical diagnosis and therapy

Scientists realised the significance of X-rays to medical diagnosis almost immediately after its discovery. By contrast, anti-matter and nuclear magnetic moments were esoteric curiosities in the early twentieth century with unclear utility. Today, they improve the human condition no less. Medical imaging relies on the flashes of gamma rays from anti-matter annihilating with matter in positron emission tomography (PET), while gyromagnetic protons enable magnetic resonance imaging. Precise imaging is vital in fields such as oncology [10] in cancer diagnosis and therapy (figure 4b). Cyclotrons originally developed to accelerate and study hadrons are now mainstays at hospital, who are the largest customers of particle accelerators. These accelerators create radioactive isotopes for medical imaging and novel radiotherapies such as cutting-edge proton therapy.

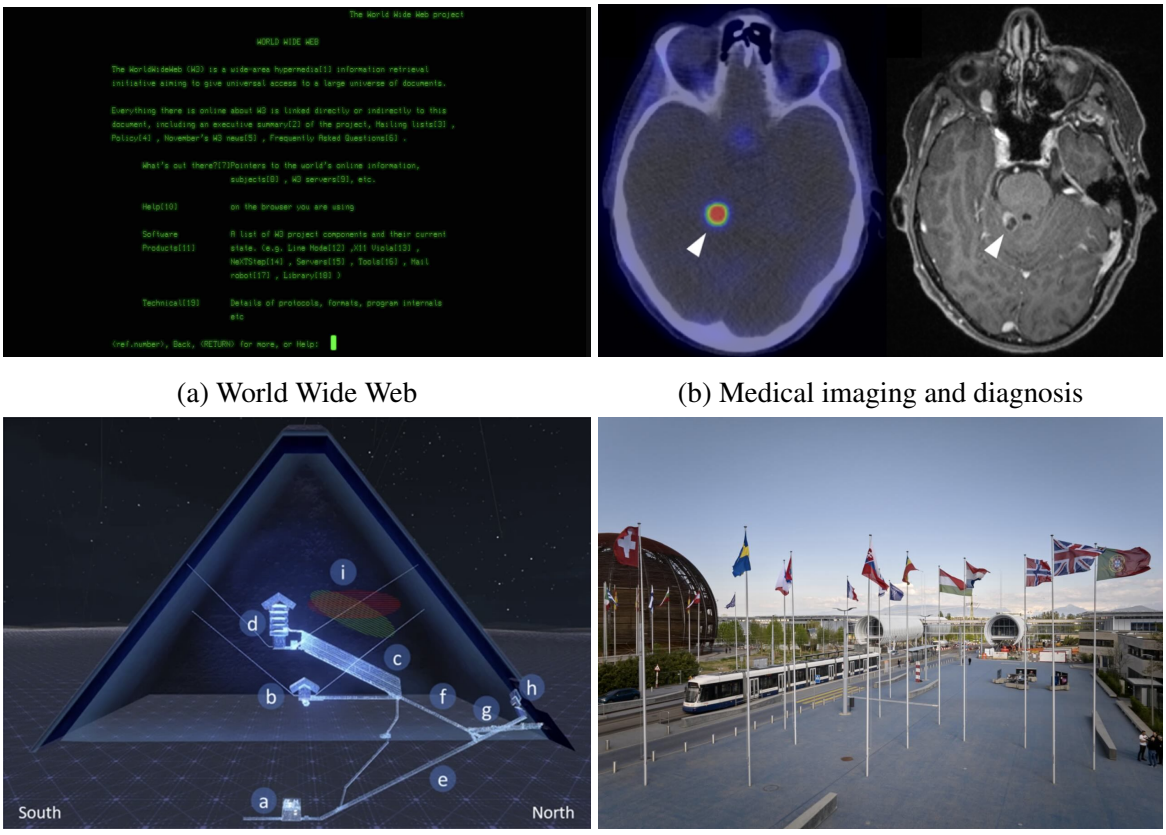

(a) World Wide Web

(b) Medical imaging and diagnosis

(c) Muon archaeology

(d) International relations

Figure 4: **Societal benefits and applications of particle physics**. World Wide Web for distributed information and computing, antimatter and nuclear magnetism applied to positron emission tomography (PET) and magnetic resonance imaging (MRI), cosmic-ray muon imaging revealing a previously unknown void in Khufu's Pyramid, and CERN as a nexus for international cooperation and cultural exchange. Images: CERN [8, 9], Cancer Imaging [10], Nature Communications [11].

Muography for archaeology and volcanology

An innovative interdisciplinary application of particle physics is muography: imaging using muons. As the flux of cosmic-ray muons is constant and well-known, it is possible to image the interiors of large stationary objects by measuring the scattering of incident muons. This recently revealed a previously unknown void in archaeological studies of Khufu's Pyramid, Egypt [11, 12] (figure 4c). This technique is also applied to probe the interior of active volcanoes. This includes the MUon RAdiography of VESuvius (MURAVES) experiment for Mount Vesuvius [13], a famously hazardous volcano given its proximity to Naples, Italy.

International relations

The European Laboratory for Nuclear Research (CERN) was established in 1954 as an international nexus for particle physics in the wake of the Second World War. It is now a model for peaceful international collaboration pursuing goals no single nation can accomplish alone (figure 4d). This is a remarkable feat of international relations and scientific diplomacy even during the Cold War.

In the arena of academic publishing, CERN brokered a landmark agreement called SCOAP^3 [14] with twelve journals, enabling nearly all particle physics publications to be open access since 2014. At a more individual level, these relations enable enriching research abroad experiences e.g. the CERN Summer Student Programme[18] to foster mutual understanding of diverse cultures and nationalities.

International cooperation towards a common goal has never been more important for tackling environmental problems that transcend borders from climate change to biodiversity degradation. This has become a heightened focus in the fundamental physics community given its enduring reliance on resource-intensive international facilities and datasets [15]. CERN has started publishing reports on its goals towards sustainable research practices [16]. No doubt these multi-disciplinary challenges facing our planet will endure in the future of international relations and particle physics.

Economic investment

The long-term benefits of research in fundamental sciences (typically needing decades) is often in tension with short-term timescales (typically a few years) that legislative agendas and research grants demand. By definition, it is challenging to predict what exploratory "blue skies" research will discover or how it will benefit society. Nonetheless, history illuminates an enviable track record.

As the story goes, William Gladstone was the Chancellor of the Exchequer[19] asked what the practical utility of electromagnetism was to Michael Faraday in the 1850s, who apocryphally replied[20]:

> "Why, sir, there is every probability that you will soon be able to tax it!"

From electric lighting and radios to computers and transportation, it would certainly be beyond their wildest dreams what technology is made possible. It would certainly be interesting

[18] https://home.cern/summer-student-programme

[19] The head of the British treasury.

[20] https://www.oxfordreference.com/display/10.1093/acref/9780191826719.001.0001/q-oro-ed4-00004273

to estimate of the tax revenue and business generated worldwide relying on electricity alone compared to the nineteenth century cost of electromagnetism research. With hindsight, this would likely qualify as a robust investment of public resources.

Cultural monuments

Understanding our origins in the cosmos is the bedrock of human culture, inspiring countless students to pursue the sciences. The Standard Model is a monument to human creativity akin to artistic and symphonic masterpieces admired across the centuries. Witnessing the scale of today's particle physics experiments inspires awe just as the engineering feats of ancient pyramids and medieval cathedrals.

One memorable exchange in the bid to fund a new accelerator was Robert Wilson's testimony at Congress in 1969, when US Senator John Pastore inquired:

> "Is there anything connected with the hopes of this accelerator that in any way involves the security of the country?"

Wilson replied rather eloquently[21]:

> "No, sir, I don't believe so…It has to do with: are we good painters, good sculptors, great poets? I mean all the things we really venerate in our country and are patriotic about. It has nothing to do directly with defending our country except to make it worth defending."

Congress subsequently approved funding for the construction of the Fermi National Accelerator Laboratory (Fermilab) just outside Chicago, Illinois.

Scientific literacy

Studying particle physics develops rigorous scientific literacy. These experiments embody exceptionally high levels of systematic control, validation, and reproducibility. Particle physicists set high standards for statistics both because the quality of data and large sample sizes enable such rigour. This training facilitates such individuals to interpret and evaluate the robustness of experiments and statistical analysis in literature from other disciplines. Quantitative reasoning, mathematical modelling, empirical inquiry, and critical thinking open successful careers in computational modelling, data science, finance, medical physics, school education, engineering, and instrumentation. Training such an advanced scientific workforce is a clear near-term benefit for modest investment of public funds.

[21] https://www.aps.org/archives/publications/apsnews/201804/history.cfm

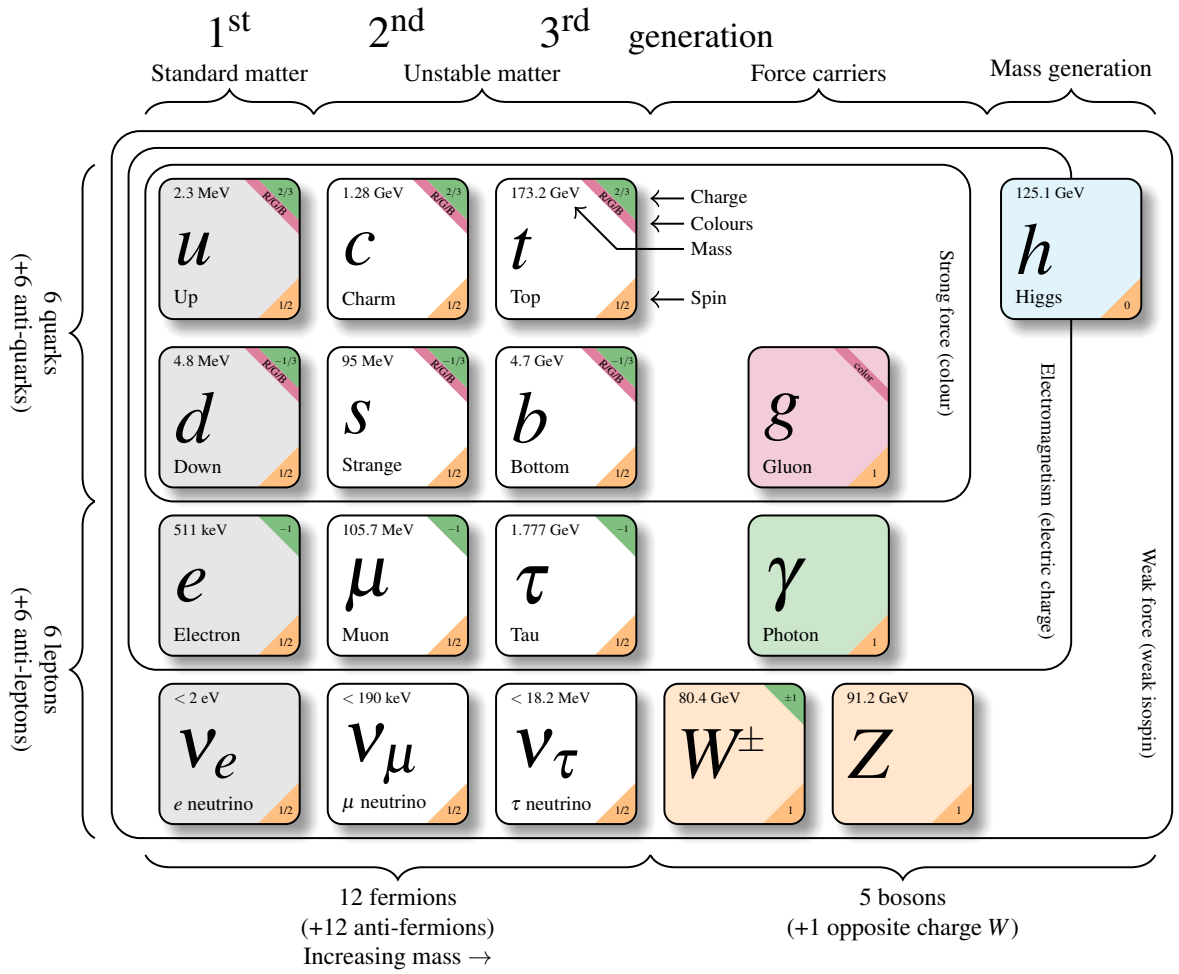

Figure 5: **Standard Model particle content and properties**. This diagram graphically summarises the experimentally known fundamental particles of matter and forces in the Standard Model. Image: adapted from Ref. [17].

1.3 Standard Model in brief

Sufficiently motivated, let us study the Standard Model. Just like arriving disorientated at an unfamiliar city, it is helpful to acquire a map whether for self-exploration or a guided tour. Figure 5 displays the particle content with their main quantum numbers such as mass and charge that underpin their interactions. This course provides a guided tour of the different parts of the SM, and this serves as the initial map to help orient you.

Particle content

The known matter in the universe comprises spin-1/2 particles called fermions categorised into quarks and leptons:

- There are 6 types of **quarks**. The different types are called their **flavour**. Quarks have fractional electric charge in units of 1/3 of the electron's charge.
- The up and down quarks are called the first **generation** of matter, which make up the neutrons and protons in everyday atoms. There are additional generation that have identical properties to the first generation of quarks, except they have heavier masses: these are the charm, strange, bottom and top. Quarks interact with the strong, weak and electromagnetic forces.
- There are 6 types of **leptons**, also called their flavour. The electron is familiar from atoms, and the (anti)electron neutrino emitted in beta decay.
- Leptons have a similar structure to quarks, where there are two copies of the first generation, which again have identical properties except their heavier mass. The heavier generations are the muon and tau-lepton, paired with their corresponding neutrinos. Leptons do not interact via the strong force.
- All the electrically charged quarks and leptons have **antiparticles** that carry opposite charge. Currently, not as much is known about the neutrinos: whether neutrinos have corresponding antiparticles, and only the mass differences between three neutrinos are measured, and there is no lower bound on the absolute neutrino mass.

Fundamental interactions are mediated by bosons with integer spin:

- **Electromagnetism**: this is mediated by a massless spin-1 boson called the **photon**, the quanta of light. These interact with all electrically charged particles.
- **Strong force**: this is mediated by a spin-1 boson called the **gluon**. These interact with all particles with colour charge, namely the quarks (and other gluons).
- **Weak force**: this is mediated by spin-1 bosons called the $W^{\pm}$ and Z bosons, or **massive gauge bosons**. These interact with particles that carry weak isospin charge, which all left-handed fermionic matter carries.
- **Mass generation**: at a fundamental level, mass is a unique manifestation of an interaction with a spin-0 boson called **Higgs boson**. This particle was observed in 2012 at

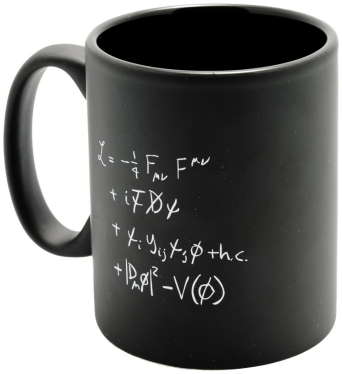

$$
\begin{aligned}
\mathscr{L} = & -\tfrac{1}{4} F_{\mu\nu} F^{\mu\nu} && \text{Force carriers} \\
& + \mathrm{i}\bar{\psi}\gamma^{\mu} D_{\mu}\psi && \text{Matter–force interactions} \\
& + \psi_i y_{ij} \psi_j \phi && \text{Matter masses \& flavour mixing} \\
& + |D_{\mu}\phi|^2 && \text{Force carrier masses} \\
& - V(\phi) && \text{Higgs mass \& self-interactions}
\end{aligned} \tag{1.6}
$$

Figure 6: **Standard Model Lagrangian art**. This summarises the mathematical structure of matter and forces. The role of each term is heuristically described and unpacking its details is a central goal of this class. The mug is available as CERN merchandise and this Ref. [18] provides a lucid account accessible for high-school teachers and students. Image: CERN.

the Large Hadron Collider and it is the physical manifestation of the scalar field that generates mass for the quarks, charged leptons along with the $W^{\pm}$ and Z bosons.

- **Gravity**: this is mediated by a spin-2 tensor field whose fluctuations are gravitational waves recently detected in 2016. The LHC probes energy regimes far below the Planck scale $E \ll M_{\text{Planck}} = \sqrt{\hbar c/G} \approx 10^{19}$ GeV. The strength of gravitational interactions has at least $1/M_{\text{Planck}}$ suppression, rendering negligible impact on particle physics.

Underlying principles

It is worth emphasising that particle physics is much more than discovering elementary particles. Indeed chemistry is no longer about discovering new chemical elements, but it remains an active and extraordinary discipline. Underpinning the periodic table of chemical elements are organising principles of quantum mechanics for its structure. Figure 6 illustrates this organising principle more mathematically. This shows the SM Lagrangian that fits neatly onto the widely-seen mug available at the CERN store. It appears remarkably simple because it is highlighting the mathematical *structure*, suppressing many details. This structure already shows how the wildly different observed behaviour of the fundamental forces actually share similar underlying physics. Figure 7 makes this similarity pictorially manifest. All four interaction diagrams share the same graph structure: two solid lines (fermionic matter and antimatter) meeting with one squiggly (spin 1) or dashed (spin 0) line at a vertex. As

mathematical art, there is of course much to unpack in figure 6 but this coffee mug art serves as a helpful memory aid as this course progresses.

Major discoveries in fundamental physics actually did not involve new particles. They instead unveiled new principles overturning prevailing paradigms of nature:

- **Antimatter**. The Dirac equation predicted the existence of a completely new kind of matter that can annihilate with matter into massless photons.
- **Symmetry and conservation laws**. Noether's theorem relates fundamental symmetries to conserved quantities, namely spacetime symmetry and local (gauge) symmetry.
- **Broken discrete symmetries**: long-cherished symmetries of nature, namely parity and charge–parity conjugation, are mysteriously broken in weak interactions.
- **Forces as geometry**. All the fundamental forces are gauge theories, where a local symmetry dictated by a Lie algebra has a geometric interpretation. Gauge theory of forces have a remarkably similar structure to general relativity describing gravity.
- **Vacuum is dynamical**: the vacuum in classical physics is a static and empty, devoid of anything. Particle physics completely upends this idea, revealing that the vacuum is a teeming sea of particles and antiparticles popping in and out of existence.
- **Confinement and asymptotic freedom**: only one fundamental force in nature exhibits this enigmatic feature that binds nuclei together.
- **Mass as breaking of local symmetry**: particle physics radically changes our picture of inertial mass as enigmatically tied to interactions with a scalar field condensate via the Brout–Englert–Higgs mechanism.
- **Quantum field theory**: this is the theoretical framework of particle physics. Fields enable theories to eschew instantaneous action at a distance: they are manifestly local and causal. Upon quantisation, particles are excitations of the same fields permeating the whole universe. Particle physics tests many salient features of QFT.

Instruments enabling discoveries

New experimental instruments and techniques are pioneered in tandem with particle physics discoveries. We can now test the heaviest Standard Model particles and interactions with remarkable compatibility between theory and experiment (figure 9). These notes endeavour to integrate the key experimental methods for revealing the Standard Model:

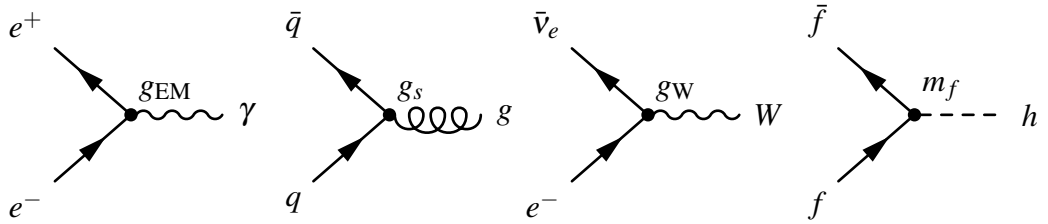

(a) Electromagnetism (b) Strong force (c) Weak force (d) Higgs interaction

Figure 7: **Standard Model interactions vertices**. These graphs show fermionic matter (solid straight lines) interacting with bosonic force carriers for the fundamental forces of particle physics.

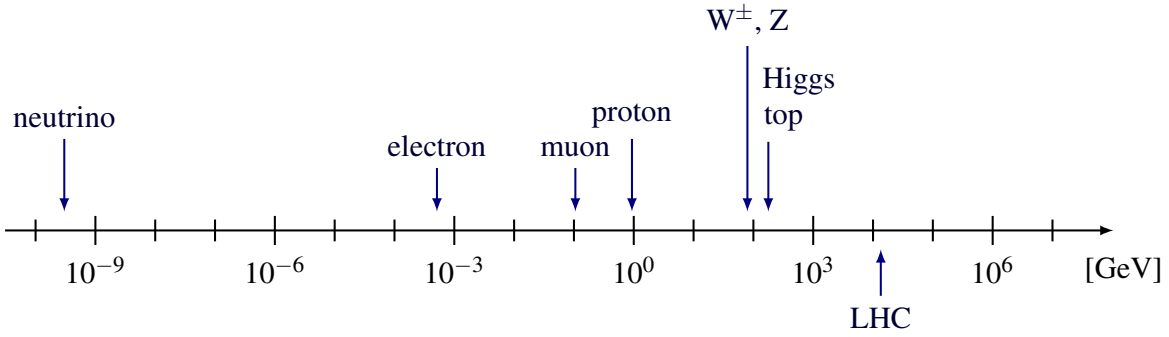

Figure 8: **Masses of selected Standard Model particles**. Also marked is the Large Hadron Collider (LHC) centre-of-mass energy. Adapted from tikz.net.

- **Radiation from the ground and sky**: the discovery of radioactivity and cosmic rays gave physicists a natural source of energetic particles. These played a key role in the foundations of nuclear and particle physics, leading to the discoveries of the strong and weak forces alongside the positron, muon, pion and kaons.

- **Particle accelerators**: Accelerators now reach far higher energies and intensities than natural sources of radiation. This enables the creation of new particles in the controlled environment of in laboratories, ushering many major discoveries. We will briefly touch upon the first linear and circular accelerators, focusing on examples to illustrate their importance for particle physics discoveries. Historically integral to particle physics, accelerator physics has developed into its own vibrant subfield in recent decades.

- **Particle detectors**: inventing new methods to detect particles flying out of colliders is pivotal to discoveries. The principles underpinning the revolutionary cloud chamber and Geiger counter remain largely how we detect particles today. We will also briefly

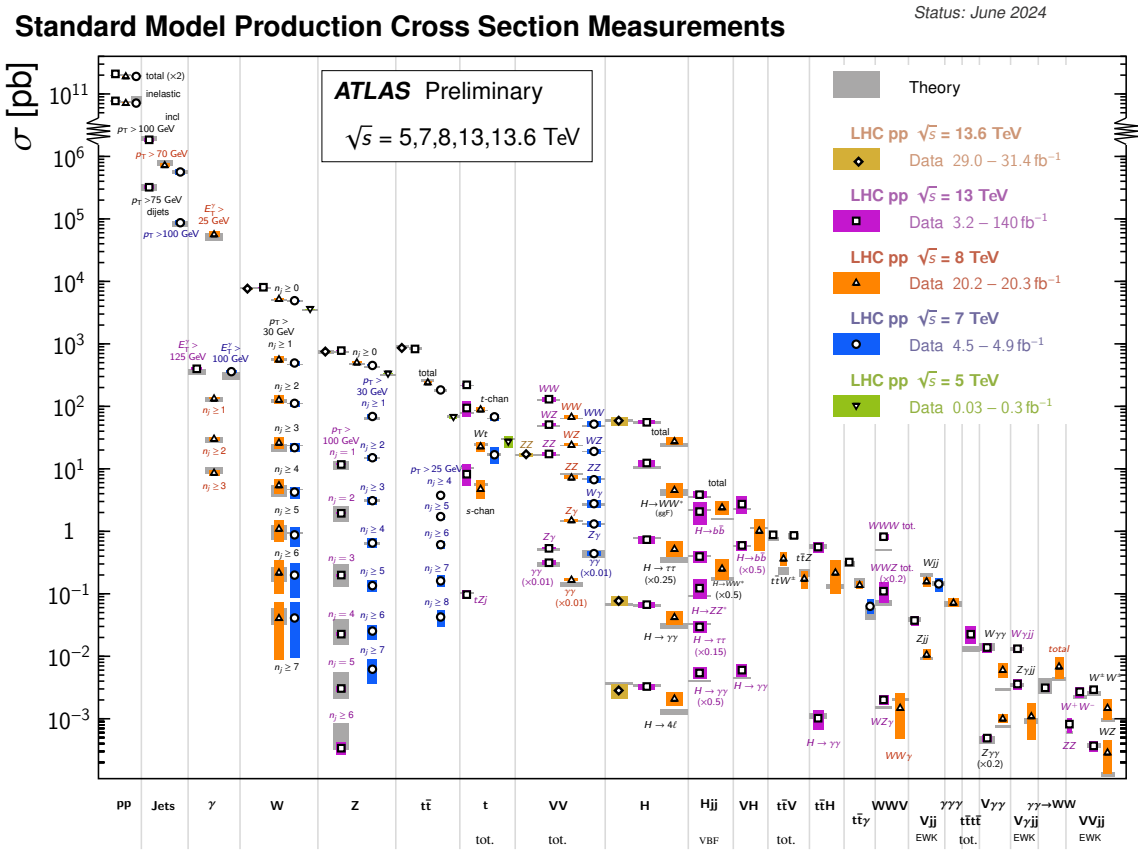

Figure 9: **Standard Model cross-sections at LHC**. Measurements and predictions by the ATLAS Collaboration compared to theoretical calculations for a wide variety of Standard Model processes across different LHC centre-of-mass energies $\sqrt{s}$ [19].

look at photographic emulsions and bubble chamber. After this, we study the general-purpose ATLAS and CMS detectors at the LHC in the context of the electroweak scale.

- **Electronics and computing**: initial particle physics experiments were meticulously by humans recording scintillations by hand or scanning photographs in optical microscopes. As particle event rates and semiconductor technology advanced, particle physics thrived off electronic automation and large-scale computing. We will only mention these topics in passing.

2 Foundational experiments

We start by illustrating landmark experimental discoveries from the late 19th and early 20th centuries. This provided the early evidence for subatomic states that form the foundations of particle physics:

$$\text{electron } (e^-),\ \text{neutrino } (\nu_e),\ \text{proton (p)},$$
$$\text{neutron (n)},\ \text{positron } (e^+),\ \text{muon } (\mu^\pm).$$

These brief accounts in this section far from replace the full history of science, but serve as important reminders for the scientific method of discovery. Experiment repeatedly surprised us. Scientific discoveries are often initially confusing and serendipitous, relying on a multitude of observations and persistent investigation usually over decades to elucidate.

2.1 Radiation and radioactivity

Cathode rays and the electron

The first particle accelerator and signature of electrons were observed in evacuated **Crookes tubes** conceived in 1869 (figure 10a), which are cathode-ray tubes. Electromagnetism was still nascent (Maxwell's equations were written in 1861), but William Crookes, Johann Hittorf and Eugen Plücker found that current can flow from a cathode to anode in the evacuated glass tube, suggesting charged rays. Crucially, they caused glass to fluoresce and phosphorescent materials illustrated their straight-line paths, with metal crosses blocking these rays to cast shadows. Hendrik Lorentz wrote down explicitly the force on moving charges, which can combine with Newton's second law to give

$$\frac{\mathrm{d}\mathbf{p}}{\mathrm{d}t} = m\ddot{\mathbf{x}} = \mathbf{f} = q(\mathbf{E} + \dot{\mathbf{x}} \times \mathbf{B}). \tag{2.1}$$

This shows that particles with the same charge-to-mass q/m ratio behave the same under electromagnetic fields. One can apply the centripetal force $f = mv^2/r$ from the magnetic field onto cathode rays balanced by the electric force $f = qE$ to relate q/m to the measured E and B field strengths:

$$\frac{q}{m} = \frac{1}{r^2}\frac{E}{B}. \tag{2.2}$$

J. J. Thomson performed this in the classic experiment at Cambridge in 1897, measuring the charge-to-mass ratio q/m for cathode rays to be a constant $q/m \approx -1.7 \times 10^{11}\ \mathrm{C\,kg^{-1}}$, three orders of magnitude larger than that of a hydrogen ion.

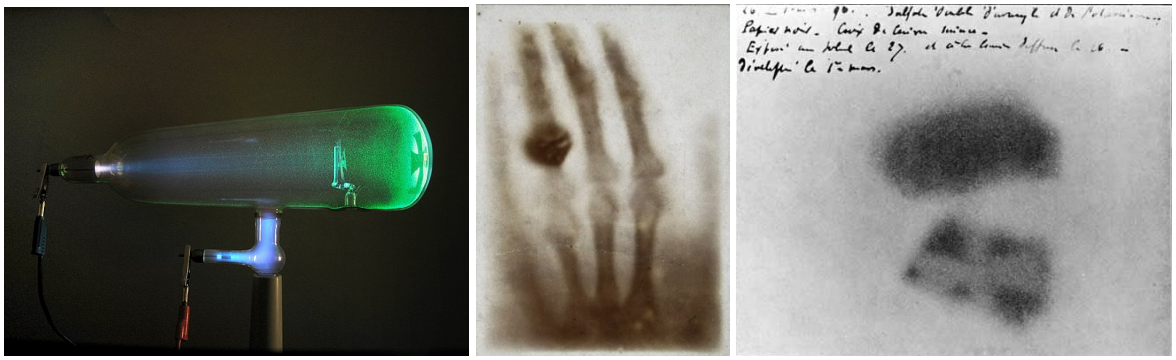

(a) Crookes tube: cathode rays (b) Röntgen: X-rays (c) Becquerel plate: radioactivity

Figure 10: **Discovery of radiation and radioactivity**. Early nineteenth century ray experiments observing: cathode rays emitted in an evacuated Crookes tube (electrons), photographic plates exposed to X-rays (photons), and radioactivity from uranium salts on photographic plate (helium nuclei and electrons). Images: D-Kuru/Wikimedia Commons, Nobel Prize/public domain, Muséum national d'histoire naturelle (Paris).

Of course, measuring this q/m ratio implies either the charge could be 1000 times larger, or the mass were 1000 smaller than hydrogen ions. The latter seemed less implausible, but the only way to experimentally disambiguate this was to directly measure the cathode ray charge. Thomson saw these charged particles cause water vapour to condense into droplets, a primitive cloud chamber. Balancing their gravitational force against an electric field determines the charge to be around 10^{-19} C, the same as hydrogen ions. This was the landmark discovery of the electron.

Like many of his contemporary scientists, Wilhelm Röntgen was also playing around with cathode-ray tubes. He covered one with black card and saw it caused nearby phosphorescent screens to glow green even over a metre away. He had discovered the emission of new invisible rays that could mysteriously travel farther than cathode rays in air, and called them X-rays. He found that they exposed photographic plates and famously imaged (figure 10b) the bejewelled hand of his wife, Anna Bertha Ludwig, which he presented to Ludwig Zehnder at Freiburg in January 1896. This serendipitous discovery caused tremendous excitement and opened the field of X-ray medical imaging that is now ubiquitous in modern society.

Radioactivity

Henri Becquerel was no less fascinated by these newly discovered X-rays and how materials phosphoresce. He was investigating phosphorescence from his uranium salts, which he

thought arose from absorbing solar radiation before re-emitting this energy as X-rays that expose photographic plates.

As the famous story of accidental discovery goes[22], the weather soon turned overcast in Paris and Becquerel stored the uranium salt and photographic plate in a dark drawer away for experiments another sunny day. Whether a moment of inspiration or impatience, he developed the photographic plate anyway on 1 March 1896. Remarkably, he instead saw a high-contrast cross imaged on the plate and reported it to the Academy of Sciences the next day (figure 10c), showing uranium emitted radiation despite not absorbing light from the Sun. Through further investigation, he later found that unlike neutral X-rays, electromagnetic fields could bend rays emitted from uranium salts.

In parallel, Marie Skłodowska-Curie and Pierre Curie discovered more radioactive elements: thorium followed by polonium and radium. In 1900, Paul Villard discovered a new radiation from radium identified as gamma rays. Ernest Rutherford classified these wide-ranging reports of radiation into three categories by their empirical properties of material penetration and ionisation power: alpha α, beta β, gamma γ, X-rays.

These luminaries formulated the fundamental ideas of radioactivity. The decay rate was related to the quantity of radioactive material. In a time interval $\mathrm{d}t$, the decrease in the number of particles $\mathrm{d}N$ is given by the number of such particles N multiplied by its quantum mechanical transition rate $\Gamma/\hbar$ ($\hbar$ being the reduced Planck's constant)

$$\mathrm{d}N = -N(\Gamma/\hbar)\mathrm{d}t. \tag{2.3}$$

Integrating gives the exponential decay formula that is ubiquitous in particle physics

$$N = N_0 \mathrm{e}^{-\Gamma t/\hbar}, \tag{2.4}$$

where we can define the proper lifetime $\tau = \hbar/\Gamma$. In cases where a particle can decay via multiple processes $\{i\}$, where we can ascribe each process i to a partial decay rate Γ_i, and the total decay rate is given by the sum $\Gamma = \sum_i \Gamma_i$.

These monumental discoveries established the instability of matter that can transmute into different elements. While far from obvious then, it also provided the first indirect hints of new fundamental interactions: the strong and weak nuclear forces.

Ionisation and cloud chambers

Meanwhile, groundbreaking instruments were invented and developed to detect radiation. In 1908, Hans Geiger conceived the concept of the **ionisation chamber** [21], using gases to de-

[22] https://www.aps.org/apsnews/2008/02/becquerel-discovers-radioactivity

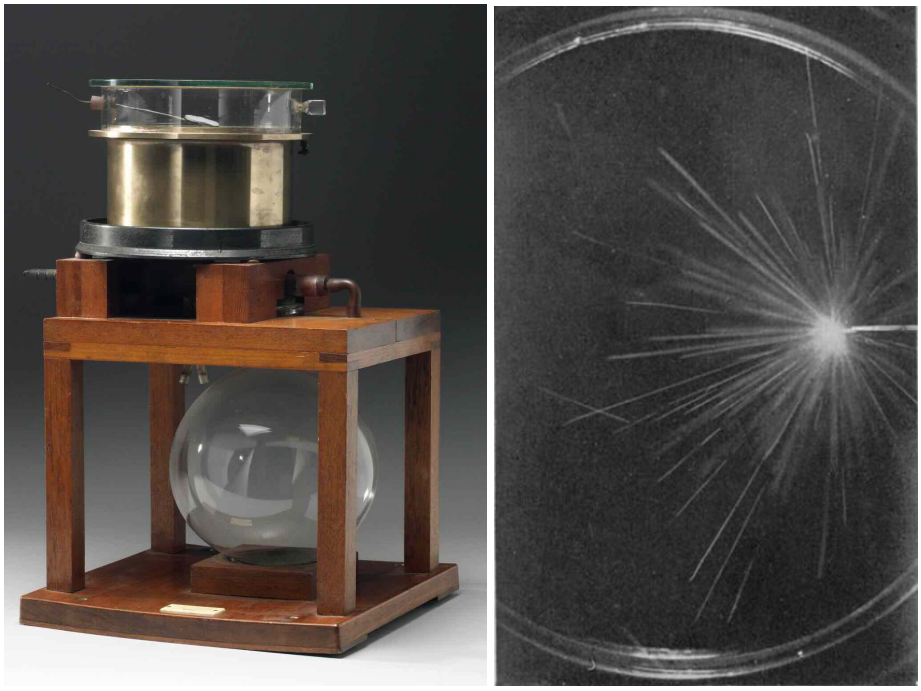

(a) Wilson cloud chamber (b) α-particles [20]

Figure 11: **Wilson expansion cloud chamber apparatus**. The cloud chamber is cylinder on the upper left around 15 cm in diameter. Also displayed is a 1912 photograph of alpha particles from a radium source. Left: Science Museum/UCL.

tect ionising particles. The principle of operation is shown in figure 12a, where a charged particle ionises a medium, inducing a measurable electrical voltage. The underlying physics of ionisation is an incident charged particle imparting sufficient energy to eject an electron originally bound to an atom. The various binding energies of atoms motivate different choices of ionisation media. This is still the fundamental principle used in charged-particle detectors today, including the famous Geiger counter.

Meanwhile, another pivotal instrument developed concurrently was the **expansion cloud chamber**. Inspired by metrological phenomena on a visit to Ben Nevis in Scotland, Charles T. R. Wilson wanted to study cloud formation in the laboratory upon returning to Cambridge. Little did he know this would make profound discoveries not in atmospheric but subatomic physics. Wilson realised by expanding a chamber of humid air, super-saturated vapour condenses in the absence of dust along the path of ionising particles.

By 1911, Wilson perfected the expansion cloud chamber [20, 22], where a piston is pulled to suddenly expand the condensation volume. This expansion is synchronised to a

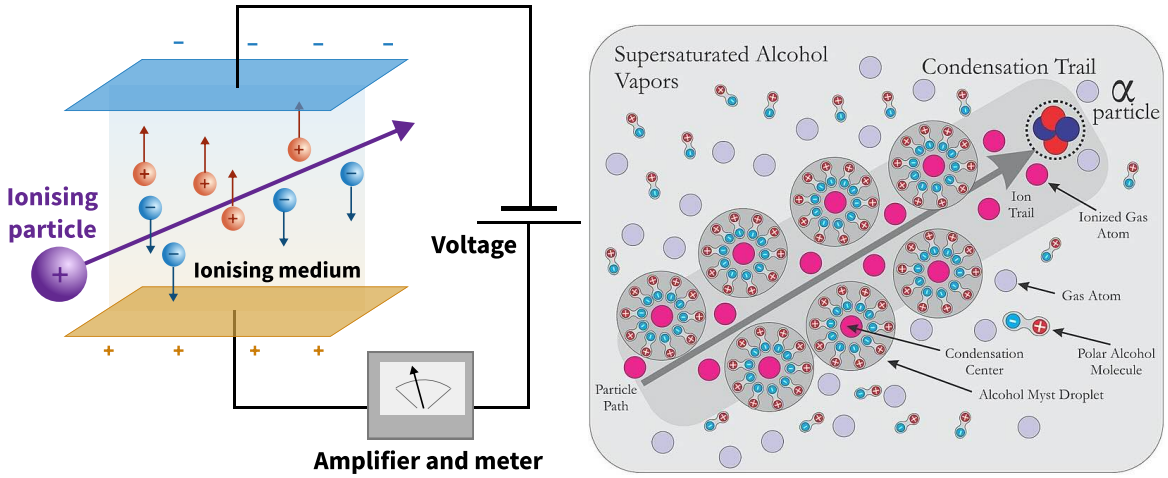

(a) Ionisation chamber (b) Diffusion cloud chamber

Figure 12: **Ionisation principles of particle detection**. A charged particle enters the ionising medium, causing this the atoms to ionise along its path. This causes a current to flow between a cathode and anode biased by a voltage, which can be amplified and measured. This principle remains the basis for how today's charged-particle detectors function. Right image: Kotarak71/Wikimedia.

flash of light and camera to record the resulting particle tracks. This enabled taking stunning photographs of charged particles (figure 11a) that would have an illustrious record of groundbreaking discoveries in ensuing years. The bubble chamber, a mainstay for particle detection in the 1960-70s, is based on similar principles but with liquid turning into gas upon ionisation (section 8). A popular education and outreach tool today is the diffusion cloud chamber[23], where a future iteration of this class with sufficient resources may consider building one as a class project.

Indirect evidence for neutrinos

At this point, it is worth mentioning the indirect evidence for neutrinos in beta decay. An everyday example of β^- decay is potassium-40 present in e.g. bananas, which can decay to calcium-40 via emission of an electron e^- and electron anti-neutrino $\bar{\nu}_e$:

$$^{40}_{19}\mathrm{K} \rightarrow ^{40}_{20}\mathrm{Ca} + e^- + \bar{\nu}_e. \tag{2.5}$$

[23] https://scoollab.web.cern.ch/cloud-chamber: CERN S'Cool LAB has a DIY manual for how to build one using isopropyl alcohol and dry ice.

Nuclear beta decay involves a change of proton number Z leaving the nucleon/mass number A unchanged. This is equivalent to a neutron decaying into a proton:

$$n \to p + e^- + \bar{\nu}_e. \tag{2.6}$$

Historically, there are two classic arguments for the existence of a third unobserved particle in β^- decay, now known as an anti-neutrino:

1. **Energy spectrum of electron**. Working in the rest frame parent nucleus, the resulting products of a two-body decay $\mathrm{X} \to e^-\mathrm{Y}$ should be equal and opposite in momentum. The emitted electron E_e should have a well-defined peak related to the masses of the parent and child particles given by energy-momentum conservation of equation (3.15):

   $$E_e = \frac{m_X^2 - m_Y^2 + m_e^2}{2m_X}. \tag{2.7}$$

   However, his process is not observed:

   $$^{40}_{19}\mathrm{K} \to {}^{40}_{20}\mathrm{Ca} + e^- \quad \text{2-body decay not observed.} \tag{2.8}$$

   This is inferred from the observation by James Chadwick that beta decay has a spectrum of energies. This is the hallmark of a three (or more) body decay.

2. **Conservation of angular momentum**. The initial neutron on its own is spin-$\frac{1}{2}$. If a proton and electron, both spin-$\frac{1}{2}$ states, were the only final states, the total final angular momentum numbers[24] are $S = 0$ or 1. Angular momentum conservation require an additional spin-$\frac{1}{2}$ particle to exist. Three spin-$\frac{1}{2}$ particles couple together to give total angular momentum numbers of $S = \frac{1}{2}$ or $\frac{3}{2}$.

The continuous spectrum of electron was historically a vexing mystery about β^- decay. If you measured the electron energy by bending them through a magnetic field and noting their radii, the spectrum is continuous has a maximum energy at 1.3 MeV like those from figure 13a. To resolve this apparent non-conservation of energy and momentum, Wolfgang Pauli proposed in 1930 that an invisible particle, which we now know to be the electron antineutrino $\bar{\nu}_e$, is carrying away the electron energy:

$$n \to p + e^- + \bar{\nu}_e \quad \text{3-body decay is observed.} \tag{2.9}$$

This explains how the available kinetic energy is shared between the electron and anti-neutrino in three-body decays. This constitutes indirect evidence for the existence of neutrinos. It took the advent of nuclear reactors and the Cowan–Reines experiment to enable direct detection of anti-neutrinos in 1956 (section 12.2).

[24] Recall the rules of angular momentum addition regarding the quantum numbers. For two particles with spins s_1 and s_2, the total spin numbers are $S = |s_1 - s_2|, |s_1 - s_2| - 1, \ldots, s_1 + s_2 - 1, s_1 + s_2$.

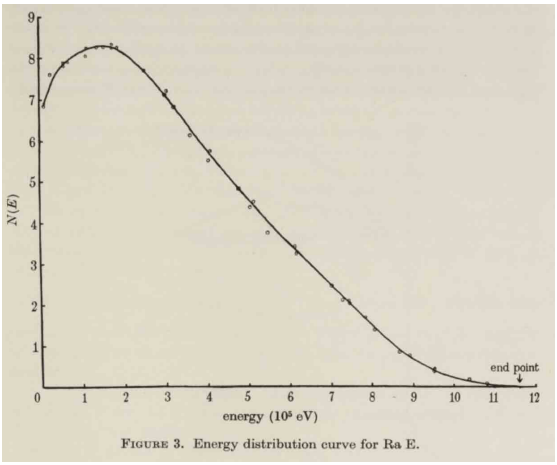

(a) Beta decay measurements [23].

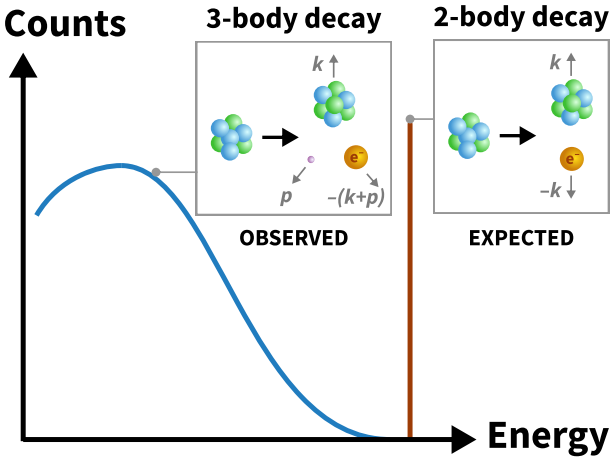

(b) Energy: 2 vs 3 body decay.

Figure 13: **Beta decay spectrum**. The early expectation of a two-body decay sees the child nucleus and electron having equal and opposite momentum, resulting in a sharp peak in energy from equation (2.7). The observed three-body decay features an additional anti-neutrino with momentum **p** smearing out the observed spectrum into a continuum.

2.2 Nuclear scattering

When we first hear the famous story of Hans Geiger, Ernest Marsden, and Ernest Rutherford discovering the atomic nucleus and proton at Manchester, we naturally ask what made them fire alpha particles at metal foils in the first place? Perhaps it was just a benign task to keep the new student Marsden busy? There was little reason to doubt J. J. Thomson's then prevailing plum-pudding model of electrons spread evenly throughout an atom.

It turns out they were actually investigating a seemingly unrelated detector imperfection. The new ionisation chamber Geiger invented in 1908 occasionally made unexplained erratic measurements from traversing alpha particles. This motivated more systematic characterisation of how alpha particles interact with matter, in another case of one advance opening further serendipitous discoveries.

Discovery of atomic nucleus

They designed their classic experiment, firing alpha particles from a radium source at metallic foil and measured how the alpha particles scattered across angles ϕ (figure 14a). They preferred gold foil due to its malleability and they could press it very thin. As a detector, they used a zinc sulfide screen that fluoresced upon being struck by scattered alpha particles. One

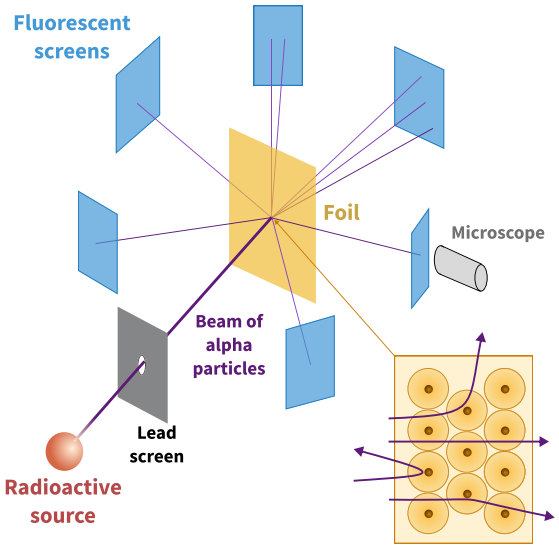

(a) Schematic of scattering experiment

610 Dr. H. Geiger *and* Mr. E. Marsden *on the Laws of*

TABLE II.

Variation of Scattering with Angle. (Collected results.)

I. Angle of deflexion, ϕ.	II. $\frac{1}{\sin^4\phi/2}$	III. Silver. Number of scintillations, N.	IV. Silver. $\frac{N}{\sin^4\phi/2}$	V. Gold. Number of scintillations, N.	VI. Gold. $\frac{N}{\sin^4\phi/2}$
150°	1·15	22·2	19·3	33·1	28·8
135	1·38	27·4	19·8	43·0	31·2
120	1·79	33·0	18·4	51·9	29·0
105	2·53	47·3	18·7	69·5	27·5
75	7·25	136	18·8	211	29·1
60	16·0	320	20·0	477	29·8
45	46·6	989	21·2	1435	30·8
37·5	93·7	1760	18·8	3300	35·3
30	223	5260	23·6	7800	35·0
22·5	690	20300	29·4	27300	39·6
15	3445	105400	30·6	132000	38·4
30	223	5·3	0·024	3·1	0·014
22·5	690	16·6	0·024	8·4	0·012
15	3445	93·0	0·027	48·2	0·014
10	17330	508	0·029	200	0·0115
7·5	54650	1710	0·031	607	0·011
5	276300	...	...	3320	0·012

(b) Deflection results [24]

Figure 14: **Manchester Geiger–Marsden–Rutherford experiment**. Schematic of experimental setup and deflection results supporting the subatomic nucleus theory and discovery of proton.

day, Rutherford suggested they see how many reflected back on itself and found a few out of 10,000 reflected back, which was a complete surprise.

Rutherford proposed a central positively charged nucleus with negatively charge surrounding it [25]. A textbook calculation of mechanics textbooks assuming Coulomb's law with conservation of energy and momentum gives the Rutherford differential cross-section

$$\frac{\mathrm{d}\sigma}{\mathrm{d}\Omega} = \left(\frac{zZe^2}{4\pi\varepsilon_0}\frac{1}{4E}\right)^2 \frac{1}{\sin^4(\theta/2)}, \tag{2.10}$$

where ze (Ze) is the incident (target nucleus) electric charge, $E = mv^2/2$ is the incident alpha-particle kinetic energy, θ is the scattering angle[25] and $\mathrm{d}\Omega = \sin\theta \mathrm{d}\theta\mathrm{d}\phi$ is the differential solid angle. Geiger and Marsden painstakingly counted scintillation hits in a darkened laboratory[26] on florescent zinc sulfide screens viewed through a microscope as they rotate through different angles to establish the high-statistics datasets. Figure 14b shows the results from the 1913 paper, where the meticulously collected data of scintillation hits $N(\theta)$ support the predicted $\sin^{-4}(\theta/2)$ dependence from Rutherford's calculations.

[25] In the historic papers (figure 14b), they use ϕ.

[26] Manually without digital electronics or computers. Scientists certainly have great patience.

Discovery of neutron

The story of the neutron discovery [26] starts with Herbert Becker and Walther Bothe in Berlin, 1930. They bombarded a beryllium target with alpha particles from a polonium source. They noticed an unknown form of highly penetrating radiation that was energetic and electrically neutral. Back then, the only known candidate for this mysterious neutral radiation was a gamma ray:

$$ {}^{4}_{2}\alpha + {}^{9}_{4}\mathrm{Be} \rightarrow {}^{13}_{6}\mathrm{C} + \gamma \quad ? \tag{2.11} $$

In the ensuing years at Paris, Irène and Frédérick Jolio-Curie[27] (figure 15a) extended the Becker–Bothe experiment. They directed the invisible radiation from the bombarded beryllium target onto paraffin wax, which is a hydrocarbon $\mathrm{C}_n\mathrm{H}_{2n+2}$ used in candles rich in hydrogen, and reported energetic protons being ejected [27]. Whatever this invisible radiation was, it was powerful stuff to knock out hefty protons. They had found evidence for the existence of a new kind of radiation, but still misidentified it as gamma rays. This was the experimental setup of what was happening:

$$ \boxed{\begin{array}{c}\text{Polonium}\\ \text{source}\end{array}} \xrightarrow{\text{alphas}} \boxed{\begin{array}{c}\text{Beryllium}\\ \text{target}\end{array}} \xrightarrow{\text{neutrons}} \boxed{\begin{array}{c}\text{Paraffin}\\ \text{wax}\end{array}} \xrightarrow{\text{protons}} \boxed{\begin{array}{c}\text{Ionisation}\\ \text{chamber}\end{array}} $$

These pioneers had not realised they discovered the neutron, but there were intriguing reasons the scientific community were both reluctant and expecting it. Indeed upon hearing the Jolio-Curie experiment, Ettore Majorana purportedly exclaimed [26]:

> "These fools have discovered the neutral proton and are not aware of it."

Back in the 1920s, scientists already noticed atomic mass numbers A increased quicker than the proton number Z, which you can see on the first rows of the periodic table (figure 1). High school students today easily ascribe this mismatched progression to neutrons. So why was history slow to propose this? It was because there was a seemingly reasonable idea that atomic nuclei contained neutral bound states of one proton with one electron. This appeared sensible to explain how beta decay induced atoms to emit electrons with MeV energies, far higher than eV energies of electrons surrounding the nuclei.

James Chadwick had sought such a neutral bound nuclear state for many years while working at Cambridge. When he heard the results from the Joliot-Curie experiment in January 1932, Chadwick quickly reproduced their experiment with the interpretation of a new

[27] Irène Curie is the daughter of Marie and Pierre Curie, who married Frédérick Jolio, and pursued research efforts together from c. 1928.

(a) Irène & Frédérick Jolio-Curie (b) Ejected proton (c) Chadwick ionisation chamber

Figure 15: **Discovery of neutron via proton ejection**. The photograph displays the aftermath of alpha particles bombarding a beryllium target, producing an e^+e^- pair from gamma ray conversion together with the thick track showing a proton that had been ejected by a neutron. Chadwick used an ionisation chamber to detect the ejected protons. Images: Gallica and London Science Museum, Cambridge Cavendish Laboratory.

particle called the neutron [28]:

$$ {}^4_2\alpha + {}^9_4\mathrm{Be} \rightarrow {}^{12}_6\mathrm{C} + {}^1_0\mathrm{n}. \tag{2.12} $$

The ionisation chamber used by Chadwick is displayed in the Cavendish Laboratory museum at Cambridge (figure 15). While history of science often cites Chadwick discovering the neutron, the first empirical evidence was already present in the Becker–Bothe and Jolio-Curie experiments.

2.3 Cosmic rays

This class mostly highlights cosmic rays as a natural source of high-energy particles before the advent of accelerators and its central role in unveiling the Standard Model. Today, cosmic-ray physics is its own vibrant field and the High Energy Astrophysics (PHYS-GA 2050) classes cover its phenomena in greater detail.

The first indirect signature of cosmic rays, with hindsight, dates back to Charles-Augustin de Coulomb (1785) reporting spontaneous discharge of electrostatic devices no matter how well-insulated he made them[28]. These enigmatic observations were confirmed by Michael Faraday (1835), while Cano Matteucci (1850) and William Crookes (1879) observed how their rate decreased at lower atmospheric pressures [29].

[28] https://timeline.web.cern.ch/first-observations-spontaneous-discharge-electrometer

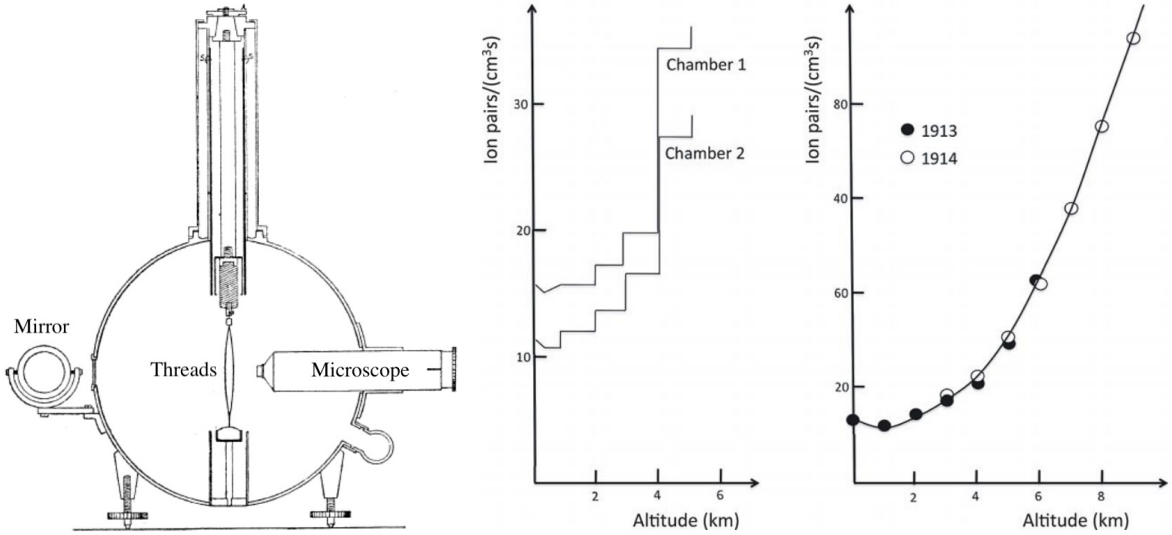

(a) Wulf electroscope

(b) Hess and Kolhörster 1912–14 balloon data

Figure 16: **Historical measurements of cosmic-ray flux**. Electroscopes measure ionisation by observing metallic threads under tension during electrostatic discharge. This enabled balloon-bourne measurements by Hess (1912) and Kolhöster (1913), illustrating the increase in flux with altitude. Images: Wulf, Phys. Zeit. 1 (1909) 152, Ref. [29].

Once radioactivity was discovered, the expectation was that the radiation should decrease with altitude assuming rocks on Earth were the sole source. Individuals including Theodore Wulf[29] and Domenico Pacini [30] presented initial evidence for the altitude dependence of radiation above and below sea level, respectively. More portable and sensitive electroscopes to measure electrostatic charge were crucial advances, which Wulf improved by replacing conventional gold leaves with metalised threads (figure 16a).

In 1912, Viktor Hess initiated the pivotal balloon-bourne measurements using Wulf electroscopes up to 5 300 m [31] (figure 16b). Electroscopes were a common ways to measure the presence of charged particles during the development of electromagnetism, often comprising gold leaves or torsion balance that detects electrostatic repulsion. With further measurements at higher altitudes over 8 km by Werner Kolhörster in 1913–1914 provided further evidence, leading to the decisive discovery of cosmic rays.

Growing interest in mountaineering around this period certainly helped those who did not fancy venturing into hot-air balloons. Many groundbreaking cosmic-ray experiments were exposed to radiation at high mountains, where photographic emulsion plates can be left

[29] https://www.aps.org/apsnews/2019/08/wulf-publishes-evidence-cosmic-radiation

undisturbed for long exposures. We shall defer this discussion of pions and kaons discovered in cosmic rays to section 8 on the strong force.

Positron and antimatter discovery

Figure 17a shows the iconic positron e^+ track as the dark track inside a Wilson cloud chamber. Anderson constructed a $(17\text{ cm})^2 \times 3$ cm chamber and took several photos of cosmic rays in Pasadena, California. The dark horizontal rectangle in the middle is a lead plate that slows down the particle, where the tighter bend above than below the lead plate implies its trajectory must be upwards. One of the innovations of was to immerse the cloud chamber in a magnetic field for charge and momentum determination via the Lorentz force law (2.1). The relationship between the momentum magnitude p traversing perpendicular to a magnetic field B with bending radius R is given by

$$\frac{p}{\text{GeV}/c} = k\left(\frac{B}{1\text{ Tesla}}\right)\left(\frac{R}{1\text{ metre}}\right), \quad k \approx 0.3 \tag{2.13}$$

This serves as a remarkably ubiquitous formula for the bending of a relativistic charged particle in accelerators and detectors. Bending anti-clockwise in the 1.5 T magnetic field pointing into the page, the particle must be positively charged. By measuring the curvature, the deduced momentum is 63 MeV below and 23 MeV above the plate.

The only known positively charged particle at the time was the proton. By assuming a proton mass, one could deduce its energy from the measured momentum. Counting the droplets per unit length, this determined the particle ionisation properties and the mean path length based on its energy. Anderson noted that the path length was "at least ten times greater than the possible length of a proton path of this curvature". By accumulating several such tracks, the mass of the particle was determined to within 20% of the electron mass. This was the stunning discovery of the **positron** and **antimatter**.

Historically and even today, experimentalists and theorists did not always appreciatae each other's work even while neighbours. When Paul Dirac published his eponymous equation in 1928 (section 3.2), few took its negative energy states seriously as physical reality. Patrick Blackett and Giuseppe Occhialini were contemporaries of Dirac at Cambridge, but were busy inventing a groundbreaking new toy in 1931: the **counter-controlled cloud chamber**. They ingeniously combined a pair of Geiger-Muller tubes sandwiching above and below a Wilson cloud chamber.

Upon traversal by an energetic cosmic ray, the Geiger–Muller tubes send an electronic signal to **trigger** the cloud chamber piston and camera shutter: neat automation underpinning all triggers of today's experiments. By contrast, Anderson's cloud chamber randomly took

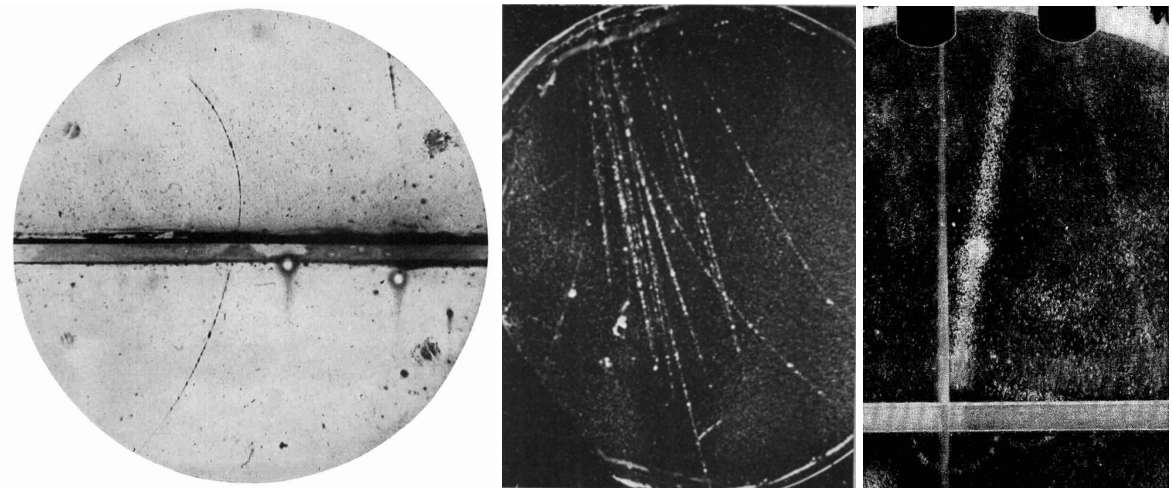

(a) Positron track [32] (b) e^-e^+ pairs [33] (c) Muon track [34]

Figure 17: **Cloud chamber discovers antimatter and muon**. (a) The dark line curving upwards anti-clockwise is the positron (B field into page). (b) The original caption writes two electrons bending clockwise, which are rather faint on the left, with two positrons bending anti-clockwise on the right of the image (B field into page). (c) The muon is the thick line.

pictures even if there were no energetic ionising particles, so he had to sift through thousands to find the positron. When Blackett and Occhialini heard Anderson's stunning discovery, they checked other photos from their new device and realised it had recorded positrons all along in great abundance (figure 17b). In a 1933 paper with a terribly understated title "Some photographs of the tracks of penetrating radiation" [33], they discovered e^-e^+ **pair production** via unmistakable mirror-image curving tracks.

In the backdrop of the positron discovery and their earlier experiments creating neutrons, the Joliot–Curies continued their pioneering work bombarding aluminium with alpha particles to create phosphorus:

$$ {}^{4}_{2}\alpha + {}^{27}_{13}\mathrm{Al} \rightarrow {}^{30}_{15}\mathrm{P} + {}^{1}_{0}\mathrm{n}. \tag{2.14} $$

This isotope of phosphorus-30 is special because it decays via positron emission with a half-life of 2.5 minutes, providing first evidence for β^+ decay:

$$ {}^{30}_{15}\mathrm{P} \rightarrow {}^{30}_{14}\mathrm{Si} + e^+ + \nu_e. \tag{2.15} $$

This novel synthesis of radioactive elements emitting positrons marked the first **laboratory production of antimatter** in 1934[30]. It is also central to nuclear medicine for the creation of radioactive isotopes at hospitals.

[30]The Jolio–Curie pair received the 1935 Nobel prize in chemistry for this discovery, the same year the prize

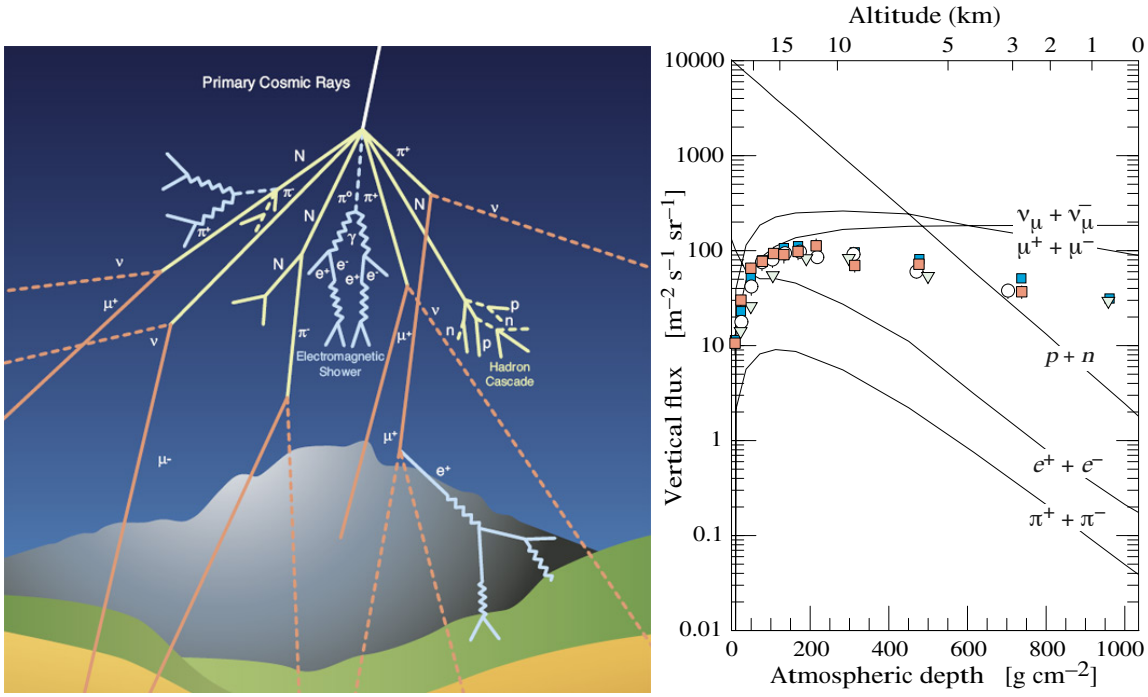

(a) Cosmic-ray air shower CERN (b) Flux composition with altitude [35]

Figure 18: **Cosmic-ray air showers**. Schematic drawing of extensive air shower induced by primary cosmic-ray striking the an atmopsheric nucleus. The contemporary flux vs altitude uses points to show various measurements of $E > 1$ GeV muons μ^-.

The muon: who ordered that

What we now call the muon was initially spotted in 1936 as cloud chamber tracks with anomalously low ionisation by Seth Neddermeyer and Carl Anderson [36] and independently by J. Street and E. Stevenson [34]. The particle (figure 17c) is assumed to have the same charge as an electron, but the reduced ionisation suggested this was a new particle with a mass in between that of an electron and proton. It was a initially misidentified as the meson responsible for binding nuclei together that Hideki Yukawa predicted just a little earlier in 1935 predicted to be around 200 MeV.

Theory and experiment seemed to be lining up nicely. However, Rossi and Nereson measured the lifetime in 1943 to be 2.2 ± 0.2 μs [37], longer than that expected for Yukawa's meson. Then in 1946 at Rome, M. Conversi, E. Pancini and O. Piccioni [38] measured the absorption rate of this particle when fired at iron and carbon nuclear targets. They saw very poor

in physics went to Chadwick for the neutron.

absorption by nuclei compared to that predicted by Yukawa's mesons. Something appeared terribly inconsistent about this particle being the mediator of the strong force. Fortunately, cosmic-ray measurements by the Bristol group had identified the pion in 1947, which we shall see in section 8.

The muon is now known as the heavier cousin to the electron, possessing the same properties except its mass. Its existence is completely unexpected. It is the first particle discovered beyond the first generation, opening the **problem of flavour**. Why are there different generations of matter? We do not know. Isodor Rabi famously quipped "who ordered that?" in reacting to the muon. This remains an open question in physics today.

Contemporary cosmic-ray spectrum

For completeness, let us briefly finish the story of cosmic rays here given their astrophysical origins are less mysterious than a century ago. Figure 18b shows the contemporary fluxes [35] of various particles with altitude, dominated by muons and neutrinos before transitioning to protons above $\gtrsim 7$ km. Atmospheric neutrinos underpin the discovery of neutrino oscillations (subsection 16.2). Figure 19 shows a composition of state-of-the-art cosmic-ray energy spectra measured by experiments worldwide and in space. The flux approximately follows a steep power law

$$\frac{\mathrm{d}N}{\mathrm{d}E} \propto E^{-\gamma}, \quad \gamma \approx 2.7. \tag{2.16}$$

The vertical axis is multiplied by E^2 to improve clarity. The plot indicates the flux of cosmic ray events per area per second as diagonal bands.

Measurements today are broadly divided into two classes:

- **Space-based low energy**. At low energies $E \lesssim 10^5$ GeV, the flux is sufficiently large that space-based experiments located in orbit can directly measure the primary cosmic ray. The first dedicated space-based cosmic-ray detector was the Payload for Antimatter Matter Exploration and Light-nuclei Astrophysics (PAMELA) and an ongoing experiment is the Alpha Magnetic Spectrometer (AMS-02) on the International Space Station. Cosmic Ray Energetics and Mass (CREAM) was a high-altitude balloon detector launched in Antarctica.

  These provide high granularity measurements up to 10^5 GeV for hadrons and 10^3 GeV for electrons above which the space-based detectors are too small to accumulate sufficient statistics. The detectors possess particle identification capabilities between hadrons, electrons, positrons, and photons. They can also distinguish nuclei species

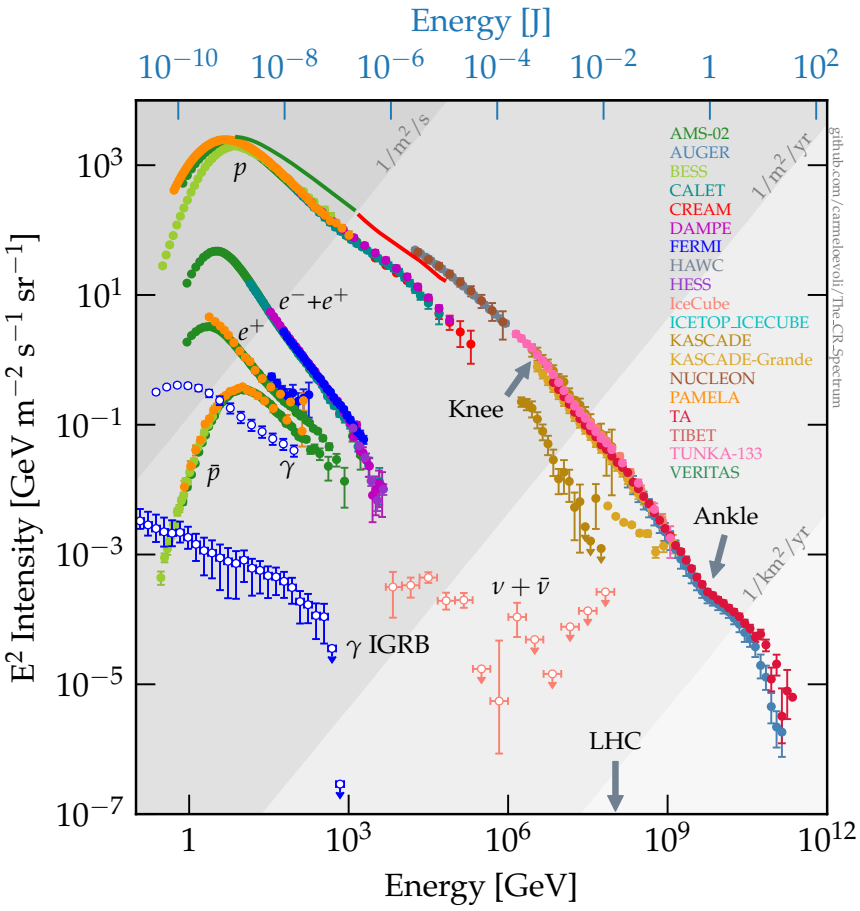

Figure 19: **Cosmic-ray energy spectrum**. The intensity is multiplied by a factor of E^2. Space-based measurements with composition identification are possible below $\lesssim 10^5$ GeV (coloured points), above which ground-based observatories are needed and only measure all-particle fluxes (black points). The main text briefly discusses the knee and ankle features. Figure from Ref. [39].

via mass spectrometry, showing that helium, oxygen to iron are not insignificant compared to protons.

- **Ground-based high energy**. At high energies $E \gtrsim 10^5$ GeV, large exposure areas are required to gather statistics at ground-based observatories. These require arrays of Cerenkov detectors covering large areas $\gtrsim 100$ km^2. However, such experiments cannot directly measure the chemical composition of the cosmic rays. They can only measure the secondary **extensive air showers** after the impact of the primary cosmic-ray particle. Non-perturbative dynamics of the strong force underpin the initial stages

of the hadron interactions, requiring phenomenological models tuned to LHC data [40]. The largest of these air shower arrays include the Telescope Array in Utah, KASCADE and Pierre Auger Observatory in Argentina. They measure the atmospheric Cerenkov light induced by such showers, effectively turning the atmosphere into a calorimeter.

Figure 19 shows interesting kinks in the spectrum deviating from the $E^{-2.7}$ trend: the **knees** around 10^{15} eV and 10^{17} eV, and **ankle** just above 10^{18} eV. Cosmic rays below $\lesssim 10^{16}$ most likely originate from inside our Milky Way galaxy. A conventional interpretation of the knees arise from supernova remnants accelerating protons to a maximum energy $E_{\text{max}}^{\text{proton}} \sim 10^{15}$ eV, sometimes called pevatrons. This scales with the nuclei proton number as

$$E_{\text{max}}(Z) = Z \times E_{\text{max}}^{\text{proton}}. \tag{2.17}$$

So the knee arises from the rate of galactic protons falling off in favour of heavier nuclei up to iron, which then also falls off at the second knee. This also coincides with the critical energies needed for extragalactic cosmic rays to penetrate our galaxy's magnetic field. This gives rise to the ankle around $E \sim 5 \times 10^{19}$ eV and by studying the arrival direction, the Auger collaboration recently reported evidence supporting their extragalactic origins [41]. Finally, the suppressed flux at the most extreme energies $E \sim 10^{20}$ eV corresponds to This likely arises from protons colliding with photons from the cosmic microwave background creating an excited Delta baryon

$$p + \gamma_{\text{CMB}} \to \Delta^{+} \to \begin{cases} p + \pi^{0} \\ n + \pi^{+} \end{cases} . \tag{2.18}$$

This is called the Greisen–Zatsepin–Kuzmin (GZK) cutoff first hypothesised in 1966.

3 Relativistic quantum mechanics

Having covered the pioneering experiments from the early twentieth century that gave birth to particle physics, we now briefly review the contemporary theoretical concepts from special relativity and quantum mechanics. This also conveniently establishes mathematical notation and units. We then make these two theories compatible, leading to the Dirac equation, the relativistic wave equation describing electron motion.

3.1 Relativity and quantum physics

We briefly review the physics of the very fast and very small. These are governed by special relativity and quantum mechanics, respectively.

Special relativity

The central tenet of special relativity is a constant speed limit c in the universe, which is the speed of light. This is defined to be exactly[31]:

$$c = 299\,792\,458 \text{ m s}^{-1} \simeq 3 \times 10^8 \text{ m s}^{-1}. \tag{3.1}$$

This is a profound statement that the speed of light is constant no matter how fast an observer is moving, and there is no absolute rest frame. The empirical foundation is the Michelson–Morley experiment in 1887 [42], and leads to the striking phenomena of time dilation and length contraction of relativity. Most particles only live briefly and let's say X has a rest lifetime τ_{rest}. Then if we run past the particle or it flies from us very quickly at speed $\beta = v/c$, we see a dilated observed lifetime:

$$\tau_{\text{observed}} = \gamma\tau_{\text{rest}} = \frac{1}{\sqrt{1-\beta^2}}\tau_{\text{rest}}, \tag{3.2}$$

where $\gamma = 1/\sqrt{1-\beta^2}$. In general, a boost along direction x at speed v results in Lorentz transformed (primed) time and space coordinates:

$$\mathsf{X}'^{\mu} = \Lambda^{\mu}_{\nu}\mathsf{X}^{\nu}, \tag{3.3}$$

$$\begin{pmatrix} ct' \\ x' \\ y' \\ z' \end{pmatrix} = \begin{pmatrix} \gamma\beta & -\beta\gamma & 0 & 0 \\ -\beta\gamma & \gamma & 0 & 0 \\ 0 & 0 & 1 & 0 \\ 0 & 0 & 0 & 1 \end{pmatrix} \begin{pmatrix} ct \\ x \\ y \\ z \end{pmatrix}. \tag{3.4}$$

[31] Since 1983 at the 17th Conférence Générale des Poids et Mesures https://www.bipm.org/en/committees/cg/cgpm/17-1983/resolution-1

The X^μ objects are four-vectors comprising time for the $\mu = 0$ index and space components in the $\mu = 1,2,3$ indices. The Λ^μ_ν is the Lorentz transformation matrix.

When objects move at speeds approaching that of light $v \to c$, space and time are not so different as they seem at low speeds i.e. ct and x have comparable magnitudes. These two coordinates are merely related by a fancy rotation called a Lorentz boost, all due to spacetime symmetries. This is analogous to physics occurring in the up-down direction (often called y) being the same as that occurring in the left-right (often called x), related by a spatial rotation. Just as we do not measure x coordinates in miles and y coordinates in millimetres with a conversion ratio

$$x = \frac{\text{mile}}{\text{millimetre}} y. \tag{3.5}$$

It is therefore convenient to adopt notation that absorbs the scale factor into the time coordinate, which amounts to setting $c = 1$. Of course, everyday life also measures distances in units of time when there is a fixed speed e.g. "I am 30 minutes away" or "my transcontinental flight is 6 hours long".

Mass–energy equivalence Einstein also showed the mass–energy equivalence. When a particle decays, it converts its mass into the energy to create its child particles and its kinetic energy. We can construct a quantity called the rest mass m_{rest} of a particle by squaring its energy and subtracting its momentum squared:

$$(m_{\text{rest}}c^2)^2 = E^2 - (\mathbf{p}c)^2. \tag{3.6}$$

This quantity is Lorentz invariant i.e. mc^2 is the same no matter how fast we run passed the particle in what are called boosts. This fact makes Lorentz invariant quantities really interesting to physicists. We can write objects with units of momentum P^μ, with superscript μ denoting components, called the four-momentum:

$$\mathsf{P}^\mu = \begin{pmatrix} E/c \\ \mathbf{p} \end{pmatrix}. \tag{3.7}$$

This is a vector with four components comprising the energy E/c and the three spatial components of the momentum vector of a particle. Then we define a dot product rule that all four-vectors obey upon multiplication, which has a minus sign for the spatial components:

$$\mathsf{P}^2 = \mathsf{P}^{\mathrm{T}} \cdot \mathsf{P} = (E/c)^2 - \mathbf{p} \cdot \mathbf{p} = (mc)^2. \tag{3.8}$$

This operation therefore reproduces the Lorentz invariant rest mass as in eq. (3.6). If we ran passed this particle such that we (in the primed frame) see the particle with boosted four-momentum $\mathsf{P}' = (E'/c, \mathbf{p}')^{\mathrm{T}}$, we still obtain the same invariant mass squared when squaring

$\mathsf{P}\cdot\mathsf{P} = (mc)^2 = \mathsf{P}'\cdot\mathsf{P}'$. We can represent this useful operation of a four-vector dot product $\cdot$ with a diagonal 4×4 matrix called the Minkowski metric

$$\eta_{\mu\nu} = \begin{pmatrix} 1 & & & \\ & -1 & & \\ & & -1 & \\ & & & -1 \end{pmatrix}, \tag{3.9}$$

where the subscripts $\mu,\nu = \{0,1,2,3\}$ number the column and row elements of the matrix. This allows us to lower and raise indices, which imparts a negative sign on the spatial components

$$\mathsf{P}_\mu = \eta_{\mu\nu}\mathsf{P}^\mu = \begin{pmatrix} E/c \\ -\mathbf{p} \end{pmatrix}. \tag{3.10}$$

Energy and momentum conservation Another feature of the universe is energy and momentum conservation. This is actually related to the fact spacetime looks the same even if we translate it in time and space due to Noether's theorem. A simple process we can illustrate this with is a particle X decaying into particle 1 and 2 (e.g. a Higgs boson decaying to a muon and antimuon $h\to\mu^-\mu^+$):

$$\begin{array}{ccccc} & & X & & \\ 2 & \longleftarrow & \bullet & \longrightarrow & 1 \end{array}$$

$$\mathsf{P}_2 = \begin{pmatrix} E_{\mathbf{p}_2}/c \\ \mathbf{p}_2 \end{pmatrix} \mathsf{K} = \begin{pmatrix} m_X c \\ \mathbf{0} \end{pmatrix} \mathsf{P}_1 = \begin{pmatrix} E_{\mathbf{p}_1}/c \\ \mathbf{p}_1 \end{pmatrix} \tag{3.11}$$

Four-vectors make it easy to simultaneously conserve energy and linear momentum:

$$\mathsf{K} = \mathsf{P}_1 + \mathsf{P}_2. \tag{3.12}$$

We can calculate the energy spectrum of each particle by squaring (setting $c=1$ for clarity)

$$\mathsf{P}_1^2 = (\mathsf{K}-\mathsf{P}_2)^2 = \mathsf{K}^2 + \mathsf{P}_2^2 - 2\mathsf{K}\cdot\mathsf{P}_2, \tag{3.13}$$

$$\Rightarrow m_1^2 = m_2^2 + m_X^2 - 2m_X E_2. \tag{3.14}$$

A similar manipulation for swapped $1\leftrightarrow 2$ labels $\mathsf{P}_2^2 = (\mathsf{K}-\mathsf{P}_1)^2$ then gives

$$E_1 = \frac{m_X^2 + m_1^2 - m_2^2}{2m_X}, \quad E_2 = \frac{m_X^2 + m_2^2 - m_1^2}{2m_X}. \tag{3.15}$$

This tells us that each particle in a 2-body decay has its energy uniquely determined by the masses of the three particles $X, 1, 2$. This is why seeing a continuous energy spectrum for electrons in beta decay provided evidence of an additional invisible particle i.e. a 3-body decay.

Electromagnetism Let us also briefly review Maxwell's equations, which in SI units look like

$$\nabla \cdot \mathbf{E} = \frac{\rho}{\varepsilon_0} \quad \nabla \times \mathbf{B} + \mu_0 \varepsilon_0 \frac{\partial \mathbf{E}}{\partial t} = \mathbf{j}, \tag{3.16}$$

$$\nabla \cdot \mathbf{B} = 0 \quad \nabla \times \mathbf{E} \quad + \frac{\partial \mathbf{B}}{\partial t} = 0. \tag{3.17}$$

The upper two equations are the equations that tell us how the electromagnetic fields respond to sources of charge and current, while the lower equations relate the fields themselves.

As undergraduates learn towards the end of a course on electromagnetism, the speed of light is built into Maxwell's equations $c^2 = 1/\sqrt{\mu_0 \varepsilon_0}$. This spectacularly unifies the naïvely disparate phenomena of wave optics, electricity and magnetism, while betraying its deep connection to relativity. In Heaviside-Lorentz units $\varepsilon_0 = 1$ and $\mu_0 = 1$ with only factors of c appearing so Maxwell's equations look like

$$\nabla \cdot \mathbf{E} = \rho \quad \nabla \times \mathbf{B} + \frac{1}{c} \frac{\partial \mathbf{E}}{\partial t} = \frac{\mathbf{j}}{c}, \tag{3.18}$$

$$\nabla \cdot \mathbf{B} = 0 \quad \nabla \times \mathbf{E} + \frac{1}{c} \frac{\partial \mathbf{B}}{\partial t} = 0. \tag{3.19}$$

This certainly looks symmetric especially in the absence of charges and currents $\rho = 0, \mathbf{j} = \mathbf{0}$, while setting $c = 1$. Recall also that vector calculus implies we can write the electromagnetic fields in terms of the scalar ϕ and vector $\mathbf{A}$ potentials defined by

$$\mathbf{E} = -\nabla \phi - \frac{\partial \mathbf{A}}{\partial t}, \quad \mathbf{B} = \nabla \times \mathbf{A}. \tag{3.20}$$

While classically equivalent, it turns out the potentials are important in quantum mechanical interactions with electromagnetism.

Quantum mechanics

Underpinning quantum mechanics is the **wave–particle duality**. In the nineteenth century, Young's slit experiments showed light behaves as waves, until the photoelectric effect evidence its particle nature. The Planck's law relates the energy E of a particle to its frequency f with Planck's constant h:

$$E = hf = \hbar\omega, \tag{3.21}$$

where the Planck's constant is

$$h = 6.62607015 \times 10^{-34} \text{ J s}. \tag{3.22}$$

It is often convenient to work in the angular frequencies $\omega = 2\pi f$ with the reduced Planck's constant $\hbar = h/2\pi$. Planck's constant has units of [action] = [energy] $\times$ [time] or [distance] $\times$ [momentum], which is related to the uncertainty principle at the heart of quantum physics:

$$\sigma_x \sigma_p \geq \frac{\hbar}{2}. \tag{3.23}$$

Similarly, the electron was first established as a particle in cathode ray experiments until double slit experiments illustrated its wave behaviour. The de Broglie relation relates a particle's linear momentum p_x (along the x axis) to its wavelength λ:

$$p_x = 2\pi/\lambda = \hbar k_x, \tag{3.24}$$

which generalises to a three-vector $\mathbf{p} = \hbar\mathbf{k}$ for the three spatial components.

Given we work with waves, it is often useful to talk about the frequency ω or wavenumber k. This can be formalised with the Fourier transform, where we work in a convention that arises naturally from particle in a box boundary conditions such that the inverse Fourier transform comes with factors of $\mathrm{d}^n k_i/(2\pi)^n$:

$$f(k) = \int \mathrm{d}^4 x \, \tilde{f}(x) \mathrm{e}^{\mathrm{i}k\cdot x}, \tag{3.25}$$

$$\tilde{f}(x) = \int \frac{\mathrm{d}^4 k}{(2\pi)^4} f(k) \mathrm{e}^{-\mathrm{i}k\cdot x}, \tag{3.26}$$

working in $n = 4$ dimensions.

Schrödinger equation In non-relativistic quantum mechanics, we can describe the an electron ψ moving freely as waves using a complex exponential to represent a wave

$$\psi = \psi_0 \mathrm{e}^{-\mathrm{i}(Et - \mathbf{p}\cdot\mathbf{x})/\hbar}. \tag{3.27}$$

This is the electron wavefunction, whose equation of motion is the Schrödinger equation. This tells us how a particle ψ of mass m moves merrily through free space with kinetic energy Hamiltonian $\hat{H} = \mathbf{p}^2/2m$:

$$\mathrm{i}\hbar \frac{\partial \psi}{\partial t} = \hat{H}\psi. \tag{3.28}$$

We can write energy and momentum as differential operators that act on the wavefunction:

$$\hat{E} = \mathrm{i}\hbar \frac{\partial}{\partial t}, \quad \hat{\mathbf{p}} = -\mathrm{i}\hbar\boldsymbol{\nabla}, \tag{3.29}$$

where $\boldsymbol{\nabla}$ is the three-vector of spatial derivatives. We will usually drop the hat $\hat{E} \to E, \hat{\mathbf{p}} \to \mathbf{p}$ notation for operators in the rest of this text where quantum mechanics is implied.

Particle spin Quantum mechanics also introduces us to the idea of **intrinsic spin** of a particle measured in units of angular momentum $\hbar$. A particle can be a boson (integer spin) or a fermion (half integer spin). When two particles in a system, exchange of labels their wavefunction has no sign change for bosons and a sign change for fermions

$$\psi_a(x_1)\psi_b(x_2) = \psi_b(x_1)\psi_a(x_2) \qquad \text{bosons,} \tag{3.30}$$

$$\psi_a(x_1)\psi_b(x_2) = -\psi_b(x_1)\psi_a(x_2) \qquad \text{fermions.} \tag{3.31}$$

Born rule The probability P of finding a particle in a particular state is given by a complex number called its quantum amplitude $\mathscr{A}$ and multiplying it by its complex conjugate, which is the Born rule:

$$P = |\mathscr{A}|^2 = \mathscr{A}^*\mathscr{A}. \tag{3.32}$$

Occasionally, we will write the wavefunction in what is called a Dirac 'ket' $|\psi\rangle$ whose complex conjugate is called a 'bra' $\langle\psi|$, so the amplitude is formed as a 'bra-ket' $\langle\psi|\psi\rangle$.

3.2 Dirac equation

A very first combination of relativity and quantum mechanics relates the Planck equation describing energy-frequency relation with the Einstein mass-energy equivalence:

$$hf = E = mc^2. \tag{3.33}$$

Using $f = c/\lambda$, this gives the (reduced) **Compton wavelength** (λ) λ_C of a particle:

$$\lambda_C = \frac{h}{mc}, \quad \lambda\!\!\!^{-}_C = \frac{\hbar}{mc}. \tag{3.34}$$

This is the wavelength of a particle when all its energy resides in its rest mass.

As an aside, particle physics works with fast and small things so it is convenient to adopt a system of units that absorb factors of $\hbar$ and c into variables like energy and distance. We will often work in **natural units** $\hbar = 1, c = 1$, where a very helpful quantity to convert energy into distance quantities is:

$$\hbar c \simeq 197 \text{ MeV fm}. \tag{3.35}$$

This tells us a particle with an energy scale around 200 MeV energy has a wavelength of around a femtometre.

Klein–Gordon equation

Now we desire a description of quantum mechanical particles at relativistic speeds beyond just the rest mass wavelength λ_C. Specifically, we seek a quantum mechanical equation of motion that respects Lorentz invariants $E^2 - (pc)^2 = (mc^2)^2$ rather than the non-relativistic kinetic energy $p^2/2m$. The simplest way is to substitute the quantum mechanical energy-momentum operators of equation (3.29) into (3.6) to obtain:

$$\left(-\frac{1}{c^2}\frac{\partial^2}{\partial t^2} + \boldsymbol{\nabla}^2\right)\phi = \left(\frac{mc}{\hbar}\right)^2 \phi, \tag{3.36}$$

such that $\phi = \mathrm{e}^{-\mathrm{i}(Et - \mathbf{p}\cdot\mathbf{x})}$ is a free-space solution that satisfies the Lorentz invariant requirement. This is the **Klein–Gordon equation**. We now know this can describe the relativistic motion of scalar fields. But this was historically set aside due to confusion around negative energy states and negative probability currents. As a notational aside, you will sometimes see the shorthand $\Box$ for the d'Alembert wave operator

$$\Box = \partial^\mu \partial_\mu = \frac{1}{c^2}\frac{\partial^2}{\partial t^2} - \nabla^2, \tag{3.37}$$

which allows us write the Klein-Gordon equation (3.36) in a compact quadratic form (setting $\hbar = c = 1$ for visual clarity)

$$(\Box + m^2)\phi = 0. \tag{3.38}$$

This uses the definition of the four-gradient ∂_μ, which is a four-vector of time and space derivatives

$$\partial_\mu = \frac{\partial}{\partial x^\mu} = \begin{pmatrix} \frac{\partial}{\partial t} \\ +\boldsymbol{\nabla} \end{pmatrix}, \quad \partial^\mu = \eta^{\mu\nu}\frac{\partial}{\partial x^\mu} = \begin{pmatrix} \frac{\partial}{\partial t} \\ -\boldsymbol{\nabla} \end{pmatrix}. \tag{3.39}$$

Constructing the Dirac equation

Historically, Paul Dirac instead sought to write an equation that was first order in time. This therefore mimics the Schrödinger equation where only the initial position (not the velocity) is required as the initial condition. The goal is to "take the square root" of the Klein–Gordon operator by somehow "completing the square", heuristically

$$\Box + m^2 \stackrel{?}{=} (\sqrt{\Box} + \mathrm{i}m)(\sqrt{\Box} - \mathrm{i}m). \tag{3.40}$$

Needless to say, "$\sqrt{\Box}$" is mathematically ill-defined: what exactly does it mean to take the square root of a second order differential operator? Undeterred, Dirac pressed ahead and

postulated an equation having only first derivatives in time and space with unknown $A, \mathbf{B}$ coefficients:

$$\left(A\frac{\partial}{\partial t} + \mathbf{B}\cdot\boldsymbol{\nabla}\right)\psi = m\psi. \tag{3.41}$$

For convenient algebraic manipulation, we define a shorthand for spacetime derivatives:

$$\partial_t \equiv \frac{\partial}{\partial t}, \quad B_i\partial_i \equiv \sum_{i=1}^{3} B_i\partial_i = B_x\frac{\partial}{\partial x} + B_y\frac{\partial}{\partial y} + B_z\frac{\partial}{\partial z} = \mathbf{B}\cdot\boldsymbol{\nabla}. \tag{3.42}$$

Focusing on the left-hand side of equation (3.41), we can square the equation by multiplying through by the differential operators then expanding to yield:

$$(A\partial_t + B_i\partial_i)^2 = [A^2\partial_t^2 + \underbrace{A\partial_t(B_i\partial_i) + (B_i\partial_i)A\partial_t}_{=(AB_i+B_iA)\partial_i\partial_t} + B_i\partial_i B_j\partial_j]. \tag{3.43}$$

We can factorise the cross-terms shown in the underbrace because (i) time and spatial partial derivatives commute $\partial_i\partial_t = \partial_t\partial_i$, and (ii) A, B_i have neither time nor space dependence so also commute with the ∂_t and ∂_i derivatives. Therefore, equation (3.41) becomes

$$[A^2\partial_t^2 + (AB_i + B_iA)\partial_i\partial_t + B_iB_j\partial_i\partial_j]\psi = m^2\psi. \tag{3.44}$$

For this to match the Klein-Gordon equation (3.36), Dirac required $A^2 = -1$ and all cross-terms in derivatives like $\partial_t\partial_i, \partial_x\partial_y$ to vanish:

$$A^2 = -1, \quad AB_i + B_iA = 0, \quad B_iB_j = \delta_{ij}, \tag{3.45}$$

where $\delta_{ij} = 0$ for $i \neq j$ and $\delta_{ij} = 1$ for $i = j$. For A and B_i to satisfy these intriguing relations, Dirac astutely realised that they must be matrices. With some notational foresight, we can define $A = \mathrm{i}\gamma^0, B_i = \mathrm{i}\gamma_i$ in terms of objects we now call Dirac matrices γ_μ, which satisfy

$$(\gamma_0)^2 = 1, \quad \gamma_0\gamma_i + \gamma_i\gamma_0 = 0, \quad \gamma_i\gamma_j = -\delta_{ij}. \tag{3.46}$$

This shows that time and spatial components multiply to give a relative negative sign while all the off-diagonal elements vanish, which sounds awfully familiar. Indeed, this tells us how swapping γ_μ gives a minus sign plus an extra bit proportional to the Minkowski metric $\eta_{\mu\nu} = \mathrm{diag}(+1,-1,-1,-1)$ (3.9):

$$\{\gamma_\mu, \gamma_\nu\} \equiv \gamma_\mu\gamma_\nu + \gamma_\nu\gamma_\mu = 2\eta_{\mu\nu}. \tag{3.47}$$

This is an **anti-commutation relation**, where the curly braces define an anti-commutator $\{a,b\} \equiv ab + ba$. we call this the Clifford algebra, after William Clifford who first studied

these anti-commuting mathematical objects in 1878. This anti-commutation is a defining feature of fermions. Substituting $A = \mathrm{i}\gamma^0, B^i = \mathrm{i}\gamma^i$ back into equation (3.41), this becomes the celebrated **Dirac equation** first written[32] in 1928

$$\boxed{\mathrm{i}\gamma^\mu \partial_\mu \psi = m\psi.} \tag{3.48}$$

This astonishing equation describes the quantum mechanical and relativistic motion of spin-half particles in free space. It also shows how anti-commuting gamma matrices γ^μ are a mathematical consequence in trying to define this operator $\sqrt{\Box} = \gamma^\mu \partial_\mu$ to make quantum mechanics consistent with special relativity.

3.3 Spinor and antimatter waves

We now explore the remarkable anatomy of the Dirac equation, first antimatter and spinors that underpin particle physics.

Weyl representation of Dirac equation

One way to write the solutions of the Dirac equation is to work in a specific representation that satisfies the defining Clifford algebra (3.47). The Weyl (chiral) representation is

$$\gamma^\mu = \begin{pmatrix} \mathbf{0} & \sigma^\mu \\ \bar{\sigma}^\mu & \mathbf{0} \end{pmatrix}, \quad \text{where} \quad \sigma^\mu = \begin{pmatrix} \mathbb{I} \\ \boldsymbol{\sigma} \end{pmatrix}, \quad \bar{\sigma}^\mu = \begin{pmatrix} \mathbb{I} \\ -\boldsymbol{\sigma} \end{pmatrix}, \tag{3.49}$$

with $\mathbb{I}$ being the 2-by-2 identity matrix and $\boldsymbol{\sigma}$ is the 3-vector of Pauli matrices familiar from quantum mechanics:

$$\boldsymbol{\sigma} = \begin{pmatrix} \sigma_x \\ \sigma_y \\ \sigma_z \end{pmatrix}, \quad \text{where} \quad \sigma_x = \begin{pmatrix} 0 & 1 \\ 1 & 0 \end{pmatrix}, \sigma_y = \begin{pmatrix} 0 & -\mathrm{i} \\ \mathrm{i} & 0 \end{pmatrix}, \sigma_z = \begin{pmatrix} 1 & 0 \\ 0 & -1 \end{pmatrix}. \tag{3.50}$$

The Lorentz index μ on γ^μ makes these objects look like a four-vector, but they are not i.e. they do *not* transform as $\gamma^\mu \to \Lambda^\mu_\nu \gamma^\nu$ because they remain invariant. When we write out the components, we can see explicitly that they are just a collection of matrices with complex numbers; the Lorentz index serves as a mnemonic for which element of a four-vector they multiply with.

[32] As it appears on a plaque situated in Westminster Abbey, London.

Equipped with this explicit representation of matrices (3.49) and $E = \mathrm{i}\partial_t, \mathbf{p} = -\mathrm{i}\boldsymbol{\nabla}$, we can write the Dirac equation (3.48) explicitly

$$\mathrm{i}\begin{pmatrix} 0 & \sigma^\mu \partial_\mu \\ \bar{\sigma}^\mu \partial_\mu & 0 \end{pmatrix} \psi = \begin{pmatrix} m & 0 \\ 0 & m \end{pmatrix} \psi \tag{3.51}$$

In the chiral representation, the **Dirac spinor** ψ is a four-component spinor made by stacking a pair of two-component Weyl spinors ϕ, χ (3.82)

$$\psi = \begin{pmatrix} \phi \\ \chi \end{pmatrix} = \begin{pmatrix} \phi_a \\ \phi_b \\ \chi_a \\ \chi_b \end{pmatrix}, \tag{3.52}$$

Writing out (3.51) gives the pair of coupled differential equations mixing the upper and lower two-spinors

$$\mathrm{i}\sigma^\mu \partial_\mu \chi = m\phi, \tag{3.53}$$

$$\mathrm{i}\bar{\sigma}^\mu \partial_\mu \phi = m\chi. \tag{3.54}$$

It will turn out that ϕ corresponds to right-handed particles and χ with left-handed particles in the massless limit, as we shall now see. Sometimes you will see this written as $\psi_R = \phi, \psi_L = \chi$.

Weyl equations and helicity

As usual in physics, it is insightful to take some limits to study its consequences. Something interesting happens in the ultra-relativistic limit $m \to 0$: the Dirac equation decouples into two independent **Weyl equations**:

$$\mathrm{i}\sigma \cdot \partial \phi = 0, \quad \text{“unbarred”} \tag{3.55}$$

$$\mathrm{i}\bar{\sigma} \cdot \partial \chi = 0, \quad \text{“barred”}. \tag{3.56}$$

Here we can refer to the two distinct equations as whether σ is “unbarred” and “barred” $\bar{\sigma}$. While mathematically undramatic, this decoupling is telling us something deep about nature: there are two types of massless fermions with a distinguishable property. It turns out this will correspond to left-handed or right-handed Weyl spinors. This difference in handedness is already implicit in equation (3.49) by the negative sign prefixing Pauli matrices in $\bar{\sigma}^\mu$ hinting this somehow distinguishes rotations. In the $m \to 0$ limit, they never mix: a left-handed Weyl fermion stays left-handed; a right-handed Weyl fermion stays left-handed.

We can solve the two Weyl equations using a plane wave ansatz

$$\phi = \begin{pmatrix} \phi_a \\ \phi_b \end{pmatrix} \mathrm{e}^{-\mathrm{i}(Et-\mathbf{p}\cdot\mathbf{x})}, \quad \chi = \begin{pmatrix} \chi_a \\ \chi_b \end{pmatrix} \mathrm{e}^{-\mathrm{i}(Et-\mathbf{p}\cdot\mathbf{x})}. \tag{3.57}$$

Because the 2×2 Pauli matrices are built in, the solutions are necessarily two components. The Weyl equations then become

$$(\boldsymbol{\sigma}\cdot\mathsf{P})\,\phi = 0, \quad \Rightarrow \quad (\mathbb{I}E - \boldsymbol{\sigma}\cdot\mathbf{p})\phi = 0, \tag{3.58}$$
$$(\bar{\boldsymbol{\sigma}}\cdot\mathsf{P})\,\chi = 0, \quad \Rightarrow \quad (\mathbb{I}E + \boldsymbol{\sigma}\cdot\mathbf{p})\chi = 0. \tag{3.59}$$

Focusing on the unbarred Weyl equation (3.58), we can align the momentum along the z-axis $p_z = |\mathbf{p}|$ to find this eigenvalue equation

$$\mathbb{I}E - \sigma_z|\mathbf{p}| = \begin{pmatrix} E-|\mathbf{p}| & 0 \\ 0 & E+|\mathbf{p}| \end{pmatrix} \begin{pmatrix} \phi_a \\ \phi_b \end{pmatrix} = 0. \tag{3.60}$$

This eigenvalue problem has two solutions with positive and negative energies, which we interpret as particles and anti-particles:

$$\phi_+ = \left(\begin{smallmatrix} 1 \\ 0 \end{smallmatrix}\right), \quad E = +|\mathbf{p}|, \quad \text{particle}, \tag{3.61}$$
$$\phi_- = \left(\begin{smallmatrix} 0 \\ 1 \end{smallmatrix}\right), \quad E = -|\mathbf{p}|, \quad \text{anti-particle}. \tag{3.62}$$

The unbarred Weyl equation (3.55) becomes

$$\frac{\boldsymbol{\sigma}\cdot\mathbf{p}}{|\mathbf{p}|}\phi = \frac{E}{|\mathbf{p}|}\phi, \tag{3.63}$$

We call this operator $\hat{h} = \boldsymbol{\sigma}\cdot\hat{\mathbf{p}}/|\mathbf{p}|$ the **helicity**. This is the projection of the spin along the direction of the momentum $\mathbf{p}$. In equation (3.51), the Pauli operator $\boldsymbol{\sigma}$ generates a sense of rotation projected onto linear momentum vector (recall $\mathbf{p} = -\mathrm{i}\nabla$) that defines the axis-of-rotation direction. The eigenstates with well-defined helicity eigenvalues h are:

$$\mathrm{i}\sigma\cdot\partial\phi = 0 \;\Rightarrow\; \begin{cases} \phi_+ = \left(\begin{smallmatrix} 1 \\ 0 \end{smallmatrix}\right), & h=+1, \quad E>0, \quad \text{right-handed particle}, \\ \phi_- = \left(\begin{smallmatrix} 0 \\ 1 \end{smallmatrix}\right), & h=-1, \quad E<0, \quad \text{left-handed anti-particle}. \end{cases} \tag{3.64}$$

This is the physical interpretation of the unbarred Weyl equation (3.55): it is the equation of motion for a right-handed $h=+1$ particle $E>0$ and left-handed $h=-1$ anti-particle $E<0$.

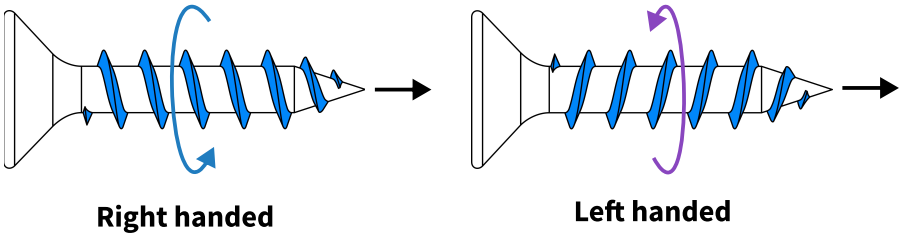

Figure 20: **Left- and right-handed threaded screw**. I constructed the left-handed screw from the original right-handed screw by performing a parity transformation (vertical flip) in my graphics software. Figures: adapted from Wikimedia

.

We determine their handedness by whether the spin operator is aligned or anti-aligned with momentum:

$$\text{RH}: \quad \underset{\mathbf{s}}{\Rightarrow} \cdot \underset{\mathbf{p}}{\rightarrow} = + = \text{aligned}, \tag{3.65}$$

$$\text{LH}: \quad \underset{\mathbf{s}}{\Rightarrow} \cdot \underset{\mathbf{p}}{\leftarrow} = - = \text{anti-aligned}. \tag{3.66}$$

So ultra-relativistic spinors are like threaded screws. Their handedness arises from a sense of rotation in the x-y plane being aligned or anti-aligned with its z-axis of rotation (figure 20).

You can repeat this exercise with the barred Weyl equation (3.59) to find the two solutions $\chi_\pm$ correspond to:

$$\mathrm{i}\bar{\sigma}\cdot\partial\chi = 0 \;\Rightarrow\; \begin{cases} \chi_+ = \binom{1}{0}, & h=+1, \quad E<0, & \text{right-handed anti-particle}, \\ \chi_- = \binom{0}{1}, & h=-1, \quad E>0, & \text{left-handed particle}. \end{cases} \tag{3.67}$$

Figure 21 summarises these four possible eigenstates of the Weyl equations. The literature often uses the following u, v notation to denote particles and antiparticles:

$$u_\text{R} = \text{right-handed particle} \quad v_\text{R} = \text{right-handed antiparticle}, \tag{3.68}$$

$$u_\text{L} = \text{left-handed particle} \quad v_\text{L} = \text{left-handed antiparticle}. \tag{3.69}$$

All these sketches make it look like the two Weyl equations are mirror images of each other. Indeed your left and right hands exchange when looking at a mirror in everyday life, which we mathematically formalise as a parity P transformation $\mathbf{r} \to -\mathbf{r}$ exchanging the handedness of Weyl spinors

$$P : \psi_{L,R} \to \psi_{R,L}, \quad \mathbf{r} \to -\mathbf{r}. \tag{3.70}$$

Spin: ⇒	Spin: ⇐	Spin: ⇒	Spin: ⇐
(a) RH particle	(b) LH anti-particle	(c) RH anti-particle	(d) LH particle
$\boldsymbol{\sigma}\cdot\mathbf{p} \propto +$ (RH)	$\boldsymbol{\sigma}\cdot\mathbf{p} \propto -$ (LH)	$\boldsymbol{\sigma}\cdot\mathbf{p} \propto +$ (RH)	$\boldsymbol{\sigma}\cdot\mathbf{p} \propto -$ (LH)
Particle $E > 0$	Anti-particle $E < 0$	Anti-particle $E < 0$	Particle $E > 0$

Figure 21: **Handedness of massless particle and anti-particle spinors**. The massless limit of the Dirac equations decouples into the two Weyl equations. Solutions can be LH or RH assigned to particle $E > 0$ or anti-particle $E < 0$. (a) and (b) are solutions to the unbarred Weyl equation $\mathrm{i}\sigma\cdot\partial\phi = 0$, while (c) and (d) are solutions to the barred Weyl equation $\mathrm{i}\bar{\sigma}\cdot\partial\chi = 0$.

Dirac mass and chirality

When restoring $m \neq 0$, the Weyl equations become coupled (3.54), mixing the left- and right-handed Weyl spinors ϕ, χ with well-defined helicities. This becomes the notion of **chirality**. Given further spoilers that the electroweak interactions couple only to left-handed Weyl spinors, it is convenient to define an operator to project out the left and right Weyl spinors from a Dirac spinor:

$$\phi = \psi_L = P_R\psi = \begin{pmatrix} \mathbb{I} & 0 \\ 0 & 0 \end{pmatrix}\psi, \quad \chi = \psi_R = P_L\psi = \begin{pmatrix} 0 & 0 \\ 0 & \mathbb{I} \end{pmatrix}\psi. \tag{3.71}$$

Working in this Weyl representation, we can construct a matrix with a curious "5" in its name

$$\gamma^5 = \begin{pmatrix} -\mathbb{I} & 0 \\ 0 & \mathbb{I} \end{pmatrix} \tag{3.72}$$

This allows us to construct **chiral projection operators** $P_{L,R}$ such that they work as (3.71), extracting the upper and lower parts of the Dirac spinor:

$$P_L = \frac{1}{2}(I + \gamma^5), \quad P_R = \frac{1}{2}(I - \gamma^5). \tag{3.73}$$

This curiously named object γ^5 satisfies these defining properties

$$\gamma^5 = -\mathrm{i}\gamma^0\gamma^1\gamma^2\gamma^3, \quad \text{satisfying} \quad \{\gamma^\mu, \gamma^5\} = 0, \quad (\gamma^5)^2 = I. \tag{3.74}$$

The physical picture of a Dirac mass are the left and right chirality states oscillating into each other:

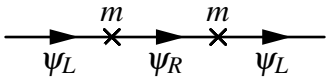

(3.75)

The rate of sloshing back and forth from left to right chirality is set by the mass m. We can also define the **Dirac adjoint** to be

$$\bar{\psi} = \psi^\dagger \gamma^0 = \begin{pmatrix} \psi_R^\dagger & \psi_L^\dagger \end{pmatrix}. \tag{3.76}$$

And a Dirac mass term looks like $m\bar{\psi}\psi$. Foreshadowing electroweak theory, the non-zero expectation value of the Higgs vacuum dynamically induces this coupling we associate with mass between left and right spinors. The Dirac equation profoundly shifts our interpretation of what mass is: this perpetual change of fermion handedness gives rise to inertial mass for Dirac particles.

Massive antimatter

We describe the negative energy states correspond to anti-particles in the massless limit as solutions to the Weyl equations. The existence of anti-particles persists for $m \neq 0$. Restoring the mass and multiplying out the Weyl equations gives

$$(\mathbb{I}E - \boldsymbol{\sigma}\cdot\mathbf{p})\chi = m\phi, \tag{3.77}$$

$$(\mathbb{I}E + \boldsymbol{\sigma}\cdot\mathbf{p})\phi = m\chi. \tag{3.78}$$

As ϕ, χ are eigenstates of energy and momentum, we can eliminate ϕ in the first equation to give

$$(\mathbb{I}E - \boldsymbol{\sigma}\cdot\mathbf{p})(\mathbb{I}E + \boldsymbol{\sigma}\cdot\mathbf{p})\chi = m^2\chi \tag{3.79}$$

Using the Pauli identity $\sigma^i\sigma^j = \delta^{ij} + \mathrm{i}\varepsilon^{ijk}\sigma^k$, this reduces to the relativistic dispersion having positive and negative energy solutions

$$E_\pm(\mathbf{p}) = \pm\sqrt{|\mathbf{p}|^2 + m^2}. \tag{3.80}$$

Upon quantisation of the spinor waves, the negative energy states are associated with **anti-matter**. When Dirac first wrote his equation, the full profound consequences of it were not fully appreciated. Historically, the negative energy states remained confusing. We shall skip the discussion on the "Dirac sea" picture often seen in textbooks. Instead, we are assured that once coupled to electromagnetism, these states correspond to electric **charge conjugation**. These are positrons e^+.

Antimatter explicitly allows non-conservation of particle number. This is a striking distinction to what we learn in chemistry, where conservation of particle number implies we cannot create or destroy carbon or oxygen atoms in a reaction because they merely rearrange. But the existence of antimatter upends this picture and is a central to relativistic quantum theories.

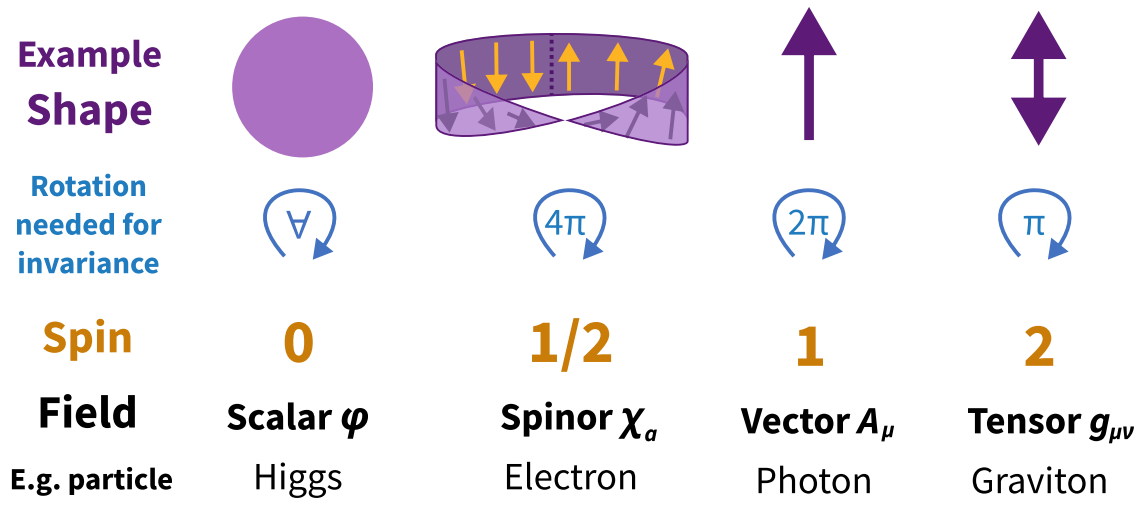

Figure 22: **Spin and rotation memory aid**. Examples of how to interpret spins as rotation with fields and particles. Spin-0 is the same for all angles, spin-1 is a single-ended arrow needing a full 2π rotation, and spin-2 is a double-ended arrow requiring a half π rotation to restore invariance. Spin half means one must perform a 4π rotation for an object to return to its original configuration: transporting an arrow round a Möbius strip is a classic example of this, where a 2π rotation results in an $\uparrow$ arrow being inverted $\downarrow$ due to the twist. I have yet to find a shape is invariant under a $4\pi/3$ rotation for a spin-3/2 particle.

Spinor rotation

Under Lorentz transformations Λ, Weyl spinors transform as

$$\psi_L \to \Lambda\psi_L = \exp\left[\frac{i\sigma_i}{2}(\theta_i - \beta_i)\right]\psi_L \tag{3.81}$$

$$\psi_R \to \Lambda\psi_L = \exp\left[\frac{i\sigma_i}{2}(\theta_i + \beta_i)\right]\psi_R \tag{3.82}$$

Note well the Pauli matrices σ_i, factor of $1/2$ and $\mp$ signs for boosts β_i and rotations θ_i. The physical picture of spin-1/2 particles is that a 2π rotation induces a negative sign, and only a 4π rotation restores the original configuration. You can visualise this in everyday life by twisting your arm while holding a plate of food, and following an single-ended arrowhead embedded on a Möbius strip. The twist means the arrow direction is inverted after a 2π transport that is only restored after 4π. This is contrasted with objects of other spin as visualised in figure 22.

We can write some explicit spinor solutions by working in polar coordinates

$$\mathbf{p} = E \begin{pmatrix} \sin\theta\cos\varphi \\ \sin\theta\sin\varphi \\ \cos\theta \end{pmatrix}, \tag{3.83}$$

we can expand out the right-handed Weyl equation with the aid of the Euler identity $\mathrm{e}^{\mathrm{i}\varphi} = \cos\varphi + \mathrm{i}\sin\varphi$ to write all the components of the eigenvalue equation explicitly:

$$(\boldsymbol{\sigma}\cdot\mathsf{P})\,u_{\mathrm{R}} = (I\mathsf{P}_0^{\pm} - \boldsymbol{\sigma}\cdot\mathbf{p}) = E \begin{pmatrix} \pm 1 - \cos\theta & -\mathrm{e}^{-\mathrm{i}\varphi}\sin\theta \\ -\mathrm{e}^{\mathrm{i}\varphi}\sin\theta & \pm 1 + \cos\theta \end{pmatrix} u_{\mathrm{R}}^{\pm} = 0, \tag{3.84}$$

where $\mathsf{P}_0^{+} = +E$ for particles (positive energy state) and $\mathsf{P}_0^{-} = -E$ for antiparticles (negative energy state). Solve this eigenvalue problem using your favourite linear algebra techniques (via pen in hand or symbolic algebra program) and apply trigonometric half-angle identities $\sin 2\theta = 2\sin\theta\cos\theta$ to obtain the normalised[33] eigenvector spinor solutions

$$u_{\mathrm{R}} \equiv u_{\mathrm{R}}^{+} = \sqrt{2E} \begin{pmatrix} \cos(\theta/2) \\ \mathrm{e}^{\mathrm{i}\varphi}\sin(\theta/2) \end{pmatrix}, \quad v_{\mathrm{R}} \equiv u_{R}^{-} = \sqrt{2E} \begin{pmatrix} \sin(\theta/2) \\ -\mathrm{e}^{\mathrm{i}\varphi}\cos(\theta/2) \end{pmatrix}. \tag{3.85}$$

Solve the left-handed Weyl equation $(\bar{\boldsymbol{\sigma}}\cdot\mathsf{P})u_{\mathrm{L}} = 0$ analogously to find:

$$u_{\mathrm{R}} = v_{\mathrm{L}} = \sqrt{2E} \begin{pmatrix} \mathrm{e}^{-\mathrm{i}\varphi/2}\cos(\theta/2) \\ \mathrm{e}^{+\mathrm{i}\varphi/2}\sin(\theta/2) \end{pmatrix}, \quad u_{\mathrm{L}} = v_{\mathrm{R}} = \sqrt{2E} \begin{pmatrix} \mathrm{e}^{-\mathrm{i}\varphi/2}\sin(\theta/2) \\ -\mathrm{e}^{+\mathrm{i}\varphi/2}\cos(\theta/2) \end{pmatrix}. \tag{3.86}$$

The spinors are equivalent up to any global phase, and we follow a convention that makes the complex phase explicit on both components by multiplying through by $\mathrm{e}^{-\mathrm{i}\varphi/2}$.

3.4 Gyromagnetic factor

Having studied the ultra-relativistic limit $E \gg m$ decouples the Dirac equation, we now turn to a key result of the non-relativistic limit. Historically, this revealed the remarkable corollary of the Dirac equation that it requires the electron intrinsic gyromagnetic factor to be $g_e = 2$. We initially approach the non-relativistic regime of the Dirac equation by taking the large mass $E \approx m$ limit $\psi_{L,R} = \chi_{L,R}\mathrm{e}^{-\mathrm{i}mt}$

$$\begin{pmatrix} -m & I\hat{E} - \boldsymbol{\sigma}\cdot\hat{\mathbf{p}} \\ I\hat{E} + \boldsymbol{\sigma}\cdot\hat{\mathbf{p}} & -m \end{pmatrix} \begin{pmatrix} \chi_L \\ \chi_R \end{pmatrix} \mathrm{e}^{-\mathrm{i}mt} = 0, \tag{3.87}$$

[33] The normalisation $u^{\dagger}u = v^{\dagger}v = 2E$ is conventional such that it transforms as a probability density, which is the zeroth component of the conserved four-vector current $j_\mu = (\rho, \mathbf{j})^{\mathrm{T}}$.

where we momentarily restore the circumflex $\hat{E}, \hat{\mathbf{p}}$ to remind ourselves that they are operators. Recognising the energy differential operator $E = \mathrm{i}\partial_t$, we use the product rule to write

$$E(\chi_{L,R}\mathrm{e}^{-\mathrm{i}mt}) = \mathrm{e}^{-\mathrm{i}mt}(m+E)\chi_{L,R}. \tag{3.88}$$

Then the Dirac equation decouples into a pair of simultaneous equations

$$-m\chi_L + (m+E-\boldsymbol{\sigma}\cdot\mathbf{p})\chi_R = 0 \tag{3.89}$$
$$-m\chi_R + (m+E+\boldsymbol{\sigma}\cdot\mathbf{p})\chi_L = 0 \tag{3.90}$$

Eliminating χ_R allows us to write

$$E + \frac{E^2}{2m} = \frac{(\boldsymbol{\sigma}\cdot\mathbf{p})^2}{2m} \tag{3.91}$$

As we are in the non-relativistic limit, we neglect the E^2 term quadratic in energy and recognising $E = \mathrm{i}\partial_t$, this is in the form of the Schrödinger equation. This allows us to recognise the non-relativistic limit of the Dirac equation recovers the Pauli Hamiltonian

$$H_{\text{Pauli}} = \frac{(\boldsymbol{\sigma}\cdot\mathbf{p})^2}{2m}. \tag{3.92}$$

The minimal coupling prescription to describe particles with charge q experiencing electromagnetism is the replacement $\mathbf{p} \to \mathbf{p} - q\mathbf{A}$

$$H_{\text{Pauli-EM}} = \frac{[\boldsymbol{\sigma}\cdot(\mathbf{p}-q\mathbf{A})]^2}{2m}. \tag{3.93}$$

Now for some vector calculus gymnastics to isolate the spin-magnetic coupling. First invoke the Pauli matrix identity[34] $(\boldsymbol{\sigma}\cdot\mathbf{x})(\boldsymbol{\sigma}\cdot\mathbf{y}) = \mathbf{x}\cdot\mathbf{y} + \mathrm{i}\boldsymbol{\sigma}\cdot(\mathbf{x}\times\mathbf{y})$ and momentum as a differential operator $\mathbf{p} = -\mathrm{i}\boldsymbol{\nabla}$ acting on a generic function $f(x)$

$$[\boldsymbol{\sigma}\cdot(\mathbf{p}-q\mathbf{A})]^2 f = (\mathbf{p}-q\mathbf{A})^2 f - \mathrm{i}\boldsymbol{\sigma}\cdot[(\mathrm{i}\boldsymbol{\nabla}+q\mathbf{A})\times(\mathrm{i}\boldsymbol{\nabla}+q\mathbf{A})]f. \tag{3.94}$$

Multiplying out the vector cross product, we find a non-vanishing cross term

$$(\mathrm{i}\boldsymbol{\nabla}+q\mathbf{A})\times(\mathrm{i}\boldsymbol{\nabla}+q\mathbf{A}) = \mathrm{i}q[\boldsymbol{\nabla}\times(\mathbf{A}f) + \mathbf{A}\times(\boldsymbol{\nabla}f)] + [\underbrace{\mathrm{i}^2\boldsymbol{\nabla}\times\boldsymbol{\nabla} + q^2\mathbf{A}\times\mathbf{A}}_{=0}]f \tag{3.95}$$
$$= \mathrm{i}q[f(\boldsymbol{\nabla}\times\mathbf{A}) - \mathbf{A}\times(\boldsymbol{\nabla}f) + \mathbf{A}\times(\boldsymbol{\nabla}f)], \tag{3.96}$$

[34] Derive this by working in index notation for the commutation and anti-commutation algebra of the Pauli matrices $[\sigma_i, \sigma_j] = 2\mathrm{i}\varepsilon_{ijk}\sigma_k$, $\{\sigma_i, \sigma_j\} = 2\delta_{ij}$, and vector product $(\mathbf{x}\times\mathbf{y})_i = \varepsilon_{ijk}x_j y_k$.

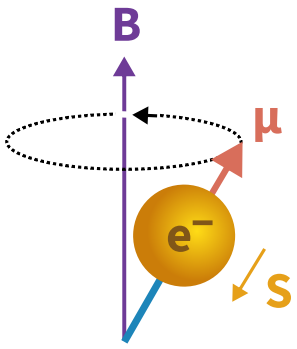

Figure 23: **Magnetic moment of intrinsic spin**. An electron with spin $\mathbf{S} = \boldsymbol{\sigma}/2$ has a magnetic moment $\boldsymbol{\mu}$, which undergoes precession in an external magnetic field $\mathbf{B}$.

recalling the antisymmetry of the cross-product yields a negative sign on applying the differentiation product rule. Identifying $\mathbf{B} = \boldsymbol{\nabla} \times \mathbf{A}$, the Pauli Hamiltonian simplifies to

$$H_{\text{Pauli-EM}} = \frac{(\mathbf{p} - q\mathbf{A})^2}{2m} - \frac{q}{2m}\boldsymbol{\sigma} \cdot \mathbf{B}. \tag{3.97}$$

Compare this with the general Hamiltonian for an intrinsic magnetic dipole moment $\boldsymbol{\mu} = (g_s q/2m)\mathbf{S}$ interacting with an external magnetic field $\mathbf{B}$

$$H_{\text{magnetic}} = -\boldsymbol{\mu} \cdot \mathbf{B} = \left(\frac{g_s q}{2m}\mathbf{S}\right) \cdot \mathbf{B} = -\left(\frac{g_s q}{2m}\frac{\boldsymbol{\sigma}}{2}\right) \cdot \mathbf{B}, \tag{3.98}$$

having used the definition $\mathbf{S} = \boldsymbol{\sigma}/2$. Figure 23 shows this spin-magnetic precession of an electron, which is usually studied in non-relativistic quantum mechanics classes. For H_{magnetic} to agree with the Pauli-EM Hamiltonian (3.97), we find the spin gyromagnetic factor g_s must be

$$\boxed{g_s = 2.} \tag{3.99}$$

Historically, this was a landmark moment in relativistic quantum theory. In Pauli theory, g_s is a free parameter relating $\boldsymbol{\mu}$ with $\boldsymbol{\sigma}$, whose value of two is determined experimentally. By contrast, Dirac theory explains this must be two by the consistent union of quantum mechanics with special relativity.

To summarise, the Dirac equation yields several profound results:

- Mass is an oscillation between left-handed and right-handed fermions.
- Unexpected prediction of antimatter, implying particle number is not conserved.
- Theoretical basis for Pauli's phenomenological description of spin.

- Minimal coupling to electromagnetism implies intrinsic gyromagnetic factor of two.

Together, these developments pave the foundations for quantum electrodynamics. While initially applied to the electron, the central importance of the Dirac equation is that it holds for all fundamental spin-1/2 particles carrying electric charge. This therefore underpins the description of charged leptons and quarks in the Standard Model.

II Quantum electrodynamics

4 Feynman diagrams

We introduce the representation of subatomic particle interactions using Feynman diagrams. Richard Feynman invented these diagrams to provide intuition of the physical problem before commencing more detailed calculations. Here we also use their intuitive simplicity as a pedagogical tool to introduce central concepts in particle physics. We will first use them in the context of quantum electrodynamics (QED) is the microscopic theory of electromagnetism containing electrons, positrons, and photons.

4.1 Electromagnetic scattering

In QED, we represent matter (and fermions generally) with an arrowed solid straight line represents while a wiggly line represent photons (and spin-one bosons generally):

(4.1)

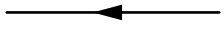

(4.2)

(4.3)

We take the convention that electrons (matter) point to the right $\rightarrow$, and positrons (antimatter) point to the left $\leftarrow$. By themselves, these diagrams represent particles freely flying through space. Next, we represent the only interaction in QED by a vertex that may only connect two fermions with one photon:

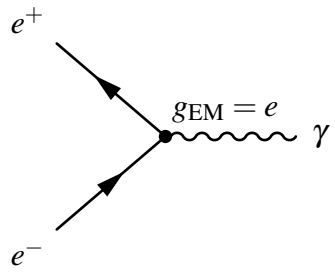

(4.4)

This represents an interaction with strength set by the electromagnetic coupling $g_{\text{EM}} \propto e$, which is proportional to the electric charge e

$$g_{\text{EM}}^2 = \frac{e^2}{\varepsilon_0 \hbar c} = 4\pi\alpha_{\text{EM}} \tag{4.5}$$

where α_{EM} is the fine structure constant. This is the small dimensionless real number

$$\alpha_{\text{EM}} = \frac{e^2}{4\pi\varepsilon_0 \hbar c} \simeq \frac{1}{137} \simeq 0.0073. \tag{4.6}$$

The electric charge has the size $e = \sqrt{4\pi\alpha\varepsilon_0\hbar c}$, such that in natural Heaviside–Lorentz units $e = \sqrt{4\pi\alpha} \approx 0.3$.

More generally, a particle with multiplicative units of electric charge $Q_f e$ simple rescales the vertex factor

$$g_{\text{EM}} \to g_{\text{EM}} Q_f. \tag{4.7}$$

The QED vertex of equation (4.4) respects charge conservation: if one arrow goes into the vertex, the other arrow must leave. This is why I like to view the direction of the arrow in the straight line as a reminder of the flow of (negative) electric charge analogous to electric current in circuits. Historically, the literature likes to talk about positrons as negative energy states flowing backwards in time $Et \to (-E)(-t)$ called the Feynman–Stückelberg interpretation. Figure 24 shows the basic anatomy of a Feynman diagram representing an interaction via the exchange of a mediator.

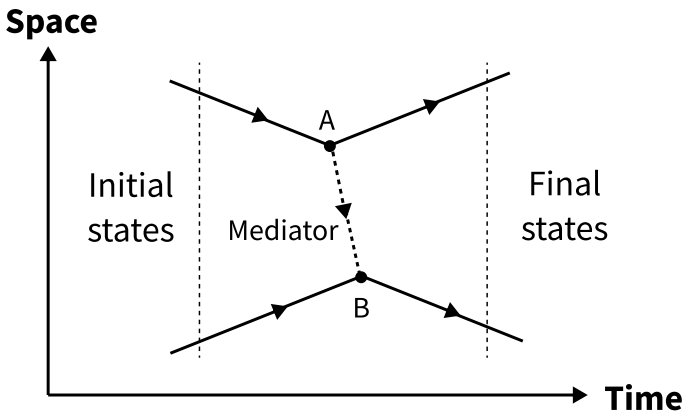

Figure 24: **Schematic of Feynman diagram**. Left shows two initial and and right shows two final states. An interaction is realised as the upper particle emits a mediator at vertex A, which is absorbed by the lower particle at vertex B.

With the basic ingredients of 4.3 and 4.4, we can draw the canonical interactions of quantum electrodynamics:

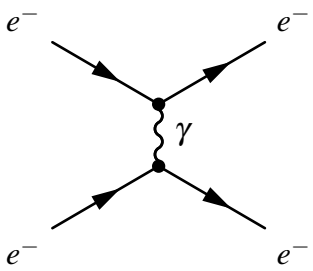

(a) $e^-e^- \to e^-e^-$: electron scattering

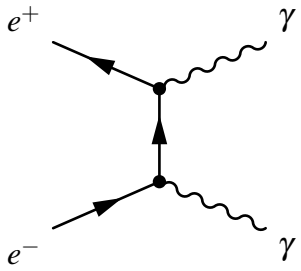

(b) $e^-e^+ \to \gamma\gamma$: pair annihilation

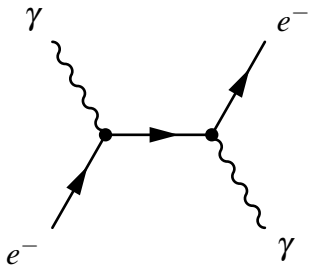

(c) $e^-\gamma \to e^-\gamma$: Compton scattering

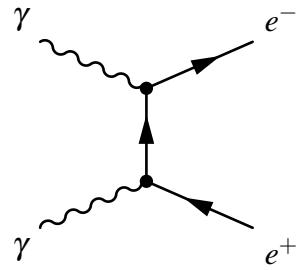

(d) $\gamma\gamma \to e^-e^+$: pair creation (Breit-Wheeler)

Figure 25: **QED 2-to-2 scattering processes**. This involves electrons, positrons and photons in quantum electrodynamics interacting via the fundamental QED vertex (4.4).

- Figure 25 shows various interactions involving electrons, positrons and photons: (25a) an electron e^- scattering off another electron via a virtual photon γ.
- Figure 25b an electron meeting a positron e^-e^+ and annihilating into two photons.
- Figure 25c shows Compton scattering where an electron scatters off a photon.
- Figure 25d shows the creation of an electron-positron pair from two photons. This is called the Breit–Wheeler process after Gregory Breit and John A. Wheeler studied this process in a Physical Review paper entitled "Collision of Two Light Quanta" [43] in 1934 while they both worked here at New York University. Today, I myself actively research this process alongside pair creation of other particles, namely $\gamma\gamma \to \mu\mu$ and $\gamma\gamma \to \tau\tau$ at the Large Hadron Collider.

We follow the common convention that places the initial states of a reaction on the left and final states on the right of a Feynman diagram.

4.2 Virtual particles

The exchange of virtual particles is the quantum mechanical description of force. Let us zoom into a particular Feynman diagram for closer analysis. Consider the interaction $1+2 \xrightarrow{X} 1'+2'$:

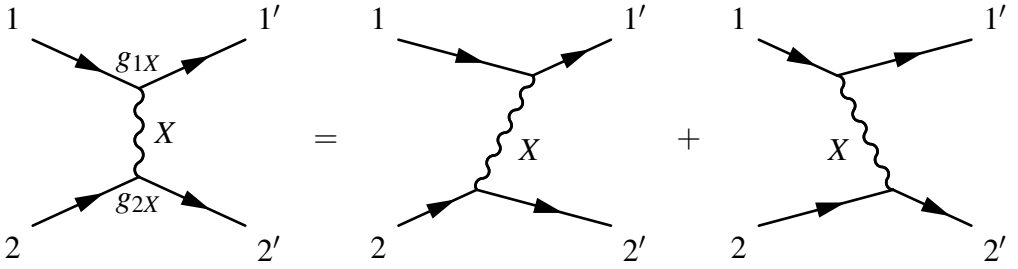

. (4.8)

We describe X as a **virtual particle** that is **exchanged** because it does not appear in the final states. For time flowing left-to-right $\to$, the Feynman diagram is equal to the superposition of the two time-ordered diagrams on the right. It is momentarily created and annihilated at the vertices. In special relativity, we can work in the rest frame of particle 1 to conserve energy and momentum at the vertex g_{1X}, writing in four-momentum notation $\mathsf{P} = (E/c, \mathbf{p}) = (E, p_x, p_y, p_z)$:

$$\mathsf{P}_1 \to \mathsf{P}_{1'} + \mathsf{P}_X \tag{4.9}$$

$$\begin{pmatrix} m_1 \\ \mathbf{0} \end{pmatrix} \to \begin{pmatrix} E_1 \\ \mathbf{p}_1 \end{pmatrix} + \begin{pmatrix} E_X \\ -\mathbf{p}_1 \end{pmatrix}. \tag{4.10}$$

So the energies of particles 1 and X on the right-hand side are

$$E_1^2 = p_1^2 + (m_1)^2 \quad \text{and} \quad E_X^2 = p_1^2 + (m_X)^2$$

where $p_1 = |\mathbf{p}_1|$. Now consider the energy difference before and after the process at vertex g_{1X}:

$$\Delta E = (E_1 + E_X) - m_1 \to \begin{cases} 2p_1, & p_1 \gg m_1 \\ m_X, & p_1 \ll m_X \end{cases}.$$

We find $\Delta E \neq 0 \; \forall \; p_1$ meaning energy cannot be conserved at the vertex g_{1X}. This seems alarming, but we recall the energy–time uncertainty relation in quantum mechanics $\Delta E \Delta t \gtrsim \hbar$. This states that it is not possible to definitively know the precise energy of a system within a finite time. The "violation" of energy conservation is allowed for a duration of $\Delta t \leq \hbar/\Delta E$. Using $\Delta E \geq m_X$, we also infer the distance d for any exchange particle X to propagate before being absorbed by particle 2 is restricted by

$$d \leq R \equiv \frac{\hbar c}{m_X c^2}. \tag{4.11}$$

We define R as the **range** of the exchange particle and by implication the force. In general, 4-momentum need not be strictly conserved at a vertex. Note that for mass particles such as photons $m_X \to 0$, $R \to \infty$ implying infinite range for electromagnetism.

Mandelstam variables Particle physicists often adopt a notational conventional for any scattering of two initial and two final states (called **2-to-2 scattering**) to describe various momenta exchanged that are Lorentz invariant. Using the labels in figure 4.8, these are called the Mandelstam variables and defined as:

$$s = (\mathsf{P}_1 + \mathsf{P}_2)^2, \tag{4.12}$$
$$t = (\mathsf{P}_1 - \mathsf{P}_{1'})^2, \tag{4.13}$$
$$u = (\mathsf{P}_1 - \mathsf{P}_{2'})^2. \tag{4.14}$$
$$\tag{4.15}$$

The $\sqrt{s}$ equivalent to the centre-of-mass energy of the initial state system, and is widely used at particle accelerators. Meanwhile, $\sqrt{t}$ is often seen when describing the momentum exchange.

4.3 Scattering and propagators

In quantum mechanics, we model interactions using potentials in the Hamiltonian of Schrödinger's equation. This allows us to calculate a matrix $\mathscr{M}$ of final state $|f\rangle$ occurring due to a potential V given we start with initial state $|i\rangle$:

$$\mathscr{M}_{fi} = \langle f|V|i\rangle = \int \psi_f V \psi_i \, \mathrm{d}\mathbf{r}. \tag{4.16}$$

This has the heuristic:

$$\mathscr{M}_{fi} = |\text{prepare initial states}\rangle \rightarrow \boxed{\text{interaction happens}} \rightarrow |\text{measure final states}\rangle. \tag{4.17}$$

At this point, let us briefly review a selection of key results from scattering theory presented in non-relativistic quantum mechanics classes. Assuming the incident particle is a momentum eigenstate $|\phi\rangle = |\mathbf{k}\rangle$ of the free Hamiltonian $H_0 = \mathbf{k}^2/2m$. We can write this in position representation as a plane wave

$$\langle \mathbf{r}|\phi\rangle = \phi_0(\mathbf{r}) = \frac{1}{(2\pi)^{3/2}} \mathrm{e}^{\mathrm{i}\mathbf{k}\cdot\mathbf{r}} \tag{4.18}$$

normalised[35] by $(2\pi)^{3/2}$. We work with **sufficiently localised potentials** such that $V \to 0$ in the limit $|\mathbf{r}| \to \infty$. Quoting some results from standard quantum mechanics textbooks, the asymptotic solution to scattering off a potential $V(\mathbf{r})$ in three dimensions is a superposition of the incident plane and spherical waves scattered forward, denoted ψ_+:

$$\psi(\mathbf{r}) \xrightarrow{r\to\infty} \phi_0(\mathbf{r}) + \psi_+(\mathbf{r}) = \frac{1}{(2\pi)^{3/2}} \left[e^{\mathrm{i}\mathbf{k}\cdot\mathbf{r}} + f(\mathbf{k}', \mathbf{k}) \frac{\mathrm{e}^{\mathrm{i}kr}}{r} \right], \tag{4.19}$$

where r is the asymptotic observation position and $f(\mathbf{k}', \mathbf{k})$ is the **scattering amplitude**:

$$f(\mathbf{k}', \mathbf{k}) = -\frac{(2\pi)^3}{4\pi} 2m \langle \mathbf{k}'|V|\psi_+\rangle. \tag{4.20}$$

This $f(\mathbf{k}', \mathbf{k})$ contains all the information about the incident waves scattering off the potential V. In (4.19), we neglect the interference between the incident wave (first term) and the scattered spherical waves (second term).

We commonly work in the regime $H_0 \gg V$ where the kinetic energy of the incident beam dominates over the scattering potential. Then the scattering beam is, to a first approximation,

[35] This slightly awkward normalisation will cause factors of $1/(2\pi)^3$ to appear in our Fourier transform like expressions going from space to momentum. This is sometimes known as the 'physicist' normalisation for Fourier transforms as opposed to the 'mathematician' $1/(2\pi)^{3/2}$ normalisation.

unchanged by V. So the final state of the system $|\psi_+\rangle$ is approximately equal to the initial momentum eigenstate $|\mathbf{k}\rangle$. It is possible to expand the scattering amplitude (4.20) as a Born series and keeping the leading term we have

$$f^{(1)}(\mathbf{k}',\mathbf{k}) = -\frac{(2\pi)^3}{4\pi} 2m\langle \mathbf{k}'|V|\mathbf{k}\rangle \tag{4.21}$$

So given a scattering potential V, we find the scattering amplitude $f^{(1)}(\mathbf{k}',\mathbf{k})$ is given by $f^{(1)}(\mathbf{k}',\mathbf{k}) \propto \langle \mathbf{k}'|V|\mathbf{k}\rangle$. Using the completeness relation $\int \mathrm{d}^3\mathbf{r}\ |\mathbf{r}\rangle\langle\mathbf{r}|$ twice, we can recast (4.21) into the position representation:

$$\langle \mathbf{k}'|V|\mathbf{k}\rangle = \int \mathrm{d}^3\mathbf{r}' \int \mathrm{d}^3\mathbf{r}\, \langle \mathbf{k}'|\mathbf{r}'\rangle\langle\mathbf{r}'|V|\mathbf{r}\rangle\langle\mathbf{r}|\mathbf{k}\rangle = \int \mathrm{d}^3\mathbf{r}\langle \mathbf{k}'|\mathbf{r}\rangle V(\mathbf{r})\langle\mathbf{r}|\mathbf{k}\rangle, \tag{4.22}$$

where in the second equality, we apply a sufficiently localised potential $\langle \mathbf{r}'|V|\mathbf{r}\rangle = V(\mathbf{r}')\delta^{(3)}(\mathbf{r}' - \mathbf{r})$ such that integrating over the $\mathbf{r}'$ sends $\mathbf{r}' \to \mathbf{r}$. Using the momentum eigenstates in position representation (4.18) we obtain

$$\boxed{\langle \mathbf{k}'|V|\mathbf{k}\rangle = \frac{1}{(2\pi)^3}\int \mathrm{d}^3\mathbf{r}\, V(\mathbf{r})\, \mathrm{e}^{\mathrm{i}\mathbf{q}\cdot\mathbf{r}}} \tag{4.23}$$

This is the central result of the **Born approximation**, which states that the scattering amplitude $f^{(1)}(\mathbf{k}',\mathbf{k})$ is proportional to the **Fourier transform of the scattering potential** $V(\mathbf{r})$ in momentum transfer space $\mathbf{q} \equiv \Delta\mathbf{k} = \mathbf{k} - \mathbf{k}'$. Recall from quantum mechanics that the probability current density formula is $\mathbf{j} = \frac{1}{2m\mathrm{i}}(\psi^*\nabla\psi - \psi\nabla\psi^*)$. Applying this to (4.19), we find the differential cross-section is the modulus square of the scattering amplitude (4.20):

$$\frac{\mathrm{d}\sigma}{\mathrm{d}\Omega} = \frac{r^2|\mathbf{j}^{\mathrm{scat}}|}{|\mathbf{j}^{\mathrm{inc}}|} = |f(\mathbf{k}',\mathbf{k})|^2. \tag{4.24}$$

This connects the theoretical scattering amplitude $f(\mathbf{k}',\mathbf{k})$ with an observable $\mathrm{d}\sigma/\mathrm{d}\Omega$. The interpretation of (4.24) is that $\mathrm{d}\sigma$ is the probability incident particles are scattered into the solid angle element $\mathrm{d}\Omega$. By performing scattering measurements of the differential cross-section (4.24), we can inverse Fourier transform to infer the scattering potential $V(\mathbf{r})$.

You may be feeling déjà-vu from optics classes? This because indeed you have seen the same effect as light or electrons passes through a single slit experiment (figure 26). The interference pattern $f(\mathbf{k})$ of wiggles you see on a screen far away from the slits is precisely the Fourier transform of the slit aperture $a(\mathbf{x})$

$$f(\mathbf{k}) \propto \int a(\mathbf{x})\mathrm{e}^{\mathrm{i}\mathbf{k}\cdot(\mathbf{x}-\mathbf{x}')}\mathrm{d}^3\mathbf{x}'. \tag{4.25}$$

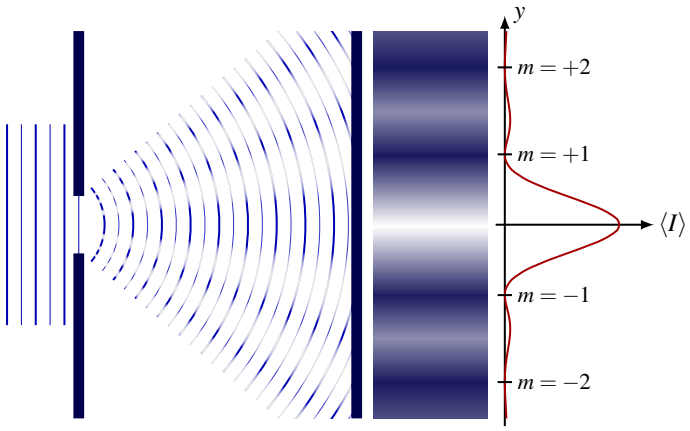

Figure 26: **Diffraction pattern as Fourier transform**. The interference pattern viewed far away by an observer is the Fourier transform of the aperture during waves scattering. In quantum mechanical scattering, the scattering amplitude is analogously the Fourier transform of the potential. Figure: tikz.net.

This is simply how waves behave! The wiggles encode all the information of ingoing waves interacting with the slits. In the quantum mechanical scattering, we have generalised the optical slits into any localised potential $V(r)$. This is actually how the path integral formulation of quantum mechanics works. As the slit width is taken to infinity, the amplitude is the sum of all possible paths taken.

We can model the range R of a force by adding an exponential function that decays rapidly $e^{-r/R}$ to a $1/r$ potential familiar from a classical Coulomb electrostatic force:

$$V_Y(r) = -\frac{g^2}{4\pi}\frac{\mathrm{e}^{-r/R}}{r}. \tag{4.26}$$

We call this the **Yukawa potential**, after Hideki Yukawa who studied this for the strong nuclear force. Here, g is the coupling constant and R is the characteristic range of the potential according to (4.11). For those who enjoy multivariate calculus, we can align the momentum transfer $\mathbf{q}$ in the z direction such that $\mathbf{q}\cdot\mathbf{r} = |\mathbf{q}|r\cos\theta$, we can perform the integral over spherical polar coordinates with $\mathrm{d}^3\mathbf{r} = r^2\sin\theta\mathrm{d}r\mathrm{d}\theta\mathrm{d}\phi$:

$$\langle\mathbf{k}'|V_Y|\mathbf{k}\rangle = -\frac{1}{(2\pi)^3}\frac{g^2}{4\pi}\int_{r=0}^{\infty}\int_{\theta=0}^{\pi}\int_{\phi=0}^{2\pi}\frac{\mathrm{e}^{-r/R}}{r}\mathrm{e}^{\mathrm{i}|\mathbf{q}|r\cos\theta}r^2\sin\theta\mathrm{d}r\mathrm{d}\theta\mathrm{d}\phi \tag{4.27}$$

To evaluate the angular parts of the integral, we can perform a change of variables $z = \cos\theta, \mathrm{d}z = -\sin\theta\mathrm{d}\theta$ to yield the radial integral

$$\langle\mathbf{k}'|V_Y|\mathbf{k}\rangle = -\frac{g^2}{(2\pi)^3}\frac{1}{2\mathrm{i}q}\int_0^{\infty}\left[\mathrm{e}^{(\mathrm{i}|\mathbf{q}|-m_X)r} - \mathrm{e}^{-(\mathrm{i}|\mathbf{q}|+m_X)r}\right]\mathrm{d}r. \tag{4.28}$$

Finishing this and overcoming some more algebra[36], the scattering amplitude becomes

$$\langle \mathbf{k}'|V_Y|\mathbf{k}\rangle = -\frac{g^2}{(2\pi)^3}\frac{1}{|\mathbf{q}|^2+(m_X)^2}. \tag{4.29}$$

The coupling constant g paramterises the strength of the interaction. The two factors of g corresponds to the two vertices where the exchange particle X is created and annihilated. In general, for an amplitude calculation involving N vertices, there are N factors of g. Thus N is the **order** of the amplitude. We also identify the **propagator**:

$$-\frac{1}{|\mathbf{q}|^2+(m_X)^2} \tag{4.30}$$

This represents the associated momentum and mass exchanged in the interaction. In relativistic formulations, this expression (4.30) generalises to the **relativistic Feynman propagator**:

$$\mathscr{P} = \frac{1}{\mathsf{Q}^2-(m_X)^2}, \tag{4.31}$$

where Q and m_X are the 4-momentum and invariant mass of the exchange particle X, respectively, involved in the interaction. For those taking quantum field theory, this is formally related to the Green's function $G(k)$ of the Klein–Gordon equation (3.36) in Fourier space:

$$(\Box+m^2)G(x-y)=\delta(x-y) \quad \Rightarrow \quad (-k^2+m^2)G(k)=1. \tag{4.32}$$

We find that these virtual particles do not satisfy the usual P^2 relation:

$$\mathsf{Q}^2 = E_X^2 - \mathbf{k}_X\cdot\mathbf{k}_X \neq (m_X)^2. \tag{4.33}$$

We call this inequality being **off mass-shell** and is required otherwise the propagator diverges. In general, the scattering amplitude of order N is related to the vertex factor gq_f and the propagator $\mathscr{P}$ of the virtual exchange particle by:

$$\langle \mathbf{k}'|V|\mathbf{k}\rangle \propto \mathscr{M}_{fi} = \frac{(gq_f)^N}{\mathsf{Q}^2-(m_X)^2}. \tag{4.34}$$

For electromagnetic interactions, we need to calculate the amplitude $\langle f|V_{\text{EM}}|i\rangle$ where V_{EM} is the Coulomb potential. This is the Yukawa potential in the infinite range limit $R\to\infty$, or equivalently the mass of the mediator to zero $m_X\to 0$, as expected for massless photons.

[36]Physically, we can invoke the far-distance argument, where the exponent vanishes $\lim_{r\to\infty}\exp[(\mathrm{i}|\mathbf{q}|-m_x)r]\to 0$ in the $r\to\infty$ limit. The imaginary part of the argument causes oscillations while the real part exponentially decays as $r\to\infty$, implying no part of the exponent grows and we can therefore assume it vanishes in a physically sensibly manner. For those who have taken complex analysis classes, a more rigorous treatment uses contour integrals to evaluate this in the complex plane and applies the residue theorem for each pole.

4.4 Gauge theory of electrodynamics

The quantum field theory classes cover this topic in far greater detail, but let us sketch out the main arguments for those not taking that course or for review. The gauge theory of electrodynamics is the simplest such theory of nature, and the prototype for generalisation to the strong and weak forces. From Maxwell's equations (3.19), we can write the electromagnetic fields in terms of the electric ϕ and magnetic $\mathbf{A}$ potentials as derivatives

$$\mathbf{E} = -\boldsymbol{\nabla}\phi - \frac{\partial \mathbf{A}}{\partial t}, \quad \mathbf{B} = \boldsymbol{\nabla} \times \mathbf{A}. \tag{4.35}$$

We can form the electromagnetic four-potential, which transforms as a four-vector

$$A^\mu = \begin{pmatrix} \phi \\ \mathbf{A} \end{pmatrix}. \tag{4.36}$$

The fields $\mathbf{E}, \mathbf{B}$ remain invariant up to a gauge transformation to a function $\chi(x)$ whose space-time derivative exist

$$A^\mu \to A'^\mu = \begin{pmatrix} \phi - \partial_t \chi \\ \mathbf{A} + \boldsymbol{\nabla}\chi \end{pmatrix}. \tag{4.37}$$

Electromagnetic fields remain invariant under such a transformation, which is a statement of **gauge invariance**. Recalling $A_\mu = \eta_{\mu\nu}A^\nu = \begin{pmatrix} \phi \\ -\mathbf{A} \end{pmatrix}$ and $\partial_\nu = \begin{pmatrix} \partial_t \\ +\boldsymbol{\nabla} \end{pmatrix}$, we can write the gauge transformation in four-vector form as

$$A_\mu \to A'_\mu = A_\mu - \partial_\mu \chi(x). \tag{4.38}$$

In classical mechanics, we can define a Lagrangian $L(x, \dot{x}) = T - V$ for kinetic T and potential V energies such that Euler–Lagrange equation gives the equation of motion $\frac{\partial L}{\partial x} = \frac{\mathrm{d}}{\mathrm{d}t}\frac{\partial \mathscr{L}}{\partial \dot{x}}$. It turns out we can extend this formalism to describe classical fields $\psi(x_\mu)$ that manifestly respect Lorentz invariance. We do this with a Lagrangian[37] $\mathscr{L}(\psi, \partial_\mu \psi) = \mathscr{T} - \mathscr{V}$ by identifying $x \to \psi(x_\mu)$ and its four-derivative $\dot{x} \to \partial_\mu \psi$ and applying the Euler–Lagrange equation yields the equation of motion

$$\frac{\partial \mathscr{L}}{\partial \psi} = \partial_\mu \left(\frac{\partial \mathscr{L}}{\partial(\partial_\mu \psi)} \right). \tag{4.39}$$

This is a ridiculously quick review of field theory, where further details about how this is quantised appears in Quantum Field Theory classes and textbooks.

[37] Technically $\mathscr{L}$ is the Lagrangian density $L = \int \mathrm{d}^4 x \, \mathscr{L}$ but textbooks often drop "density" for brevity.

The Dirac equation of motion (3.48) is given by to the Lagrangian

$$\mathscr{L}_{\text{Dirac}} = \bar{\psi}(\mathrm{i}\gamma^\mu \partial_\mu - m)\psi. \tag{4.40}$$

The minimal coupling prescription of spin-half particles interacting with electromagnetism promotes the partial derivative in the Dirac equation to a **covariant derivative**:

$$\partial_\mu \to D_\mu = \partial_\mu + \mathrm{i}eA_\mu. \tag{4.41}$$

So the Dirac Lagrangian becomes:

$$\mathscr{L} = \bar{\psi}(\mathrm{i}\gamma^\mu D_\mu - m)\psi. \tag{4.42}$$

The Lagrangian (4.42) is invariant under a global complex phase. Mathematically, we see this with the transformation

$$\psi \to \psi' = \psi(x)e^{-\mathrm{i}\alpha}, \quad \text{global U(1)} \tag{4.43}$$

where α is a constant and the Lagrangian remains invariant because the $\bar{\psi}$ introduces a factor of $\mathrm{e}^{+\mathrm{i}\alpha}$. We call this a **global U(1) symmetry** of Dirac theory. This is a continuous symmetry so by Emmy Noether's theorem[38], there is a conserved current

$$j^\mu = \bar{\psi}\gamma^\mu\psi. \tag{4.44}$$

This spinor current j^μ couples to the electromagnetic field A_μ in the covariant derivative leading to the QED interaction vertex:

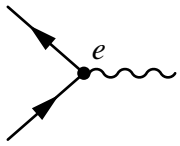

$$= \mathrm{i}eA_\mu j^\mu = \mathrm{i}eA_\mu \bar{\psi}\gamma^\mu\psi. \tag{4.45}$$

Now let us change the global complex phase into a local complex phase such that it depends on spacetime $\alpha \to \alpha(x)$

$$\psi \to \psi' = \psi(x)\mathrm{e}^{-\mathrm{i}\alpha(x)}, \quad \text{local U(1)}. \tag{4.46}$$

[38]For field theorists among our readers, this is technically a slightly stronger requirement that there is a symmetry of the action $S = \int \mathrm{d}^4x\,\mathscr{L}_{\text{Dirac}}$, where $\mathscr{L}_{\text{Dirac}} = \bar{\psi}(\mathrm{i}\gamma^\mu D_\mu - m)\psi$ is the Dirac Lagrangian. In this case, this global U(1) symmetry exists for the equation of motion, Lagrangian, and action.

We call this a **local U(1) transformation**. As the exponent is now a function of spacetime, the product rule applies for the derivative so the Dirac equation becomes

$$(\mathrm{i}\gamma^\mu D_\mu - m)\psi \to [\mathrm{i}\gamma^\mu(\partial_\mu - \underbrace{\mathrm{i}\partial_\mu\alpha}_{\text{extra}} + \mathrm{i}eA_\mu) - m]\psi'. \tag{4.47}$$

We now see this seems to have lost the U(1) symmetry due to the extra piece $\mathrm{i}\partial_\mu\alpha(x)$ from the product rule.

But worry not, we can restore the invariance via the gauge transformation of the photon field (4.38): $A_\mu \to A'_\mu = A_\mu - \partial_\mu\chi(x)$. If we perform the local U(1) transformation on $\psi \to \psi\mathrm{e}^{-\mathrm{i}\alpha(x)}$ and gauge transformation $A_\mu \to A_\mu + \partial_\mu\chi(x)$ *simultaneously*, we can restore the invariance of the Dirac equation by identifying

$$\chi(x) = \frac{\alpha(x)}{e}. \tag{4.48}$$

So now we can state equation (4.42) is invariant under the simultaneous transformations:

$$\psi \to \psi\mathrm{e}^{-\mathrm{i}\alpha(x)}, \qquad \text{local U(1) transformation,} \tag{4.49}$$

$$A^\mu \to A^\mu - \frac{1}{e}\partial^\mu\alpha(x), \quad \text{gauge transformation.} \tag{4.50}$$

This is the gauge theory of electromagnetism. Its mathematical simplicity belies its profundity that forces are deeply intertwined with local spacetime and gauge symmetries. By itself, embedding the two $\pm$ physical polarisations of the photon $\varepsilon_\pm$ into the four degrees of freedom of a Lorentz vector A_μ results in gauge redundancy.

However, in quantum mechanics, the potential A_μ seems more fundamental, which is what that couples to the complex phase of particle amplitudes. Figure 27 shows an electron traversing spacetime. Its wavefunction ψ acquires a complex phase that changes with its position and time, which is determined by the gauge freedom of the electromagnetic potential A_μ. In the case of U(1) electromagnetism, the phase traces out a circle, which is sometimes called the internal space. This is a manifestation of the Aharanov–Bohm effect, which is an experimental demonstration that a non-zero potential A_μ imparts a phase shift to the wavefunction even when the fields (first derivative of potentials) are zero.

The electromagnetic field strength tensor is given by

$$F^{\mu\nu} = \partial^\mu A^\nu - \partial^\nu A^\mu. \tag{4.51}$$

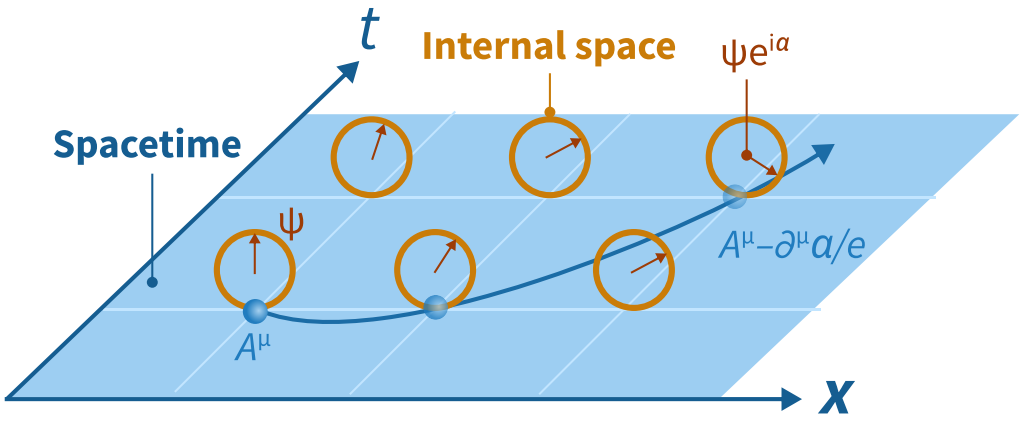

Figure 27: **Sketch of gauge theory**. A particle moving through spacetime in the presence of a non-trivial vector potential A^μ. The wavefunction acquires a change in local phase $\psi \to \psi e^{-i\alpha(x)}$, whose internal space of U(1) electromagnetism is a circle. The phase change corresponds to a change in the gauge potential $A^\mu \to A^\mu - \frac{1}{e}\partial^\mu \alpha$.

It is a traceless antisymmetric object that transforms as a tensor $F'^{\mu\nu} = \Lambda^\mu_\rho \Lambda^\nu_\sigma F^{\rho\sigma}$. We can write out in time-space coordinates in terms of the electric **E** and magnetic **B** fields as:

$$F^{\mu\nu} = \begin{pmatrix} 0 & -E_x & -E_y & -E_z \\ E_x & 0 & -B_z & B_y \\ E_y & B_z & 0 & -B_x \\ E_z & -B_y & -B_x & 0 \end{pmatrix}. \tag{4.52}$$

The field tensor $F^{\mu\nu}$ is gauge invariant by construction i.e. is invariant under a gauge transformation (4.50). The inhomogeneous Maxwell equations, namely Gauss' and Ampère's laws, in the presence of sources j_ν is written in manifestly covariant form as

$$\partial_\mu F^{\mu\nu} = j^\nu. \tag{4.53}$$

The source-free Maxwell equations are then written as

$$\partial_\mu F^{\mu\nu} = \Box A^\nu - \partial^\nu(\partial_\mu A^\mu) = 0. \tag{4.54}$$

The Lagrangian that produces this equation of motion upon applying the Euler–Lagrange equation is

$$\mathscr{L}_{\text{Maxwell}} = -\frac{1}{4} F_{\mu\nu} F^{\mu\nu}. \tag{4.55}$$

The homogeneous Maxwell equations (no magnetic monopoles and Faraday's law) are captured by the Bianchi identity $\partial_\mu F_{\nu\sigma} + \partial_\nu F_{\sigma\mu} + \partial_\sigma F_{\mu\nu} = 0$. Combining the Maxwell and Dirac Lagrangian (4.42) gives

$$\boxed{\mathscr{L}_{\text{QED}} = -\frac{1}{4}F_{\mu\nu}F^{\mu\nu} + \bar{\psi}(\mathrm{i}\gamma^\mu D_\mu - m)\psi.} \tag{4.56}$$

This is the Lagrangian for the theory of quantum electrodynamics. It is a marvel that this is our most precise description of electromagnetism and the prototype for the nuclear forces in the Standard Model.

Gauge fixing

We are always free to *choose* A^μ to satisfy the **Lorenz**[39] **gauge**

$$\partial_\mu A^\mu = 0. \tag{4.57}$$

To see this, say we acquired a gauge field A^μ that instead satisfies

$$\partial_\mu A^\mu = f(x), \tag{4.58}$$

where $f(x)$ is some non-zero well-behaved function. We are always free to perform a gauge transformation (4.50) to yield

$$\partial_\mu A^\mu - \Box\chi = f(x). \tag{4.59}$$

If we wish to recover the Lorenz gauge $\partial_\mu A^\mu = 0$, we require this condition to hold:

$$\Box\chi = -f(x). \tag{4.60}$$

This is the inhomogeneous wave equation which may always be solved for solutions. Hence we are always free to choose the Lorenz gauge.

In the Lorenz gauge, Maxwell's equations (4.54) reduce to a wave equation

$$\Box A^\mu = 0, \tag{4.61}$$

[39] This is named after Ludvig Lorenz (1829–1891), not Hendrik Lorentz (1853–1928) of the Lorentz transformations. Sometimes the literature calls this the 'Lorentz' gauge. Unfortunate misattribution aside, it is indeed a Lorentz covariant choice. Even worse, the pair have a Lorenz-Lorentz equation named after them. All this is not to be confused with Edward Lorenz (1917–2008) of the Lorenz attractor, pioneer of chaos theory.

which has solutions of the form

$$A^\mu = \int \frac{\mathrm{d}^4 k}{(2\pi)^4} \varepsilon^\mu(k) \mathrm{e}^{-\mathrm{i}k\cdot x}. \tag{4.62}$$

This has the form of a massless Klein–Gordon equation so analogous to (4.31), the relativistic photon propagator is simply

$$\mathscr{P} = \frac{1}{k^2}. \tag{4.63}$$

All our wonderful mathematics seem to imply the free electromagnetic field has four degrees of freedom. We know that there are two polarisations of free electromagnetic waves. There must be two constraints to ground us back to reality:

1. **Choose (Lorenz) gauge**
   In (4.62) ε^μ is the **polarisation vector**. The Lorenz gauge (4.57) now becomes a statement of 4-orthogonality:

   $$k_\mu \varepsilon^\mu = 0. \tag{4.64}$$

   This now fixes one component of ε^μ in terms of the other three. For example, given our vectors are

   $$k^\mu = \begin{pmatrix} k^0 \\ \mathbf{k} \end{pmatrix}, \quad \varepsilon^\mu = \begin{pmatrix} \varepsilon^0 \\ \boldsymbol{\varepsilon} \end{pmatrix}, \tag{4.65}$$

   the timelike component is completely determined by the spacelike ones:

   $$k_0 \varepsilon^0 = \mathbf{k} \cdot \boldsymbol{\varepsilon}. \tag{4.66}$$

   We are down to 3 spatial independent components of ε^μ. One more to go.

2. **Fix residual gauge freedom**
   Gauge freedom (4.50) in Fourier space becomes

   $$A^\mu \to \tilde{A}^\mu = A^\mu + a k^\mu, \tag{4.67}$$

   where a is some scalar. From (4.62) corresponds to the polarisation vector being defined up to scalar multiple of k^μ i.e. we can take

   $$\varepsilon^\mu \to \tilde{\varepsilon}^\mu = \varepsilon^\mu + a k^\mu \tag{4.68}$$

   This still satisfies the gauge condition (4.64) because $k^\mu k_\mu = 0$ for free fields. As we are free to add multiples of k^μ to ε^μ, let us choose $a = -\varepsilon^0/k^0$ such that the timelike

component of our redefined polarisation vector vanishes $\varepsilon^0 = 0$. Then we obtain a statement of 3-orthogonality in the spatial degrees of freedom:

$$\mathbf{k} \cdot \boldsymbol{\varepsilon} = 0. \tag{4.69}$$

This is in fact equivalent to imposing the **Coulomb gauge $\nabla \cdot \mathbf{A} = 0$. There are thus only two independent components of $\boldsymbol{\varepsilon}$ perpendicular to k.**

Without loss of generality we can align our z axis along the momentum of our electromagnetic wave, allowing us to choose k^μ and our two polarisation vectors $\varepsilon^\mu_{1,2}$ to be

$$k^\mu = \begin{pmatrix} k^0 \\ 0 \\ 0 \\ k^0 \end{pmatrix}, \quad \varepsilon^\mu_1 = \begin{pmatrix} 0 \\ 1 \\ 0 \\ 0 \end{pmatrix}, \quad \varepsilon^\mu_2 = \begin{pmatrix} 0 \\ 0 \\ 1 \\ 0 \end{pmatrix}. \tag{4.70}$$

This is equivalent to vertical and horizontal polarised photons. One could also choose circular polarised photons

$$\varepsilon^\mu_1 = \frac{1}{\sqrt{2}} \begin{pmatrix} 0 \\ 1 \\ \mathrm{i} \\ 0 \end{pmatrix}, \quad \varepsilon^\mu_2 = \frac{1}{\sqrt{2}} \begin{pmatrix} 0 \\ 1 \\ -\mathrm{i} \\ 0 \end{pmatrix}. \tag{4.71}$$

The polarisation vectors satisfy the orthonormality condition:

$$\boldsymbol{\varepsilon}_\lambda \cdot \boldsymbol{\varepsilon}_{\lambda'} = \delta_{\lambda\lambda'} \quad \Leftrightarrow \quad (\varepsilon_\lambda)^\mu (\varepsilon_{\lambda'})_\mu = -\delta_{\lambda\lambda'}. \tag{4.72}$$

Finally the full Fourier decomposition of A^μ is

$$A^\mu(x) = \int \frac{\mathrm{d}^3 k}{(2\pi)^3 2E_{\mathbf{k}}} \sum_{\lambda=1}^{2} \left[a_{\mathbf{k},\lambda} \varepsilon^\mu_\lambda(\mathbf{k}) \mathrm{e}^{-\mathrm{i}k\cdot x} + a^*_{\mathbf{k},\lambda} \varepsilon^\mu_\lambda(\mathbf{k}) \mathrm{e}^{-\mathrm{i}k\cdot x} \right] \tag{4.73}$$

These are the plane wave solutions, showing the photon as a superposition of the two polarisation states $\lambda = 1,2$ over all available momenta $\mathbf{k}$.

QED Feynman rules

A class in particle physics would not be complete without stating some Feynman rules. These are algorithms for calculating a cross-section or decay, which are usually derived in QFT

classes. You can look these up in textbooks and for completeness, let us print them here. For on-shell initial and final states, we have:

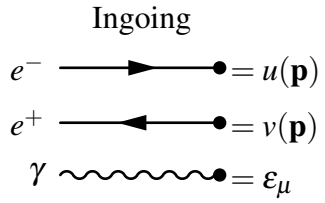

(4.74)

(4.75)

(4.76)

For off-shell internal lines denoted by $*$, the propagators are

(4.77)

(4.78)

The interaction vertex is the electric charge e:

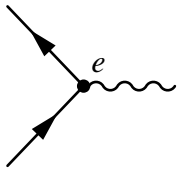

(4.79)

Using these Feynman rules, we can draw Feynman diagrams then immediately write down the mathematical amplitude. As an example, Bhabba scattering involves $e^-e^+ \to e^-e^+$ for which an s-channel diagram is

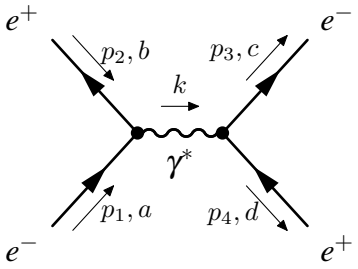

$$\propto \underbrace{[\bar{v}^d(\mathbf{p}_4)(\mathrm{i}e\gamma^\mu)u^c(\mathbf{p}_3)]}_{\text{outgoing}} \underbrace{\frac{\eta_{\mu\nu}}{(p_1+p_2)^2}}_{\text{propagator}} \underbrace{[\bar{v}^a(\mathbf{p}_1)(\mathrm{i}e\gamma^\nu)u^b(\mathbf{p}_2)]}_{\text{ingoing}}, \tag{4.80}$$

where we apply momentum conservation for $k = p_1 + p_2$ and the letters a, b, c, d denote the spinor indices.

5 Scattering experiments

Scattering forms the experimental basis for studying particle physics. We just saw how to draw electromagnetic scattering processes as Feynman diagrams to represent the microscopic interaction. We now turn to connecting this to experiments of how we actually electrons and positrons to high energy before measuring how they interact. Typical experiments involve measuring the production rates of final states when a beam of particles is incident on a target.

5.1 Linear particle accelerators

Without realising it, the Crookes tubes used in the nineteenth century to study cathode rays constituted the first electron linear accelerators. The principle of a linear accelerator (linac) is to exploit the fact electric charges experience the Lorentz force and therefore accelerate in an electric field. Accelerating charged particles feel the Lorentz force

$$m\frac{\mathrm{d}^2\mathbf{x}}{\mathrm{d}t^2} = \mathbf{f} = Q\left(\mathbf{E} + \frac{\mathrm{d}\mathbf{x}}{\mathrm{d}t} \times \mathbf{B}\right). \tag{5.1}$$

A motivation was Gamow's calculations that there is a finite probability of overcoming the Coulomb potential of a lithium nucleus using a proton into two helium nuclei:

$$p + {}^{7}_{3}\mathrm{Li} \to {}^{4}_{2}\mathrm{He} + {}^{4}_{2}\mathrm{He} \tag{5.2}$$

In 1932, John Cockcroft and Ernest Walton built the eponymous **Cockroft–Walton generator** could accelerate protons up to 700 keV at the Cavendish Laboratory, Cambridge (figure 28a). This apparatus constituted the first linear accelerator of a hadron that reached sufficient energies above 150 keV to induce the artificial transmutation of atomic nuclei [44]. They were also able to test the energy–mass equivalence $E = mc^2$. Figure 28b shows a quaint model built for museum display of the original experiment at the Cavendish Laboratory [40].

The key technological development was the voltage multiplier converting low-voltage alternating current into high-voltage direct current via a series of capacitors and diodes. This became a successful technology that was used by the likes of Fermilab and CERN as the initial stages of proton injection through the twentieth century (figure 29b). A contemporaneous device was the van der Graff generator.

Another major development is the **drift tube linac** (figure 30). Inside a vacuum drift tube, a series of cylindrical tubes establishes a series of uniform electric field between each

[40] A wonderful photograph of Walton himself sitting in the viewing chamber is available here: https://cudl.lib.cam.ac.uk/view/PH-CAVENDISH-P-00557/1

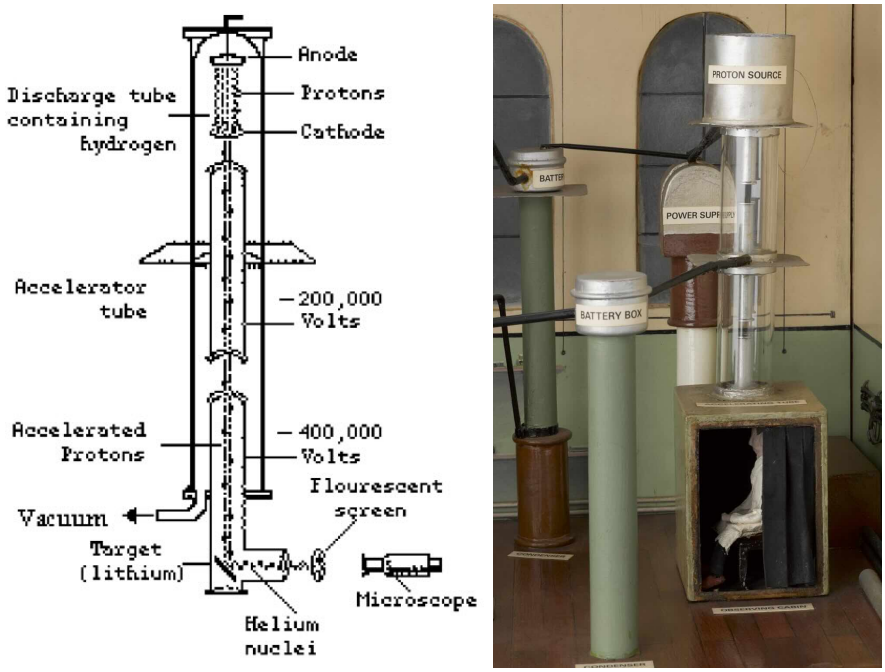

(a) Schematic diagram (b) Scale model

Figure 28: **Cockroft–Walton accelerator apparatus**. The first linear accelerator of protons was constructed in 1932 at Cambridge University and used in the first artificial transmutation of atomic nuclei. Images: Fermilab, Science Museum/W Lamprey.

tube. The injected charged particle, here an electron e^-, experiences a force $\mathbf{f} = e\mathbf{E}$ and accelerates between the tubes.

When the electron exits the first tube, a radio frequency driver generating a square wave inverts the voltage polarity of all tubes $\pm V \rightarrow \mp V$. This ensures the force vector always points in the same direction so the particle keeps accelerating.

If the polarity inversion were not synchronised to each electron exit, the electric field would decelerate the electron. We can then repeat this principle to accelerate beams up to very high energies and is highly efficient because the electron does not lose energy in any region. The main engineering limitations are a) producing large enough potential differences between each tube and b) constructing very long beamlines. Among the most powerful linear accelerator built is the Stanford Linear Accelerator (figure 31), which reaches two miles in length.

Rolf Widerøe developed the drift tube concept. For an oscillation frequency f of the driving oscillator, the length l_i of drift tube i, and β_i the velocity of the accelerated particle

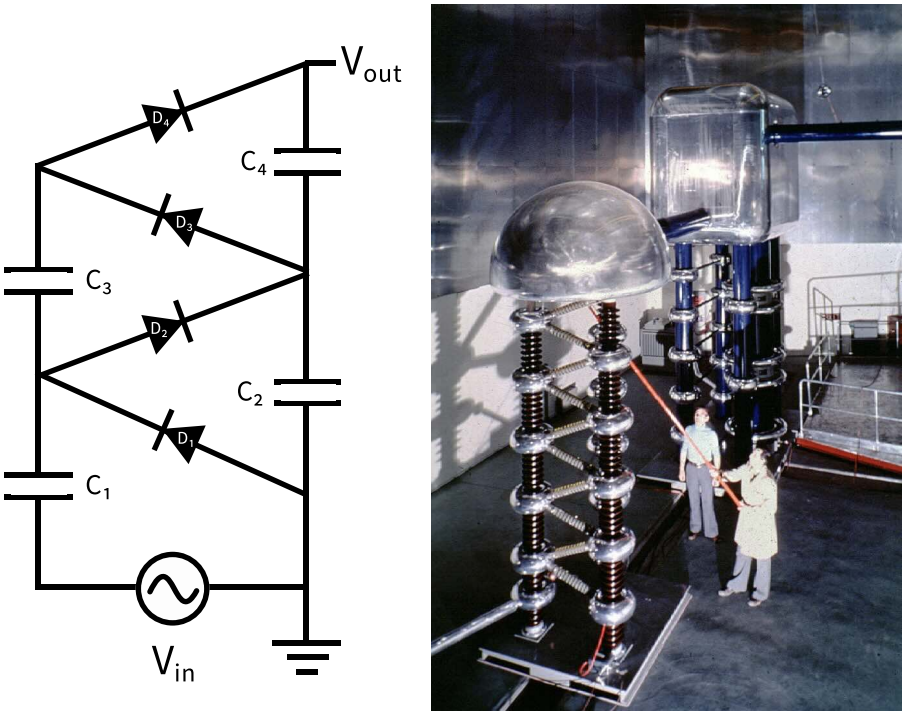

(a) Voltage multiplier (b) CERN CW multiplier

Figure 29: **Cockroft–Walton (CW) voltage multiplier**. (a) Crucial to reaching large voltages was the invention of the CW voltage multiplier scheme charging capacitors with an alternating current. (b) the 800 kV CW generator used until 1993 at CERN for pre-injection into the linear accelerator. Image: CERN [45].

when entering it, the condition that the particle remains in phase is established whenever

$$l_i = \frac{\beta_i c}{2f}. \tag{5.3}$$

5.2 Luminosity and cross-sections

To do science, we must use our theory to make measurable predictions. The cross-section is the most common observable in scattering experiments which justifies its study.

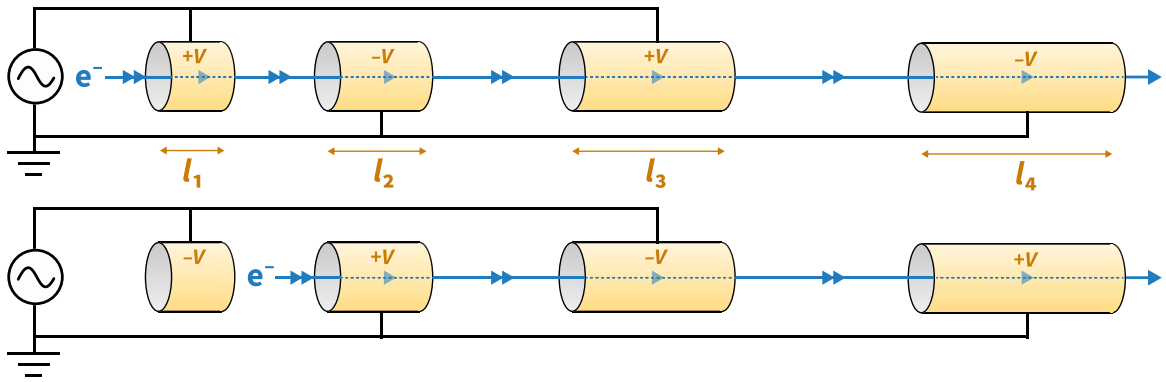

Figure 30: **My cartoon of the drift tube linac concept**. The injected particle accelerates outside the drift tubes wherein the particle traverses at constant velocity (single arrowhead). The acceleration region is in between the drift tubes (double arrowhead), which must increase in length l_i with increasing particle velocity. The lower sketch depicts the inverted polarity to ensure the particle accelerates in the same direction as before.

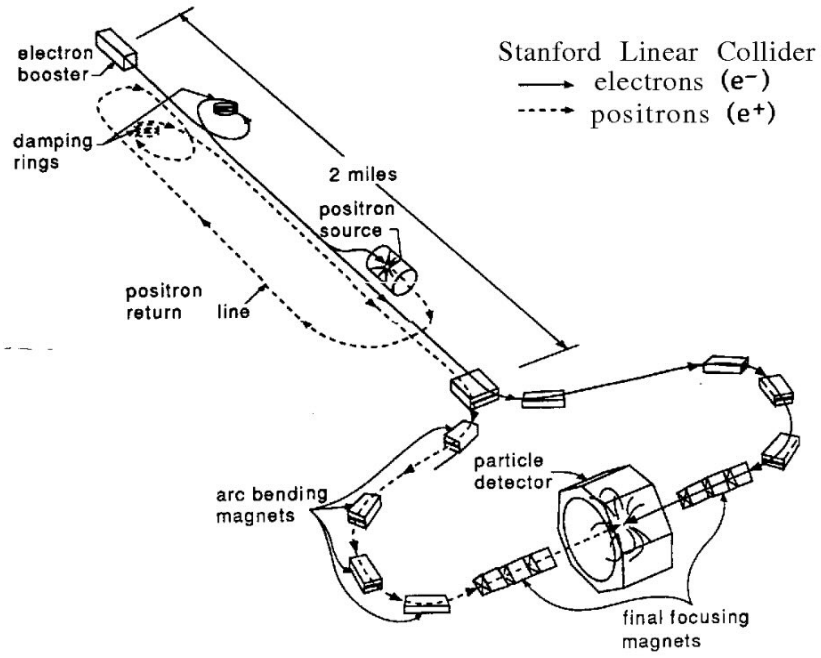

Figure 31: **Stanford Linear Accelerator**. This was the most powerful linear accelerator of electrons and positrons [46].

Particle accelerators have two beams that are aimed at each other:

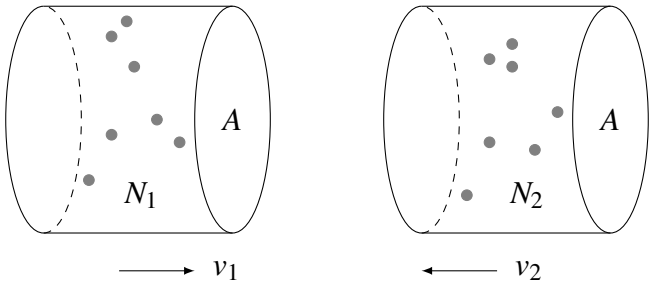

The particle flux Φ of a beam is the number of particles per unit area per unit time

$$\Phi = n_i v_i = \frac{\dot{N}_i}{A} \tag{5.4}$$

- n_i: particle number density (number per unit volume) of incident beam,
- v_i: velocity of incident particles in beam,
- $\dot{N}_i$: rate of incident projectiles number per unit time,
- A: cross-sectional area of incident beam.

Given the incident beam illuminates N_t targets, the effective area of interaction is $S = N_t \sigma_r$, where σ_r is **cross-section** of the reaction r with rate w_r

$$\sigma_r = \frac{w_r}{\Phi N_t}. \tag{5.5}$$

To obtain a better feel for this expression, rewrite this using (5.4):

$$w_r = \dot{N}_i N_t P_{\text{scat}}, \tag{5.6}$$

where $P_{\text{scat}} \equiv \sigma_r / A$ is interpreted as the scattering probability. So we see the reaction rate w_r is the rate of incident projectiles $\dot{N}_i$ incident on N_t targets multiplied by the probability of interaction. Often we consider the number density of the targets n_t in some material of thickness x such that $N_t = n_t A x$.

High-energy colliders use the term **instantaneous luminosity** for two colliding beams:

$$\mathscr{L} = \frac{\text{\# particles crossing one another}}{\text{time interval} \times \text{unit transverse area}} = \frac{N_1 N_2}{\Delta t A}, \tag{5.7}$$

where $\Delta t = 1/f$ is the time interval (inverse frequency) between particle bunches, N_1 and N_2 are the number of particles in each bunch, and A is the transverse area of the beam. Accelerator physicists commonly use instantaneous luminosity with units of inverse area per unit time, where $\text{cm}^{-2}\,\text{s}^{-1}$.

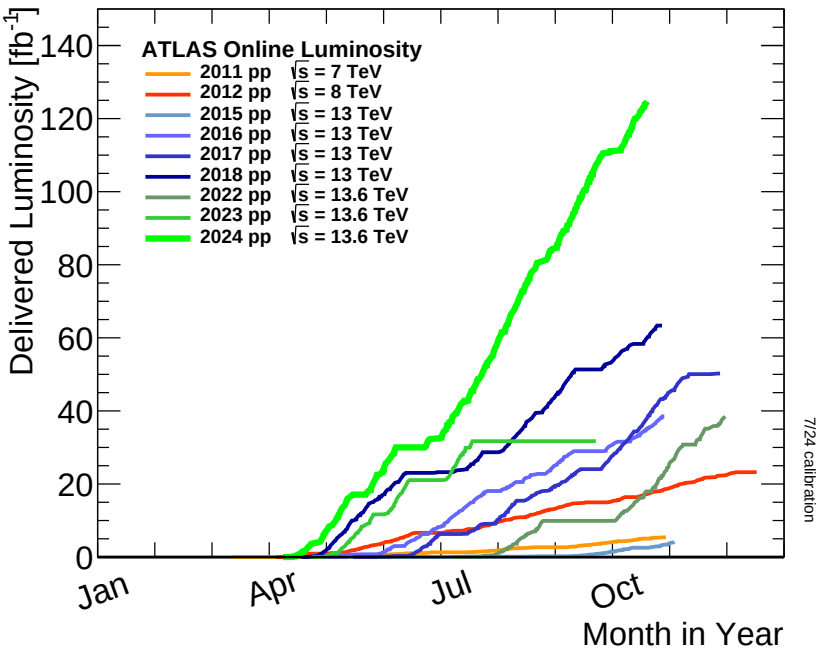

Figure 32: **Integrated luminosity delivered to ATLAS Experiment**. This shows the integrated luminosity $\int \mathscr{L}\,\mathrm{d}t$ of the LHC delivered to ATLAS Experiment during different years. Figure: ATLAS Luminosity Group.

The number of scattering events N_{events} is given by

$$N_{\text{events}} = \sigma \int \mathscr{L}\,\mathrm{d}t, \tag{5.8}$$

where σ is the **total scattering cross-section** and instantaneous luminosity $\mathscr{L}$. We can also express this differentially in time as the **event rate** $R_{\text{events}} = \frac{\mathrm{d}N_{\text{events}}}{\mathrm{d}t}$. The experimental cross-section σ harbours all the physics of the interaction while $\mathscr{L}$ is a machine parameter. As scattering cross-sections of elementary particles are tiny, particle physicists use the unit **barn**

$$1\,\text{barn} = 10^{15}\,\text{fb} = 10^{-24}\,\text{cm}^2. \tag{5.9}$$

The LHC has integrated luminosities reaching

$$L = \sigma \int \mathscr{L}\,\mathrm{d}t = 10^{-34}\,\text{cm}^{-2}\,\text{s}^{-1} = 10\,\text{nb}^{-1}\,\text{s}^{-1} \approx 100\,\text{fb}^{-1}\,\text{year}^{-1}. \tag{5.10}$$

So the colloquialism “amount of data taken” in a year is usually expressed in units of inverse area fb^{-1}. The actual delivered luminosities to ATLAS are displayed in figure 32. So if there is an process that has a cross-section $\sigma = 20$ fb, a machine delivering an integrated luminosity of $L = 100\ \text{fb}^{-1}$ would produce around $N = \sigma L = 2000$ events of that process.

5.3 Fermi's golden rule

This is a review of the standard non-relativistic derivation found in all quantum mechanics textbooks, which is sketched here for completeness. This applies time-dependent perturbation theory to model the time evolution of dynamics induced by a small perturbation. We start with the unperturbed Hamiltonian $\hat{H}_0$ and a small $\lambda \ll 1$ time dependent perturbation $\hat{H}_1(t)$ to give

$$\hat{H} = \hat{H}_0 + \lambda \hat{H}_{\text{int}}(t). \tag{5.11}$$

We can express the time dependent state $|\psi(t)\rangle$ as a linear superposition of the eigenstates of $\hat{H}_0$

$$|\psi(t)\rangle = \sum_n c_n(t) \mathrm{e}^{-\mathrm{i}E_n^{(0)}t} |n^{(0)}\rangle \tag{5.12}$$

Substituting this into the time-dependent Schrödinger equation $\mathrm{i}\frac{\mathrm{d}|\psi\rangle}{\mathrm{d}t} = \hat{H}|\psi\rangle$ then multiplying through by the final state $\langle f^{(0)}|$ gives

$$\frac{\mathrm{d}c_f}{\mathrm{d}t} = \frac{1}{\mathrm{i}} \sum_n c_n \mathrm{e}^{\mathrm{i}(E_f^{(0)} - E_n^{(0)})t} \langle f^{(0)}|\hat{H}_{\text{int}}|n^{(0)}\rangle. \tag{5.13}$$

We now approximate using perturbation theory by expanding c_n as a power series in λ: $c_n(t) = c_n^{(0)} + \lambda c_n^{(1)} + \ldots$. Equating the first order terms gives the 1st order correction to the expansion coefficients

$$c_f^{(1)}(t) = \frac{1}{\mathrm{i}} \sum_n c_n^{(0)} \int_{t_0}^{t} \mathrm{e}^{\mathrm{i}(E_f^{(0)} - E_n^{(0)})t'} \langle f^{(0)}|\hat{H}_{\text{int}}|n^{(0)}\rangle \mathrm{d}t'. \tag{5.14}$$

Consider the case where at $t = 0$, the system is in the 'initial' state $|i\rangle$ such that $c_n^{(0)} = 1$ is non-zero only for $n = i$. Equation (5.14) becomes

$$c_f^{(1)}(t) = \frac{1}{\mathrm{i}} \int_0^t \mathrm{e}^{\mathrm{i}\Delta E_{fi}t'} \langle f^{(0)}|\hat{H}_{\text{int}}|i^{(0)}\rangle \mathrm{d}t', \tag{5.15}$$

where $\Delta E_{fi} \equiv E_f^{(0)} - E_i^{(0)}$. Evaluating the integral gives

$$c_f^{(1)}(t) = \frac{1}{\mathrm{i}} \langle f^{(0)}|\hat{H}_{\text{int}}|i^{(0)}\rangle \frac{\mathrm{e}^{\mathrm{i}\Delta E_{fi}t} - 1}{\mathrm{i}\Delta E_{fi}}. \tag{5.16}$$

Taking the modulus square of this gives the probability of transition from $|i^{(0)}\rangle$ to $|f^{(0)}\rangle$ due to the perturbation

$$P_{i\to f} = |c_f^{(1)}(t)|^2 = |\langle f^{(0)}|\hat{H}_{\text{int}}|i^{(0)}\rangle|^2 t^2 \operatorname{sinc}^2\left(\frac{\Delta E_{fi}t}{2}\right), \tag{5.17}$$

where $\text{sinc}(x) \equiv \sin(x)/x$. Let the perturbation induce a transition into a continuum set of final states $|f\rangle$ with a continuous energy spectrum $E_f \to E(p_f)$ where p_f is the momentum. The transition probability is as given by (5.17) integrating over the final continuum set of states

$$P_{i\to f} = \int_0^\infty \left|\langle f|\hat{H}_{\text{int}}|i\rangle\right|^2 t^2 \text{sinc}^2\left(\frac{\Delta E_{fi} t}{2}\right) \mathrm{d}p_f, \tag{5.18}$$

where $\text{sinc}(x) \equiv \sin(x)/x$. Changing variables of the argument of the sinc function

$$q = \frac{\Delta E_{fi} t}{2}, \quad \mathrm{d}q = \frac{\mathrm{d}E(p_f)}{\mathrm{d}p_f}\mathrm{d}p_f \frac{t}{2}. \tag{5.19}$$

We introduce the **density of states**

$$\rho(E_f) = \frac{\mathrm{d}p_f}{\mathrm{d}E_f}, \tag{5.20}$$

which measures the quantity of continuum final states contained within $[p_f, p_f + \mathrm{d}p_f]$ given an energy interval $[E_f, E_f + \mathrm{d}E_f]$. We assume the transition amplitude $\langle f|\hat{H}_{\text{int}}|i\rangle$ occurs on a much faster timescale than measurements involving the time evolution of q so is effectively time-independent. We can therefore take $\langle f|\hat{H}_{\text{int}}|i\rangle$ out of the time integral and extend the limits to $\pm\infty$

$$P_{i\to f} \simeq 2t\rho(E_f)|\langle f|\hat{H}_{\text{int}}|i\rangle|^2 \int_{-\infty}^{\infty} \text{sinc}^2(q)\mathrm{d}q. \tag{5.21}$$

The integral evaluates to π. Differentiating with respect to time gives the rate of transition probability to the continuum set of states

$$\boxed{\frac{\mathrm{d}P_{i\to f}}{\mathrm{d}t} = 2\pi \underbrace{|\langle f|\hat{H}_{\text{int}}|i\rangle|^2}_{\text{dynamics}} \underbrace{\rho(E_f)}_{\text{kinematics}}}. \tag{5.22}$$

This is the **Fermi golden rule**. This tells us the rate $w_{fi} = \frac{\mathrm{d}P_{i\to f}}{\mathrm{d}t}$ of an initial state $|i\rangle$ to transition into final state $|f\rangle$. The matrix element $\mathscr{M}_{fi} = \langle f|H_{\text{int}}|i\rangle$ captures the dynamics of the Hamiltonian H_{int} represented by Feynman diagrams, while $\rho(E_f)$ captures kinematics and is sometimes called *phase space*.

$$\begin{pmatrix}\text{Transition}\\ \text{rate}\end{pmatrix} = 2\pi \times \begin{pmatrix}\text{Feynman}\\ \text{diagrams}\end{pmatrix} \times \begin{pmatrix}\text{Phase}\\ \text{space}\end{pmatrix}. \tag{5.23}$$

This holds when the time scale for transition $|i\rangle \to |f\rangle$ is much faster than the measurement time and the interaction potential is weak compared to the kinetic energies of the incident particles.

The cross section is related to the transition probability divided by the flux factor Φ_{inc} of incident particles

$$\sigma = \frac{2\pi}{\Phi_{\text{inc}}} \left|\mathscr{M}_{fi}\right|^2 \rho(E_f). \tag{5.24}$$

Given particles in incident beams 1 and 2, we can write the Lorentz invariant (frame independent) flux factor in various forms

$$\Phi_{\text{inc}} = 2E_1 2E_2 \left|\mathbf{v}_1 - \mathbf{v}_2\right| \tag{5.25}$$

$$= 4\sqrt{(p_1 \cdot p_2)^2 - m_1^2 m_2^2} \tag{5.26}$$

$$= 2\sqrt{(s - m_1^2 - m_2^2)^2 - 4m_1^2 m_2^2}. \tag{5.27}$$

This simplifies for the cases of ultrarelativistic incident particles $s \gg m_{1,2}$. For fixed-target experiments with particle 2 at rest, this reduces to

$$\Phi_{\text{inc}}^{\text{fixed-target}} = 2E_1 2m_2 |\mathbf{v}_1|. \tag{5.28}$$

The cross-section for two particles colliding with energy E_1 and E_2 is,

$$\sigma_{12\to X} = \frac{1}{2E_1 2E_2} \frac{1}{|v_1 - v_2|} 2\pi \left|\mathscr{M}_{fi}\right|^2 \rho(E_f). \tag{5.29}$$

In real experiments, a particle detector might only see a small solid angle of scattered events. Therefore, it is useful to define the **differential cross-section** $\mathrm{d}\sigma_r/\mathrm{d}\Omega$ for the number of events scattered into a particular solid angle $\mathrm{d}\Omega = \sin\theta \mathrm{d}\theta \mathrm{d}\phi$ as:

$$\frac{\mathrm{d}N}{\mathrm{d}\Omega} = \frac{\mathrm{d}\sigma_r(\theta,\phi)}{\mathrm{d}\Omega} \times \int \mathscr{L} \mathrm{d}t. \tag{5.30}$$

5.4 Density of states

We now study the study the density of states $\rho(E_f)$ in more detail. In non-relativistic quantum mechanics, textbooks consider a free particle with wavefunction $\psi(x) = N\mathrm{e}^{-\mathrm{i}(Et - p_x x)}$ in a box of length L. Requiring the modulus square of the wavefunction to integrate to unity (to gives a probability) fixes the normalisation N:

$$\int_0^L \psi^* \psi \, \mathrm{d}x = 1, \quad \Rightarrow \quad N = \frac{1}{\sqrt{L}}. \tag{5.31}$$

Periodic boundary conditions for a particle in a box $\psi(x+L) = \psi(x)$ implies $e^{ipx} = e^{ip(x+L)}$. Expressing unity as a periodic complex number $1 = e^{i(2\pi n)}$ for integer n, the momenta are quantised:

$$e^{i(pL)} = 1 = e^{i(2\pi n)}, \quad \Rightarrow \quad p_n = \frac{2\pi n}{L}. \tag{5.32}$$

We can then write how many states squished into the (infinitesimal) interval $[n, n+dn]$ have momentum $[p, p+dp]$ as

$$dn = \frac{dp}{2\pi} L. \tag{5.33}$$

In the final calculations, every final state particle will introduce a factor of $1/L$ in the matrix element squared $|\mathscr{M}_{fi}|^2$. This cancels with the L in the density of states factor, so we can henceforth drop the factors of L. Generalising this to the four dimensions of energy-momentum, we can write this in terms of the infinitesimal four-momentum space volume $d^4\mathsf{P} = dE\,dp_x\,dp_y\,dp_z$

$$d^4 n = \frac{d^4\mathsf{P}}{(2\pi)^4}. \tag{5.34}$$

This turns out to be Lorentz invariant and many textbooks write this in a form with physical constraints, namely that the final-state particles are on their mass shell $\mathsf{P}^2 = m^2$ imposed and they have positive mass $m > 0$. Formally, they do this by integrating over the energy component of the four-momentum $\mathsf{P}^0 = E$ using a Dirac delta function[41] $(2\pi)\delta(\mathsf{P}^2 - m^2)$ for the on-mass-shell condition and a step function to enforce mass positivity[42] $m > 0$, yielding:

$$d^3 n = \frac{d^3\mathbf{p}}{(2\pi)^3} \int \frac{dE}{2\pi} (2\pi)\delta(\mathsf{P}^2 - m^2) = \frac{d^3\mathbf{p}_f}{2E_f(2\pi)^3}. \tag{5.35}$$

We can perform the integral using a change of variables $x = E^2, dx = 2E\,dE$. Every final state particle with momentum $\mathbf{p}_f$ comes with a factor of phase space and one set of delta functions (with factors of $(2\pi)^4$ for Fourier normalisation) to impose energy-momentum conservation $(2\pi)^4\delta^{(4)}(\sum_f \mathsf{P}_f - \sum_i \mathsf{P}_i)$ momentum conservation:

$$d^{(3N)} n = (2\pi)^4 \delta^{(4)} \left[\sum_f \mathsf{P}_f - \sum_i \mathsf{P}_i \right] \prod_{f=1}^{N} \frac{d^3\mathbf{p}_f}{2E_f(2\pi)^3}, \tag{5.36}$$

where $\mathsf{P}_{i(f)}$ are the initial-state (final-state) four-momenta. What is the physical meaning of all this? This tells us that the density of available states is related to the momentum available to the final states.

[41] The delta function is defined by $\int_{-\infty}^{\infty} \delta(x-a) f(x) dx = f(a)$ and $\int_{-\infty}^{\infty} \delta(x) dx = 1$.

[42] The Heaviside step function is defined as $\Theta(m) = 1$ for $m > 0$, $\Theta(m) = 0$ for $m < 0$.

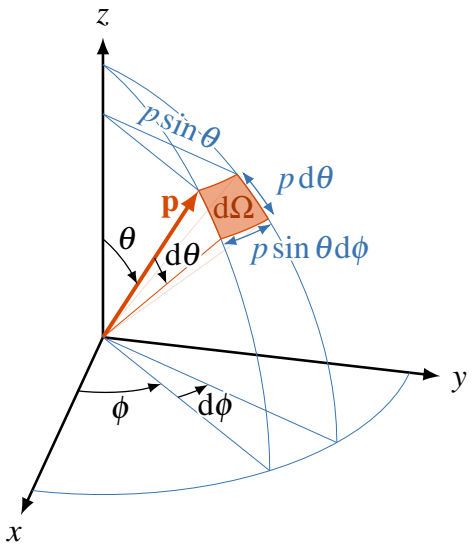

Figure 33: **Spherical coordinates**. Momentum expressed in spherical coordinates with infinitesimal angular elements $\mathrm{d}^3\mathbf{p} = p^2 \mathrm{d}p\,\mathrm{d}\Omega$, where the solid angle is $\mathrm{d}\Omega = \sin\theta \mathrm{d}\theta \mathrm{d}\phi$. Drawing adapted from I. Neutelings.

Two body final state

We can calculate the density of states for the simplest case of two particles in the final state. Using the situation set up in figure 3.11, we have to write

$$\mathrm{d}n = \frac{\mathrm{d}^3\mathbf{p}_1}{2E_1(2\pi)^3}\frac{\mathrm{d}^3\mathbf{p}_2}{2E_2(2\pi)^3}(2\pi)^4\delta(E_1+E_2-E_{\mathrm{CM}})\delta^{(3)}(\mathbf{p}_1+\mathbf{p}_2) \tag{5.37}$$

Integrating over $\mathrm{d}^3\mathbf{p}_2$ imposes momentum conservation as the delta function fixes $\mathbf{p}_1 = -\mathbf{p}_2$. We denote this final-state momentum $\mathbf{p}_f = \mathbf{p}_1 = -\mathbf{p}_2$ with subscript f:

$$\mathrm{d}n = \frac{1}{2E_1 2E_2}\frac{\mathrm{d}^3\mathbf{p}_f}{(2\pi)^2}\delta(E_1+E_2-E_{\mathrm{CM}}). \tag{5.38}$$

We now write $\mathrm{d}^3\mathbf{p}_f$ in spherical coordinates $\mathrm{d}^3\mathbf{p}_f = p_f^2 \mathrm{d}p_f \mathrm{d}\Omega$, where $p_f \equiv |\mathbf{p}_f|$ and $\mathrm{d}\Omega$ is the solid angle visualised in figure 33. To help integrate the delta function, we perform the substitution $x = E_1 + E_2 - E_{\mathrm{CM}}$ then use the chain rule because $E_a = E_a(p_f)$ is a function of p_f:

$$\mathrm{d}x = \left(\frac{\mathrm{d}E_1}{\mathrm{d}p_f} + \frac{\mathrm{d}E_2}{\mathrm{d}p_f}\right)\mathrm{d}p_f = \left(\frac{p_f}{E_1} + \frac{p_f}{E_2}\right)\mathrm{d}p_f = \left(\frac{E_1+E_2}{E_1E_2}\right)p_f \mathrm{d}p_f, \tag{5.39}$$

where the second equality differentiated the energy-momentum relation

$$E_a^2 = p_f^2 + m_a^2 \Rightarrow \frac{\mathrm{d}E_a}{\mathrm{d}p_f} = \frac{p_f}{E_a}. \tag{5.40}$$

We can now substitute $\mathrm{d}p_f$ from the change of variables (5.39) to convert equation (5.38) into an integral over x:

$$\mathrm{d}n = \frac{1}{4}\frac{p_f}{E_1+E_2}\frac{\mathrm{d}\Omega}{(2\pi)^2}\delta(x)\mathrm{d}x. \tag{5.41}$$

Performing the delta function integration enforces $x = 0 \Rightarrow E_1 + E_2 = E_{\mathrm{CM}}$, yielding the two-body phase space expression:

$$\boxed{\mathrm{d}n_{\text{two-body}} = \frac{1}{2}\frac{p_f}{E_{\mathrm{CM}}}\frac{\mathrm{d}\Omega}{(4\pi)^2}.} \tag{5.42}$$

Given how often processes have two particles in the final state, this is a very useful result.

6 Electron–position annihilation

We now illustrate all these concepts in a concrete and classic calculation of QED, the 'hydrogen atom of particle physics'. This is electron–positron annihilation via the electromagnetic interaction to produce a muon–antimuon pair:

$$e^- e^+ \to \gamma \to \mu^- \mu^+. \tag{6.1}$$

The corresponding Feynman diagram with momenta labelled looks like this:

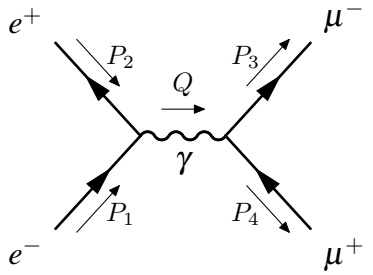

(6.2)

This is the only tree-level Feynman diagram for $e^- e^+ \to \mu^- \mu^+$, making it among the simplest QED process to calculate with high pedagogical value. Indeed we cannot write down a t-channel diagram that is possible for $e^- e^+ \to e^- e^+$ (figure 25a) because one QED vertex cannot change an electron to a muon (QED conserves flavour). Such calculations will nonetheless find renewed experimental importance at the highest energies in the coming decades because the likely successor to the Large Hadron Collider will be an $e^- e^+$ machine to study the Higgs boson precisely.

There are various techniques to calculate the quantum amplitude of figure 6.2. In QFT classes, you will likely learn Dirac gamma matrix algebra with spinor trace sum identities, which are powerful algorithms. However, we shall analyse the helicity amplitudes (e.g. Larkoski and Thomson textbooks) to expose the underlying physics. We take the ultra-relativistic limit $m \to 0$ from the outset and invoke various physical principles to further reduce the calculation to a handful of matrix multiplications that is tolerable with pen and paper.

Dimensional analysis prelude As usual in physics, it is useful to get a feeling for how the answer should depend on key physical quantities before commencing an extended calculation. First, we can work in the centre-of-mass frame to let the four-momenta of the electron, positron and (virtual) photon be

$$\mathsf{P}_{e^-} = \begin{pmatrix} E_e \\ \mathbf{p} \end{pmatrix}, \qquad \mathsf{P}_{e^+} = \begin{pmatrix} E_e \\ -\mathbf{p} \end{pmatrix}, \qquad \mathsf{Q}_\gamma = \mathsf{P}_{e^-} + \mathsf{P}_{e^+} = \begin{pmatrix} 2E_e \\ \mathbf{0} \end{pmatrix}. \tag{6.3}$$

The cross-section (with dimensions length squared) must be proportional to the inverse square of centre-of-mass energy (given $(\hbar c)^2$ having units of length-energy squared). Meanwhile, we count there are two electromagnetic vertices in the Feynman diagram giving a factor of e^2 for the amplitude, which upon squaring gives $e^4 = (4\pi\alpha_{\text{EM}})^2$.

The Feynmann diagram (figure 6.2) has 2 vertices involving particles of unit charge. The vertex factor is then

$$g_{\text{EM}}^2 = 4\pi\alpha_{\text{EM}}$$

The only scale in our system is the centre-of-mass energy, so we can write with the Mandelstam variable $s = E_{\text{CM}}^2 = (2E_e)^2$ and can assemble our dimensional analysis expectation

$$\sigma \propto \frac{\alpha_{\text{EM}}^2}{s}. \tag{6.4}$$

Remarkably, this by itself is only a factor of $4\pi/3$ different from the full calculation that account for all the flux, spin and phase space factors if you take a sneak peek ahead to equation (6.24).

We can also obtain the correct $(1+\cos^2\theta)$ angular dependence in the differential cross-section, by arguing the photon mediator means we can write the circular polarisation vectors $(0, \mathrm{i}, \pm 1, 0)$ then performing a rotation in the polar angle.

6.1 Spinor–helicity analysis

Naïvely inspecting the process $e^-e^+ \to \mu^-\mu^+$, we see 4 distinct particles in the problem (electron, positron, muon, antimuon), each of which can have one of two charges $(+,-)$ and two helicities (L, R), giving 16 possible distinct combinations. Fortunately, we are physicists who can invoke the physical argument of angular momentum conservation to reduce this down to only four possibilities. The photon is spin 1, so the combination of spin for the initial and final states must also sum to 1 to respect angular momentum conservation. To see what these combinations are, we see forbidden combinations are those whose helicity states are in opposite directions:

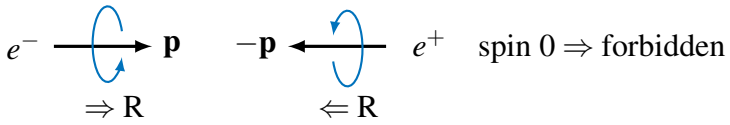

(6.5)

By contrast, these helicity states intuitively sums to spin one and is therefore allowed:

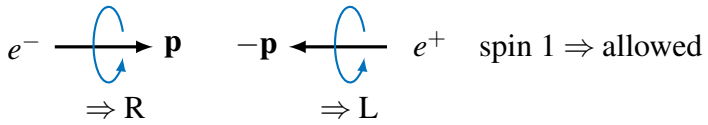

(6.6)

This applies to both initial and final states so the only allowed helicity combinations are ones where the particle-antiparticle pair have opposite helicity such that the spin sums to one:

$$\begin{array}{llll} e^- & e^+ & \to \mu^- & \mu^+ \\ \mathrm{R} & \mathrm{L} & \to \mathrm{R} & \mathrm{L} \\ \mathrm{R} & \mathrm{L} & \to \mathrm{L} & \mathrm{R} \\ \mathrm{L} & \mathrm{R} & \to \mathrm{R} & \mathrm{L} \\ \mathrm{L} & \mathrm{R} & \to \mathrm{L} & \mathrm{R} \end{array} \tag{6.7}$$

Charge conjugation & flavour universality

We can further halve the number of distinct amplitudes we need to explicitly calculate. Complex conjugation of an initial state vertex gives us a final state vertex

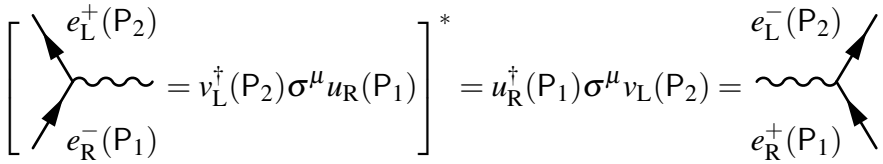

(6.8)

This means complex conjugation of an amplitude $\mathscr{A}^*$ swaps initial with final states and inverts their charge. Moreover, the photon interacts identically to electrons and muons i.e. **QED respects flavour universality**, so we are free to exchange flavour labels $e \leftrightarrow \mu$ and the amplitude remains the same. These two facts mean we can write these equalities

$$\mathscr{A}^*\left(e_{\mathrm{R}}^- e_{\mathrm{L}}^+ \to \mu_{\mathrm{R}}^- \mu_{\mathrm{L}}^+\right) \overset{*}{=} \mathscr{A}\left(\mu_{\mathrm{L}}^- \mu_{\mathrm{R}}^+ \to e_{\mathrm{L}}^- e_{\mathrm{R}}^+\right) \overset{e\leftrightarrow\mu}{=} \mathscr{A}\left(e_{\mathrm{L}}^- e_{\mathrm{R}}^+ \to \mu_{\mathrm{L}}^- \mu_{\mathrm{R}}^+\right). \tag{6.9}$$

Given the final cross-section is always the modulus square of the amplitude $\sigma \propto \mathscr{A}^*\mathscr{A} = |\mathscr{A}|^2$, these equalities imply we can reduce our problem to only having two distinct amplitudes to evaluate:

$$|\mathscr{A}_{\mathrm{RL}\to\mathrm{RL}}|^2 = |\mathscr{A}_{\mathrm{LR}\to\mathrm{LR}}|^2, \tag{6.10}$$

$$|\mathscr{A}_{\mathrm{LR}\to\mathrm{RL}}|^2 = |\mathscr{A}_{\mathrm{RL}\to\mathrm{LR}}|^2. \tag{6.11}$$

Calculating spinor currents

Let us take the negatively (positively) charged particle as having momentum pointing $+\mathbf{p}$ ($-\mathbf{p}$). After all these simplifications, we are left with only having to calculate two combina-

tions

$\ell^-_{\mathbf{p}}$	$\ell^+_{-\mathbf{p}}$	Calculate	
R	L	$v_{\mathrm{L}}^{\dagger}\sigma^{\mu}u_{\mathrm{R}}$	(6.12)
L	R	$v_{\mathrm{R}}^{\dagger}\bar{\sigma}^{\mu}u_{\mathrm{L}}$	(6.13)

With the initial states are aligned along the the z axis, the vector $\mathbf{p}$ points $(\theta,\varphi)=(0,0)$ in spherical coordinates. To obtain $\mathbf{p}\to-\mathbf{p}$, we invert through the origin (called a parity transformation), which implies $\theta\to\pi-\theta,\varphi\to\varphi+\pi$, so the $-\mathbf{p}$ vector points $(\theta,\varphi)=(\pi,\pi)$. We insert this into eq. (3.86) to evaluate the spinors

$$u_{\mathrm{R}}(\mathbf{p})=\sqrt{2E}\begin{pmatrix}1\\0\end{pmatrix},\qquad v_{\mathrm{L}}(-\mathbf{p})=\sqrt{2E}\begin{pmatrix}0\\\mathrm{i}\end{pmatrix}, \tag{6.14}$$

$$u_{\mathrm{L}}(\mathbf{p})=\sqrt{2E}\begin{pmatrix}0\\-1\end{pmatrix},\quad v_{\mathrm{R}}(-\mathbf{p})=\sqrt{2E}\begin{pmatrix}-\mathrm{i}\\0\end{pmatrix}. \tag{6.15}$$

For each of the four components we have to evaluate the action of the Pauli matrices on the spinors for each of the four vector components equation (3.50):

$$v_{\mathrm{L}}^{\dagger}\sigma^{\mu}u_{\mathrm{R}}=2E\begin{pmatrix}0&-\mathrm{i}\end{pmatrix}\begin{pmatrix}I\\\boldsymbol{\sigma}\end{pmatrix}\begin{pmatrix}1\\0\end{pmatrix}=2E\begin{pmatrix}0\\-\mathrm{i}\\1\\0\end{pmatrix}, \tag{6.16}$$

$$v_{\mathrm{R}}^{\dagger}\bar{\sigma}^{\mu}u_{\mathrm{L}}=2E\begin{pmatrix}\mathrm{i}&0\end{pmatrix}\begin{pmatrix}I\\-\boldsymbol{\sigma}\end{pmatrix}\begin{pmatrix}0\\-1\end{pmatrix}=2E\begin{pmatrix}0\\\mathrm{i}\\1\\0\end{pmatrix}. \tag{6.17}$$

Interestingly, this is precisely proportional to the two independent (circular) polarisation states of the photon $\varepsilon^{\circlearrowleft}_{\mu},\varepsilon^{\circlearrowright}_{\mu}$ that we learn in the classical theory of electromagnetic waves.

The final-state $\mu^-\mu^+$ pair cannot be created with any preferred direction φ in the x-y plane (the two 3-momentum vectors must sum to zero) because the initial state e^-e^+ had no overall linear momentum in the x-y plane. Nonetheless, we let the $\mu^-\mu^+$ pair have any θ and account for these possibilities by rotating the $\mu^-\mu^+$ vector in the x-z plane via the rotation matrix R_θ:

$$R_\theta\left[v_{\mathrm{L}}^{\dagger}\sigma^{\mu}u_{\mathrm{R}}\right]=\begin{pmatrix}1&0&0&0\\0&\cos\theta&0&\sin\theta\\0&0&1&0\\0&-\sin\theta&0&\cos\theta\end{pmatrix}\begin{pmatrix}0\\-\mathrm{i}\\1\\0\end{pmatrix}=\begin{pmatrix}0\\-\mathrm{i}\cos\theta\\1\\\mathrm{i}\sin\theta\end{pmatrix} \tag{6.18}$$

6.2 Scattering amplitude and cross-section

Finally putting it all together with the photon propagator $\eta_{\mu\nu}/\mathrm{Q}^2$, with $\mathrm{Q}^2 = 2E$, this results in a four-vector dot product to obtain the two unique amplitudes:

$$\mathscr{A}_{\mathrm{LR}\to\mathrm{RL}} = \left[u_{\mathrm{R}}^{\dagger}\bar{\sigma}v_{\mathrm{L}}\right]\cdot\left[R_{\theta}v_{\mathrm{L}}^{\dagger}\sigma u_{\mathrm{R}}\right] = -e^2(1+\cos\theta), \tag{6.19}$$

$$\mathscr{A}_{\mathrm{RL}\to\mathrm{RL}} = \left[v_{\mathrm{L}}^{\dagger}\bar{\sigma}u_{\mathrm{R}}\right]\cdot\left[R_{\theta}v_{\mathrm{L}}^{\dagger}\sigma u_{\mathrm{R}}\right] = -e^2(1-\cos\theta). \tag{6.20}$$

Traditionally, electron-positron accelerators do not collide beams with known polarisation state, so half they time for each electron and positron they are in the L state and the other half R state. Moreover, particle detectors cannot directly measure the spin state of each outgoing muons so we sum over the four non-zero amplitudes. This gives the overall amplitude as:

$$\frac{1}{4}\sum_{\text{spins}}|\mathscr{M}|^2 = \frac{1}{4}\left(2\left|e^2(1+\cos\theta)\right|^2 + 2\left|e^2(1-\cos\theta)\right|^2\right) = e^4(1+\cos^2\theta). \tag{6.21}$$

Assembling this in the Fermi golden rule and phase space for two ultrarelativistic particles gives the differential cross-section as a function of $\cos\theta$:

$$\frac{\mathrm{d}\sigma(e^-e^+\to\mu^-\mu^+)}{\mathrm{d}\cos\theta} = \frac{\pi\alpha_{\mathrm{EM}}^2}{2s}(1+\cos^2\theta). \tag{6.22}$$

To obtain the total cross-section, integrate over the full range of $\cos\theta$:

$$\sigma = \frac{\pi\alpha_{\mathrm{EM}}^2}{2s}\int_{-1}^{1}(\mathrm{d}\cos\theta)(1+\cos^2\theta), \tag{6.23}$$

which gives the final result:

$$\sigma(e^-e^+\to\mu^-\mu^+) = \frac{4}{3}\frac{\pi\alpha_{\mathrm{EM}}^2}{s}. \tag{6.24}$$

This can be compared with the PETRA accelerator at DESY as precision tests of QED at high energies (figure 34b). At higher-energies, the Z boson resonance exchange becomes important, which is shown later in figure 102 when we discuss electroweak interactions.

6.3 Breit–Wigner resonances

In s-channel annihilation reactions like $e^-e^+\to X\to\mu^-\mu^+$, intermediate resonances with non-zero mass can appear as X such as a Z boson. We can consider reactions of the form $i\to X\to f$ with an unstable intermediate state X, which we describe as a Breit–Wigner

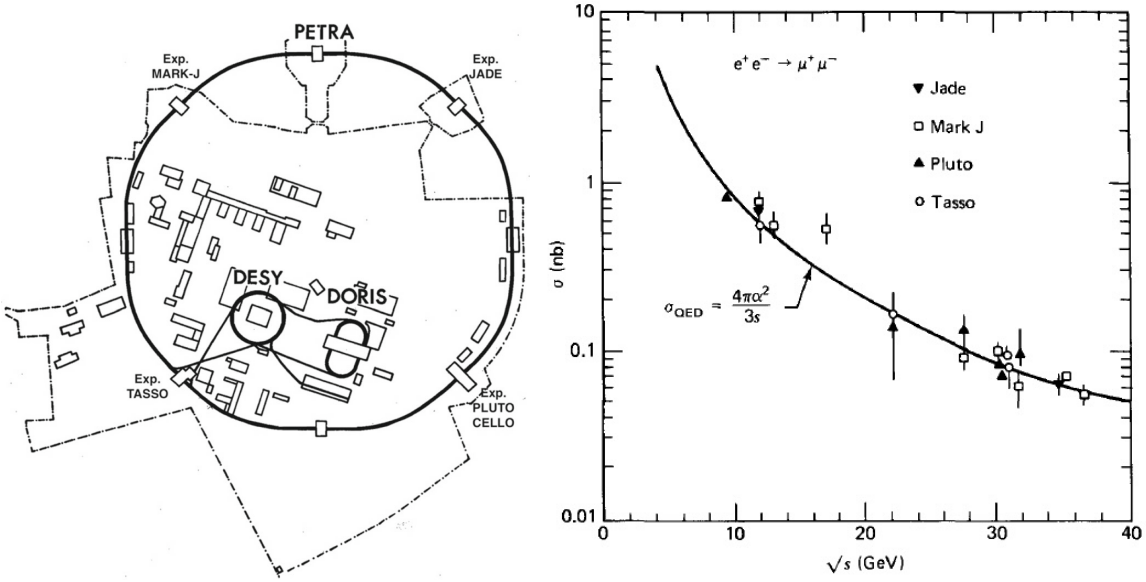

(a) PETRA Collider, DESY [47]

(b) $e^-e^+ \to \mu^-\mu^+$ cross-section vs $\sqrt{s}$.

Figure 34: **PETRA collider tests of QED**. Plot from Hazel and Martin (1984)

resonance. We can write the wave function ψ_t of a state with energy E_0 and lifetime $\tau = 1/\Gamma$ is

$$\psi_t = \psi_0 \mathrm{e}^{-\mathrm{i}E_0 t} e^{-t/2\tau} = \psi_0 \mathrm{e}^{-(\mathrm{i}E_0 + \Gamma/2)t}. \tag{6.25}$$

The evolution of ψ_t as a function of time as a function of energy ψ_E is given by the Fourier transform

$$\psi_E = \int \mathrm{e}^{-\mathrm{i}Et} \psi_t = \psi_0 \int \mathrm{e}^{-t[\mathrm{i}(E_0 - E) + \Gamma/2]} \,\mathrm{d}t \propto \frac{1}{(E - E_0) - \mathrm{i}\Gamma/2} \tag{6.26}$$

The cross-section is then the modulus square $\sigma \propto \psi_E^* \psi_E$ to give the **Breit-Wigner formula**. This describes the cross-section of a reaction $i \to X \to f$ in energy E space:

$$\sigma_{i \to X \to f} = \frac{\pi}{p_{\text{in}}^2} \frac{\Gamma_i \Gamma_f}{(E - E_X)^2 + (\Gamma/2)^2} \tag{6.27}$$

Multiplying through by $(E + E_X)$ and applying $E \approx E_X = M_X$ when needed, this is often rewritten in a form that makes Lorentz invariance more manifest

$$\sigma_{i \to X \to f} = \frac{\pi}{p_{\text{in}}^2} \frac{\Gamma_i \Gamma_f M_X^2}{(s - M_X^2)^2 + (M_X \Gamma/2)^2}. \tag{6.28}$$

This is a useful phenomenological description of observed unstable particles in experiments. Here is a list of useful vocabulary often used to describe decays of particles:

- **Natural width** $\Gamma = 1/\tau$: rate of (decay) reaction is inversely related to the rest lifetime τ, which corresponds to a width in energy units.
- **Decay channels** $X \to f, f \in \{1, 2 \dots\}$: All the possible final states an unstable state may decay to.
- **Partial widths** Γ_f: the natural width associated with the specific decay channel f.
- **Total width** $\Gamma = \sum_f \Gamma_f$: the sum over all decay channels' partial widths.
- **Branching ratio** $B_f = \Gamma_f/\Gamma$: The proportion of the rate of a particular decay channel to the total rate of decay.
- **Incident momentum** p_{in}, momentum of the incident particle.
- **System energy** $s = E^2$.
- **Resonance mass** M_X: invariant mass of the intermediate resonance.

We can include extra factors accounting for the multiplicity of spins for the resonance state s_X and initial (say two) particles $s_{1,2}$:

$$\sigma_{i\to X\to f}^{\text{with spin}} = \frac{2s_X+1}{(2s_1+1)(2s_2+1)}\sigma_{i\to X\to f}$$

In practice we perform scattering experiments over various system energies E. If an unstable intermediate state X is produced the cross-section (6.27), and thus probability of decaying to final state f, enhances. This increases the number of events of f at the energy E_X corresponding to the rest mass energy $m_X c^2$ of the **resonance state**.

7 Vacuum loop effects

During 1947 in New York City, a pair of landmark experiments performed at Columbia University revealed the vacuum is dynamical, laying the foundations for quantum field theory. No new particles were discovered, yet these results opened a major paradigm shift in physics. Today, their modern incarnations provide among the most precise tests of quantum field theory.

We discuss the experimental manifestations of three classes of one-loop effects in QED (figure 35). This serves as the experimental complement to QFT classes, where you learn the theoretical techniques to calculate loop diagrams. The fundamental problem is that integrating over all internal loop momenta causes divergences. Particle physics textbooks do not always cover experimental tests of QED loop effects, perhaps because they involve atomic physics techniques; nonetheless I found the Bettini textbook has some nice experimental discussion.

7.1 Lamb shift

Solving the hydrogen atom using the Dirac rather than Schrödinger equation shifts the energy levels by a term of order α^2:

$$E_{n,j} = -\frac{13.6\text{ eV}}{n^2}\left[1+\frac{\alpha^2}{n^2}\left(\frac{1}{j+1/2}-\frac{3}{4n}\right)\right]. \tag{7.1}$$

The additional relativistic term is small ($\alpha^2 \approx 1/18\,700$) compared to the eV scales of the principal energy levels. This represents the correction from the relativistic motion of an

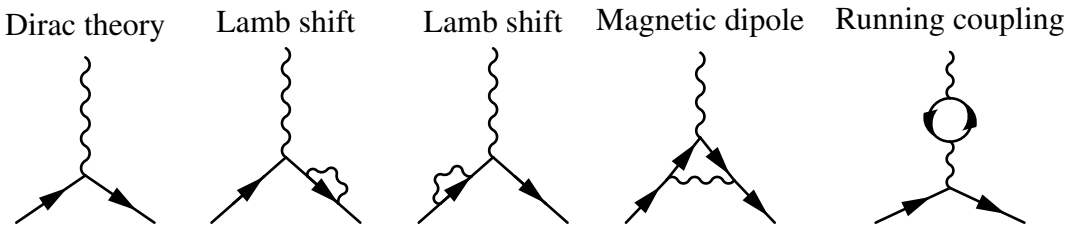

Figure 35: **Tree-level (Dirac theory) and one-loop QED diagrams**. The Lamb shift arises from the external electron propagators interacting with a photon loop. The anomalous magnetic moment $g-2$ arises from the electron–photon vertex loop. The running coupling arises from vacuum polarisation inducing an e^+e^- pair loop in the photon propagator.

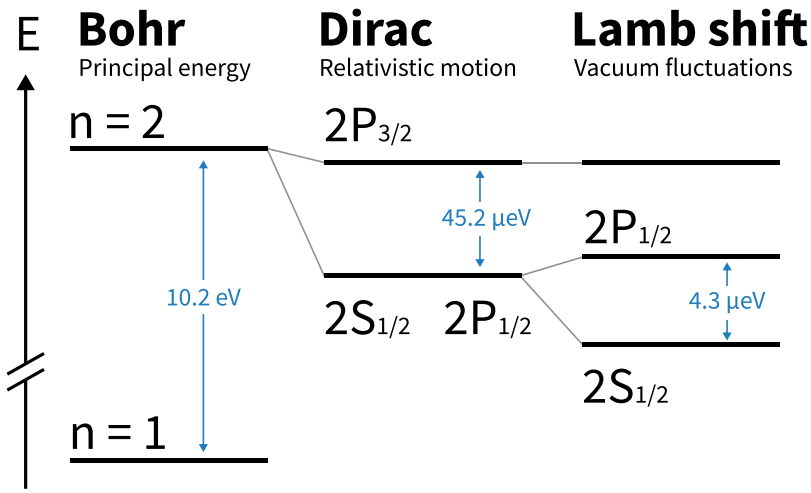

Figure 36: **Hydrogen $n = 2$ energy levels**. These are sketched for the Bohr model solving the Schrödinger equation with a Coulomb potential, Dirac equation accounting for relativistic electron motion. The electron interacting with fluctuations in the electromagnetic vacuum induces the Lamb shift that splits the $2S_{1/2}$ and $2P_{1/2}$ energy levels otherwise degenerate in the Dirac model.

electron in the Coulomb potential.

A consequence of spin-orbit coupling is that all the $L \neq 0$ states split into e.g. $2P_{1/2}, 2P_{3/2}$, with notation nL_j. But states with the same principal energy level n and total angular momentum j but different orbital L number can have degenerate energies (figure 36). This degeneracy between the $2S_{1/2}$ and $2P_{1/2}$ states is a predicted by Dirac theory:

$$\Delta E_{\text{Dirac}} = E\left(2S_{1/2}\right) - E\left(2P_{1/2}\right) = 0. \tag{7.2}$$

To test this degeneracy, Willis Lamb and Robert Retherford performed precision microwave measurements of the hydrogen fine structure in 1947 [48].

They utilise the usual Zeeman effect of splitting energy levels by applying a magnetic field to the hydrogen atom. What they measured is shown in figure 38. For nonzero magnetic field $B \neq 0$, they measure energy-level transitions with respect to the reference $2P_{3/2}$ state, where the azimuthal angular momentum states $m = +\frac{3}{2}, +\frac{1}{2}, -\frac{1}{2}$ correspond to the different branches. The dashed line shows the expectation from Dirac theory alone. The measured values have lines drawn that extrapolate to a common value for $B = 0$. There is a clear systematic shift of around a 1000 megacycles per second (megahertz), which was measured (more precisely by 1952) to be

$$\Delta E_{\text{Lamb}} = 1057.8 \pm 0.1 \text{ MHz} = 4.3747 \pm 0.0004 \ \mu\text{eV}. \tag{7.3}$$

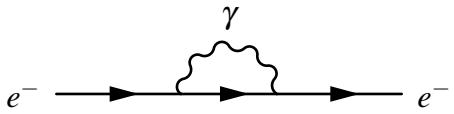

Figure 37: Mass renormalisation loop.

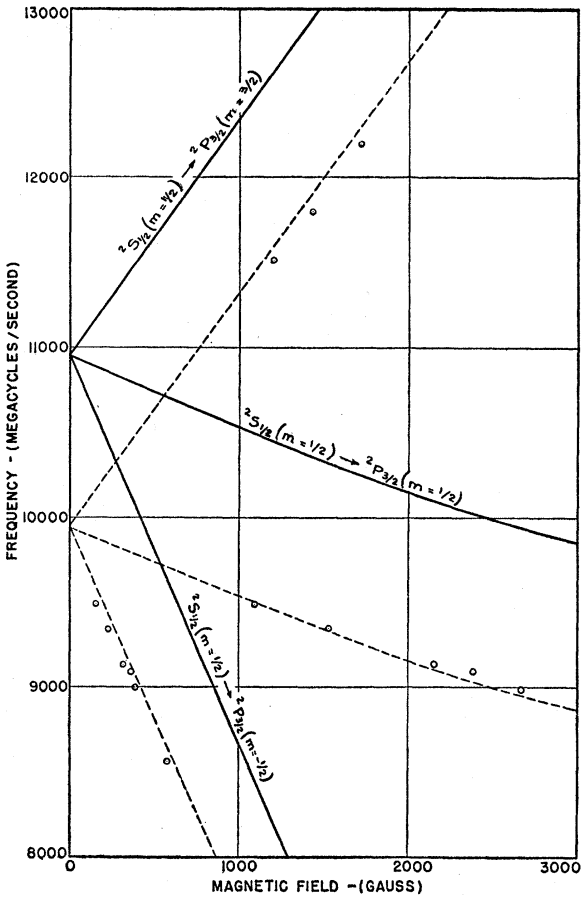

Figure 38: **Lamb–Retherford measurement of Lamb shift**. Figure: Ref. [48].

This is a watershed moment in physics. It shows that the electromagnetic field is not static, as assumed in classical physics. The field itself is quantum mechanical and therefore exhibits quantum fluctuations, imparting measurable dynamics onto the electron.

7.2 Anomalous magnetic moment

Also working at Columbia in New York, Polykarp Kusch and Henry Foley measured the magnetic moment of the electron to high precision [49, 50]:

$$g_s = 2(1.00119 \pm 0.00005). \tag{7.4}$$

This is the proportionality constant prefixing the Hamiltonian for a magnetic moment in an external field:

$$\mathscr{H} = -\boldsymbol{\mu} \cdot \mathbf{B} = -\frac{g_s e}{2m_f} \mathbf{S} \cdot \mathbf{B}. \tag{7.5}$$

The relevant tree-level and one-loop QED vertex diagrams for the g-factor are:

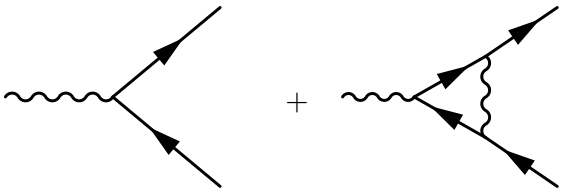

$$g \quad = \quad 2 \quad + \quad \frac{\alpha}{\pi} \tag{7.6}$$

The value of 2 is predicted by the Dirac equation and the one-loop α/π contribution. This one-loop correction to the QED vertex was first calculated by Julian Schwinger in 1948 [51]:

$$a_e^{\text{1-loop}} = \frac{g_e - 2}{2} = \frac{\alpha}{2\pi} \simeq 0.00116. \tag{7.7}$$

Calculating this is somewhat involved and is taught in an advanced quantum field theory class covering renormalization.

Today, the state-of-the-art experimental and theoretical values are simply astounding. The most accurate value of a_e is measured by an electron cyclotron Penning trap at Northwestern University [2]. The main idea for their direct measurement is that the cyclotron ω_c spin-precession ω_s frequencies are equal for $g = 2$:

$$\boldsymbol{\omega}_c = -\frac{e\mathbf{B}}{\gamma m} \qquad \text{cyclotron charged particle in B field,} \tag{7.8}$$

$$\boldsymbol{\omega}_s = -\frac{e\mathbf{B}}{\gamma m}\left[1 + \gamma\left(\frac{g-2}{2}\right)\right] \qquad \text{Larmor precession of spin in B field.} \tag{7.9}$$

Their measured differences are therefore approximately related to the anomalous precession frequency $\omega_a \simeq \omega_c - \omega_s \propto g - 2$:

$$\omega_a \simeq \omega_c - \omega_s \propto \frac{g-2}{2}\frac{e}{m}B. \tag{7.10}$$

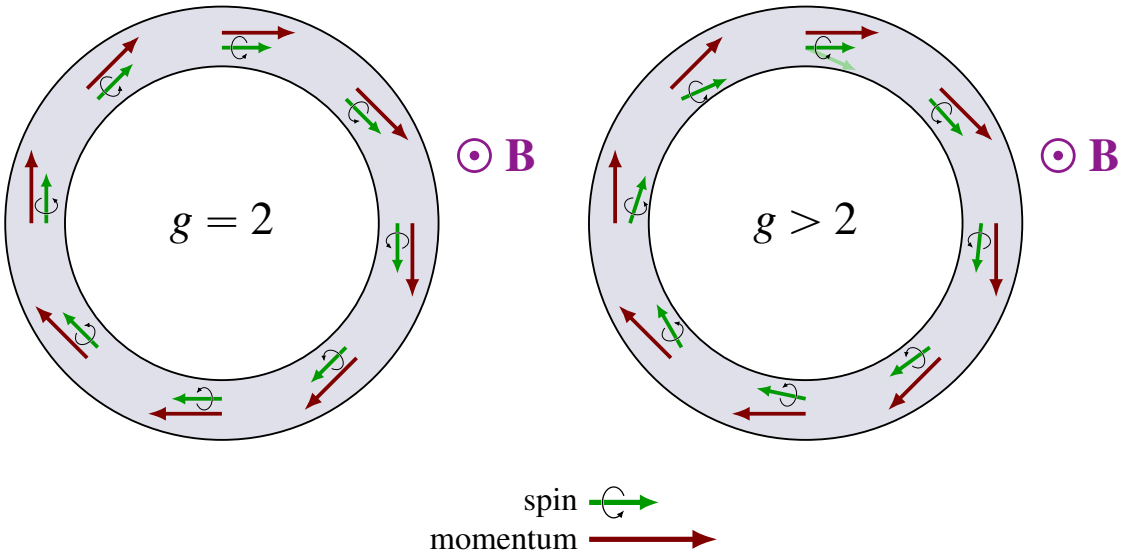

Figure 39: **Penning trap spin-precession measurement schematic**. This shows the spin precession and momentum vectors for $g = 2$ and $g \neq 2$. Figures: tikz.net.

The main experimental aspect that needs to be known very well is the magnetic field B.

This is compared to theory predictions from 10th order QED calculations, which require inputs from fine-structure constant α_{EM} measurements at Paris [3] and Berkeley [52]. The state-of-the-art values are displayed in figure 41 with all the digits spectacularly printed [53]:

$$a_e^{\text{exp}}(\text{cyclotron}) = 0.001\,159\,652\,180\,59\,(13) \qquad [2], \qquad (7.11)$$

$$a_e^{\text{theory}}\left(\alpha_{\text{EM}}^{\text{Rb}}\right) = 0.001\,159\,652\,182\,037\,(720)_{\alpha_{\text{EM}}^{\text{Rb}}}\,(11)_{\text{theory}}\,(12)_{\text{hadron}} \qquad [3] \qquad (7.12)$$

$$a_e^{\text{theory}}\left(\alpha_{\text{EM}}^{\text{Cs}}\right) = 0.001\,159\,652\,181\,606\,(229)_{\alpha_{\text{EM}}^{\text{Cs}}}\,(11)_{\text{theory}}\,(12)_{\text{hadron}} \qquad [52]. \qquad (7.13)$$

The three parentheses refer to the uncertainties from fine-structure constant measurements (α_{EM}), numerical evaluation of the tenth-order loop calculations (theory), and the hadronic contributions (hadron). At tenth order in α_{EM}, there are 12,672 diagrams correcting the vertex calculations involving mesmerising loop diagrams [54], ten of which are shown in figure 40. Even more remarkably, the dominant uncertainty on these calculations arise from experimental systematic uncertainties in the measurements of the fine-structure constant α_{EM}. The Standard Model does not predict the value of α_{EM}, which is why we must measure it independently.

Fine structure constant measurements are independently performed using the **atomic recoil method** [3, 52]. This measure the recoil velocity $v_{\text{rec}} = \hbar k/M$ of a cold atom with

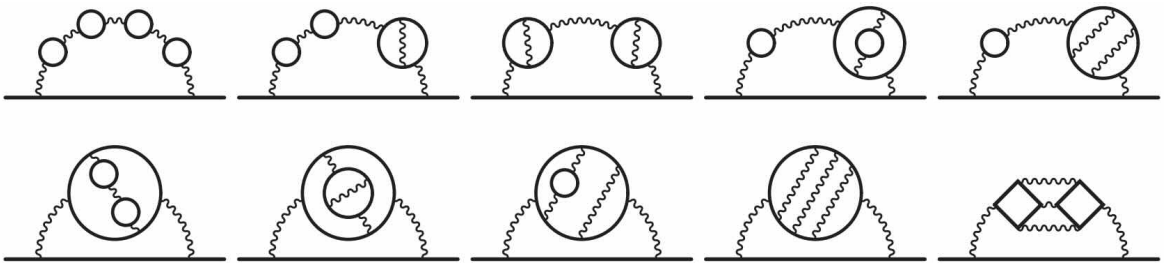

Figure 40: **Example digrams from tenth order QED**. Image: Ref. [54]

mass M when absorbing a photon with momentum $\hbar k$ from an external laser. This determines the ratio h/M which can be related to the fine structure constant via the Rydberg formula:

$$\alpha_{\mathrm{EM}}^2 = \frac{2R_\infty}{c}\frac{M}{m_e}\frac{h}{M}. \tag{7.14}$$

The prefactors to h/M are known to extraordinary accuracy from CODATA [55]: the Rydberg constant R_∞ is known to parts per trillion (ppt) from hydrogen spectroscopy, while the atom-to-electron mass ratio M/m_e is determined from the relative atomic mass being 69 (30) ppt for rubidium (electron).

Evidently, resolving the tension between the two measurements of α_{EM} made by rubidium and caesium atoms is essential to make progress in testing the Standard Model. Nonetheless, that we are confronting discrepancies at better than parts per trillion is just spectacular for experiment and theory. These are monumental triumphs of scientific inquiry.

7.3 Running coupling

Another profound consequence of quantum field theory is that couplings we initially call 'constants of nature' actually depend on the energy at which we measure them. The underlying physical effect is **vacuum polarisation**. The physical picture is that the vacuum around a particle actually polarises i.e. the vacuum is surrounded by a cloud of positive and negative particles (figure 42). These electron-positron $(-+)$ pairs are spontaneously created and annihilated from the vacuum as quantum fluctuations. The higher the energy the particle we use to probe another, the more we probe this polarisation. This picture means far away from the electron, we see a lower effective charge because the positive charges cancel out the negative charge of the electron.

But if we accelerate a probe particle with high momentum, this can wade through the cloud of virtual particles and see a higher effective charge. This leads to the notion that the measured electromagnetic coupling increases with momentum transfer due to the existence of

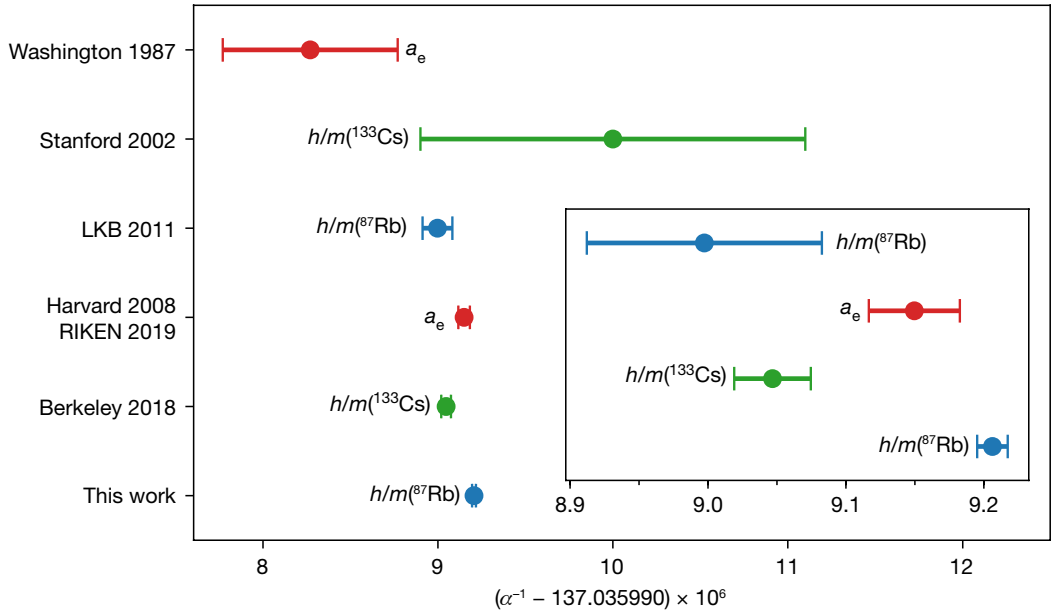

Figure 41: **Fine-structure constant measurements**. The determination of the fine-structure constant via the matter recoil method (blue and green) compared with Penning trap cyclotron measurements of the electron anomalous magnetic moment a_e (red). Figure: Ref. [3].

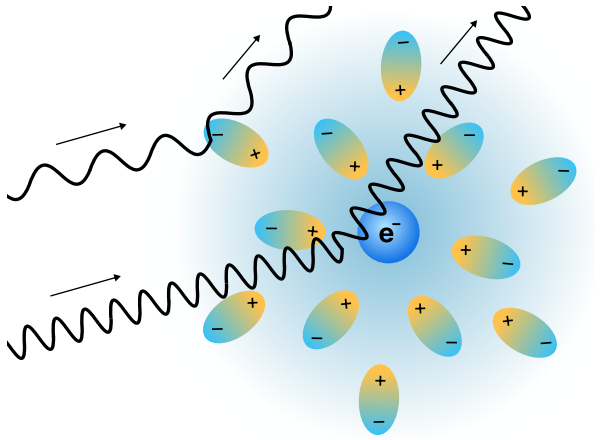

Figure 42: **Vacuum polarisation as a cloud of virtual particles**. Interactions of a low energy (longer wavelength) particle probing an electron are screened by the cloud, resulting in a smaller measured coupling. A high energy (shorter wavelength) particle can probe deeper into the cloud, resulting in a larger measured coupling.

quantum fluctuations. Specifically, the photon propagator receives corrections from fermion

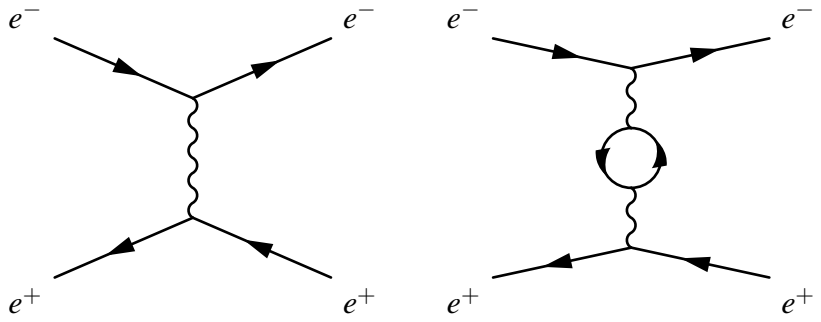

Figure 43: **Bhabba scattering**. Tree-level (left) and one-loop (right) vacuum polarisation diagrams in t-channel exchange.

loops:

$\Pi_{\text{meas}} =$  $+\ldots$ (7.15)

We can write the structure of the physical photon propagator Π_{phys} as a perturbative expansion in the bare coupling α_0 and bare photon propagator Π, with each fermion loop contributing a negative sign:

$$\Pi_{\text{phys}} = \Pi + \ \Pi e(-1)I(q^2)e\,\Pi_0 + \Pi\, eI(q^2)e\ eI(q^2)e\,\Pi_0 - \ldots \tag{7.16}$$

$$= \Pi_0 - \alpha_0 \Pi I(q^2)\,\Pi \qquad + \alpha_0^2 \Pi I(q^2)\,\Pi I(q^2)\,\Pi - \ldots \tag{7.17}$$

Quantum Field Theory classes teach us how to evaluate loop integral $I(q^2)$. We could look up the result in a textbook [1] to find that the amplitude changes by $1 - I(q^2)$:

$$I\left(q^2\right) = \frac{\alpha}{3\pi}\int_{m_e^2}^{\Lambda^2} \frac{\mathrm{d}k^2}{k^2} - \frac{2\alpha}{\pi}\int_0^1 \mathrm{d}x(1-x)\ln\left[1 - \frac{q^2 x(1-x)}{m_e^2}\right]. \tag{7.18}$$

We shall now sketch the process of renormalisation in a page. The first term of the loop integral is famously infinite when integrating over all momentum k. We admit that we cannot know physics at arbitrarily small distance (or large energy) scales and impose an energy cutoff Λ. At high momentum transfers $q^2 \gg m_e^2$ limit, the integral becomes

$$I\left(q^2\right) = \frac{\alpha}{3\pi}\ln\left(\frac{\Lambda^2}{-q^2}\right). \tag{7.19}$$

The perturbative expansion to higher loops orders can be summed as a geometric series $S = 1/(1-r)$:

$$1 - I\left(q^2\right) + \left[I\left(q^2\right)\right]^2 - \left[I\left(q^2\right)\right]^3 + \cdots = \frac{1}{1 + (\alpha/3\pi)\ln\left(\Lambda^2/Q^2\right)}, \tag{7.20}$$

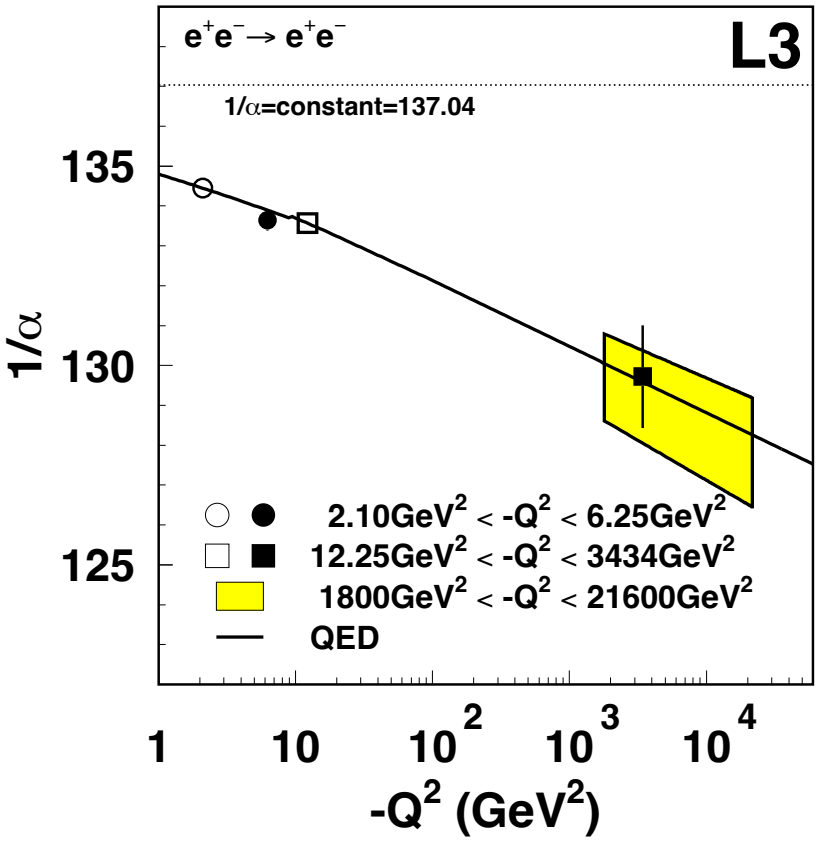

Figure 44: **Running electromagnetic coupling**. Electromagnetic coupling as a function of momentum transfer squared Q^2 measured by the L3 Experiment.

where we have defined $Q^2 = -q^2$. The net impact of this is a shift in the coupling $\alpha(Q^2)$ constant measured at scale Q^2 relative to the bare coupling constant α_0

$$\alpha\left(Q^2\right) = \frac{\alpha_0}{1 + (\alpha_0/3\pi)\ln\left(\Lambda^2/Q^2\right)}. \tag{7.21}$$

We can make measurements of $\alpha\left(Q^2 = \mu^2\right)$ at a reference mass scale μ (e.g. the electron mass $\mu = m_e$), which allows us eliminate α_0 by subtracting $\alpha^{-1}(Q^2) - \alpha^{-1}(\mu^2)$ to obtain

$$\alpha\left(Q^2\right) = \frac{\alpha(\mu^2)}{1 - [\alpha(\mu^2)/3\pi]\ln\left(Q^2/\mu^2\right)}. \tag{7.22}$$

This remarkable result shows that by considering only measurable values of $\alpha(Q^2)$, we remove the dependence on the arbitrary cutoff scale Λ. This is the process of **renormalisation** via the cutoff method, and μ is the **renormalisation scale**. The result is that the coupling now depends on the momentum scale Q^2. The differential equation describing this evolution

is called the **beta function**:

$$\frac{\partial \alpha_{\mathrm{EM}}}{\partial Q} = \beta(\alpha_{\mathrm{EM}}) = \frac{2\alpha_{\mathrm{EM}}^2}{3\pi}. \tag{7.23}$$

Figure 44 shows high-energy electron-positron accelerator measurements of $e^+e^- \to e^+e^-$ at the L3 Experiment [56]. We can see that measured values at the different energy scales are

$$\alpha_{\mathrm{EM}}(q^2 \to 0) \simeq \frac{1}{137}, \tag{7.24}$$

$$\alpha_{\mathrm{EM}}(q^2 = m_Z^2) \simeq \frac{1}{128}. \tag{7.25}$$

In quantum electrodynamics, the effective coupling α_{EM} grows with energy scale.

III Strong force

8 Unveiling the particle zoo

The timeline of particle discoveries span just over a century for the fundamental SM particles and various composite states called hadrons, shown in figure 45. Particularly striking in this history is a plethora of particles that appeared in experiments around the late 1940s to mid-1960s. The pion was widely anticipated as the mediator of the strong nuclear force, the kaons were more peculiar and the greatest surprise was the sheer multitude of ostensibly fundamental particles appear in experiments. This triggered detailed characterisation of their properties, inspiring the designation of *particle zoo*. This eluded deeper organising principles until the quark model of mesons and baryons comprising up, down, strange quarks. In the 1970s, new resonances yielded evidence for the charm and bottom quarks alongside the gluon. This was the decade many aspects of what we now know as the Standard Model fell into place.

It became clear that this remarkable richness of states was evidence for a single theory of the strong force, quantum chromodynamics (QCD), which is the subject of this chapter. The top quark discovery was widely anticipated but would wait until the mid-1990s. Hadrons remain an active area of research in the 21st century, as the Large Hadron Collider continues to discover new exotic states comprising four or even five quarks (tetraquarks and pentaquarks).

8.1 Nuclear magnetic moments

Early on in the 1930s, mysterious measurements of the proton and neutron magnetic moments revealed the first indirect evidence that they were not fundamental Dirac fermions. The expectation from Dirac theory is that electrically charged point-like spin-1/2 particles should have $g = 2$ and neutral particles cannot have a magnetic moment $g = 0$ as they are not electrically charged:

$$g^{\text{Dirac}}_{\text{proton}} = 2, \tag{8.1}$$

$$g^{\text{Dirac}}_{\text{neutron}} = 0. \tag{8.2}$$

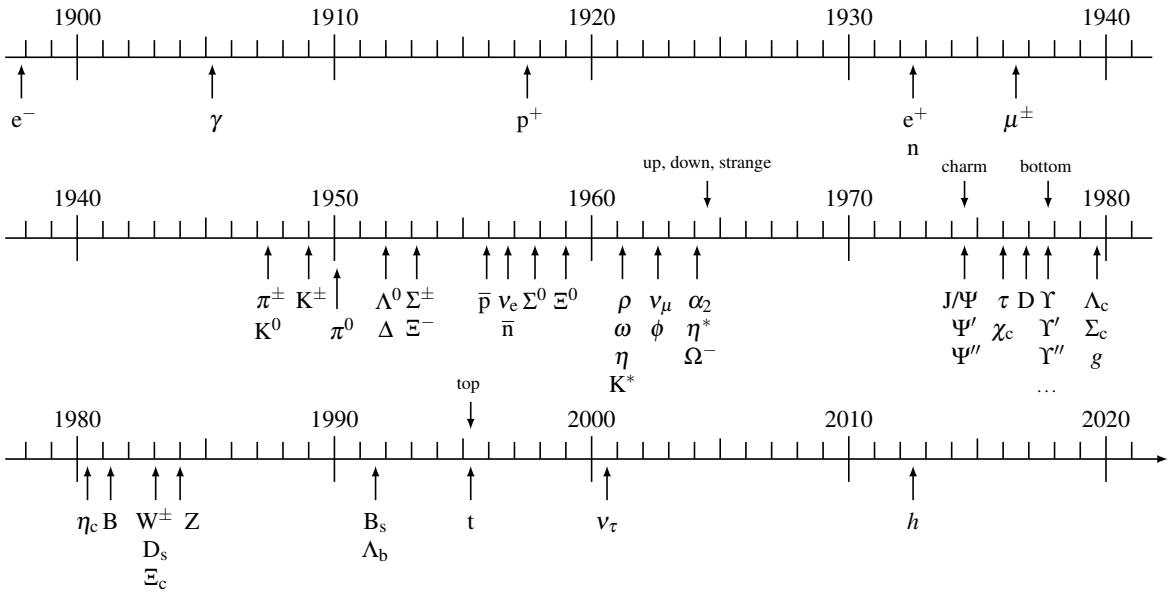

Figure 45: **Timeline of particle discoveries**. Displayed are various fundamental SM particles and composite hadrons. Figure: adapted from Ref. [57]

However, the measured magnetic moments could not be more different, quoting the modern values with uncertainties in parentheses from CODATA [55]:

$$g_{\text{proton}}^{\text{measured}} = +5.585\,694\,689\,3\,(16), \tag{8.3}$$

$$g_{\text{neutron}}^{\text{measured}} = -3.826\,085\,52\,(90). \tag{8.4}$$

This is an utter rejection of Dirac theory. We could imagine some alternative reality where the anomalous magnetic moments were at per-mille like that for the electron e.g. $g^{?}_{\text{proton}} = 2.005, g^{?}_{\text{neutron}} = 0.007$. But for once, nature was refreshingly not even subtle about defying the prevailing Dirac theory. The first measurements revealing a non-zero neutron magnetic moment around 1933 using atomic hyperfine measurements were especially viewed with suspicion. How can an electrically neutral particle possess a magnetic moment? It took several years of experimental development to obtain more accurate and direct measurements to establish the values beyond doubt.

The nuclear magneton μ_N is written in terms of the proton mass

$$\mu_N = \frac{e\hbar}{2m_p}. \tag{8.5}$$

We then express the magnetic moment $\boldsymbol{\mu}$ of a nucleus in terms of the g-factor g and nuclear spin $\mathbf{I}$

$$\boldsymbol{\mu} = g\mu_N \mathbf{I}/\hbar. \tag{8.6}$$

Robert Frisch and Otto Stern discovered the proton magnetic moment in 1933 at Hamburg by deflecting hydrogen through an inhomogeneous magnetic field as in the Stern–Gerlach experiment for electron spin. Already in 1934, the Columbia University group led by Isidor Rabi determined the proton to have unexpectedly large $\mu_p = (3.2 \pm 0.3)\mu_N$ [58] and deuteron unexpectedly small $\mu_d = (0.7 \pm 0.2)\mu_N$ [59] magnetic moments. They developed nuclear magnetic resonance techniques to improve such measurements to per-mille accuracy by 1940, enabling an indirect measurement of the neutron counterpart μ_n:

$$\begin{aligned} \mu_p &= (+2.785 \pm 0.002)\mu_N \\ \mu_d &= (+0.855 \pm 0.002)\mu_N \end{aligned} \quad \Rightarrow \quad \mu_n \approx -2\mu_N. \tag{8.7}$$

Deuterium has spin 1, which implies the the proton and neutron each with spin 1/2 should be aligned $|\uparrow\rangle_p|\uparrow\rangle_n$ so the magnetic moments are additive $\mu_d = \mu_p + \mu_n$. This implies the neutron magnetic moment is around $-2\mu_N$. In 1940, Alvarez and Bloch [60] used the cyclotron at Berkeley to create a beam of free neutrons in an inhomogenous magnetic field, enabling the first direct measurement of the neutron magnetic moment

$$\mu_n = (-1.93 \pm 0.02)\mu_N. \tag{8.8}$$

This was of course the first clue for compositeness, nuclear substructure, and a new fundamental force. This predates the hadron zoo and proposal of quarks that took decades to establish. An important scientific lesson we learn from this is to experimentally test all predictions, even if theory says we should expect to measure nothing, as was the case for the neutron. Today, we now use the magnetic moment of nucleons for medical applications in magnetic resonance imaging.

8.2 Hadrons in nuclear emulsions

A key advance in hadron physics was the invention of nuclear emulsion photographic plates to detect and record energetic charged particles. Marietta Blau developed this method and the plates were manufactured by Ilford and Kodak. Suspended in a thick emulsion on a glass plate are silver halide crystals with heightened concentration to raise particle detection sensitivity. The size of the grains can be smaller than μm, enabling exceptional spatial resolution. When energetic radiation traverses the plate, some of the silver halide crystals along the ionising trajectory turn into silver, which are chemically developed into photographs for permanent record. By counting the grain density, one could determine the ionisation energy loss of the particle.

(a) Kurz's logbook for pion discovery (b) Bristol cosmic-ray group 1949

Figure 46: **Bristol cosmic-ray research group**. Notebook of Marietta Kurz who analysed the photographic emulsions, searching for interesting images and one with her annotation "double meson", the first sign of the pion. From Physics World/Bristol University Special Collections. Right shows Cecil Powell's cosmic-ray research group at Bristol in 1949, photo from CERN Courier **27** (1987) 8.

Charged pions

Cecil Powell assembled a large cosmic-ray research group at the University of Bristol with scanners scouring the photographs under microscopes for interesting particle track events. One such track is shown in figure 46 as logged in the notebook of Marietta Kurz. In many of the landmark discovery papers In 1947, Occhialini and Powell reported the first photos of a pion[43] decaying to a muon. In 1948, specially developed electron-sensitive emulsions were developed by Kodak enabling measurement of the electron from the decaying muon (figure 47). This established the full decay chain of charged particles in the leptonic decays of the pion:

$$\begin{array}{ll} \pi^+ \to \mu^+ + \nu_\mu & \pi^- \to \mu^- + \bar{\nu}_\mu \\ \quad\downarrow & \quad\downarrow \\ \quad\mu^+ \to e^+ + \nu_e + \bar{\nu}_\mu & \quad\mu^- \to e^- + \bar{\nu}_e + \nu_\mu\,. \end{array} \tag{8.9}$$

[43]The June 1997 issue of CERN Courier provides an interesting history of the pion during the 50th anniversary of its discovery https://cds.cern.ch/record/1732689.

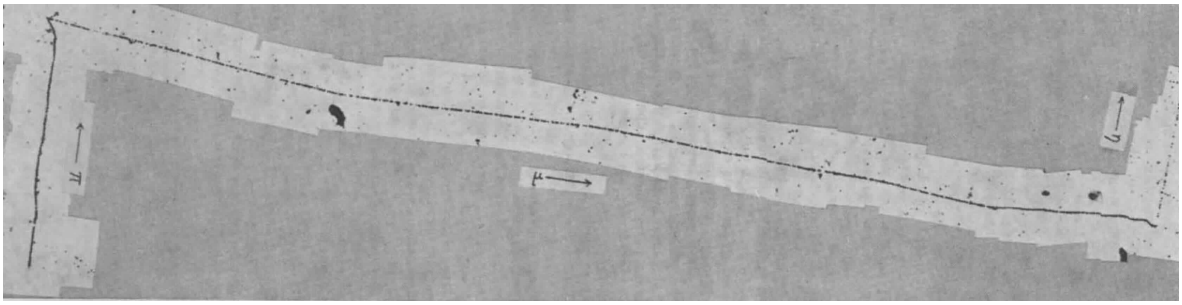

Figure 47: **Charged pion discovery photo**. Historical photographic plate form 1949 showing a charged pion (leftmost line, going up) decaying to muon (long line from left to right) decaying to electron (faint rightmost line, going up) $\pi \to \mu \to e$ (the electron is labelled η in this image). Identified by Rosemary Brown in the Bristol Cosmic Ray Research group, reproduced from Ref. [61].

Kaons

Kaons, or K-mesons, were discovered in a series of cosmic-ray experiments in the Manchester and Bristol groups [44]. Originally, there were neutrals decaying into a pair of charged particles. This gave a distinct "V" fork to the Manchester cloud-chamber tracks shown in figure 48, which was called V^0. Today this corresponds to the neutral kaon with a mass around half that of the proton $m_{K^0} \approx 497.6$ MeV.

Meanwhile, the Manchester group identified charged particles decaying into a charged plus neutral called $\theta^\pm$ while the Bristol group found the three charged pion decay mode named $\tau^\pm$:

$$\theta^\pm \to \pi^\pm \pi^0, \tag{8.10}$$

$$\tau^\pm \to \pi^\pm \pi^\pm \pi^\mp. \tag{8.11}$$

Figure 49 shows a "K track" $\tau^\pm \to \pi^\pm \pi^\pm \pi^\mp$, evidencing a kaon decay from cosmic rays, captured with nuclear emulsion detectors.

The decay signatures were so different that contemporary physicists thought they had discovered different particles. However, what was completely puzzling was that they shared the same mass of around 493.7 MeV and lifetime of around 12.4 ns. Such mysteries were called the "tau–theta puzzle". The particles had other peculiar properties that they dubbed

[44] There is a lovely historical account of this history in a 1997 CERN Courier article entitled *Half a century ago the pion pioneers* https://cds.cern.ch/record/1732677. Rosemary Fowler (nèe Brown) discovered the kaon as a doctoral student in Cecil Fowler's group, published in Nature article 1949 https://www.nature.com/articles/163082a0

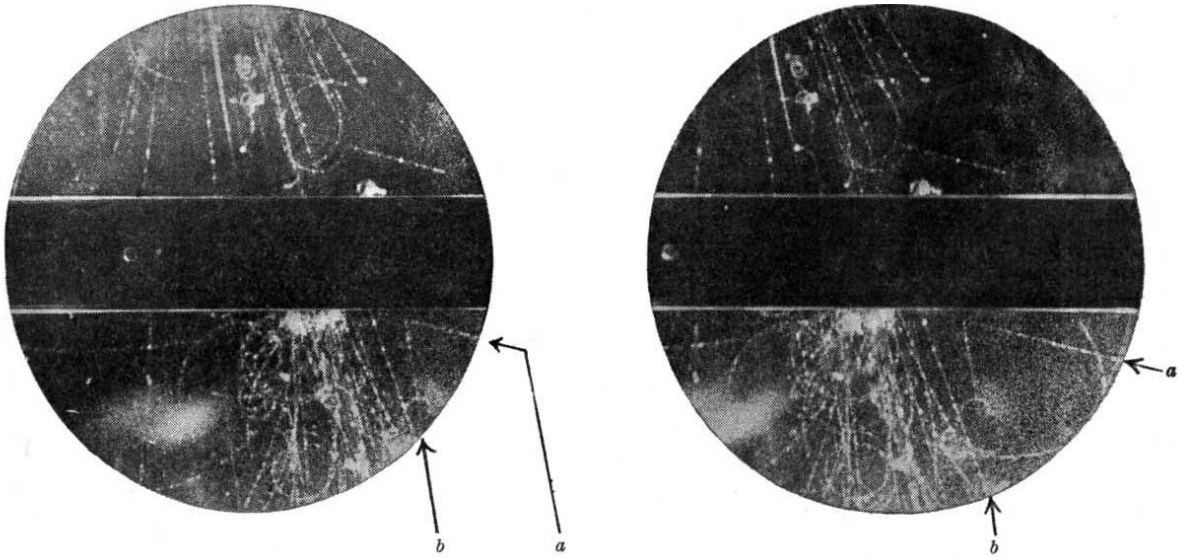

Figure 48: **Manchester kaon discovery photos**. The original caption was: "stereoscopic photographs showing an unusual fork (a b) in the gas by Rochester and Butler at Manchester [62]. The direction of the magnetic field is such that a positive particle coming downwards is deviated in an anticlockwise direction". Neutral particle decaying into two charged pions; a charged particle decaying into a charged pion and a neutral particle.

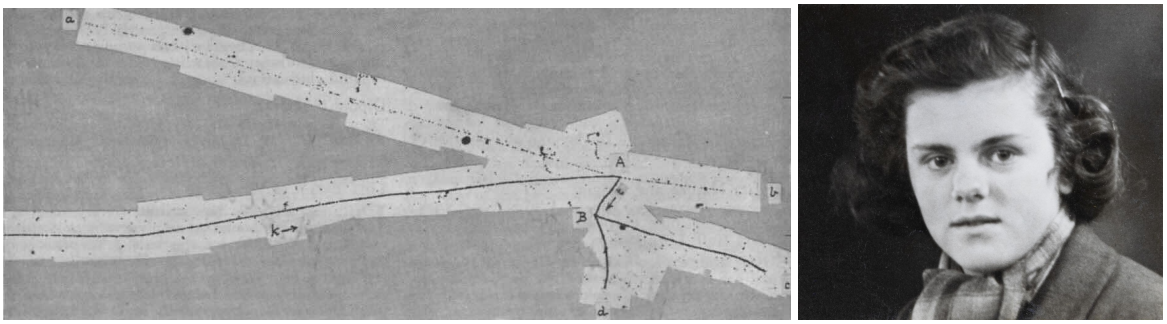

(a) Kaon track (b) Rosemary Brown

Figure 49: **Bristol kaon discovery photo**. Kaon track found by W. J. van der Merwe in a photographic plate: V shaped tracks in cosmic ray from Ref. [61]. Photo showing Rosemary Brown who analysed such events.

"strange", which we shall re-visit in the discussion of the strange quark where the name has stuck. It took a decade to realise the these were the same particles and $\theta^{\pm}, \tau^{\pm}$ are retired in favour of the charged kaon $K^{\pm}$.

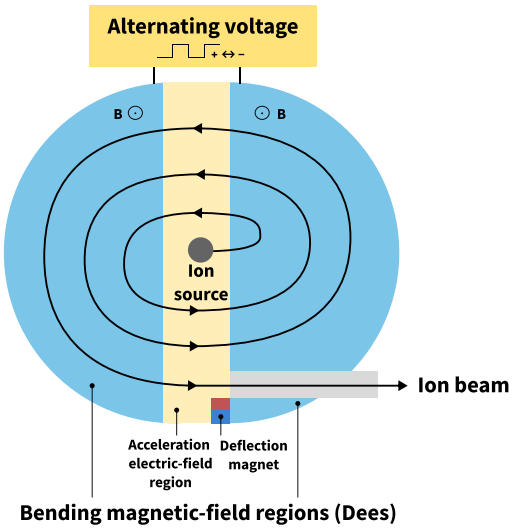

(a) Schematic diagram

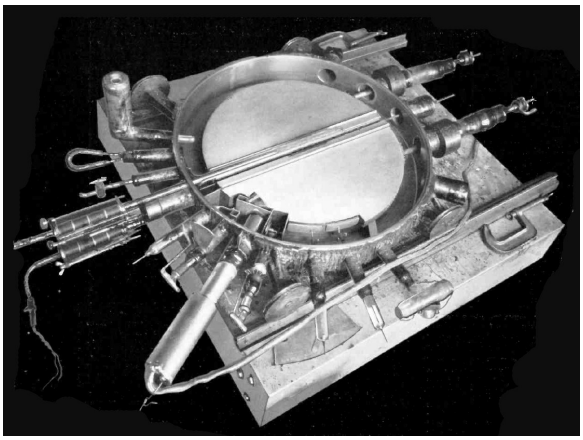

(b) 27 inch cyclotron

Figure 50: **Cyclotron schematic and photo**. Left: schematic diagram of a cyclotron accelerator. Right: the 27 inch cyclotron built by Lawrence and Livingston from John B. Livingood, "Radioactivity by Bombardment" *Electronics* Magazine (1935)

8.3 Cyclotrons to synchrotrons

The deluge of the particle zoo arose from concurrent advances in particle accelerators.

Cyclotron

A more compact alternative to a linear accelerator is to wrap the above setup into a circular geometry to create a circular accelerator, which has a complementary set of advantages and disadvantages. The key idea is to exploit the magnetic part of the Lorentz force to generate a centripetal force mv^2/r via a perpendicular magnetic force of magnitude $f = QvB$:

$$\frac{mv^2}{r} = QvB. \tag{8.12}$$

With the angular speed $\omega = v/r$, we find the **cyclotron frequency** is

$$f = \frac{\omega}{2\pi} = \frac{QB}{2\pi m}. \tag{8.13}$$

The key idea here is that the frequency is independent of the particle velocity. So acceleration only requires an alternating voltage at constant frequency, which is simple to engineer.

A cyclotron comprises two 'D'-shaped objects where the electric polarity oscillates to provide acceleration in the gap. Meanwhile, the magnetic field within each dee ensures particle always experiences a centripetal force towards the same centre turning the particle. The source of particles are injected at the centre and spiral outwards as its velocity and therefore bending radius increases with acceleration. The ions in the accelerating region are attracted to one of the Dees. A final deflection magnet then allows the particle to exit at a well-defined energy.

Ernest Lawrence and Stanley Livingston constructed the first cyclotron[45] at Berkeley, California in 1931 (figure 50). Reaching 1 MeV allowed reproducing the Cockcroft–Walton experiment that split the atom at Cambridge. This new class of machine saw rapid progress, reaching around 20 MeV by the end of the 1930s. By such energies, the mass of the proton receives noticeable relativistic correction from the gamma factor $\gamma = E/m$. From equation (8.13), we see that to maintain constant frequency for the alternating voltage, we can steadily ramp up the magnetic field B to compensate for the increasing m. This modification to synchronise the magnetic field with particle energy goes by the name of **synchro-cyclotron**.

In 1948, the first synchro-cyclotron machine at Berkeley reached a colossal (for the time) 184 inches in size and weighed 10^7 kg, accelerating alpha particles from 380 MeV to 720 MeV. The was technologically possible thanks to the invention of phase stability in V. Vecksler and independently by E. Macmillan, where successive beam focusing and de-focusing allows stable orbits. Remarkably, such singular focus on increasing cyclotron energy meant nobody added a detector until Lattes moved from Powell's Bristol group to Berkeley and suggested placing photographic emulsions to image collision debris from such a powerful machine. The beam energies of 380 MeV were enough to create the charged pions in great abundance earlier observed by the British cosmic-ray groups. The neutral pion π^0 was more difficult to find as it is electrically and does not appear in photographic emulsions. The neutral pion decays electromagnetically via its hallmark di-photon signature with a branching ratio of 99.8%:

$$\pi^0 \to \gamma\gamma, \quad m_\pi = 135 \text{ MeV}. \tag{8.14}$$

The neutron pion was discovered at Berkeley in 1950 by Panofsky, Steinberger, and Steller.

Today, there are thousands of active cyclotrons around the world that benefit the human condition. Many of these are in hospitals, producing indispensable radioisotopes for medical imaging including Positron Emission Tomography (PET). They are also now used for

[45] As often in history, the Nobel prize recognising such groundbreaking research went to Lawrence, but not Livingston who was a graduate student at the time.

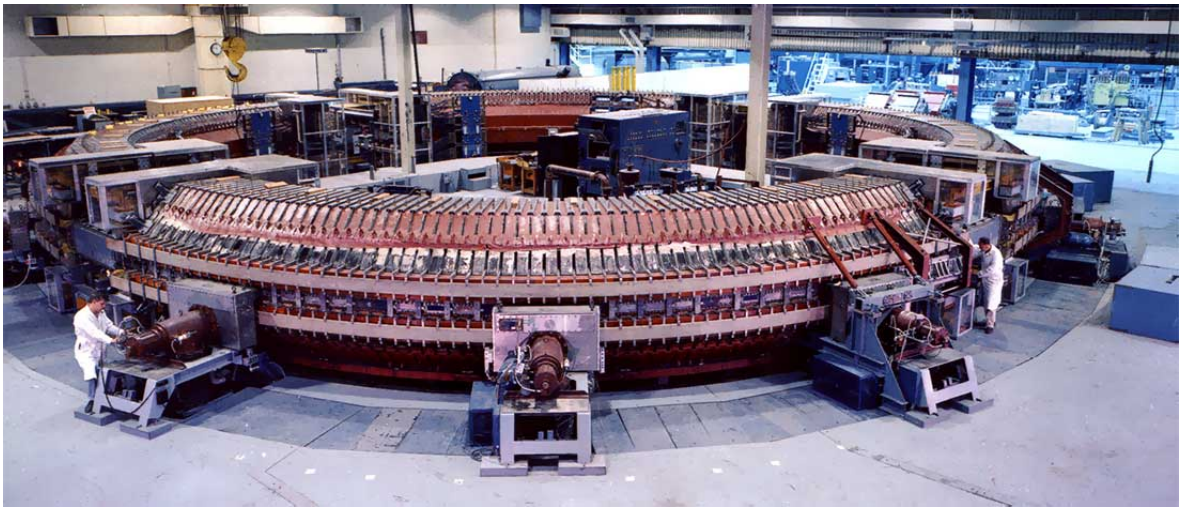

Figure 51: **Brookhaven Cosmotron**. BNL, a synchrotron operated in 1952–1966.

cutting-edge proton therapy, where a cyclotron accelerates protons to destroy cancerous cells with reduced dose to surrounding healthy tissue via the Bragg peak technique. Indeed, there are several cyclotrons in New York City, including the NYU Department of Radiology[46] and New York Proton Center[47]. These are beautiful examples of how a research breakthrough for fundamental physics later finds applications that routinely save human lives. Nonetheless, these devices are large and expensive, occupying very large rooms and costing $\gtrsim 10^7$ dollars. Perhaps you will be inspired to join accelerator science research not just to create more compact machines for fundamental physics but also make therapies more accessible, affordable and portable for society.

Synchrotron

The synchrotron is an evolution of the synchro-cyclotron such that the bending radius is constant. This combines electric field regions for increasing particle energy and bending to steer particles in such a way that it is synchronised to the particle energy. The main downside is synchrotron radiation, which is a consequence of Maxwell's equation that all accelerated charges emit electromagnetic radiation. The power emitted P by a charged particle radiates in one revolution is given by Larmour's formula

$$P = \frac{2}{3}\frac{e^2}{4\pi\varepsilon_0 mc^2}\frac{m}{\rho^2}\left(\frac{E}{m}\right)^4 \propto \frac{E^4}{m^4}\frac{1}{\rho^2}. \tag{8.15}$$

[46] https://med.nyu.edu/departments-institutes/radiology/research
[47] https://www.nyproton.com/about-proton-therapy

Here, m and e are the mass and charge of the particle being accelerated, ρ is the radius of curvature and E is the energy of the particle. Combating synchrotron radiation requires as large a radius as possible. Synchrotrons involving heavier particles also result in reduced comparative radiated emission, justifying proton colliders over electron colliders having higher centre-of-momentum energies. From equation (2.13) $R/\mathrm{m} = (pc/\mathrm{GeV})/[0.3(B/1\ \mathrm{T})]$, we find the momentum and magnetic field sets the bending radius and thus size of a circular accelerator.

The Cosmotron at Brookhaven National Laboratory (figure 51) opened in 1952 and accelerated protons up to 3 GeV. Berkeley built the Bevatron two years later and reached up to 7 GeV.

8.4 Bubble chamber

The bubble chamber is a spiritual successor to the cloud chamber and was a key detector technology in particle physics discoveries invented by D. Glazer and L. Alvarez in the 1950s. While particle tracks appear from condensation in cloud chambers, the bubble chamber inverts this phase transition such that charged particles trigger the liquid to boil into gas bubbles. The main benefit is the higher material density offered by liquid compared to gas to increase interaction probability. The liquid can act as both target and detector, with hydrogen being a proton target and deuterium having neutrons, while heavier atomic materials are more suited to neutrino detection.

Figure 52a shows a schematic diagram of the bubble chamber detection process. The steps to detection are as follows:

Beam arrives → Piston expands → Liquid superheated → Beam strikes liquid → Particles produced → Tracks of bubbles

Originally, liquid hydrogen was used, which has a boiling point of 20.3 K at 1 atmosphere pressure, requiring sophisticated cryogenics and safety interlocks. The liquid is kept under pressure just below its boiling point and the moment before the beam arrives, a piston relaxes to lower the pressure. This causes the liquid to become *superheated*, meaning its temperature is above the boiling point but remains in its liquid phase. As charged particles traverse this superheated liquid, the ionization triggers the boiling process to leave a tracks bubbles with high spatial resolution. Cameras surrounds the bubble chambers to capture the tracks bending inside a magnetic field, allowing particle charge and momentum measurements.

Figure 52b shows the Big European Bubble Chamber together with its piston at the CERN Microcosm exhibit (figure 52c), the last and largest such detector to have operated

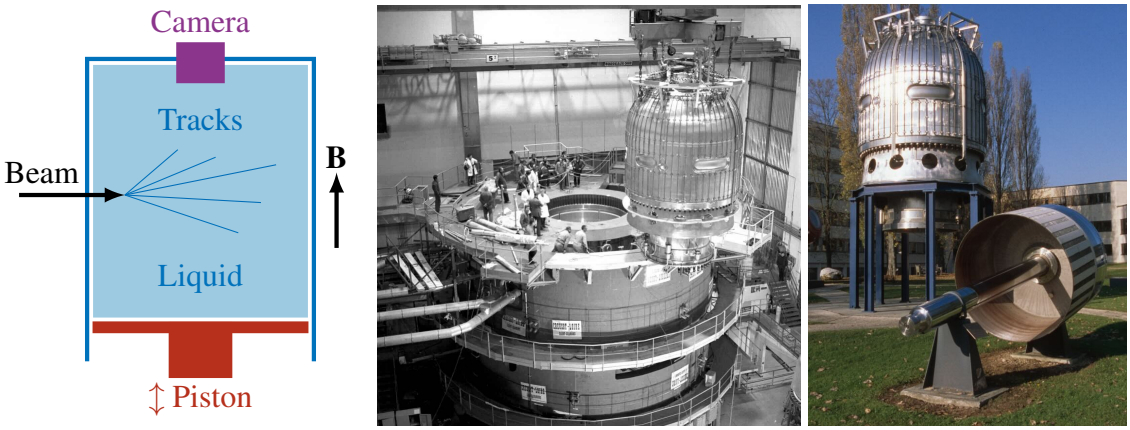

(a) Schematic sketch (b) Installation into cryostat (c) Piston

Figure 52: **Bubble chamber schematic and photos**. Schematic sketch shows the principle of operation for a bubble chamber. The photos display the Big European Bubble Chamber (BEBC) at CERN. (b) Installation into the cryostat in 1971 CERN. (c) Piston in front of the bubble chamber at the CERN Microcosm museum CERN-PHOTO-SIS-68681.

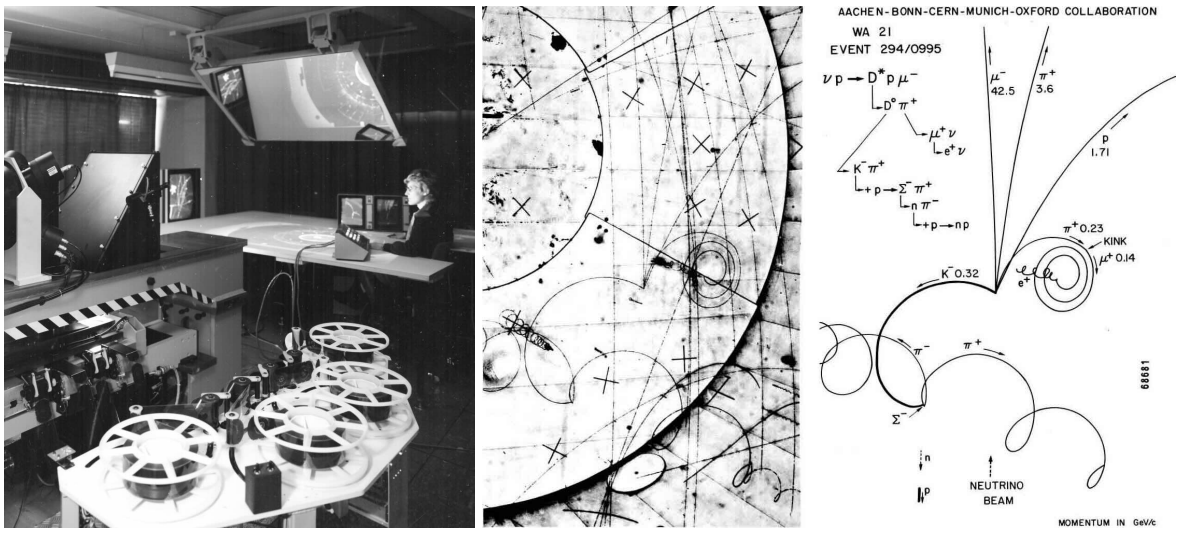

(a) Scanning film photos (b) D-meson bubble chamber tracks

Figure 53: **Analysing Big European Bubble Chamber (BEBC) data**. Madeleine Znoy using the Electron RAy Scanning and Measuring Equipment (ERASME) film scanner imaging BEBC events CERN. Event showing D-meson production and decay from neutrino beam from WA21 experiment CERN-PHOTO-SIS-68681.

during the 1970s. Human scanners had to sift through the cornucopia of film photographs in projectors (figure 53a) and initially the tracks are manually traslated onto cards. The exquisite spatial resolution of the bubble chamber and sensitivity to charged particles were the key advantages of this technology (figure 53b). The main downside of this detector technology was the relatively large time required to reset the detector after each image is taken, given this requires resetting the piston.

During this period 1960–70s, automation developed rapidly in parallel to electronic computers aiding spatial measurement of photographed tracks. During the 1980s, bubble chambers retired in favour of electronic readout capabilities of spark chambers and semiconductor sensors that would become the de facto standard for charged-particle tracking. Bubble chambers are now museum pieces as monuments of scientific discovery, scattered across particle physics laboratories such as Fermilab and CERN.

9 Quarks and hadrons

We now study some of the phenomenological organising principles underlying the particle zoo of quarks and hadrons. Quarks[48] are proposed as the matter constituents of nucleons. The modern interpretation is that they are a set of elementary fermions with spin-$\frac{1}{2}$ that interact via the **strong force**. There are six **flavours** of quarks paired into three generations:

$$\begin{pmatrix} u \\ d \end{pmatrix}, \quad \begin{pmatrix} c \\ s \end{pmatrix}, \quad \begin{pmatrix} t \\ b \end{pmatrix}. \tag{9.1}$$

called up, down, charm, strange, top and bottom quarks respectively. Their antiparticle partners are denoted by overbars. Table 1 presents all the quantum numbers: charge (Q), strangeness (S), charm (C), bottomness (B), topness (T), and their masses (m) of all known quarks.

9.1 How to build a hadron

We now construct some hadrons using the lightest quarks: up and down. Free quarks are never directly observed. We instead find them as bound states called **hadrons**, which we call mesons and baryons[49], according to their quark content:

[48] Merriam Webster provides an interesting discussion of the etymology and pronunciation of *quark*. I pronounce *quark* rhyming with *mark* as used in "Three quarks for Muster Mark!" from James Joyce's *Finnegans Wake*, though Murray Gell-Mann originally rhymed it with *fork*.

[49] The etymology comes from Greek *mesos* meaning middle and *barýs* meaning heavy, which are helpful to remember that baryons have higher quark content than mesons.

Quark	Symbol	Q [e]	S	C	B	T	m [GeV]
Down	d	$-\frac{1}{3}$	0	0	0	0	<1
Up	u	$+\frac{2}{3}$	0	0	0	0	<1
Strange	s	$-\frac{1}{3}$	-1	0	0	0	<1
Charm	c	$+\frac{2}{3}$	0	1	0	0	≈ 1.3
Bottom	b	$-\frac{1}{3}$	0	0	-1	0	≈ 4.3
Top	t	$+\frac{2}{3}$	0	0	0	1	≈ 174

Table 1: Quantum numbers and masses of known quarks. For antiquarks, invert the sign of all the quantum numbers. Q: electric charge, S: strange number, C: charm number, B: bottom number, T: top number.

Meson	Quark content	J^P	Q [e]	Rest mass [MeV]
π^+	$u\bar{d}$	0^-	+1	139.57018 (35)
π^0	$u\bar{d}$ or $d\bar{u}$	0^-	0	134.9766 (6)
π^-	$d\bar{u}$	0^-	−1	139.57018 (35)
ρ^+	$u\bar{d}$	1^-	+1	775.4 (4)
ρ^0	$u\bar{d}$ or $d\bar{u}$	1^-	0	775.49 (34)
ρ^-	$d\bar{u}$	1^-	−1	775.4 (4)

Table 2: The lightest mesons of spin-0 (π) and spin-1 (ρ).

- **Mesons**: integer spin states composed of a quark and an antiquark $q\bar{q}$.
- **Baryons**: half-integer spin states composed of three quarks qqq.
- **Antibaryons**: half-integer spin states composed of three antiquarks $\bar{q}\bar{q}\bar{q}$.

In recent years, experiments such as LHCb at CERN have discovered more exotic states comprising four (tetraquarks $q\bar{q}q\bar{q}$) and even five (pentaquarks $qqqq\bar{q}$) quarks[50]. We shall not discuss them, but they are an interesting active field of research.

Parity By convention, quarks have parity $P_q = +1$ while antiquarks $P_{\bar{q}} = -1$. The general prescription for calculating parity of a hardon is to multiply the parities of the individual quarks/antiquarks with the orbital angular momentum L. For mesons and baryons respectively, this gives

$$\begin{aligned} P_{\text{meson}} &= P_q P_{\bar{q}} (-1)^L = (-1)^{L+1} \\ P_{\text{baryon}} &= P_{q_1} P_{q_2} P_{q_3} (-1)^L = (-1)^L \end{aligned} \tag{9.2}$$

We usually denote the final angular momentum J (usually $J = S$ as we consider $L = 0$ states) and parity $P = \pm 1$ states together in the compact notation J^P.

Mesons Consider first the mesons whereby we couple two spin-$\frac{1}{2}$ particles – a quark and an antiquark. The lightest spin-0 states correspond to **pions** while the spin-1 states are **rho mesons** (table 2). The pions with $J^P = 0^-$ is sometimes called a **pseudoscalar**.

Baryon	Quark content	J^P	Q [e]	Rest mass [MeV]
p	uud	$\frac{1}{2}^+$	+1	938.272046 (21)
n	udd	$\frac{1}{2}^+$	0	939.565378 (21)
Δ^{++}	uuu	$\frac{3}{2}^+$	+2	1 232 (2)
Δ^+	uud	$\frac{3}{2}^+$	+1	1 232 (2)
Δ^0	udd	$\frac{3}{2}^+$	0	1 232 (2)
Δ^-	ddd	$\frac{3}{2}^+$	−1	1 232 (2)

Table 3: The lightest baryons of spin-$\frac{1}{2}$ (p,n) and spin-$\frac{3}{2}$ (Δ)

Baryons We now couple three quarks together. The spin-$\frac{1}{2}$ states correspond to our familiar nucleons while the spin-$\frac{3}{2}$ states are Delta baryons of slightly higher mass (table 3).

With this quark model involving up and down quarks, we can understand reactions involving the formation of pions:

$$\begin{aligned} p \quad + \quad p \quad \rightarrow \quad p \quad + \quad p \quad + \pi^+ + \pi^- \\ (uud) + (uud) \rightarrow (uud) + (uud) + (u\bar{d}) + (d\bar{u}) \end{aligned} \tag{9.3}$$

We can also follow the quarks during resonant production of a Delta baryon:

$$\begin{aligned} p \quad + \quad \pi^- \rightarrow \quad \Delta^0 \quad \rightarrow \quad n \quad + \pi^0 \\ (uud) + (d\bar{u}) \rightarrow (udd) \rightarrow (udd) + (u\bar{u}) \end{aligned} \tag{9.4}$$

Every quark/antiquark has a baryon number of $\frac{1}{3}/-\frac{1}{3}$. We make an important observation:

Total baryon number and **quark flavour** are conserved in strong interactions.	(9.5)

9.2 Strangeness and kaons

In the late 1940s, the Manchester and Bristol cosmic-ray groups observed new hadronic particles. One type was the kaon $K^\pm$ which was produced by a strong interaction:

$$p + p \rightarrow p + p + K^+ + K^- \tag{9.6}$$

Peculiarities arise when we examine the decay of a kaon. One decay mode with branching ratio of 0.21 is

$$\begin{aligned} K^+ \quad &\rightarrow \pi^+ + \pi^0 \\ (u\bar{d})? \ &\rightarrow (u\bar{d}) + (u\bar{u}) \end{aligned} \tag{9.7}$$

[50] https://cds.cern.ch/record/2814136

By conservation of baryon number, we rule out $K^+ = (uud)$ so kaons must be mesons and we hypothesise $K^+ = (u\bar{d})$. If this were the case, by the strong interaction we expect this to decay with a mean lifetime of order $\sim 10^{-23}$ s. Instead, we observe the mean lifetime of (9.7) to be $\sim 10^{-8}$ s, consistent with the weak interaction.

Gell-Mann and Nishijima resolved this by introducing a new quantum number called strangeness S, which we now attribute to the strange quark s. By (historical) convention, a strange quark s has strangeness $S = -1$ and charge $Q = -1/3$. The kaon formation (9.6) via the strong interaction is now explained by

$$\begin{aligned} p \quad + \quad p \quad &\to \quad p \quad + \quad p \quad + K^+ + K^- \\ (uud) + (uud) &\to (uud) + (uud) + (u\bar{s}) + (\bar{u}s) \\ \text{strangeness}: \quad 0 \qquad 0 \quad &\to \quad 0 \qquad 0 \qquad (+1) \quad (-1) \end{aligned}$$

while the kaon decay (9.7) via the weak interaction reads

$$\begin{aligned} K^+ \quad &\to \quad \pi^+ \quad + \quad \pi^0 \\ (u\bar{s}) \quad &\to (u\bar{d}) + (u\bar{u}) \\ \text{strangeness}: \quad (+1) \quad &\to \quad 0 \qquad 0 \end{aligned}$$

We make the historically important observation about strangeness:

Conservation of strangeness is obeyed in strong but violated in weak interactions.

9.3 Meson & baryon multiplets

Gell-Mann sought order out of the seemingly unwieldy number of mesons and baryons formed from lightest 3 quarks: up, down and strange. We focus on the lightest hadronic states with $L = 0$.

Mesons: figure 54 illustrate using wight diagrams the possible combinations of quark-antiquark $q\bar{q}$ pairings using up, down and strange. There are nine particles where we have the **pseudoscalar** and **vector** meson nonets corresponding to spin-parity $J^P = 0^-$ and 1^- respectively.

Baryons: we can do similar for the baryons giving figure 55. These show the possible combinations of $q_1q_2q_3$ using up, down and strange. We notice the absence of uuu, ddd, sss states in the spin-parity $J^P = \frac{1}{2}^+$ case. We also note there are two states made of uds in the $J^P = \frac{1}{2}^+$ case.

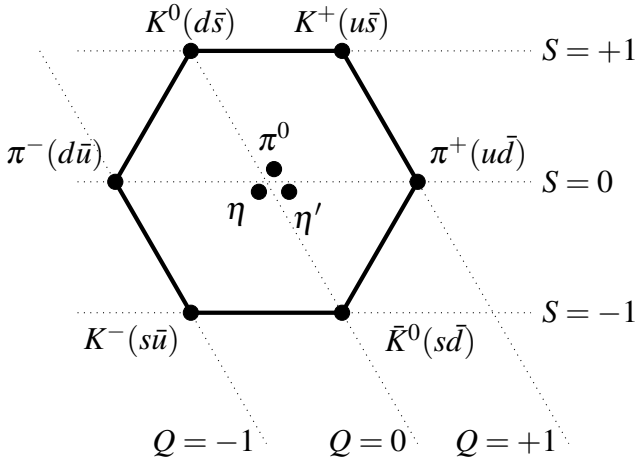

(a) $J^P = 0^-$ meson pseudoscalar nonet.

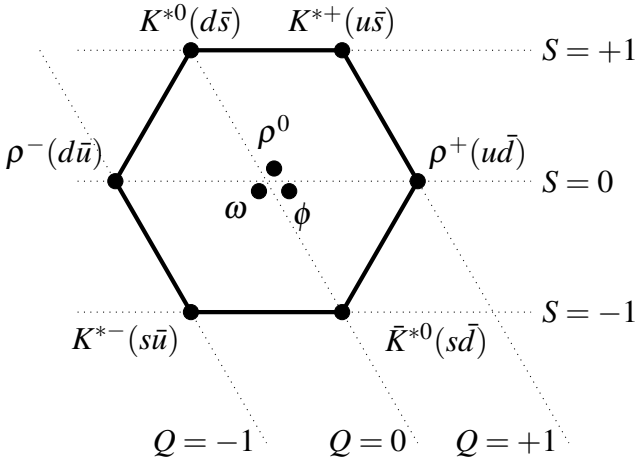

(b) $J^P = 1^-$ meson vector nonet.

Figure 54: **Meson nonets**. This is for spin-parity $J^P = 0^-$ (a) and 1^- (b) composed of up, down and strange quarks and antiquarks. Here, Q and S are charge and strangeness, respectively.

To account for the differences between the $J^P = \frac{1}{2}^+$ and $J^P = \frac{3}{2}^+$ multiplets, we impose the fact that the spin and spatial parts of the baryon wavefunction must be *symmetric* with respect to label exchange. (We note baryons, being fermions, require the total wavefunction to be *antisymmetric*; we resolve this apparent paradox when we acknowledge the existence of an antisymmetric colour wavefunction for the quarks.) In the lowest level $L = 0$, so spatial states are symmetric (even parity $P = (-1)^{L=0} = +1$). So to obtain a symmetric spin-spatial

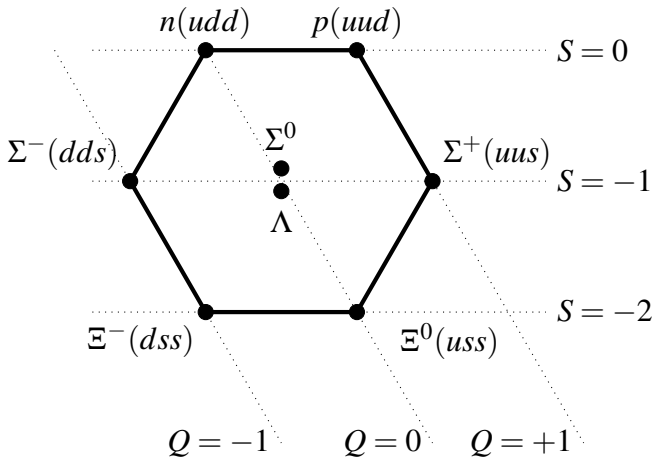

(a) $J^P = \frac{1}{2}^+$ pseudoscalar baryon octet.

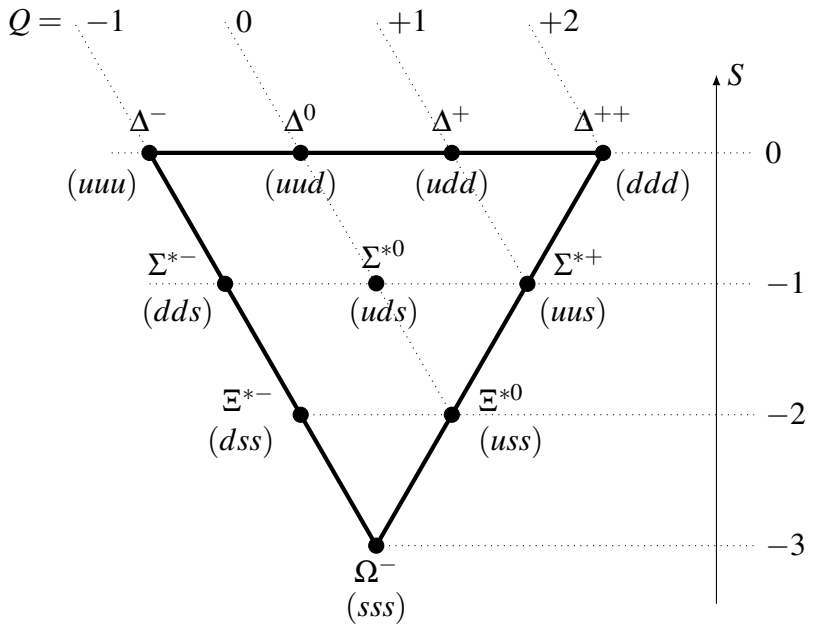

(b) $J^P = \frac{3}{2}^+$ baryon vector decuplet.

Figure 55: **Baryon octet and decuplet**. This is for spin-parity $J^P = \frac{1}{2}^+$ (a) and $\frac{3}{2}^+$ (b) respectively composed of up, down and strange quarks and antiquarks. Here Q and S are charge and strangeness respectively.

state, the spin wavefunction must also be symmetric.

We now consider the possible quark combinations:

- **Two like quarks**: For a pair of identical quarks $q_1 q_1$, the only way to construct a symmetric state is to align their spins i.e. $|\uparrow_1\uparrow_1\rangle$ giving spin-1. By the rules of angular momentum addition, introducing a third quark $q_2 \neq q_1$ to the system gives spin-$\frac{1}{2}$ or spin-$\frac{3}{2}$. So the quark combinations with two like quarks

$$uud,\ uus,\ ddu,\ dds,\ ssu,\ ssd$$

  can be in states $J = \frac{1}{2}$ or $\frac{3}{2}$.

- **Three like quarks**: In the case of all three identical quarks

$$uuu, ddd, sss$$

  the only way to obtain symmetric spin state is for all of their spins to align i.e. $|\uparrow_1\uparrow_1\uparrow_1\rangle$ to give $J = \frac{3}{2}$ only.

- **No like quarks**: For the last case of no like quarks uds, let us consider the pair ud first. We now have two cases:

  1. ud in spin-0 state – adding s results in $J = \frac{1}{2}$ state.
  2. ud in spin-1 state – adding s results in $J = \frac{1}{2}$ of $\frac{3}{2}$ state.

Counting everyone up, we find indeed we have eight $J^P = \frac{1}{2}^+$ states and ten $J^P = \frac{3}{2}^+$ states.

9.4 Colour charge

As suggested by the name quantum chromodynamics (QCD), a defining feature of the strong force is a new type of charge called colour. Every quark possesses one of three **colours charges**, which we can call red r, green g, blue b. Antiquarks posses anticolour: anti-red $\bar{r}$, anti-green $\bar{g}$, anti-blue $\bar{b}$. This is analogous to how electromagnetism has a single electric charge e, such that particles with electric charge feel the electromagnetic force. Colour is a generalisation of this idea where a force can have three distinct charges. Indeed, we could have called this the 'strong force charge' rather than colour. We can explicitly label a quark q with its charge q_i with $i = \{r, g, b\}$ (and antiquarks $\bar{q}_i$ with anticolour $i = \{\bar{r}, \bar{g}, \bar{b}\}$) or as a vector

$$q = \begin{pmatrix} q_r \\ q_g \\ q_b \end{pmatrix}. \tag{9.8}$$

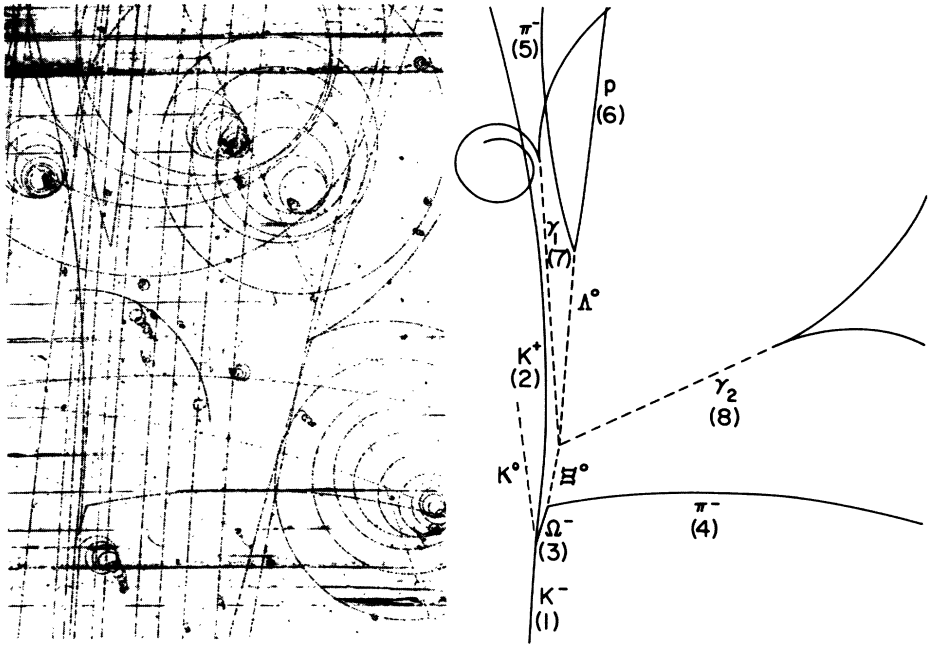

Figure 56: **Triple strange omega baryon discovery** Bubble chamber figure of the Ω^- baryon observed from Ref. [63].

Why introduce yet another quantum number? The historical arguments are interesting in themselves. Colour was motivated by Greenberg in 1964 to ensure hadronic wavefunctions are consistent with the Fermi–Dirac statistics from quantum mechanics, which requires identical fermions to be antisymmetric upon exchange of labels. The total baryon wavefunction comprises spatial, flavour, spin and colour parts:

$$|\Psi\rangle = |\psi_{\text{spatial}}\rangle|\psi_{\text{flavour}}\rangle|\psi_{\text{spin}}\rangle|\psi_{\text{colour}}\rangle \tag{9.9}$$

Let us consider the Ω^- particle with quark content *sss* and spin-parity $J^P = \frac{3}{2}^+$. This particle was significant in being made of three strange quarks and was discovered at Brookhaven in 1964, where figure 56 shows the original bubble chamber event.

- **Spatial**: The parity is positive: $P = (-1)^{L=0} = +1$ implying a symmetric spatial state with respect to exchange of labels.
- **Flavour**: The flavour state is $|s\rangle_1|s\rangle_2|s\rangle_3$ for quarks labelled 1,2,3 and is symmetric.
- **Spin**: With no orbital angular momentum $L = 0$, the only way to obtain $J = \frac{3}{2}$ is to have all the quarks' spins aligned $|\uparrow\rangle_1|\uparrow\rangle_2|\uparrow\rangle_3$, which is symmetric.

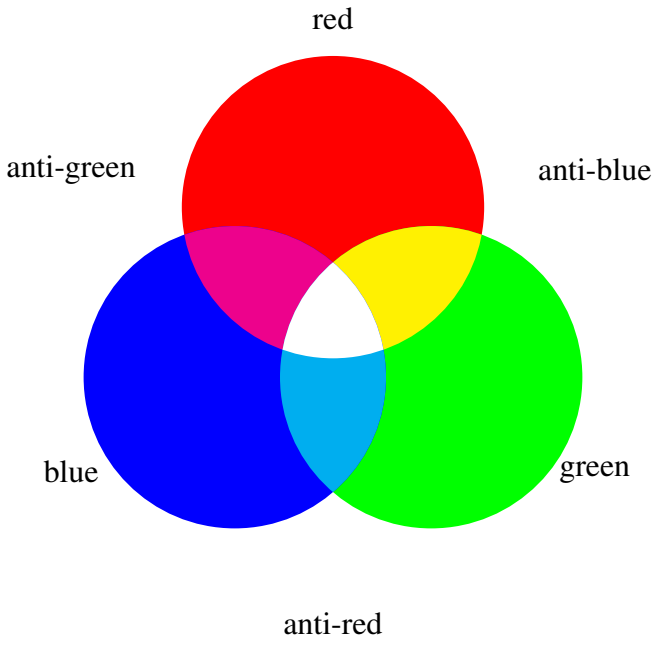

Figure 57: **Mnemonic for colour charge addition**. Analogy with colour theory for the addition of charge associated with the strong force.

- **Colour**: The space-flavour-spin combined wavefunction is symmetric. As baryons are fermions, they must be antisymmetric with respect to exchange of labels. By introducing a new degree of freedom for quarks, we can satisfy this condition. We call this **colour** because it is a helpful analogy to the fact only colour-neutral states are experimentally observed. We can define the colour wavefunction to be manifestly antisymmetric via a 3×3 determinant (normalised by $1/\sqrt{6}$):

$$|\psi_{\text{colour}}\rangle = \frac{1}{\sqrt{6}} \begin{vmatrix} r_1 & g_1 & b_1 \\ r_2 & g_2 & b_2 \\ r_3 & g_3 & b_3 \end{vmatrix} \tag{9.10}$$

  This determinant flips sign if we exchange the labels on any two rows, satisfying antisymmetry with respect to label exchange.

The analogy of colour charge with the additive colour theory of light. This combination of three colours is colour-neutral:

$$\text{red} + \text{green} + \text{blue} = \text{neutral}. \tag{9.11}$$

But this combination of colour and anticolour is also colour-neutral:

$$\text{blue} + \text{anti-blue} = \text{neutral}. \tag{9.12}$$

Equating the two neutral states, we can therefore conclude that

$$\text{red} + \text{green} = \text{anti-blue}. \tag{9.13}$$

Interestingly, this works analogously to the additive colours of light of adding red and green light to make yellow, and the 'opposite of yellow' is indeed blue (figure 57).

While these colours are not how hadrons literally look, this certainly serves as a useful memory aid. Finally, colour is related to the **confinement hypothesis**:

> Confinement hypothesis: coloured objects cannot exist in isolation.

This provides an initial phenomenological rule for why free quarks are not observed in nature and instead confined within colourless hadrons. Given this, how we can ever hope to experimentally test the existence of quarks?

The idea that quarks are elementary particles initially proved controversial as nothing more than mere mathematical constructs. Explaining the particle zoo via symmetry arguments was theoretically appealing but the existence of quarks was unclear. This mirrors how the reality of atoms remained inconclusive throughout the nineteenth century, yet was a helpful construct to explain the observed law of multiple proportions. Fractional electric charges certainly sounded outlandish. Quark scepticism endured for many years, yielding eloquent quotations[51] by Murray Gell-Mann (c. 1966):

> "The idea that mesons and baryons are made primarily of quarks and gluons is hard to believe."

and James Bjorken (c. 1967):

> "Additional data are necessary and very welcome to destroy the picture of elementary constituents."

As we shall now see, a landmark series of experiments firmly establish the existence and properties of quarks and colour.

[51] https://indico.cern.ch/event/147420/contributions/1384964

10 Revealing nuclear substructure

This section explores the empirical evidence addressing these questions:

- How do we know protons and neutrons are not point-like?
- How do we measure the size and shape of protons and nuclei?
- How do we show there are point-like substructure inside protons?
- How do we acquire evidence for the existence of quarks?
- How do we know quarks are spin-half fermions and have fractional charge?

Gathering evidence for these questions required ambitious high-energy scattering experiments. Figure 58 shows schematically the process of probing the proton and its structure from low to higher energies. This parallels the process of the Manchester experiments discovering the atomic nucleus.

Fortuitously in 1961, US Congress approved construction of a two-mile long accelerator at Stanford Linear Accelerator Center, California devised in the prior decade. The landmark experiments spearheaded by Jerome Friedman, Henry Kendall, and Richard Taylor began in 1966. Increasing energies of accelerators enabled measuring the finite size and eventually substructure of the proton precisely, firmly establish the existence and dynamics of quarks.

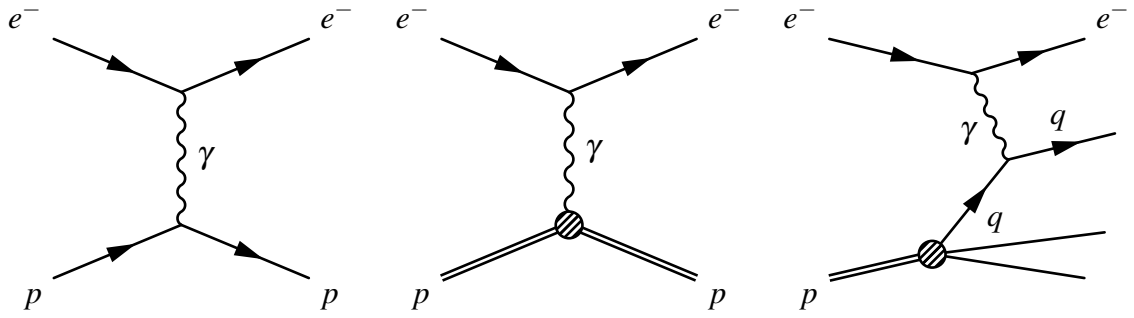

(a) **Low energy**
$\lambda_e \gg r_p$: point-like proton

(b) **Medium energy**
$\lambda_e \sim r_p$: finite-sized proton

(c) **High energy**
$\lambda_e \ll r_p$: quarks in proton

Figure 58: **Electron–proton scattering at increasingly high energies**. At low energies, the electron wavelength λ_e is sufficiently large to interact with the proton as a point-like particle. At a critical wavelength $\lambda_e \sim r_p$ where the electron wavelength and proton size is comparable, the finite size effects become detectable. At higher energies with electron wavelength much smaller than the proton size $\lambda_e \ll r_p$, the electrons scatter off the internal substructure, namely quarks.

This eventually led to the discovery of the charmonium as bound states of charm quarks. These experiments form the precursor to quantum chromodynamics.

10.1 Nuclear form factors

The central idea of nuclear scattering parallels Geiger–Marsden–Rutherford scattering five decades earlier revealing the existence of the proton as atom substructure. We bombard a target with sufficiently high energy particles i.e. with de Broglie wavelengths reach the order of magnitude of the target's size. This allows us to resolve any substructure in the target characterised by a **form factor**.

Rutherford scattering probed atoms to reveal the nucleus and later deep inelastic scattering probed nuclei to reveal quark substructure.

Scattering as Fourier transform We can define the spatial distribution of the nuclear charge density $\rho(\mathbf{r})$ to be[52]

$$\int \rho(\mathbf{r})\,\mathrm{d}^3\mathbf{r} = Ze. \tag{10.1}$$

The potential energy for a particle of charge ze with coordinate $\mathbf{r}$ incident on the target nucleus of charge Z is then ($\hbar = c = \varepsilon_0 = 1$)

$$V(\mathbf{r}) = \frac{ze}{4\pi}\int \frac{\rho(\mathbf{r}')}{|\mathbf{r}-\mathbf{r}'|}\mathrm{d}^3\mathbf{r}'. \tag{10.2}$$

where $\mathbf{r}'$ is the coordinate from the origin to a charge element of the nucleus. Applying the Born approximation (weak potential i.e. nucleus does not recoil), the scattering amplitude $\langle\mathbf{k}'|V|\mathbf{k}\rangle$ is the Fourier transform of this potential (equation (4.23))

$$\langle\mathbf{k}'|V|\mathbf{k}\rangle = \frac{1}{(2\pi)^3}\int \mathrm{d}^3\mathbf{r}\,\mathrm{e}^{\mathrm{i}\mathbf{q}\cdot\mathbf{r}}\left[\frac{ze}{4\pi}\int\frac{\rho(\mathbf{r}')}{|\mathbf{r}-\mathbf{r}'|}\mathrm{d}^3\mathbf{r}'\right]. \tag{10.3}$$

Substituting $\mathbf{R} = \mathbf{r} - \mathbf{r}'$, holding $\mathbf{r}'$ fixed so that $\mathrm{d}^3\mathbf{R} = \mathrm{d}^3\mathbf{r}$, we obtain

$$\langle\mathbf{k}'|V|\mathbf{k}\rangle = \underbrace{\frac{Zze^2}{4\pi}\frac{1}{(2\pi)^3}\int\frac{\mathrm{e}^{\mathrm{i}\mathbf{q}\cdot\mathbf{R}}}{|\mathbf{R}|}\mathrm{d}^3\mathbf{R}}_{\text{Point-like}}\underbrace{\left[\frac{1}{Ze}\int\mathrm{d}^3\mathbf{r}'\,\rho(\mathbf{r}')\mathrm{e}^{\mathrm{i}\mathbf{q}\cdot\mathbf{r}'}\right]}_{\text{Form factor } F(\mathbf{q})}. \tag{10.4}$$

We define the **nuclear form factor**

$$\boxed{F(\mathbf{q}) \equiv \frac{1}{Ze}\int\rho(\mathbf{r}')\,\mathrm{e}^{\mathrm{i}\mathbf{q}\cdot\mathbf{r}'}\mathrm{d}^3\mathbf{r}'} \tag{10.5}$$

[52] Some texts describe the nuclear charge distribution as given by $Ze\rho(\mathbf{r})$ such that $\int\rho(\mathbf{r})\mathrm{d}^3\mathbf{r} = 1$. Our definition has the factor of Ze effectively absorbed into $\rho(\mathbf{r})$.

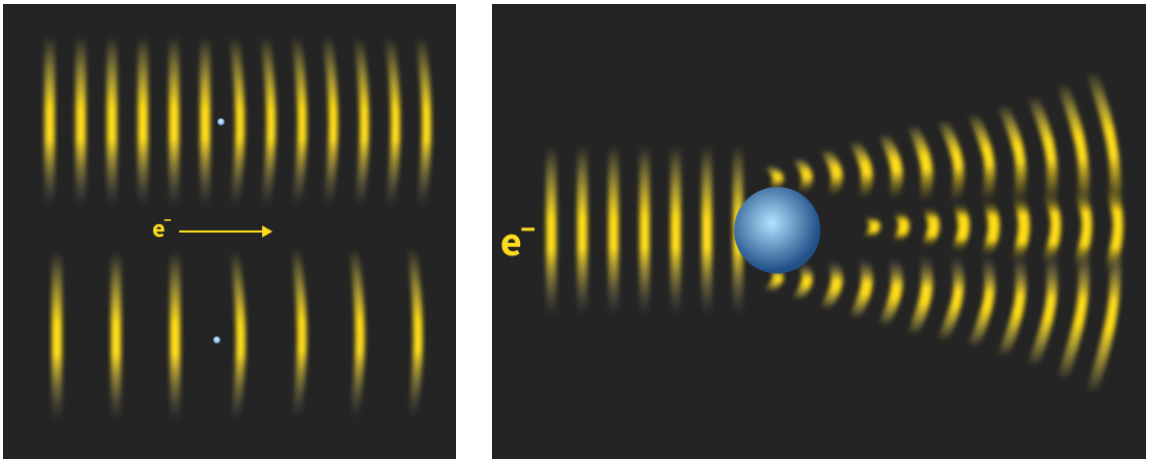

(a) Point-like target (b) Finite-size target

Figure 59: **My impressionistic cartoon of electron waves scattering off targets**. This is displayed in real space, showing the electron as yellow plane waves and target as a blue sphere. When the target is a point-like object (e.g. quarks or insufficient energy to resolve proton size), the electron waves respond identically for high (upper) and low (lower) frequencies as there is no intrinsic scale. When the electron wavelengths are comparable to the proton size, a non-trivial scattering pattern appears, which is the Fourier transform of the target spatial distribution.

Crucially, the measurable differential cross-section is

$$\frac{\mathrm{d}\sigma}{\mathrm{d}\Omega} = |F(\mathbf{q})|^2 \left(\frac{\mathrm{d}\sigma}{\mathrm{d}\Omega}\right)_{\text{Point-like}} . \tag{10.6}$$

The form factor is a simple multiplicative modification of the point-like differential cross-section when measuring in momentum transfer space $\mathbf{q}$. In scattering experiments, we can therefore measure the form factor $F(\mathbf{q})$ and inverse Fourier transform to obtain the spatial charge distribution of the target. Fourier transforming a charge distribution is of course not confined to nuclear scattering physics, but indeed all of quantum scattering with matter waves. This also applies to X-ray crystallography and neutron scattering to decipher the spatial structure of wide-ranging materials from crystals lattices to DNA.

To illustrate these concepts, figure 58 shows the physical picture of probing the nucleus with increasingly high energy electron waves. This shows the historical progress in understanding protons from point-like particle, to determination of its finite size, and finally proton substructure that laid the foundations for quarks. If electron with energies $< 1\,\mathrm{GeV}$ collide with nucleons, the interactions are dominated by elastic scattering. As we increase this en-

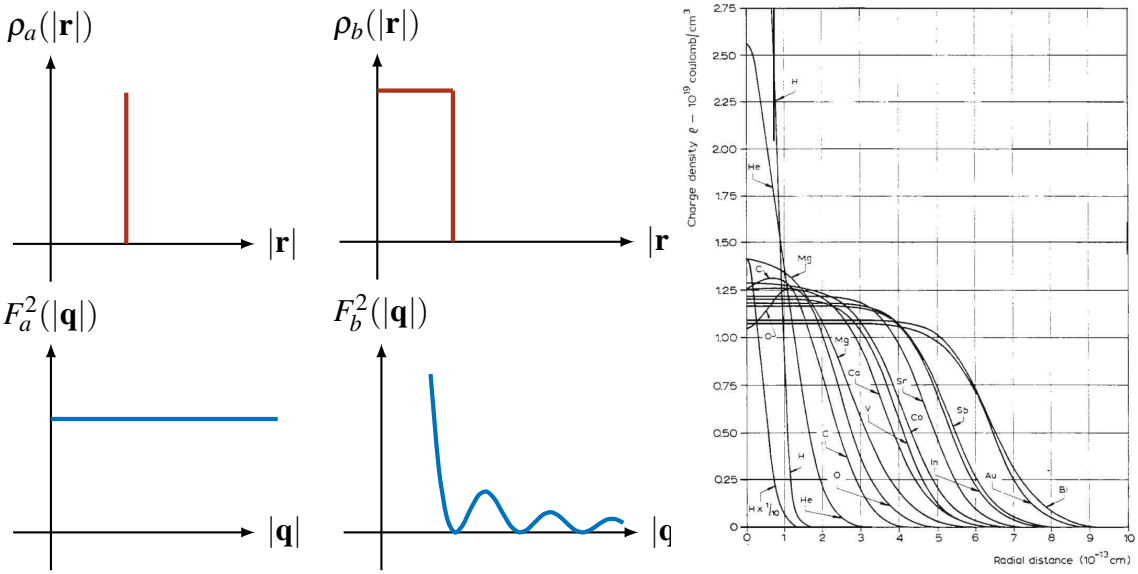

(a) Point-like $\rho(r)$ (b) Hard sphere $\rho(r)$ (c) Nuclear charge densities

Figure 60: **Charge spatial distributions and their Fourier transform**. Distributions $\rho(|\mathbf{r}|)$ (upper) and the corresponding form factor $F(|\mathbf{q}|)$ corresponding to their Fourier transform (lower). Displayed examples are the point-like and hard sphere models of the nucleus. The plot summarises various nuclear charge densities determined in the 1950s from electron scattering experiments; figure from Hofstadter Nobel lecture (1961), Ref. [64].

ergy > 1 GeV, the elastic scattering cross-section decreases dramatically. Elastic scattering of electron-proton interactions models the proton as a point-like particle that stays intact

$$e^- + p \to e^- + p. \tag{10.7}$$

At higher energies, it became clear the proton had a finite size due to its measured form factor.

Point-like proton: Mott scattering

At low energies where the probe electron wavelength was much larger than the proton size $\lambda_e \ll \lambda_p$, the electron effectively interacts with the proton as a point-like particle. As there is no physical scale to the target, the electron has the same scattering behaviour for all incident energies. This effective scale invariance of the scattering is sketched in figure 59a, where outgoing waves are the same in both energies. Mathematically, this is reflected in the Fourier transform shown in figure 60a.

We can model the nucleus as a point charge at the origin using a delta function

$$\rho_1(\mathbf{r}') = Ze\delta^{(3)}(\mathbf{r}') \tag{10.8}$$

Applying (10.5), the form factor is the Fourier transform of a delta function at the origin which evaluates to unity

$$F_1(|\mathbf{q}|) \equiv \frac{1}{Ze}\int Ze\delta^{(3)}(\mathbf{r}')\, \mathrm{e}^{\mathrm{i}\mathbf{q}\cdot\mathbf{r}'}\mathrm{d}^3\mathbf{r}' = 1 \tag{10.9}$$

A point-like charge distribution is modelled as a delta function $\rho(\mathbf{r}) = Qe\delta(\mathbf{r})$, so the form factor $F(\mathbf{q})$ is constant versus the probe momentum transfer $|\mathbf{q}|^2$. This is equivalent to Rutherford scattering ${}^4_2\alpha\, p \to {}^4_2\,\alpha p$.

Relativistic electrons with initial energy E_i scattering off a proton with negligible recoil $m_e \ll E_i \ll m_p$ is known as **Mott scattering** $e^- p \to e^- p$. The cross-section is given by (see Thomson chapter 7)

$$\left(\frac{\mathrm{d}\sigma}{\mathrm{d}\Omega}\right)_{\text{Mott}} = \left[\left(\frac{e^2}{4\pi}\right)^2 \frac{1}{4E_i^2\sin^4(\theta/2)}\right]\cos^2\frac{\theta}{2}. \tag{10.10}$$

The part in square brackets has the familiar form of the Rutherford scattering cross-section.

Finite-size proton As the electron energy increases to become comparable to the proton size $\lambda_e \sim r_p$, the finite size. This is the next-to-minimal model, where we can model the nucleus as a hard sphere of radius a with a spherically symmetric uniform charge density of ρ_0:

$$\rho_2(r') = \begin{cases} \rho_0 & r' \le a \\ 0 & r' > a \end{cases} \tag{10.11}$$

Evaluating the angular dependence, the form factor for a generally spherically symmetric charge distribution $\rho(\mathbf{r}') = \rho(r')$ is

$$F_2(|\mathbf{q}|) = \frac{4\pi}{Ze|\mathbf{q}|}\int_0^\infty r'\rho(r')\sin\left(r'|\mathbf{q}|\right)\mathrm{d}r' \tag{10.12}$$

Using (10.11), we obtain

$$F(|\mathbf{q}|) = \frac{3}{\beta^3}[\sin(\beta) - \beta\cos(\beta)], \quad \text{where} \quad \beta \equiv a|\mathbf{q}|. \tag{10.13}$$

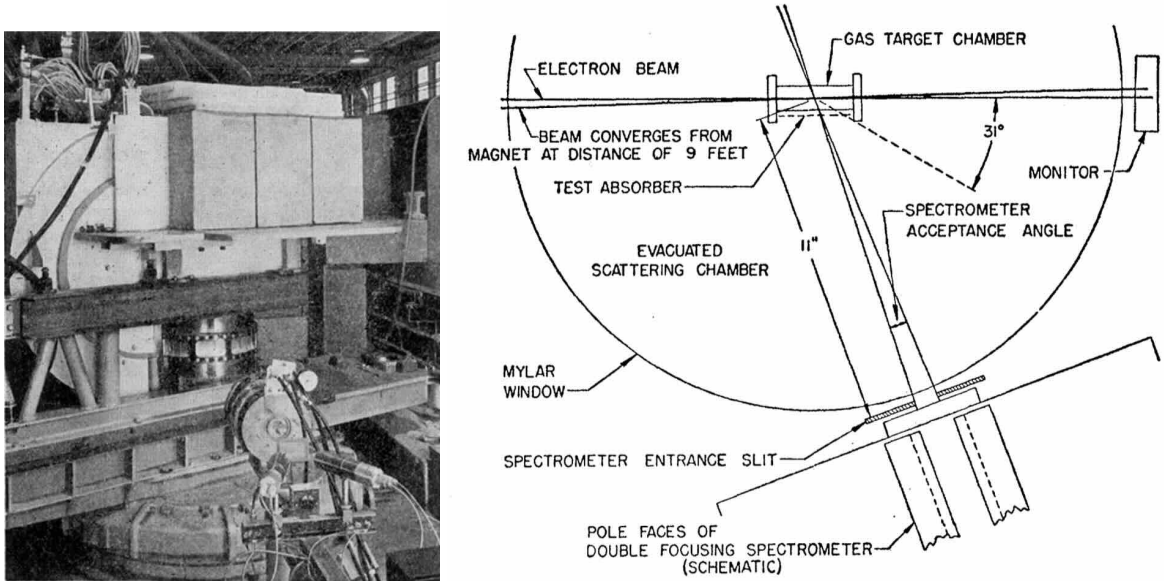

(a) Spectrometer photo

(b) Target chamber schematic [65]

Figure 61: **Apparatus of 190 MeV Stanford electron scattering experiment in 1954**. In the photo, the spectrometer is the larger semi-circular device on the left of the photo with the rectangular blocks to its right comprising the lead/paraffin shielding, with the thin target windows surrounding the scattering chamber just below these. Figures from Ref. [64].

This form factor is sketched heuristically in figure 59b and the exact Fourier transform is plotted in figure 60b. The physical picture is that the finite-size sphere induces an modulated scattering pattern, set by a concrete scale a, namely the size of the sphere. This looks uncannily similar to what we learn in wave optics diffraction pattern through a single slit $\propto \sin(ka)/(ka)$. Of course, this is not completely unexpected given light and matter are both waves.

Stanford electron scattering experiments

In 1954 at Stanford, Robert Hofstadter and Robert McAllister speared landmark experiments using electron beams up to 190 MeV scatter off nuclei (figure 62). Hofstadter notes in his Nobel lecture[53] how Eva Wiener designed the high-pressure, thin-wall gas chambers crucial for housing hydrogen targets but did not live to see the remarkable scientific results of her apparatus.

[53] https://www.nobelprize.org/uploads/2018/06/hofstadter-lecture.pdf

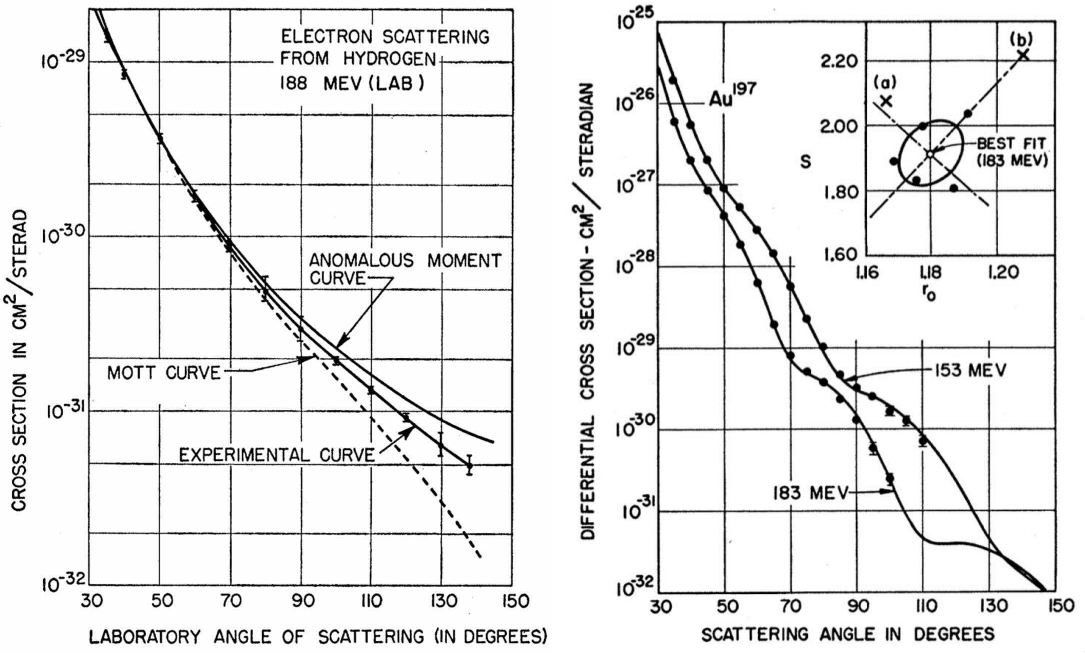

(a) Electron–proton scattering [66] (b) Electron–gold scattering [65]

Figure 62: **Results of electron scattering off proton and gold**. Electron–proton and electron–nucleus scattering experiments performed at Stanford in 1955–56. .

The electron scattering results revealed that the proton has finite size rather than being point-like with a magnetic moment as electrons do (figure 62a). Fits to the data determined to proton to have an exponential charge distribution $\sim \exp\left(-r^2/R^2\right)$ with a root-mean-square radius of around 0.8×10^{-15} m [66].

Using the nuclear form factors calculated by theorists Donald Yennie and colleagues [67], this enabled detailed characterisation of nuclei. Figure 62b shows one of these scattering patterns, with the characteristic $\sim \sin(x)/(x)$ modulation of a quasi-hard sphere. These series of landmark experiments are lucidly reviewed in Ref. [64].

Following these experiments were precise determination of nuclear form factors up to 900 MeV electron energies up to what was called "Mark III". However, pushing beyond 1 GeV required far greater resources. Meeting with Wolfgang Panosfky in 1956, Hofstadter lobbied for an order of magnitude increase in electron energies to be built at Stanford, a proposal known affectionately as "Project M" for Monster[54]. A detailed proposal was drawn up in 1957 for a two-mile accelerator, what was to become the Stanford Linear Accelerator

[54] https://www.slac.stanford.edu/vault/pubvault/ST14no3_Panofsky.pdf

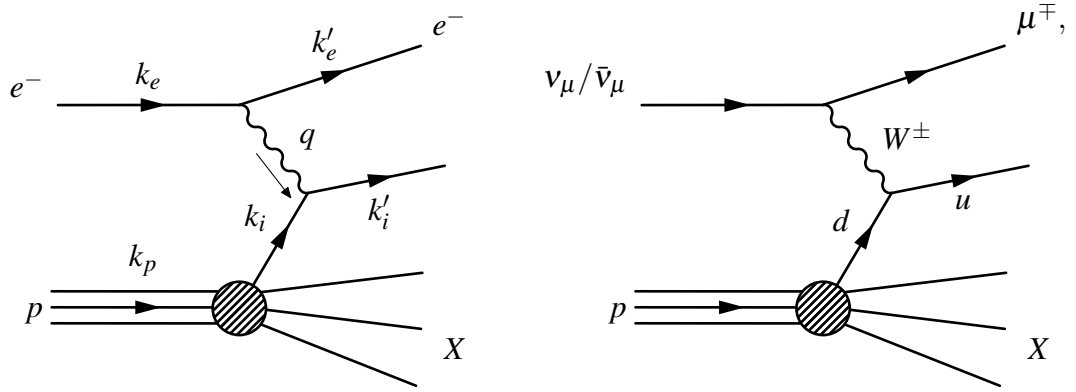

(a) Electron–quark with momentum labels

(b) Neutrino deep inelastic scattering

Figure 63: **Deep inelastic scattering (DIS) diagrams**. An electron e^- strikes the proton p, with the following momentum labels. We measure the outgoing k'_e relative to initial k_e electron with $q = k_e - k'_e$ momentum transferred to the probe photon. The photon scatters off internal substructure (a quark) inside the proton (labelled i), which has initial k_i and outgoing k'_i momentum. The initial proton momentum is k_p, while the remnants of the proton breakup is denoted X. On the right, the analogous diagram with neutrino DIS via a charged current interaction mediated by a $W^\pm$ boson.

Center. Congress approved funding in 1961 and construction started in 1962. This set the stage for deep inelastic scattering to look inside the proton.

10.2 Deep inelastic scattering

Ramping up the incident electron energies to well over a GeV enables it to scatter off much smaller scales than the size of the proton. This contrasts with elastic scattering where the outgoing proton stays intact $e^- p \to e^- p$. Deep inelastic scattering instead probes inside the proton and results in the outgoing proton breaking up into a hadron system X:

$$e^- + p \to e^- + (p \to X). \tag{10.14}$$

Deep inelastic scattering (figure 63) provides direct evidence for substructure, namely quarks in nucleons. The electron interacts with the internal substructure, namely a quark, via a photon mediating the electromagnetic interaction.

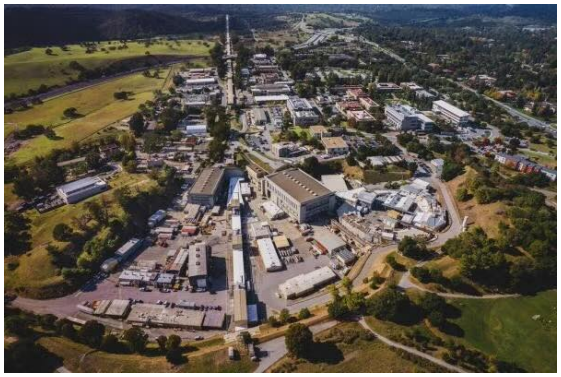

(a) SLAC aerial view

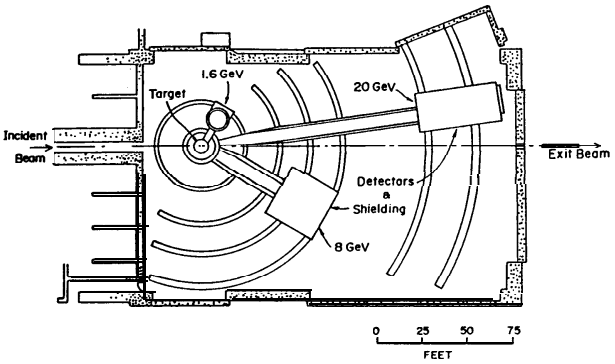

(b) End station A plan view

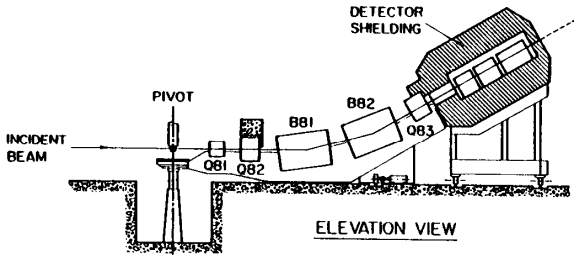

(c) 8 Gev arm elevation view

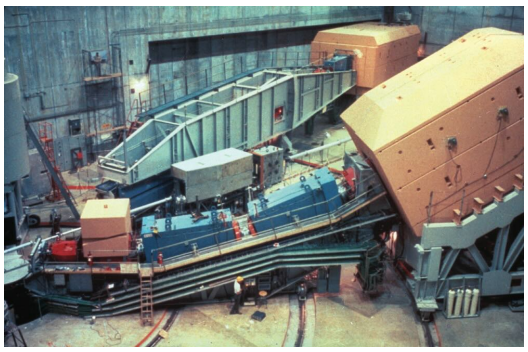

(d) Photo of 8 GeV spectrometer

Figure 64: **Apparatus of MIT–SLAC deep inelastic scattering experiments**. Electrons are accelerated by a two-mile long beam line up to 20 GeV. This strikes a hydrogen target and magnetic spectrometers measure the scattered electron energy loss relative to the incident energy $\nu = E - E'$. These can be rotated to measure the scattered electron at various angles relative to the beamline $\theta_{ee'}$. Figures from SLAC National Accelerator Laboratory, 1990 Kendall Nobel prize lecture and R. Muffley/SLAC/APS.

For the kinematics of figure 63, we use k to denote the four-momenta (to save confusion with p for proton)

$$k_e = \begin{pmatrix} E_e \\ \mathbf{k}_e \end{pmatrix}, \quad k'_e = \begin{pmatrix} E'_e \\ \mathbf{k}'_e \end{pmatrix}, \quad k_p = \begin{pmatrix} M_p \\ \mathbf{0} \end{pmatrix}. \tag{10.15}$$

We define the momentum transferred q to the photon in terms of initial and outgoing electron

$$q = k_e - k'_e = \begin{pmatrix} E_e - E'_e \\ \mathbf{q} \end{pmatrix}. \tag{10.16}$$

Conserving momentum at the photon–internal-structure vertex $k_i' = k_i + q$ then squaring gives

$$(k_i')^2 = q^2 + k_i^2 + 2k_i \cdot q. \tag{10.17}$$

Neglecting the mass of the internal substructure $k_i^2 = k_i'^2 \approx 0$ gives

$$2k_i \cdot q = -q^2. \tag{10.18}$$

The internal substructure carries a fraction x of the proton momentum $k_i = xk_p$ and working in the proton rest frame gives:

$$x = \frac{-q^2}{k_p \cdot q} = \frac{-q^2}{2(E_e - E_e')M_p}. \tag{10.19}$$

Following notation of most textbooks and historical papers[55], we define $Q^2 = -q^2$ and $\nu = E_e - E_e'$ to yield the Bjorken-x formula:

$$x = \frac{Q^2}{2\nu M_p}. \tag{10.20}$$

Another useful observable is the inelasticity y, which corresponds to the fractional energy lost by the electron

$$y = 1 - \frac{E_e'}{E_e} = \frac{\nu}{E_e}. \tag{10.21}$$

This arises from the Lorentz invariant quantity $y = (k_p \cdot q)/(k_p \cdot k_e)$ evaluated in the proton rest frame.

Conserving momentum at the electron–photon vertex $q = k_e - k_e'$ and squaring, we find

$$\begin{aligned} q^2 &= (k_e - k_e')^2 && (10.22)\\ &= k_e^2 + k_e'^2 - 2k_e \cdot k_e' && (10.23)\\ &= 2m_e^2 - 2(E_e E_e' - \mathbf{k}_e \cdot \mathbf{k}_e') && (10.24) \end{aligned}$$

In the ultra-relativistic limit $m_e \to 0$, this simplifies down to

$$Q^2 = -q^2 = 2E_e E_e'(1 - \cos\theta_{ee'}). \tag{10.25}$$

[55] The literature can cause nightmares by flip-flopping between uppercase and lowercase q, Q to denote momentum transfer $q^2 = \pm(k - k')^2$, quark charge $q = \frac{1}{3}e, \frac{2}{3}e, \ldots$, and quark flavour $q = u, d, s \ldots$. Sometimes p, P interchanges between proton and momentum, rendering proton momentum P_p. My past futile attempts for disambiguation denoted four-vectors by sans-serif Q or electric charge by calligraphic $\mathscr{Q}$ script, but these are difficult to distinguish in handwriting. Like linguistic ambiguity, e.g. *lead* can denote directing a team or the chemical element with 82 protons, context usually brings clarity. Apologies to notational purists.

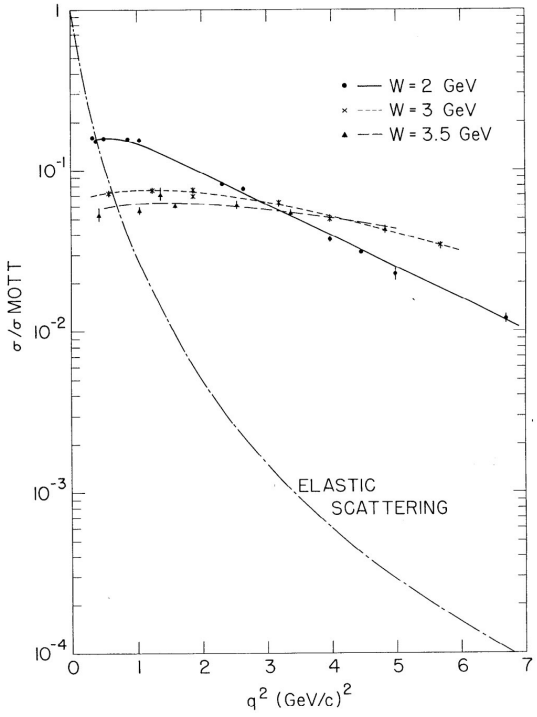

(a) Cross-sections vs q^2

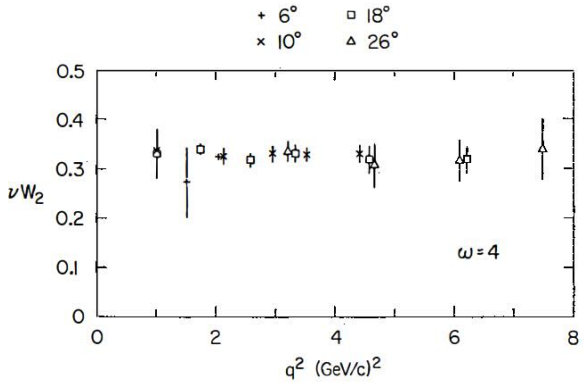

(b) Scaling vs q^2

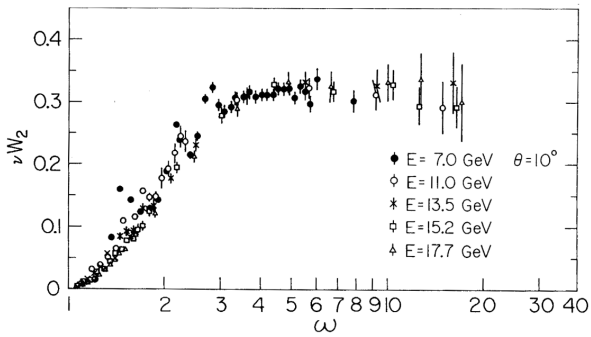

(c) Scaling vs $\omega = 1/x$

Figure 65: **Deep inelastic scattering data**. This supports the hypothesis of electron scattering off point-like internal substructure of the proton. Note how the product of the proton structure function (historical notation W_2) with $\nu = E_e - E'_e$ is nearly independent of q^2 for $x = 1/\omega = 1/4$, exhibiting scale invariance. Figures from Refs. [68, 69].

Finally, the invariant mass W of the system of hadrons comprising the fragmented proton X is inferred by momentum conservation

$$W_X = (k_p + q)^2. \tag{10.26}$$

Given we know the incoming electron beam energy E_e, we only need to measure two observables to determine Q^2 and ν: the outgoing scattered electron energy E'_e and scattered angle relative to the incident $\theta_{ee'} = \theta'_e - \theta_e$.

The MIT and SLAC groups performed such landmark experiments in the late 1960s, accelerating electrons between 5 and 20 GeV onto a liquid hydrogen target. The historical experimental apparatus for this is shown in figure 64.

In the deep inelastic regime where $Q^2 \gg m_p^2 y^2$, the Lorentz invariant differential cross-

section for a single photon exchange in terms of Q, x, y is given by (see Thomson Chapter 8):

$$\frac{\mathrm{d}^2\sigma}{\mathrm{d}Q\,\mathrm{d}x} = \frac{4\pi\alpha^2 s}{Q^4}\left[y^2 F_1(x,Q^2) + \frac{(1-y)}{x}F_2(x,Q^2)\right]. \tag{10.27}$$

The objects $F_1(x,Q^2), F_2(x,Q^2)$ are called structure functions. In the elastic case, F_1 corresponds to the purely magnetic interaction while F_2 has electric and magnetic contributions. To experimentally determine this, we measure the event rates as a function of the observables Q, x, y. We can first count events holding x fixed and scanning y by varying the incident electron energy E_e. We then use these measurements of how $\mathrm{d}^2\sigma/(\mathrm{d}Q\,\mathrm{d}x)$ varies with y to disentangle the relative sizes of the two structure functions. In modern statistical analysis, this corresponds to a simultaneous differential fit of the Q, x, y variables to extract F_1, F_2.

Figure 65 shows the initial data [68]. The suppression of the elastic cross-section at high Q^2 is not observed. This suppression arises from the so-called Rosenbluth formula, which extends the Mott cross-section to include the electric G_E and magnetic G_M dipoles of the proton (see Thomson chapter 7)

$$\frac{\mathrm{d}\sigma}{\mathrm{d}\Omega} = \left[\frac{G_E^2 + cG_M^2}{1+c} + 2cG_M^2\tan^2\frac{\theta}{2}\right]\frac{E_e'}{E_e}\left(\frac{\mathrm{d}\sigma}{\mathrm{d}\Omega}\right)_{\text{Mott}}, \tag{10.28}$$

where $c = Q^2/4m_p^2$. The magnetic dipole has the empirically determined form $G_M^2 \propto (1 + Q^2/0.71\ \text{GeV}^2)^{-2}$ and dominates in the high Q^2 limit, giving a fast suppression to the elastic cross-section

$$\left(\frac{\mathrm{d}\sigma}{\mathrm{d}\Omega}\right)_{\text{elastic}} \propto \frac{1}{Q^6}\left(\frac{\mathrm{d}\sigma}{\mathrm{d}\Omega}\right)_{\text{Mott}}. \tag{10.29}$$

Instead the much broader spectrum is observed showing inelastic scattering. The inelastic cross-section for production of hadrons remains relatively constant and begins to dominate at high energies.

For low x (high $\omega = 1/x$) values, there is the same characteristic **scale invariance** for different beam energies. This is sometimes called Bjorken scaling. The physical interpretation of this observed arises from the electrons probing targets that lack any size or scale, i.e. there are point-like objects inside the proton.

The electron de Broglie wavelength becomes small enough to scatter incoherently off the any point-like entities within the nucleon. Historically these were called **partons** when quark theory remained controversial. By measuring the kinematic properties of the scattered electron, we can deduce properties regarding the nucleon substructure. We observe the scattered quarks as hadrons, mainly mesons, due to confinement.

10.3 Evidence for quark properties

We now discuss the empirical evidence for quark properties easily taken for granted and even trivialised as "historical". The conundrum is that quarks are confined inside protons and neutrons by colour confinement. These objects that seem to be unobservable, by construction. So how is it possible to empirically study their properties such as spin, charge, and flavour composition? This is where ingenuous phenomenological arguments and experimental data are needed.

Evidence for spin-half. Electrons scattering off a distinct spin-half point-like charged particle such as a muon is given by (section 9 of Ref. [1])

$$\frac{\mathrm{d}^2\sigma}{\mathrm{d}Q\,\mathrm{d}x} = \frac{2\pi\alpha^2 s}{Q^4}\left[1+(1-y)^2\right]. \tag{10.30}$$

To consider electron–quark scattering inside a nucleon, we consider the fact quarks have fractional charge labelled q_i for flavour i, so we replace $\alpha \to \alpha\sum_i q_i^2$ and they carry x_i momentum fraction so we replace $s \to x f_i(x) s$, where $f_i(x)$ is the probability distribution of quark i. The resulting differential cross-section is then

$$\frac{\mathrm{d}^2\sigma}{\mathrm{d}Q\,\mathrm{d}x} = \frac{4\pi\alpha^2 s}{Q^4}\sum_i q_i^2 x f_i(x)\left[(1-y)+\frac{1}{2}y^2\right]. \tag{10.31}$$

By assuming electrons scatter off effectively free spin-half point-like fermions with fraction charge, this fixes the coefficients prefixing $(1-y)$ and y^2. Equating these coefficients with the phenomenological differential equation (10.27) that link to observables gives

$$2xF_1(x) = F_2(x). \tag{10.32}$$

This central result is the **Callan–Gross relation** by Curtis Callan and David Gross in 1969 [70]. Scattering off a spin-0 particle would result in $F_1(x) = 0$. Historically, the SLAC experiments measured this quantity to test the different spin predictions of the quark–parton model:

$$\frac{2xF_1(x)}{F_2(x)} = \begin{cases} 0 & \text{spin-0 quarks,} \\ 1 & \text{spin-1/2 quarks.} \end{cases} \tag{10.33}$$

Figure 66 displays the experimental data from SLAC, providing evidence for the spin-1/2 nature of quarks and disfavouring spin-0.

The quark–parton model also constrains

$$F_2(x,Q^2) = \sum_i q_i^2 x f_i(x). \tag{10.34}$$

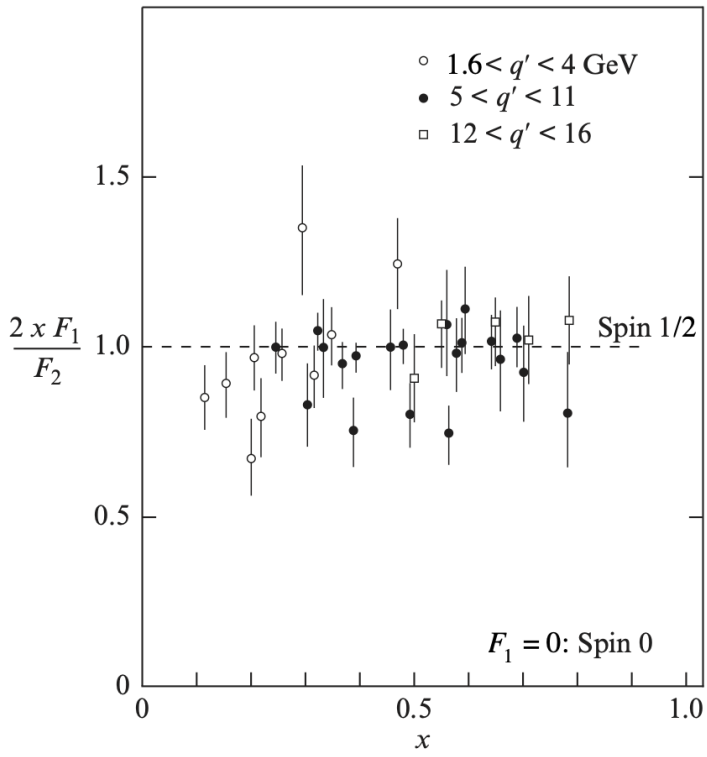

Figure 66: Data testing the Callan–Gross relation (10.33), favouring quarks being spin-1/2 rather than spin-0 particles. Adapted from Ref. [1].

This extends the Bjorken-x scaling to show that F_2 only depends on x and not Q^2.

Evidence for fractional charge: In 1972, the muon-neutrino beam created by the Proton Synchrotron at CERN is directed at the Gargemelle bubble chamber (figure 67).

Figure 63b shows the neutrino–quark scattering via a $W^{\pm}$ boson, a charged-current interaction before the discovery of the $W^{\pm}$. We can measure this process and compare this against the SLAC data for electron–quark scattering. Neglecting strange quarks, the key results are comparing electron–nucleon scattering with neutrino–nucleon:

$$\frac{\frac{1}{2}\int \mathrm{d}x\,\left[F_2^{ep}(x)+F_2^{en}(x)\right]}{\frac{1}{2}\int \mathrm{d}x\,\left[F_2^{\nu p}(x)+F_2^{\nu n}(x)\right]} = \frac{Q_u^2+Q_d^2}{2} = \frac{5}{18} = \frac{1}{3.6}. \tag{10.35}$$

Figure 68 shows the data supporting this, which firmly establish the fractional charge of quarks [71].

Evidence for 3 valence quarks: The Gross–Llewellyn-Smith (GLS) sum rule provides

Figure 67: Gargamelle detector now on display at the CERN park for visitors. Image: CERN

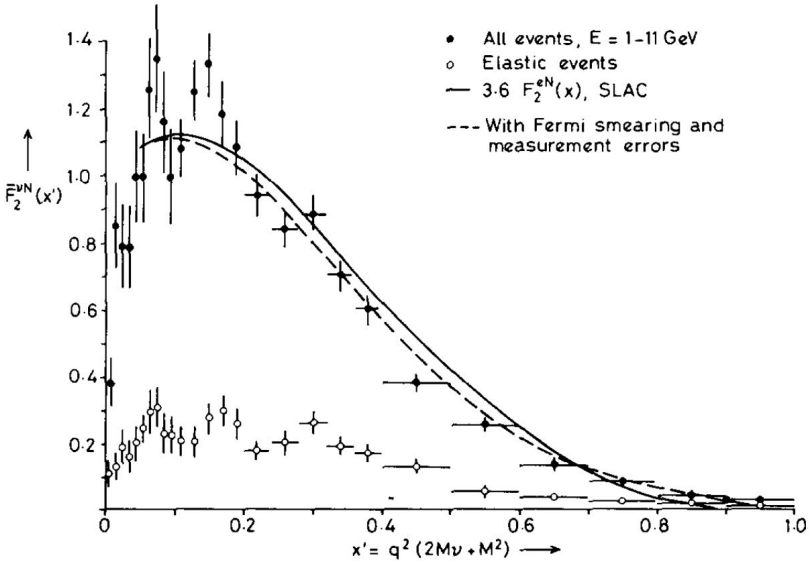

Figure 68: Combined SLAC–Gargamelle data [71] supporting the fractional charges of quarks. The black points are the neutrino-quark data, compared to the lines based on the electron-quark data scaled by $2/(Q_u^2 + Q_d^2) = 18/5 = 3.6$.

evidence for the number of valence quarks in a proton and neutron:

$$\int F_3^{\nu n}(x) = \int [u_v(x) + d_v(x)]\mathrm{d}x = N_q^{\text{valence}} - N_{\bar{q}}^{\text{valence}} = 3.2 \pm 0.6. \tag{10.36}$$

The actual value is closer to 2.5, with the remainder arising from the gluons.

Evidence for gluon: Finally, the total momentum carried by the quark content of a nucleon N and should equal unity:

$$S_q^{\text{theory}} = \int_0^1 \mathrm{d}x F_2^{\nu N}(x) = \int_0^1 \mathrm{d}x x \left[u(x) + \bar{u}(x) + d(x) + \bar{d}(x) + s(x) + \bar{s}(x)\right] = 1. \quad (10.37)$$

However, Gargemelle measures this to be half the expected value to be

$$S_q^{\text{experiment}} = \int_0^1 \mathrm{d}x F_2^{\nu N}(x) = 0.49 \pm 0.07. \quad (10.38)$$

This implies that half the momentum of the proton is carried by its constituents do not couple to the electroweak interactions. What else is inhabiting the proton? This is of course the first indication for the existence of particles that only interact via the strong force: the gluon.

10.4 Charmonium

Before turning to the gluon, which completes the picture for quantum chromodynamics, we recount a key discovery that coincided with the acceptance of the quark–parton model. This is the charmonium, comprising a bound state of charm and anti-charm quarks. Advances in accelerator technology in the late 1960s and 70s were needed to discover heavier quarks.

The J/ψ state was discovered in 1974 at Brookhaven National Laboratory [72] observed this in e^+e^- pairs (figure 69a). Simultaneously, the SPEAR experiment at SLAC Linear Accelerator Center [73] observed the same peak of events in $e^+e^- \to$ hadrons as well as charged pairs of $e^+e^-, \mu^+\mu^-, \pi^+\pi^-, K^+K^-$ channels.

There's no need for careful statistical analysis to see a great peak at a di-electron mass m_{ee} of around 3.1 GeV in figure 69. This triggered what was known as the November 1974 revolution with the discovery of the charm quark. Soon after, excited states such as the Ψ' were discovered at slightly higher energies.

After spin quantum numbers were measured, we could classify the states analogously to atomic spectroscopy. We can illustrate the energy level diagram for bound states of the charmonium $c\bar{c}$ for the lowest angular momentum states (figure 70).

- The $J/\Psi(3097)$ particle, where the number in the bracket denotes the rest mass $M(c\bar{c})$ in MeV/c^2 is not the lightest $c\bar{c}$ state.
- The lightest state is actually the $\eta_c(2980)$ with $n = 1$ and spin-parity $J^P = 0^-$).
- Instead $J/\Psi(3097)$ is the lightest $n = 1$ with spin-parity of $J^P = 1^-$, exactly that of the photon allowing conservation of angular momentum in the electromagnetic interaction.
- The first excited $n = 2$ bound state of $c\bar{c}$ with spin-parity $J^P = 1^-$, is the $\Psi'(3686)$.

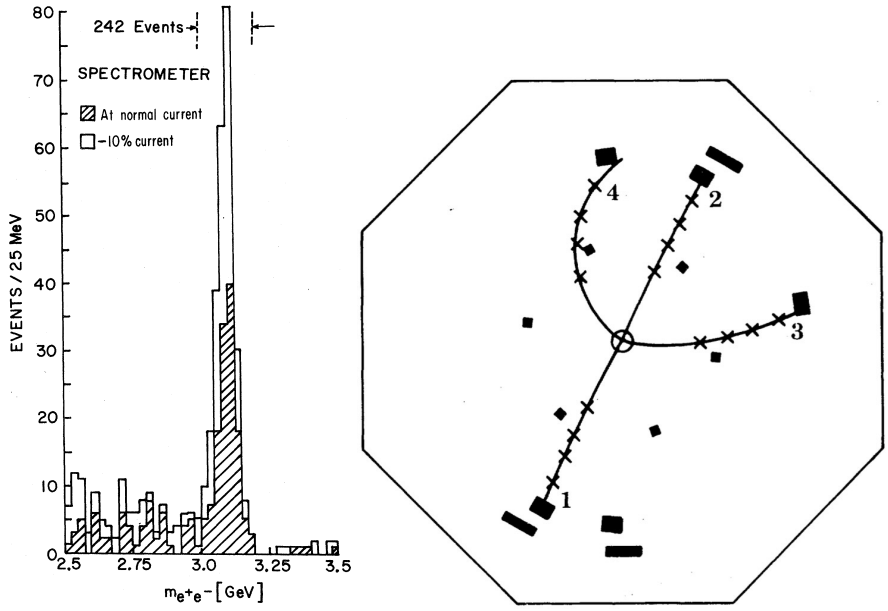

(a) BNL J/ψ [72] (b) $\psi' \to \psi\mu^+\mu^-$ [74]

Figure 69: Discovery of J/ψ and ψ' particles.

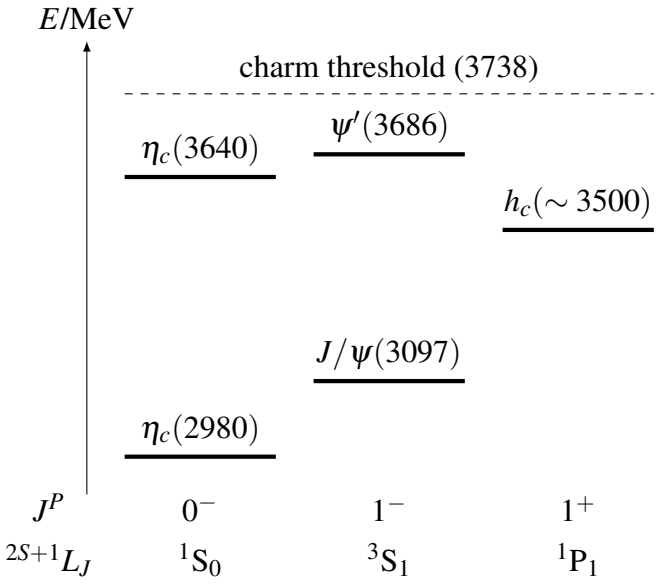

Figure 70: Bound states of charmonium system.

We use the spin-parity J^P notation as well as the spectroscopic notation $^{2S+1}L_J$ alluding to atomic spectra. More energetic states can radiatively decay into lower states via the electromagnetic interaction such as

$$J/\psi(3097) \to \eta_c(2980) + \gamma. \tag{10.39}$$

We discuss the charm threshold below, but we chiefly can understand it as the minimum energy for rapid decays to charmed states.

Bound states of charmonium

We can model the strong interaction between a static quark (coloured) and antiquark (anti-coloured) pair by the potential

$$V(r) = -\frac{4}{3}\frac{\alpha_s \hbar c}{r} + \lambda r \tag{10.40}$$

The first term dominates for distances $r < 0.1$ fm and has a coupling strength α_s given by the strong force analogue of the electromagnetic fine structure constant α_{EM}. Their relative sizes are

$$\frac{\alpha_s}{\alpha_{\text{EM}}} \sim 137$$

The second term dominates for distances $r > 1$ fm with $\lambda \sim 1\,\text{GeV fm}^{-1}$ and offers to explain confinement. Loosely speaking, it models the increasing strength of higher order gluon-gluon interactions that arises as the quark-antiquark pair are pulled apart.

When their separation becomes sufficiently large, it becomes energetically more favourable to produce new quarks from the vacuum rather than increasing $V(r)$ further. These newly formed quarks arrange themselves into colourless hadrons which we observe as narrow cones of jets due to the headlight beaming effect. So this non-vanishing energy as quarks and anti-quarks are drawn apart confines them within hadrons.

We investigate the charm–anti-charm $c\bar{c}$ bound system, known as a **charmonium**, somewhat similar to a hydrogen atom (with proton and electron masses being equal). The charm quarks are sufficiently massive such that much of the bound meson mass is comprised of its quark mass. So we can use the non-relativistic Schrödinger equation to deduce the bound states of the $c\bar{c}$ system. Working in the centre-of-mass frame, we the reduced mass $\mu = m_c/2$ to give

$$\left[-\frac{\nabla^2}{2\mu} + V(r)\right]\Psi(\mathbf{r}) = E\Psi(\mathbf{r})$$

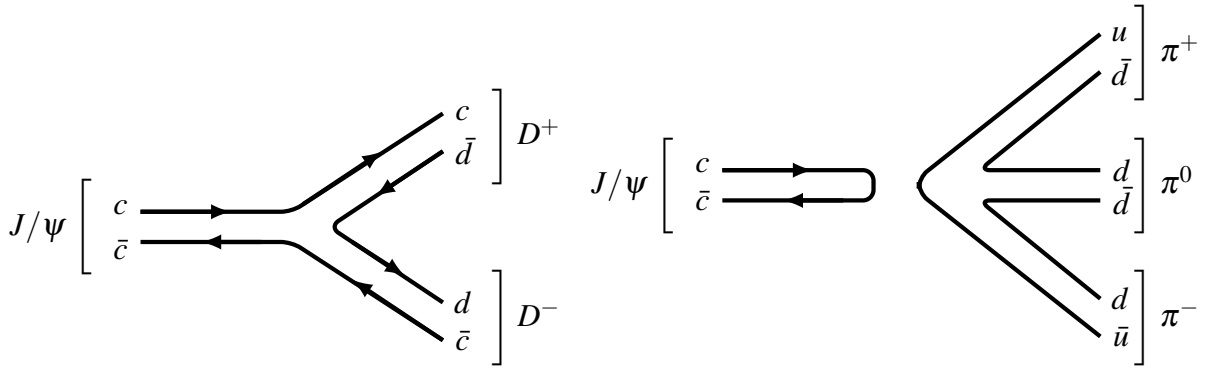

(a) Kinematically forbidden (b) Kinematically allowed but suppressed

Figure 71: Quark-line diagrams for charmonium decays.

Let the binding potential be the $1/r$ dependent first term of (10.40). We should obtain energy spectra analogous to that of hydrogen:

$$E_n = -\frac{\mu}{2}\left(\frac{4\alpha_s}{3}\right)^2 \frac{1}{n^2} \tag{10.41}$$

The resulting bound state masses are then

$$M(c\bar{c}) = 2m_c + E_n. \tag{10.42}$$

Longevity of charmonium

The $J/\Psi(3097)$ state predominantly decays to hadrons with branching ratio of 0.86. Mediated by strong interactions, we expect the decay width to be $\sim$ MeV but instead the measured width is $\approx 90\,\text{keV}$. Figure 71a illustrates the preferred mechanism of decay. The energy $2M_Dc^2$ is the **charm threshold**, as $M_D = 1869\,\text{MeV}/c^2$ is the rest mass of the lightest meson with non-zero charm. Charmonium states heavier than this threshold readily decay into $D^0\bar{D}^0$ or D^+D^- mesons via the strong interaction.

It is tempting to argue the J/ψ can proceed via this diagram in figure 71a. This shows the preferred by the quark lines (only needing one gluon exchange to form the $d\bar{d}$ pair) but it is kinematically forbidden given the $J/\Psi(3097)$ bound state is less than twice the charmed $D^{\pm}(1869)$ meson mass.

Meanwhile the $J/\Psi(3097)$ state $M_{J/\psi} < 2M_D$ is below this threshold. This can only annihilate via the electromagnetic interaction or decay to charmless hadronic states, shown

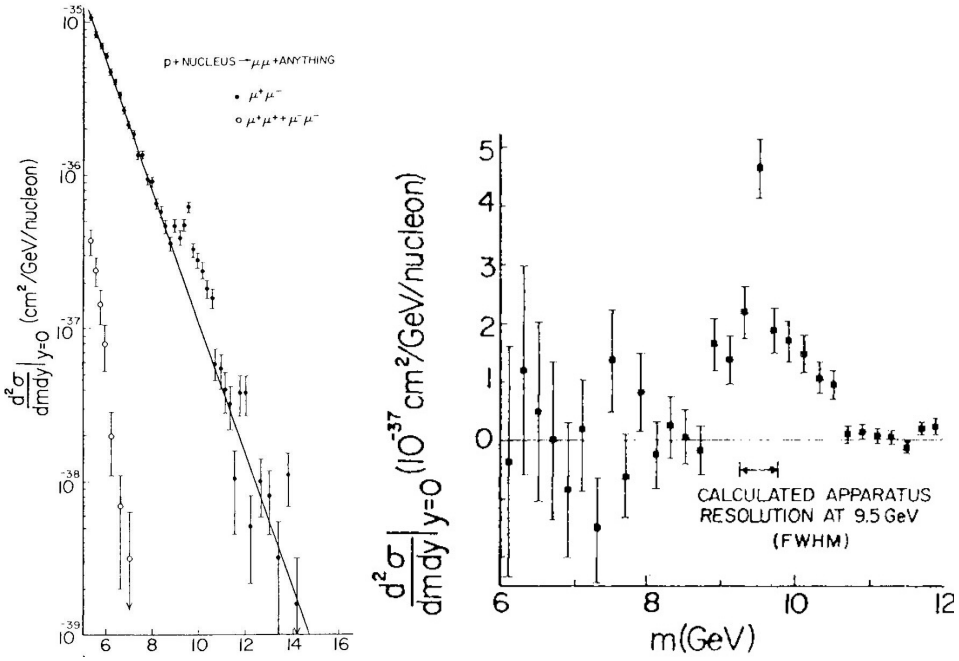

(a) Mass spectrum in GeV (b) Continuum subtracted

Figure 72: Upsilon ($b\bar{b}$) discovered in invariant mass distributions from the 1977 Fermilab E288 experiment. CERN Courier **17** (1977) 7-8

in figure 71b. Kinematically allowed but highly suppressed decay of $J/\psi(3097)$ to charmless π mesons. We understand quark lines being broken between initial and final states are highly suppressed decays, known as OZI suppression. In QCD, we can also understand this as the need for three gluon lines to connect the $c\bar{c}$ to the $u\bar{u}$ and pair of $d\bar{d}$ lines. Historically, this understanding was evidence suggesting the existence of a quark flavour other than u, d, s existing.

An analogous structure of bound states of the bottom quark b known as bottomonium $b\bar{b}$. This was discovered as the Υ meson by the E288 experiment at Fermilab led by Leon Lederman (figure 72). The mass was around 9.46 GeV in dimuon decays and its excited states was discovered a few years later.

11 Quantum chromodynamics

We now discuss empirical evidence for the gauge theory of the strong force: quantum chromodynamics. On first impression, the electromagnetic force and the strong nuclear force could not be more different in nature. Electrodynamics propagates light from the Sun over 150 million miles to our eyes, while jiggling electrons emit light from this screen printing these words. The strong force reveals itself at tiny femtometre distance scales binding protons together and preventing nuclei self-disintegration from electrostatic repulsion.

Though historically far from self-evident, quantum chromodynamics is formally the (non-Abelian) generalisation of quantum electrodynamics. It is a deeply profound and unexpected unification in physics that electromagnetism has a similar mathematical structure as the strong force, and as it turns out the weak force. Indeed, even the gravitational force has a similar structure e.g. the spacetime covariant derivatives in General Relativity.

11.1 Gluons and colour flow

The mediator of the strong force is a spin-one massless boson called the **gluon**. They interact with particles that have colour charge. All quarks carry colour and the fundamental quark-gluon vertex is

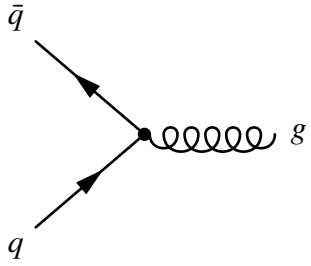

(11.1)

Conventionally, we use a spring to represent the gluon pictorially as a mnemonic for its binding behaviour. The interaction strength of this vertex is given by the strong coupling g_s proportional to the square root of the strong fine structure constant $g_s = \sqrt{4\pi\alpha_s}$, analogous to quantum electrodynamics.

Colour flow

The quark-gluon vertex conserves colour such that all colour charges entering the vertex equals that leaving. Gluons change the colours of participating quarks while leaving their flavour unchanged. We can pictorially represent this in an example involving quark-antiquark annihilation $u\bar{u} \to s\bar{s}$ in its Feynman diagram (left) and corresponding colour flow (right)

representations:

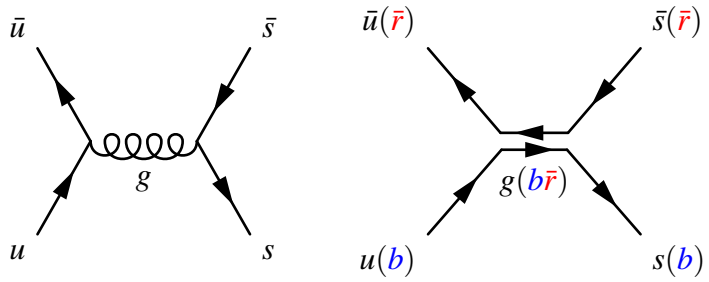

(11.2)

For illustration, we consider an u quark carrying b colour charge and $\bar{u}$ antiquark carrying $\bar{r}$ colour charge. The colour flow is conserved as the gluon carries blue and anti-red charge $g(b\bar{r})$. The quarks retain their respective flavours $u \to u$, $s \to s$ at each vertex, but exchange their colours $r \to b$, $b \to r$. Colour is still conserved at the vertex but the anti-red and blue flow from the individual quarks into the gluon.

Each gluon generally possess colour and anti-colour, and we can conventionally write them as eight linearly independent states:

$$\begin{array}{lll} \frac{1}{\sqrt{2}}(|r\bar{g}\rangle + |\bar{r}g\rangle), & \frac{\mathrm{i}}{\sqrt{2}}(|\bar{r}g\rangle - |r\bar{g}\rangle), & \frac{1}{\sqrt{2}}(|r\bar{r}\rangle + |\bar{b}b\rangle), \\ \frac{1}{\sqrt{2}}(|r\bar{b}\rangle + |\bar{r}b\rangle), & \frac{\mathrm{i}}{\sqrt{2}}(|\bar{r}b\rangle - |r\bar{b}\rangle), & \frac{1}{\sqrt{2}}(|r\bar{r}\rangle + |b\bar{b}\rangle - |g\bar{g}\rangle), \\ \frac{1}{\sqrt{2}}(|g\bar{b}\rangle + |\bar{g}b\rangle), & \frac{\mathrm{i}}{\sqrt{2}}(|\bar{b}g\rangle - 2|b\bar{g}\rangle). & \end{array}$$

We may expect there to be $3 \times 3 = 9$ possible gluon states but one state is colourless:

$$\frac{1}{\sqrt{3}}\left(|r\bar{r}\rangle + |g\bar{g}\rangle + |b\bar{b}\rangle\right).$$

We do not experimentally observe colourless gluons (which would mediate unobserved long-range forces) so we restrict the theory to one that describes nature using the eight independent gluon states with net colour.

A detour on SU(3)

Quantum chromodynamics mathematically represents these eight gluons as a set of unitary 3×3 matrices λ_{ij}^{a} (the a index runs from 1 to 8 for the eight gluons while the ij indices run from 1 to 3 for the three colours) with unit determinant, called the Gell-Mann matrices. At the quark-gluon vertex of a strong interaction (figure 11.2), these gluon matrices act on the quark colours represented by the 3-vector of equation 9.8 as $\lambda_{ij}q_j$. The Gell-Mann matrices are the 3×3 generalisation of the 2×2 Pauli matrices familiar from quantum mechanics describing fermion spin.

Mathematical physicists refer to this group of gluon matrices acting on quark vectors[56] as the 'Special Unitary group of 3-by-3 matrices' i.e. 'SU(3)'. The 'special' refers to the extra condition that the unitary matrices have a real determinant 1 rather than complex $e^{i\phi}$. We say SU(3) is a symmetry because the entire theory of QCD remains unchanged if we swapped the colour labels from red to green, green to blue, and blue to red:

$$|r\rangle \to |g\rangle \to |b\rangle \to |r\rangle; \quad \text{theory remains invariant.} \tag{11.3}$$

The mathematics of *Lie Groups* underpin this description of SU(3), which are further elaborated in group theory and quantum field theory classes, but this miniature technical detour hopefully gives a heuristic of why particle physicists refer to the strong force by 'SU(3)'.

11.2 Evidence for three colours

Among the definitive evidence for the quark model and the existence of three colour states is found by considering the ratio

$$R = \frac{\sigma(e^+e^- \to \text{hadrons})}{\sigma(e^+e^- \to \mu^+\mu^-)}, \tag{11.4}$$

as a function of centre-of-mass energy $\sqrt{s}$. From our understanding of electromagnetic scattering, the vertex factor contributes a the electric charge Q_i^2 for the final-state quarks and muons involved

$$R = \frac{\sigma_{\text{hadrons}}}{\sigma_{\text{muons}}} = \frac{\sum_i Q_i^2}{Q^2_{\mu^+\mu^-}}. \tag{11.5}$$

At large energies the density of states factor for both cross-sections are nearly equal, so this ratio is well-approximated by

$$R = \frac{Q^2_{u\bar{u}} + Q^2_{d\bar{d}} + Q^2_{s\bar{s}} + Q^2_{c\bar{c}} + Q^2_{b\bar{b}}}{Q^2_{\mu^+\mu^-}} = \left(\frac{2}{3}\right)^2 + \left(-\frac{1}{3}\right)^2 + \left(-\frac{1}{3}\right)^2 + \left(\frac{2}{3}\right)^2 + \left(-\frac{1}{3}\right)^2. \tag{11.6}$$

This gives our theoretical prediction of the ratio for 5 quarks as

$$R_{\text{the}} = \frac{11}{9}. \tag{11.7}$$

Now we compare with experimental data (figure 73). Below $\sqrt{s} \sim 4\,\text{GeV}$, we have only sufficient energies for up, down and strange quark pair production $e^+e^- \to u\bar{u}, d\bar{d}, s\bar{s}$. For

[56] Formally, the gluon matrices are in the *adjoint representation* while the (anti)quarks vectors are in the *(anti)fundamental representation* of SU(3).

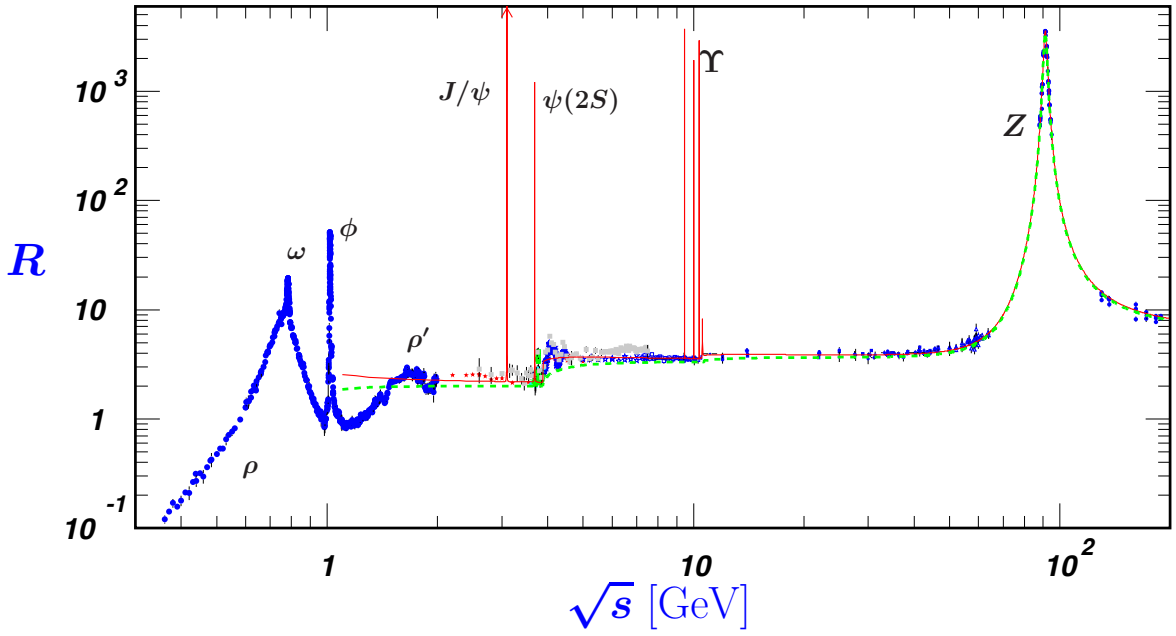

Figure 73: Ratio of the branching ratios of electron position annihilation to hadrons and muons $R = \sigma(ee \to \text{hadrons})/\sigma(ee \to \mu\mu)$. Reproduced from Particle Data Group [75].

$4 < \sqrt{s} < 10\,\text{GeV}$ we reach the kinematic threshold for the charm quark $e^+e^- \to c\bar{c}$, which adds to the rate of total hadron production. Above $\sqrt{s} \approx 10$ GeV, we reach the threshold for production of the bottom quark pair production $e^+e^- \to b\bar{b}$. Experiment finds

$$R_{\text{exp}} \approx 3 \tag{11.8}$$

for $\sqrt{s} > 4\,\text{GeV}$ sufficient for production of charm/bottom quark. There is a discrepancy between the theoretical and experimental ratio R of about a factor of 3. This suggests there exists 3 additional degrees of freedom left unaccounted in our model of quarks. This is strong evidence for colour.

11.3 Yang–Mills theory

This is a brief review of Yang–Mills theory applied to QCD, which those taking QFT classes will study in greater mathematical detail. The strong force is analogous to QED, extending the local symmetry from U(1) $e^{iI\alpha(x)}$ with the 1×1 unitary matrix (the identity I) to 3×3 unitary matrices t_a, the SU(3) group. The photon four-potential $A_\mu(x)$ extends to the gluon potential $t_a G^a_\mu$ with these eight 3×3 matrices attached to it. The corresponding QCD

covariant derivative extends the QED covariant (4.41) derivative to become:

$$\partial_\mu \to D_\mu = \partial_\mu + \mathrm{i} g_s t_a G^a_\mu, \tag{11.9}$$

where g_s is the dimensionless strong coupling and $t_a = \lambda_a/2$, with λ_a being the Gell-Mann matrices. For completeness, we print these matrices in a particular basis to look at:

$$\begin{aligned}
\lambda_1 &= \begin{pmatrix} 0 & 1 & 0 \\ 1 & 0 & 0 \\ 0 & 0 & 0 \end{pmatrix}, \quad \lambda_2 = \begin{pmatrix} 0 & -\mathrm{i} & 0 \\ \mathrm{i} & 0 & 0 \\ 0 & 0 & 0 \end{pmatrix}, \quad \lambda_3 = \begin{pmatrix} 1 & 0 & 0 \\ 0 & 1 & 0 \\ 0 & 0 & 0 \end{pmatrix}, \\
\lambda_4 &= \begin{pmatrix} 0 & 0 & 1 \\ 0 & 0 & 0 \\ 1 & 0 & 0 \end{pmatrix}, \quad \lambda_5 = \begin{pmatrix} 0 & 0 & -\mathrm{i} \\ 0 & 0 & 0 \\ \mathrm{i} & 0 & 0 \end{pmatrix}, \quad \lambda_6 = \begin{pmatrix} 0 & 0 & 0 \\ 0 & 0 & 1 \\ 0 & 1 & 0 \end{pmatrix}, \\
\lambda_7 &= \begin{pmatrix} 0 & 0 & 0 \\ 0 & 0 & -\mathrm{i} \\ 0 & \mathrm{i} & 0 \end{pmatrix}, \quad \lambda_8 = \frac{1}{\sqrt{3}} \begin{pmatrix} 1 & 0 & 0 \\ 0 & 1 & 0 \\ 0 & 0 & -2 \end{pmatrix}.
\end{aligned} \tag{11.10}$$

You can see the first three are precisely the Pauli matrices describing SU(2) in the upper-left corner. These matrices obey the algebra $[t_a, t_b] = \mathrm{i} f_{abc} t_c$ involving the SU(3) structure functions f_{abc}. The covariant derivative acts non-trivially on the quark Dirac spinors $q_i(x)$, which experience the local transformation transform

$$q_i(x) \to q'_i(x) = \exp\left[\mathrm{i} g_s (\lambda^a_{ij}/2) G^a_\mu(x)\right] q_j(x). \tag{11.11}$$

There is quite a large number of indices to keep track of here, which we can walk through in turn:

- **Lorentz** $\mu = \{0,1,2,3\}$: this runs over the Lorentz four-vector index;
- **Gluon** $a = \{1,2,\ldots,8\}$: this runs over the eight Gell-Mann matrices corresponding to the eight gluons in nature. In group theory language, gluons are described by the *adjoint representation* of SU(3);
- **Colour** $i, j = \{1,2,3\}$: this runs over the elements of the 3×3 matrices, which we can interpret as the colours of the quarks. In group theory language, quarks are described by the *fundamental representation* of SU(3);
- **Flavour** $q = \{u,d,s,c,b,t\}$: this runs over the six quark flavours in nature.
- **Spinor**: we have suppressed the four Dirac spinor indices on the quarks that the γ^μ matrices act on.

The gluon field strength $G_{\mu\nu} = t_a G^a_{\mu\nu}$ has a similar structure to the electromagnetic field strength $F_{\mu\nu}$

$$G_{\mu\nu} = \frac{1}{\mathrm{i}g_s}[D_\mu, D_\nu] = \partial_\mu G_\nu - \partial_\nu G_\mu + \mathrm{i}g_s[t_b G^b_\mu, t_c G^c_\nu]. \tag{11.12}$$

The non-commuting t_a matrices gives an extra bit involving the SU(3) structure functions, which we can write as

$$G^a_{\mu\nu} = \partial_\mu G^a_\nu - \partial_\nu G^a_\mu - g_s f^{abc} G^b_\mu G^c_\nu. \tag{11.13}$$

Under a gauge transformation, the gauge function acquires an extra non-commuting term relative to how this worked for the photon field A_μ:

$$G^a_\mu \to \tilde{G}^a_\mu = G^a_\mu - \chi^a_\mu, \quad \chi^a_\mu = \partial_\mu \Lambda^a + g_s f^{abc} \Lambda^b G^c_\mu. \tag{11.14}$$

The kinetic term in the Lagrangian governing the motion of gluon fields is given by

$$\mathscr{L}^{\text{kinetic}}_{\text{gluon}} = -\frac{1}{2}\mathrm{tr}\left(G_{\mu\nu}G^{\mu\nu}\right) = -\frac{1}{4}G^a_{\mu\nu}G^{\mu\nu}_a, \tag{11.15}$$

using the fact the t_a matrices conventionally satisfy the trace relation $\mathrm{tr}(t_a t_b) = \frac{1}{2}\delta_{ab}$. Combining this with the Dirac Lagrangian term for quarks, this gives the QCD Lagrangian governing the interactions of quarks and gluon:

$$\boxed{\mathscr{L}_{\text{QCD}} = -\frac{1}{4}G^a_{\mu\nu}G^{\mu\nu}_a + \mathrm{i}\bar{q}\gamma^\mu(\partial_\mu + \mathrm{i}g_s t_a G^a_{\mu\nu})q.} \tag{11.16}$$

The quantisation and renormalisation of this Lagrangian and non-Abelian gauge theories are rather complicated, to use some understatement, due to the non-propagating gauge degrees of freedom. Showing this is well beyond the scope of this class, but the crucial breakthroughs of Veltmann and 't Hooft in the 1970s demonstrated QCD was a viable theory of nature.

The extra term given by the non-commuting gluon fields $g_s f^{abc} G^b_\mu G^c_\nu$ is makes QCD a **non-Abelian gauge theory** and is a hallmark of Yang–Mills theory. This non-commuting term endows QCD with qualitative phenomenological differences compared to the Abelia gauge theory of QED. Expanding out the kinetic Lagrangian gives terms that feature three $\sim GG(\partial G)$ and four $\sim GGGG$ gluon fields. This implies the existence of gluon self-interactions at tree-level shown in figure 74. This is related to the fact that gluons have non-zero net colour. They feel the strong force and can therefore interact with other gluons. This contrasts with photons carrying no electric charge and have no self-interactions at tree-level. Gluons can therefore source other gluons under the strong interaction, and offers an explanation for confinement.

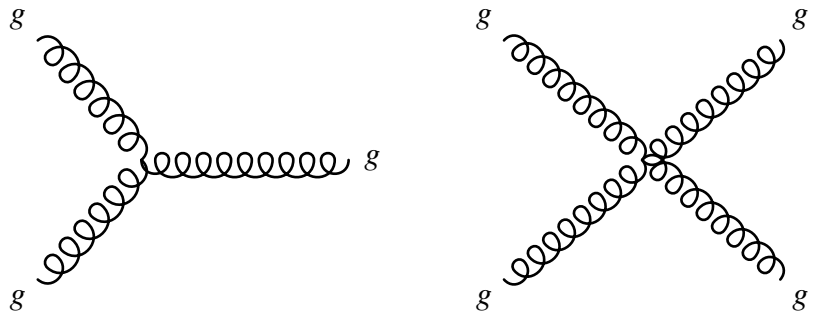

(a) 3 gluon vertex (b) 4 gluon vertex

Figure 74: Gluon self-interaction vertices due to the non-Abelian structure of quantum chromodynamics.

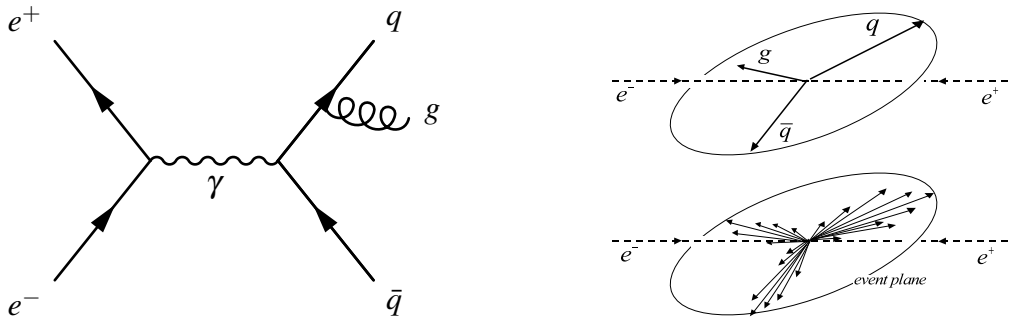

(a) Feynman diagram (b) Planarity of three jets [76]

Figure 75: Diagrams for the gluon bremsstrahlung discovery process $e^-e^+ \to q\bar{q}g$.

11.4 Asymptotic freedom

The gluon was discovered in 1979 via the gluon bremsstrahlung process (figure 75a). A distinctive feature of these events was that all three jets resulting from the quarks and gluon are approximately coplanar due to momentum conservation (figure 75b). The four experimental collaborations at PETRA in DESY, Hamburg (figure 34a) sought evidence for this process, which was promptly observed by all four experiments (figure 76a).

In 1972, the renormalisation of QCD was completed by 't Hooft and Veltman. Then Politzer, Gross and Wilczek calculated the beta function of QCD in 1973 and discovered it decreased with energy scales.

The strong force coupling α_{QCD} in quantum chromodynamics decreases with energy scale. It is more difficult to draw pretty pictures for why this happens, but some texts discuss a concept of "anti-screening". The QCD beta function, in terms of the number of active

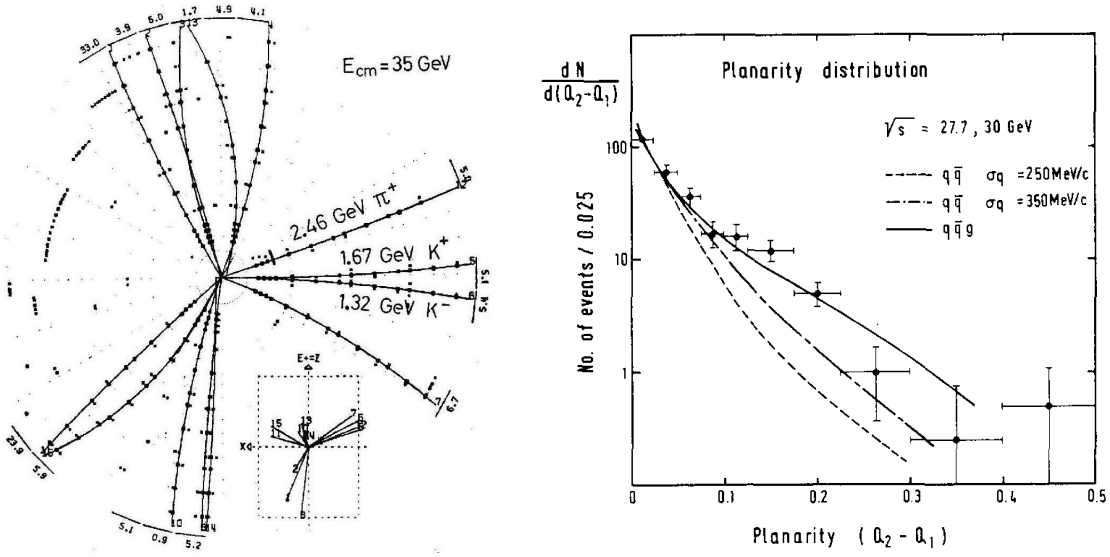

(a) TASSO three-jet event (b) JADE data on qqg [77]

Figure 76: Discovery of gluon in $ee \to qqg$ three-jet events.

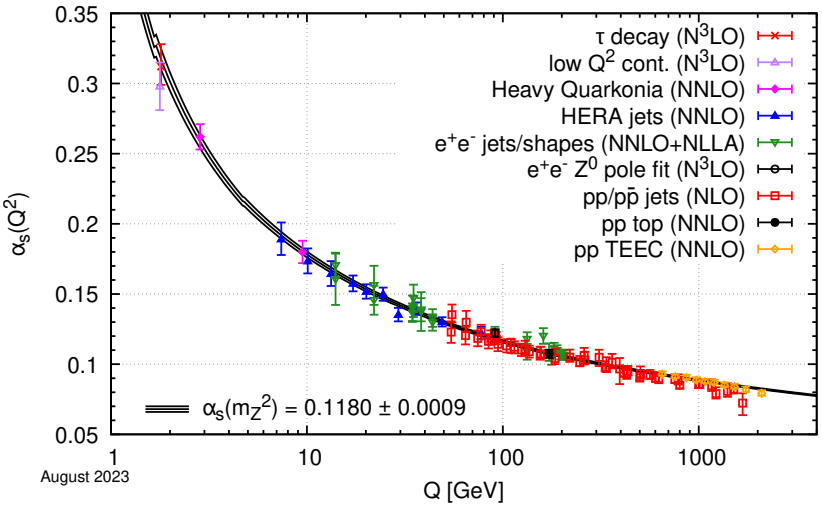

Figure 77: **Running of strong coupling**. Displayed is the strong coupling $\alpha_s(Q^2)$ as a function of momentum transfer Q^2 from Ref. [75]. The measurements are performed using various probes, and the line shows the five-loop running taking $\alpha_s(m_Z^2) = 0.1180 \pm 0.0009$ as input.

flavours N_f with colour charge, is:

$$\beta(\alpha_{\text{QCD}}) = -\left(33 - 2N_f\right)\frac{\alpha_{\text{QCD}}^2}{6\pi}. \tag{11.17}$$

In the Standard Model, $N_f = 6$, giving a negative beta function. The measured values at various Q^2 are summarised figure 77.

One conceptually simple way to probe this is to measure the ratio of three-jet to two-jet events:

$$R_{32} = \frac{\sigma(ee \to qqg)}{\sigma(ee \to qq)} \propto \alpha_s(Q), \tag{11.18}$$

where $Q = \frac{1}{2}(p_{\mathrm{T}}^{j1} + p_{\mathrm{T}}^{j2})$ is the average transverse momentum of the two jets with the highest p_{T}. This can be extended to hadron colliders, where CMS made among the first measurements out to $Q \approx 900$ GeV in 2013 [78]. At hadron colliders, there are more diagrams such as gluon scattering to consider.

IV Electroweak interactions

We now turn to the electroweak interactions, which is arguably the most subtle and mysterious of forces that remain at the forefront of research. We first look at some of the measurements at low energies mostly in the 1950s concerning weak interactions, in particular broken discrete symmetries. Historically, this was first manifested by nuclear beta decay of nuclei and then by muon and pion decays. Today, we now know these weak interactions are mediated by the $W^{\pm}$ boson and Z bosons, which require constructing city-sized colliders and house-sized experiments to create. Finally, we discuss more contemporary topics of the Higgs boson and neutrino oscillations.

12 Low-energy beta decay

Decades after beta decay had been discovered, we now know the fundamental interaction is a W^- boson mediating a neutron turning into a proton alongside an electron and anti-neutrino:

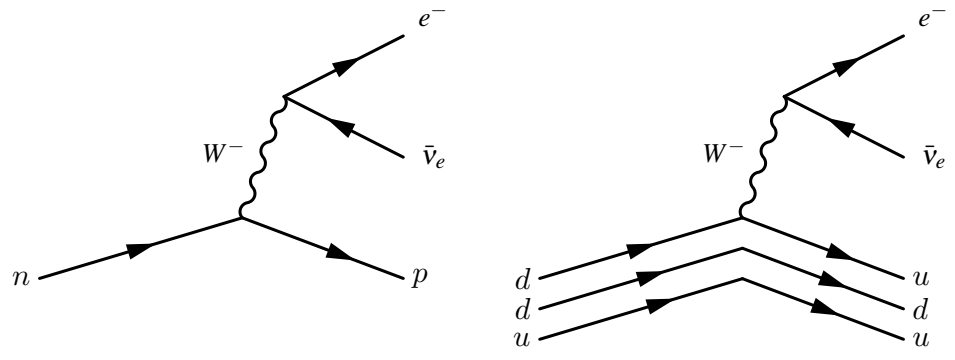

(12.1)

The right diagram shows but with quark lines for the neutron and proton, illustrating the down transformed into an up quark with the other two spectator quarks unchanged.

The simplest beta decay involves purely leptonic interactions such as muon decay

$$\mu^- \to e^- + \bar{\nu}_e + \nu_\mu . \tag{12.2}$$

The Feynman diagram for this process is:

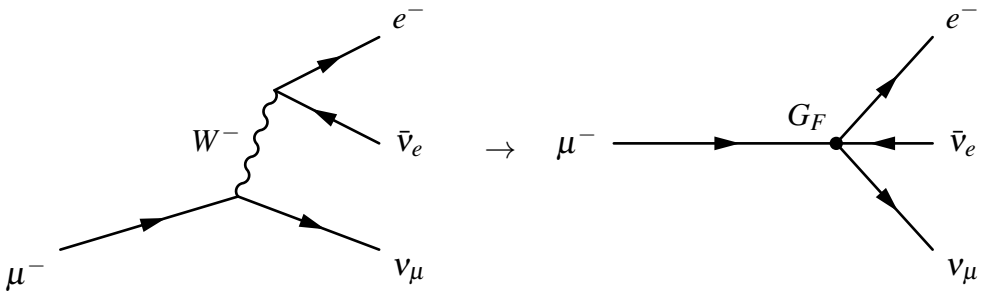

(12.3)

This shows the low-energy limit, where W^- is highly off-shell so can be described by a three-point Fermi interaction vertex.

The tau-lepton is the heaviest lepton with 1.776 GeV mass and therefore can also beta decay via a highly off-shell $W^\pm$ boson to both electrons and muons:

$$\tau^- \to e^- + \bar{\nu}_e + \nu_\tau, \tag{12.4}$$

$$\tau^- \to \mu^- + \bar{\nu}_\mu + \nu_\tau. \tag{12.5}$$

This dual-flavour decay is the pivotal signature for how the tau-lepton was discovered in 1975 at the SPEAR electron–positron collider in SLAC, California. When they ramped the beam energy above around $\sqrt{s} = 4$ GeV, this triggered production of opposite-charge different-flavour leptons plus missing momentum:

$$e^+e^- \to e^\pm\mu^\mp + \geq 2 \text{ invisible particles}, \tag{12.6}$$

with no other charged particles or photons. The authors conclude pretty frankly [79]:

> "We have no conventional explanation for these events."

This was the tell-tale discovery of a new particle: the tau-lepton $\tau^\pm$.

12.1 Fermi theory of weak decays

The electroweak fine structure coupling α_{EW} around the Z boson mass:

$$\alpha_{\text{EW}} \simeq \frac{1}{30} \tag{12.7}$$

Intriguingly, this is larger than the electromagnetic fine structure constant $\alpha_{\text{EM}} \simeq 1/128$. The weakness of the weak force arises due to the heaviness of the electroweak bosons. The Fermi coupling is a dimensionful quantity

$$G_F \simeq \frac{\pi}{\sqrt{2}} \frac{\alpha_{\text{EW}}}{m_W^2} \simeq 1.166 \times 10^{-5}\ \text{GeV}^{-2} = 90\ \text{eV fm}^3. \tag{12.8}$$

We can see the smallness of G_F is due to the factor of $1/m_W^2$ suppressing this. For momentum transfer q, the propagator Π_W for the W boson has a dependence

$$\Pi_W \propto \frac{1}{q^2 - m_W^2}. \tag{12.9}$$

When the momentum transfer is much smaller than the W mass $q^2 \ll m_W^2$, this reduces to the form seen in the Fermi constant. In the case of nuclear beta decays, the typical energies are on the order of 100s of MeV at most, which is far below m_W. This is an example of an effective field theory.

Fermi proposed the first successful theory to explain and predict beta decay rates. The theory assumes 4 particle interactions take place at a single point in spacetime whose amplitude is governed by the **Fermi coupling constant**. This ignores the Coulomb interaction and is a good approximation for sufficiently high electron energies. At the low energies in Fermi theory, we assume G_F to be a universal constant.

Consider beta β^- decay. Let the initial state be $|i\rangle$ and the final state $|f\rangle$ be

$$|i\rangle = |\psi_i\rangle, \qquad |f\rangle = |\psi_f\rangle|\psi_e\rangle|\psi_\nu\rangle$$

where the product of the final nuclear, electron and anti-neutrino respectively states We wish to calculate the interaction amplitude $\mathscr{M}_{fi} = \langle f|H_{\text{int}}|i\rangle$ given by

$$\langle f|\mathscr{A}|i\rangle = \int G_F \psi_e^* \psi_\nu^* \psi_f^* \psi_i \, \mathrm{d}^3\mathbf{r} \tag{12.10}$$

Now assume the outgoing electron and anti-neutrino are plane waves

$$\langle \mathbf{r}|\psi_e\rangle = \frac{\mathrm{e}^{\mathrm{i}\mathbf{p_e}\cdot\mathbf{r}}}{L^{3/2}}, \qquad \langle \mathbf{r}|\psi_\nu\rangle = \frac{\mathrm{e}^{\mathrm{i}\mathbf{p}_\nu\cdot\mathbf{r}}}{L^{3/2}}, \tag{12.11}$$

where L^3 is some normalising volume (that will cancel in the end result). Taylor expand the product $\psi_e^*\psi_\nu^*$:

$$\psi_e^*\psi_\nu^* \approx 1 - \mathrm{i}(\mathbf{p}_e + \mathbf{p}_\nu)\cdot\mathbf{r} \tag{12.12}$$

Provided the first term is non-vanishing on integration, we expect it to dominate. We justify the higher ordered terms are small by noting the nuclear energies pc and sizes r are of order MeV and 10 fm respectively

$$\left|\frac{(\mathbf{p}_e + \mathbf{p}_\nu)\cdot\mathbf{r}}{\hbar}\right| \sim \frac{pc}{\hbar c} r \sim \frac{\text{MeV}}{197 \text{ MeV fm}} 10 \text{ fm} \sim \frac{1}{20} \tag{12.13}$$

with $\hbar c \approx 197$ MeV fm. So the amplitude (12.10) is related by the Fermi constant G_F and a matrix element $\mathscr{M}_{fi}$ dependent only on the initial and final nuclear states:

$$\mathscr{M}_{fi} = \frac{1}{L^3}\int G_F \psi_f^* \psi_i \mathrm{d}^3\mathbf{r} = \frac{G_F}{L^3} M_{\text{nucl}} \tag{12.14}$$

The differential rate of transitioning from an initial state $|i\rangle$ to some final state $|f\rangle$ with electron energy in interval $[E_e, E_e + \mathrm{d}E_e]$ is given by the Fermi golden rule:

$$\frac{\mathrm{d}w}{\mathrm{d}E_e} = 2\pi |\langle f|\mathscr{H}_{\text{int}}|i\rangle|^2 \frac{\mathrm{d}N_\nu}{\mathrm{d}E_\nu}\frac{\mathrm{d}N_e}{\mathrm{d}E_e} \tag{12.15}$$

where $\mathrm{d}N_{\nu,e}/\mathrm{d}E_{\nu,e}$ are the densities states of the free neutrino and electron. Here w is the decay rate, related to the mean lifetime τ by $w = 1/\tau$. The neutrino density of states is

$$\frac{\mathrm{d}N_\nu}{\mathrm{d}p_\nu} = \left(\frac{L}{2\pi}\right)^3 p_\nu^2 \mathrm{d}p_\nu \mathrm{d}\Omega \tag{12.16}$$

Integrating over the solid angle and using $\mathrm{d}p_\nu/\mathrm{d}E_\nu = E_\nu/p_\nu$, we obtain

$$\frac{\mathrm{d}N_\nu}{\mathrm{d}E_\nu} = \left(\frac{L}{2\pi\hbar}\right)^3 4\pi p_\nu E_\nu \tag{12.17}$$

With a similar expression for the electron density of states, the Fermi Golden Rule becomes

$$\frac{\mathrm{d}w}{\mathrm{d}E_e} = 2\pi G_F^2 \left|M_{\text{nucl}}\right|^2 \frac{(4\pi)^2}{(2\pi)^6} p_\nu E_\nu p_e E_e \tag{12.18}$$

Changing variables to p_e and letting the neutrino be massless such that $E_\nu = p_\nu c$, we obtain

$$\frac{\mathrm{d}w}{\mathrm{d}p_e} = \frac{\mathrm{d}E_e}{\mathrm{d}p_e}\frac{\mathrm{d}w}{\mathrm{d}E_e} = \frac{G_F^2 \left|M_{\text{nucl}}\right|^2}{2\pi^3} p_e^2 E_\nu^2 \tag{12.19}$$

Letting $\mathscr{Q} = E_e - E_\nu$ be the total energy released in the beta decay, we obtain

$$\frac{\mathrm{d}w}{\mathrm{d}p_e} = \frac{G_F^2 \left|M^{\text{nucl}}\right|^2}{2\pi^3} p_e^2 (Q - E_e)^2 \tag{12.20}$$

In the ultrarelativistic limit $E_e \approx p_e c$, we can integrate over the electron energies analytically to obtain **Sargent's rule**

$$\boxed{w \propto \int_0^{\mathscr{Q}} E_e^2 (\mathscr{Q} - E_e)^2 \mathrm{d}E_e = \frac{\mathscr{Q}^5}{30}} \tag{12.21}$$

The rate of beta decay w is proportional to the fifth power of the energy released $\mathscr{Q}^5$. In the case of muon lifetime τ_μ, the muon mass is converted into energy released and we have the lifetime

$$\frac{1}{\tau_\mu} = \Gamma_\mu \propto G_F^2 m_\mu^5. \tag{12.22}$$

12.2 Neutrino direct detection

Clyde Cowan and NYU alumnus Frederick Reines led a definitive experiment in 1956 that enabled the first direct detection of neutrinos [80]. This utilised nuclear reactor at the Savannah River Plant in South Carolina as the source of neutrinos from neutron beta decay. Beta decays $n \to p + e^- + \bar{\nu}_e$ occurs at nuclear reactors and they proposed detecting the anti-neutrinos via inverse beta decay:

$$\bar{\nu}_e + p \to n + e^+. \tag{12.23}$$

From Fermi theory, Hans Bethe and Rudolf Peierls first calculated in 1934 [81] that for a neutrino with 2.3 MeV energy, this process would have an very small cross-section no larger than

$$\sigma \lesssim 10^{-44}\ \text{cm}^2. \tag{12.24}$$

They concluded that:

> "It seems highly improbable that, even for cosmic ray energies, the cross-section becomes large enough to allow the process to be observed."

Fortunately, they could neither foresee the development of large neutrino fluxes from nuclear reactions nor experimental ingenuity.

Cowan and Reines were originally thinking of detecting the neutrinos from a nuclear explosion. Luckily, they concluded it is safer to use nuclear power plants as a more controlled source of neutrinos. They constructed a stack of large water tanks using protons in H_2O as the target medium. This pioneering detection method comprising water forms the basis of many important neutrino detectors at the Sudbury Neutrino Observatory, Kamiokande, and Homestake Experiments that would reveal neutrino oscillations. The detection of inverse beta decay occurs in two stages:

- The e^+ annihilates with an electron, producing a distinctive pair of back-to-back gamma rays. These are detected by a total of 100 photomultipliers surrounded each of the three tanks of water.

- The small central tanks of water are doped with cadmium chloride enables the neutron to be detected via ^{108}Cd capture. The resulting ^{108}Cd state is a metastable isotope that decays into a gamma ray

$$n + {}^{108}\text{Cd} \to {}^{109}\text{Cd}^* \to {}^{108}\text{Cd} + \gamma \tag{12.25}$$

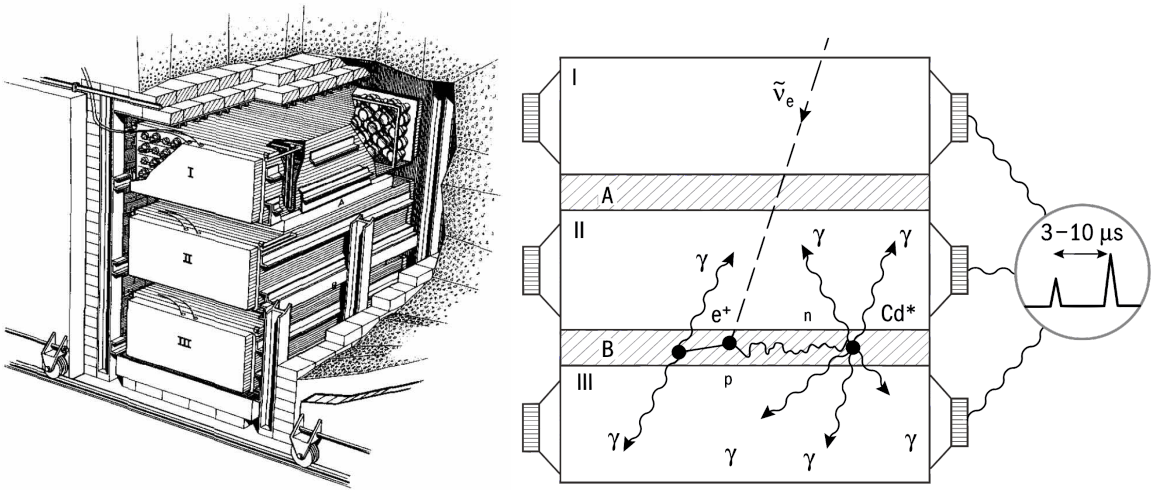

(a) Savannah River experiment

(b) Neutrino detection [82]

Figure 78: **Cowan–Reines neutrino detection experiment**. The experimental setup at Savannah River has three 1400-litre tanks of liquid scintillator (I, II, III) with 100 photomultipliers, and two tanks of Cadmium-doped water (A, B). Images: CERN Courier (July 2016)

> The neutron performs a random walk in the liquid before cadmium absorption resulting in a measurable three to ten microseconds delay. The coincidence of this signal with the first diphoton signature provided excellent signal discrimination.

They ran the experiment for 1371 hours in 1956. When the reactor was on, they detected 3.0 ± 0.2 neutrino candidates per hour. This experiment has the great benefit of having a reliable way to switch off the signal when the reactor is off to carefully determine the background rates. They also measured the neutrino-proton cross-section and found this to be compatible with estimates from Fermi theory:

$$\sigma_{\text{experiment}} = 12^{+7}_{-4} \times 10^{-44}\ \text{cm}^2, \tag{12.26}$$

$$\sigma_{\text{Fermi-theory}} = (5 \pm 1) \times 10^{-44}\ \text{cm}^2 \tag{12.27}$$

When they made this unambiguous detection, they sent a telegram to Pauli then at a conference in CERN[57]

> "We are happy to inform you that we have definitely detected neutrinos from fission fragments by observing inverse beta decay of protons. Observed cross

[57] See Reines' Nobel lecture https://www.nobelprize.org/uploads/2018/06/reines-lecture.pdf

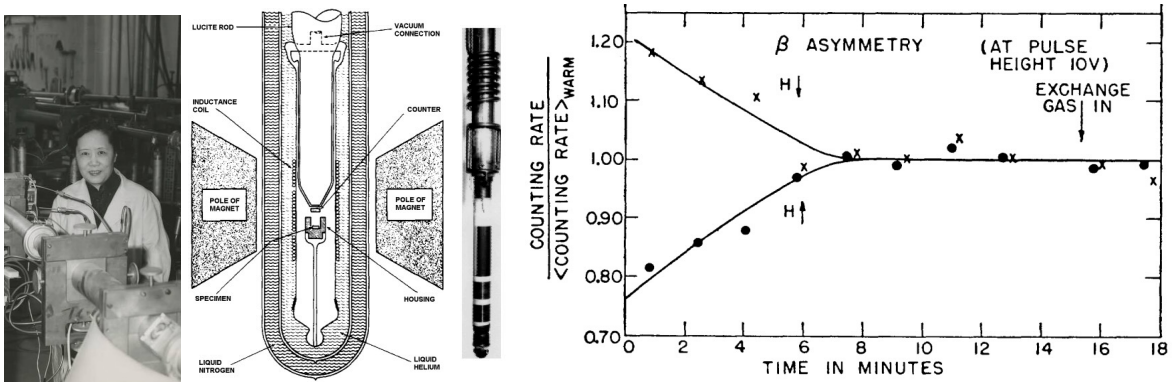

(a) C.-S. Wu (b) Co-60 experiment (c) Polarisation asymmetry vs warm-up time

Figure 79: **Wu et al. Cobalt-60 experiment**. The plot shows the beta asymmetry from the discovery paper [83], which illustrates the magnetic field polarisation up $H\uparrow$ and down $H\downarrow$ vs warm-up time of six minutes. Images: Smithsonian Institute Archives, National Institute of Standards and Technology, Ref. [83].

> section agrees well with expected six times ten to minus forty four square centimeters."

Pauli must have been thrilled to learn that the particle once thought to be undetectable had been discovered via direct means. Around 1986, his student C. P. Enz uncovered the response Pauli composed but Cowan and Reines never received:

> "Thanks for the message. Everything comes to him who knows how to wait."

12.3 Parity violation

The discovery of parity violation is a defining unexpected feature of the weak force uncovered in low-energy beta decays. We first study the famous Colbat-60 experiment led by Chien-Shiung Wu before turning to helicity suppression in pion decays. Electromagnetism, gravity, and the strong force all respect parity. The weak force remains the only fundamental force observed to do so. Why is nature like this? Why does the weak force not interact with right-handed states but only to left-handed ones? We do not know. This remains an open problem in physics.

As a quick review, the **parity operator** P maps coordinates $\mathbf{r} = (x, y, z)$ to its inverse $-\mathbf{r} = (-x, -y, -z)$ through the origin:

$$P\colon \mathbf{r} \mapsto -\mathbf{r} \tag{12.28}$$

Polar vectors $\mathbf{v}_{\text{po}}$, such as momentum $\mathbf{p}$ and electric field $\mathbf{E}$, acquire a negative sign. By contrast, **axial vectors** $\mathbf{v}_{\text{ax}}$, such as angular momentum $\mathbf{l} = \mathbf{r} \times \mathbf{p}$ and magnetic field $\mathbf{B}$, remain unchanged under parity transformations:

$$P\colon \mathbf{v}_{\text{po}} \mapsto -\mathbf{v}_{\text{po}} \tag{12.29}$$

$$P\colon \mathbf{v}_{\text{ax}} \mapsto \mathbf{v}_{\text{ax}} \tag{12.30}$$

The electromagnetic and strong interactions are invariant under parity transformations.

In 1956, Chien-Shiung Wu (figure 79a) led a team comprising Ernest Ambler, Raymond Hayward, Dale Hoppes, and Ralph Hudson at the National Bureau Standards to demonstrate parity violation in beta decay [83]. The cobolt-60 is cooled inside a cryogenic dewar shown in figure 79b. It involved aligning the nuclear magnetic moments of ^{60}Co to an external magnetic field at temperatures of 0.01 K. The ^{60}Co undergoes beta decay

$$^{60}\text{Co} \to {}^{60}\text{Ni}^{*} + e^{-} + \bar{\nu}_e \tag{12.31}$$

Under parity transformations, the nuclear magnetic moment $\boldsymbol{\mu}_n$, being axial, remains unchanged while the electron momentum $\mathbf{p}_e$, being polar, acquires a negative sign:

$$P : \boldsymbol{\mu}_n \mapsto \boldsymbol{\mu}_n, \qquad P : \mathbf{p}_e \mapsto -\mathbf{p}_e$$

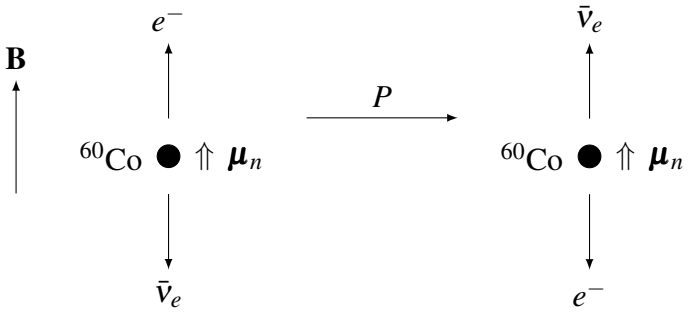

Performing a parity transformation on beta decay of ^{60}Co, the applied magnetic $\mathbf{B}$ field aligns the nuclear magnetic moment $\Uparrow \boldsymbol{\mu}$ in a fixed direction. The thin arrows indicate the linear momenta of the electron and antineutrino. If parity were conserved i.e. the parity transformation leaves the physics of the interaction invariant, we expect the detection rate of electrons in the $+\mathbf{B}$ hemisphere to be equal to that in the $-\mathbf{B}$ hemisphere.

However, the contrary is measured: the decay was preferentially emitting electrons in the $-\mathbf{B}$ direction (figure 79c). Therefore, this is empirical evidence that:

$$\boxed{\text{Weak interactions violate parity conservation.}} \tag{12.32}$$

Particle	Helicity h	Diagram	Handedness
ν	$-\frac{1}{2}$	$\xrightarrow{p}$ $\Leftarrow h$	left-handed
$\bar{\nu}$	$+\frac{1}{2}$	$\xrightarrow{p}$ $\Rightarrow h$	right-handed

Table 4: Observed helicities of neutrinos and antineutrinos.

Remarkably, the weak interactions violate parity symmetry not just by a little bit, but in a maximal way. The weak force appears all and nothing: left-handed (massless) particles feel the weak force, but right-handed particles do not at all. This is why you sometimes see subscript L by the SU(2) group describing the weak force: "$\mathrm{SU}(2)_\mathrm{L}$". We could imagine a universe where the weak force couples to left-handed particles 2.5% times stronger than right-handed particles and this effect would be much more subtle to observe. But this time, nature surprised us in the most striking manner.

Helicity suppression

Helicity h is the projection of the particle spin along the momentum. For ultrarelativistic particles $v \to c$, it is given by the operator

$$h = \frac{\mathbf{s}\cdot\mathbf{p}}{|\mathbf{p}|}, \qquad v \to c \tag{12.33}$$

where $\mathbf{s}$ and $\mathbf{p}$ are the spin and momentum vectors.

Under a parity transformation, helicity acquires a negative sign:

$$P : h \mapsto -h \tag{12.34}$$

Neutrinos are observed to violate parity conservation; their helicities are preferentially $h = +\frac{1}{2}$. Table 4 shows the following properties:

- Neutrinos are always 'left-handed' with helicity $h = -\frac{1}{2}$.
- Antineutrinos are always 'right-handed' with helicity $h = +\frac{1}{2}$.

This result generalises for other ultrarelativistic particles:

> For ultrarelativistic particles, charged current weak interactions only couple to **left-handed particles** and **right-handed antiparticles**. (12.35)

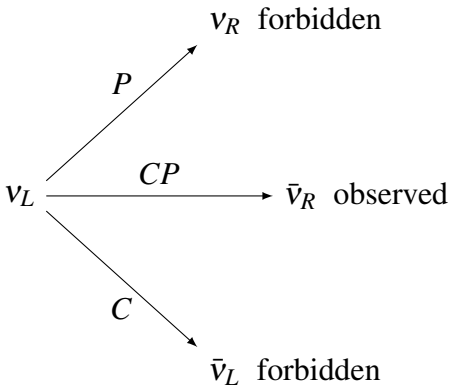

Figure 80: Neutrinos states after C, P and CP transformations.

This is an example of **charge-conjugation–parity conservation**, or **CP invariance**. Charge conjugation is the transformation that maps a particle to its antiparticle

$$C : a \mapsto \bar{a} \tag{12.36}$$

The following are illustrated in figure 80:

- Charge conjugation turns a left-handed neutrino into a left-handed antineutrino, which is not observed.
- Parity transformation turns a left-handed neutrino into a right-handed neutrino, which is not observed
- By performing charge conjugation and parity transformations, we turn a left-handed neutrino into a right-handed antineutrino, which is observed.

Pion decay helicity suppression

Published at the same time as the cobalt-60 experiment by Richard Garwin, Leon Lederman, and graduate student Marcel Weinrich using Columbia's Nevis Cyclotron Laboratory [84] about 20 up to Hudson river from Manhattan, where pions are created (figure 81a).

Consider a pion in its rest frame decaying into kinematically accessible leptons

$$\pi^+ \to \ell^+ + \nu_\ell, \qquad \ell = [e, \mu] \tag{12.37}$$

For e^+, we have $m_\pi \gg m_e$ so we work in the ultrarelativistic limit. By result (12.35), this means the electrons must be right-handed and the neutrino left-handed as depicted in figure 81 (a).

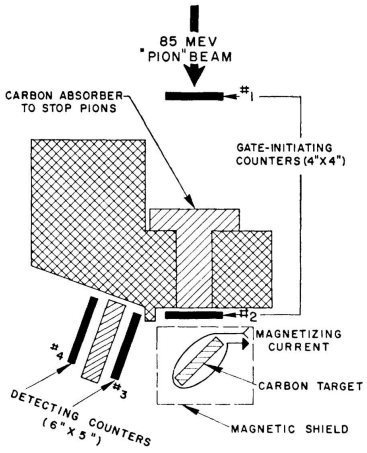

(a) Experimental setup [84]

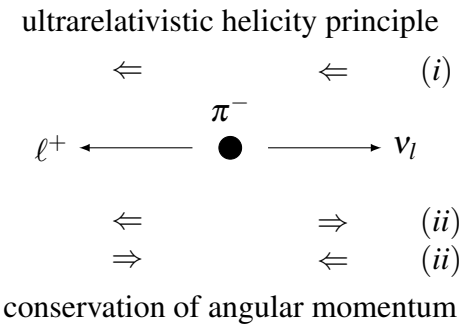

(b) Helicity of pion decay

Figure 81: The singly solid arrows denote linear momentum and double arrows denote spin. In the ultrarelativistic limit, we must have left-handed particles (neutrino) and right-handed antiparticles (antilepton) as depicted by (i) by principle 12.35. However a pion has spin-0. To conserve angular momentum, the spins of the antilepton and neutrino must be 'anti-aligned', as depicted in (ii) or (iii).

Now pions are spin-0 implying the spins of the positron and neutrino must be antialigned to conserve angular momentum. This means we have both particles must be either 'anti-aligned', as illustrated in figure 81 (b) or (c). So by demanding conservation of angular momentum, we violate the handedness principle (12.35) for charged weak interactions. Of course, the particles are not truly massless so decay into the electron type channel is not entirely forbidden. For decay involving muon flavoured leptons, these are of a similar mass to the pion and we are no longer in the ultrarelativistic limit. Pion decays to muons are not helicity suppressed.

Vector–axial (V-A) interaction

The implication of parity violation is that Fermi's theory of beta decay needs modifications. There are several ways to combine Dirac spinors in Lorentz covariant bilinears:

$$\bar{\psi}\psi \quad \text{scalar}, \tag{12.38}$$

$$\bar{\psi}\gamma^5\psi \quad \text{pseudo-scalar}, \tag{12.39}$$

$$\tfrac{1}{2}\bar{\psi}(\gamma^\mu\gamma^\nu - \gamma^\nu\gamma^\mu)\psi \quad \text{tensor}, \tag{12.40}$$

$$\bar{\psi}\gamma^\mu\psi \quad \text{vector}, \tag{12.41}$$

$$\bar{\psi}\gamma^\mu\gamma^5\psi \quad \text{axial-vector}. \tag{12.42}$$

The full electroweak interaction uses the vector and axial bilinears of Dirac spinors, which for beta decay looks like

$$\mathscr{M}_{fi} = \left[\bar{\psi}_p\gamma^\mu\frac{1-\gamma^5}{2}\psi_n\right]\frac{g_W}{\sqrt{2}}\left[\frac{\eta_{\mu\nu}}{q^2-m_W^2}\right]\frac{g_W}{\sqrt{2}}\left[\bar{\psi}_e\gamma^\nu\frac{1-\gamma^5}{2}\psi_\nu\right]. \tag{12.43}$$

We identify the charged current propagator $\eta_{\mu\nu}/(q^2-m_W^2)$ together with the weak vertex factors $g_W/\sqrt{2}$. Crucially, parity violation is explicitly encoded via the left-handed projection operators $P_L = \frac{1}{2}(1-\gamma^5)$ of the fermion currents. In the low-energy limit $q^2 \ll m_W^2$, we identify the prefactors with the Fermi constant

$$\frac{G_F}{\sqrt{2}} = \frac{g_W^2}{8m_W^2}. \tag{12.44}$$

12.4 Flavour mixing

We can extend the formulation of the weak interaction to quarks by claiming each generation of leptons and quarks have a one-to-one correspondence:

$$\begin{pmatrix}\nu_e\\ e^-\end{pmatrix} \to \begin{pmatrix}u\\ d\end{pmatrix} \quad \text{and} \quad \begin{pmatrix}\nu_\mu\\ \mu^-\end{pmatrix} \to \begin{pmatrix}c\\ s\end{pmatrix} \tag{12.45}$$

This is the *lepton–quark symmetry principle*, which asserts that quarks of the same generation have exactly the same coupling constant as the corresponding generations of leptons:

$$g_W = g_{ud} = g_{cs} \quad \text{[no flavour mixing]} \tag{12.46}$$

This works well for reactions as pion decay

$$\pi^+ \to \mu^+ + \nu_\mu \quad \Leftrightarrow \quad (d\bar{u}) \to \mu^+ + \nu_\mu \tag{12.47}$$

But this seems to preclude reactions when flavour changes involve crossing generations such as

$$K^+ \to \mu^+ + \nu_\mu \quad \Leftrightarrow \quad (s\bar{u}) \to \mu^+ + \nu_\mu \tag{12.48}$$

Cabibbo remedied this theoretical problem by introducing primed versions of d and s quarks, which are the actual ones interacting with the weak force:

$$\begin{pmatrix} u \\ d' \end{pmatrix} \quad \begin{pmatrix} c \\ s' \end{pmatrix}, \tag{12.49}$$

where d' and s' undergo weak interactions by linear superpositions given by

$$\begin{pmatrix} d' \\ s' \end{pmatrix} = \begin{pmatrix} \cos\theta_c & -\sin\theta_c \\ \sin\theta_c & \cos\theta_c \end{pmatrix} \begin{pmatrix} d \\ s \end{pmatrix}. \tag{12.50}$$

Here we introduce the **Cabibbo angle**, which has a measured value of $\theta_c \simeq 13^\circ \approx \pi/14$ or equivalently $\sin\theta_W \simeq 0.22$. We recognise the matrix has the form of a rotation and is known as the Cabibbo matrix. The unprimed d and s quarks are identified as mass eigenstates i.e. that feel the Higgs boson. The primed d' and s' quarks are identified as the gauge eigenstates i.e. that feel the W gauge boson. We can illustrate the effect of this by considering an up quark interacting via the W boson. The up quark can actually annihilate with the observed d' and s' quarks (in the mass basis) as a superposition of the underlying d and s quarks (in the flavour basis) by:

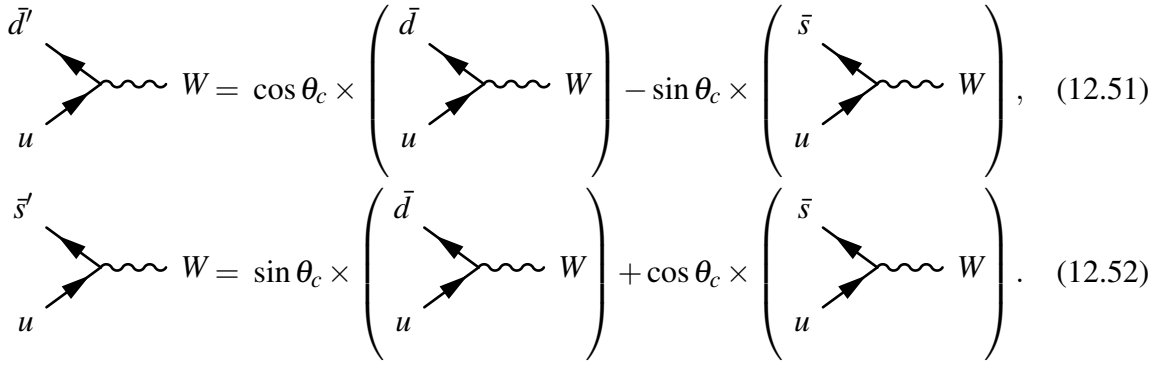

(12.51)

(12.52)

Accounting for this flavour mixing, we obtain the vertex factors

$$\begin{aligned} g_{ud} &= g_{cs} = g_W \cos\theta_c \\ g_{us} &= -g_{cd} = g_W \sin\theta_c \quad \text{[with flavour mixing]} \end{aligned} \tag{12.53}$$

So we interpret weak processes involving a change of generation in quark flavour have their coupling constants suppressed by a factor of $\sin\theta_c$. We shall see that this extends to the 3×3 Cabibbo–Kobayashi–Maskawa matrix in section 15.4.

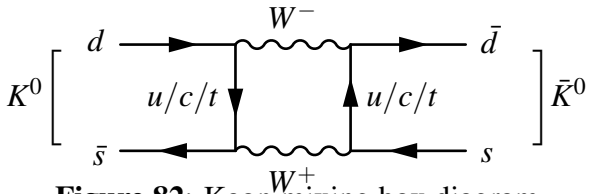

Figure 82: Kaon mixing box diagram.

12.5 Charge-parity violation in kaons

The evidence for broken charge-parity symmetry in nature was first observed in kaons. A consequence of quark mixing is that the neutral kaon $K^0 = d\bar{s}$ and its antiparticle $\bar{K}^0 = \bar{d}s$ can oscillate into each other via box diagrams (figure 82): The u quark can also be c and t but these are suppressed by the CKM matrix elements. These kaon oscillations were already first noticed by Gell-Mann and Abraham Pais in 1955 [85]. The Bettini textbook chapter 8 provides a lucid, more detailed account including kaon oscillations.

The kaons are pseudoscalars and have the transformation properties under parity P and charge conjugation C operations:

$$P|K^0\rangle = -|K^0\rangle, \quad C|K^0\rangle = |\bar{K}^0\rangle, \tag{12.54}$$

$$P|\bar{K}^0\rangle = -|\bar{K}^0\rangle, \quad C|\bar{K}^0\rangle = |K^0\rangle, \tag{12.55}$$

where charge conjugation swaps the quark charges $C|d\bar{s}\rangle = |\bar{d}s\rangle$. We can then construct eigenstates of CP operators:

$$|K_{\text{even}}\rangle = \frac{1}{\sqrt{2}}(|K^0\rangle - |\bar{K}^0\rangle), \quad CP \text{ even}, \tag{12.56}$$

$$|K_{\text{odd}}\rangle = \frac{1}{\sqrt{2}}(|K^0\rangle + |\bar{K}^0\rangle), \quad CP \text{ odd}. \tag{12.57}$$

We call these the CP-even ($CP|K_{\text{even}}\rangle = |K_{\text{even}}\rangle$) and CP-odd ($CP|K_{\text{odd}}\rangle = -|K_{\text{odd}}\rangle$) eigenstates, which you can verify by directly applying (12.55). To respect CP symmetry, there should be two different decays distinguished by their pion decay multiplicity:

$$K_{\text{even}} \to \pi\pi, \quad \text{CP even} \tag{12.58}$$

$$K_{\text{odd}} \to \pi\pi\pi, \quad \text{CP odd}. \tag{12.59}$$

To work out the CP transformation of decaying pions, we consider the operations of charge conjugation combined with intrinsic and orbital parity:

$$CP = C \times P_{\text{intrinsic}} \times P_{\text{orbital}}. \tag{12.60}$$

Stepping through the two and three pion decays separately:

- **Two-pion systems are CP even**: $CP|\pi\pi\rangle = +|\pi\pi\rangle$.

  We first see each pion is a pseudoscalar so has intrinsic parity -1, so a pair of pions has even parity

  $$P_{\text{intrinsic}}(\pi\pi) = (-1)^2 = +1. \tag{12.61}$$

  The two pions decay from a spin-zero kaon so the orbital angular momentum is $L = 0$, giving a total parity of

  $$P_{\text{orbital}}(\pi\pi) = (-1)^L = +1. \tag{12.62}$$

  We then consider C for the neutral and charged pairs separately:

  – *Neutral pair* $|\pi^0\pi^0\rangle$: neutral pions comprise a superposition of same-flavour quarks $|\pi^0\rangle = \frac{1}{\sqrt{2}}(|u\bar{u}\rangle - |d\bar{d}\rangle)$, so are individually even under the charge conjugation $C = +1$. The pair of neutral pions then has

  $$C(\pi^0\pi^0) = +1. \tag{12.63}$$

  Therefore, $|\pi^0\pi^0\rangle$ is CP-even.

  – *Charged pair* $|\pi^+\pi^-\rangle$: charge conjugation is equivalent to swapping their spatial positions, which is the same as a parity operation $C|\pi^+\pi^-\rangle = |\pi^-\pi^+\rangle = P|\pi^+\pi^-\rangle = (-1)^L$. Given $L = 0$, we find

  $$C(\pi^+\pi^-) = +1. \tag{12.64}$$

  Therefore, $|\pi^+\pi^-\rangle$ is also CP-even.

- **Three-pion systems are CP odd**: $CP|\pi\pi\pi\rangle = -|\pi\pi\pi\rangle$.

  The intrinsic parity of three pions is odd

  $$P_{\text{intrinsic}}(\pi\pi\pi) = (-1)^3 = -1. \tag{12.65}$$

  We now consider P_{orbital} and C separately for the cases with and without charged pions:

  – *Neutral triplet* $|\pi^0\pi^0\pi^0\rangle$. This is even under charge conjugation

  $$C(\pi^0\pi^0\pi^0) = (+1)^3 = +1. \tag{12.66}$$

  For orbital angular momentum, there are two independent axes: L_1 for the first pair orbiting each other, and L_2 for the third pion orbiting the first pair. So the orbital parity is $P_{\text{orbital}}(\pi^0\pi^0\pi^0) = (-1)^{L_1} \times (-1)^{L_2}$. Angular momentum sums

according to the usual rules of quantum-mechanical addition $|L_1+L_2|, |L_1+L_2-1|, \ldots |L_1-L_2|$. This can only include the spin-zero of the initial kaon if $L_1 = L_2$, implying orbital parity is always even

$$P_{\text{orbital}}(\pi^0\pi^0\pi^0) = (-1)^{2L_1} = +1. \tag{12.67}$$

Therefore, $|\pi^0\pi^0\pi^0\rangle$ is CP-odd.

– *Charged triplet* $|\pi^+\pi^-\pi^0\rangle$. Like the $|\pi^0\pi^0\pi^0\rangle$ case, the total orbital angular momentum being zero again constrains $L_1 = L_2$ such that orbital parity is even

$$P_{\text{orbital}}(\pi^+\pi^-\pi^0) = (-1)^{2L_1} = +1. \tag{12.68}$$

Charge conjugation of π^0 is still even but the charged pair is now more subtle. We still have $C(\pi^+\pi^-) = P(\pi^+\pi^-) = (-1)^{L_1}$ but unlike the two-pion case (12.64), L_1 is now no longer fully constrained to be zero. Nonetheless, we can invoke kinematic arguments. The three-pion system has very little phase space because of the small mass difference $m(K^0) - 2m(\pi^\pm) - m(\pi^0) \approx 498 - 2\times 139.6 - 135 \approx 83$ MeV. The $L_1 = 1$ case is therefore highly suppressed because the three pions must share the low kinetic energy and requires significant impact parameter. Therefore, the zero orbital angular momentum state $L_1 = 0$ dominates. This leads to the charge conjugation to be even

$$C(\pi^+\pi^-\pi^0) = P(\pi^+\pi^-)\times C(\pi^0) \simeq (-1)^{L=0}\times(+1) = +1. \tag{12.69}$$

Therefore, the combined $|\pi^+\pi^-\pi^0\rangle$ state is well approximated to be CP-odd.

The two states K_{even} and K_{odd} mix into two experimentally distinct states distinguishable by their lifetimes. We call the observed mass eigenstates of neutral kaons "K-short" K^0_{short} and "K-long" K^0_{long}. Their decay lifetimes differ strikingly by three orders of magnitude due to phase space differences Δm:

$$K^0_{\text{short}} \to \pi\pi, \quad \Delta m(K, 2\pi) \approx 220 \text{ MeV}, \quad \tau_{\text{rest}}(K^0_{\text{short}}) \approx 9\times 10^{-11} \text{ s}, \tag{12.70}$$

$$K^0_{\text{long}} \to \pi\pi\pi, \quad \Delta m(K, 3\pi) \approx 90 \text{ MeV}, \quad \tau_{\text{rest}}(K^0_{\text{long}}) \approx 5\times 10^{-8} \text{ s}. \tag{12.71}$$

If nature respected CP, the observed mass eigenstates would equal these CP eigenstates distinguished by pion multiplicity:

$$K^0_{\text{short}} = K_{\text{even}}, \quad K^0_{\text{long}} = K_{\text{odd}}, \quad \text{CP conservation condition.} \tag{12.72}$$

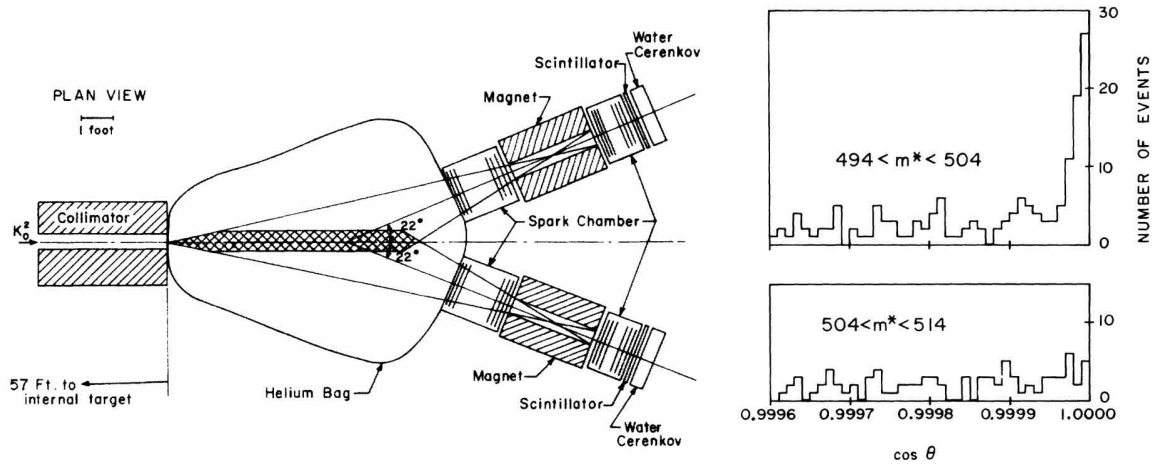

(a) Experimental apparatus (b) Di-pion system

Figure 83: **Experiment discovering kaon CP violation**. Note K_0^2 is what we call the K_{long}. The plot shows the pion invariant mass distributions at high scattering angle $\cos\theta > 0.9995$ inside for signal (upper) and above (lower) the kaon mass to estimate background; the peak shows the two pions originate from a kaon. Diagrams from Ref. [86].

To test this hypothesis, J. Christenson, James Cronin, Val Fitch, and Rene Turlay constructed an experiment at the Brookhaven Alternating Gradient Synchrotron (AGS) in 1964 [86]. Protons accelerated to 30 GeV bombard a Be target, and a resulting beam of neutral kaons enter an 18 m decay chamber. For relativistic kaons with energy greater than a few GeV, the decay length $c\tau_{\text{rest}}$ for K^0_{short} and K^0_{long} is 2.7 cm and 15.6 m, respectively, so nearly all the short-lived K^0_{short} states decay. The exiting beam is then highly pure in K^0_{long}, so they could observe if K^0_{long} indeed decayed to three pions and thus respected CP conservation.

Instead, they produced a high-statistics K^0_{long} sample and counted a significant number of two-pion decays:

$$\frac{N(K^0_{\text{long}} \to \pi^0\pi^0) + N(K^0_{\text{long}} \to \pi^+\pi^-)}{N(K^0_{\text{long}} \to \text{all decays})} = \frac{45}{22\,700} \neq 0. \tag{12.73}$$

Therefore, CP symmetry is not conserved in weak decays. Historically, this was an utterly shocking discovery. This 0.2% deviation from the CP conservation condition (12.72), $K^0_{\text{short}} \neq K_{\text{even}}, K^0_{\text{long}} \neq K_{\text{odd}}$, identifies the mass eigenstates as a small ε superposition of the

CP-violating contribution:

$$|K^0_{\text{short}}\rangle = \frac{1}{\sqrt{1+\varepsilon^2}}(|K^0_{\text{even}}\rangle - \varepsilon|K^0_{\text{odd}}\rangle), \tag{12.74}$$

$$|K^0_{\text{long}}\rangle = \frac{1}{\sqrt{1+\varepsilon^2}}(|K^0_{\text{even}}\rangle + \varepsilon|K^0_{\text{odd}}\rangle), \tag{12.75}$$

with $\varepsilon \approx 2 \times 10^{-3} \neq 0$ measured. While this effect is at a subtle per-mille level in the neutral kaon system, an analogous but larger effect is also observed in B-mesons. While it is far from obvious from these first observations, the existence of CP violation in the quark sector requires there to be at least three generations of quarks. We shall see the modern prescription of CP violation in the quark sector arising from one complex phase in the Cabibbo–Maskawa–Kobayashi matrix in section 15.4.

13 City-sized collider experiments

Unveiling the dynamics at the electroweak scale requires constructing colliders the size of cities and detectors the size of cathedrals. The reason we require such powerful machines to explore this sector is because of high energies required to probe the large $\mathcal{O}(100\ \text{GeV})$ mass scales and intense beam luminosities to probe the comparatively rare event rates of electroweak interactions.

13.1 High energy accelerators

Table 5 shows some notable particle colliders. The Large Electron Positron Collider and Large Hadron Collider (LHC) are the largest synchrotons constructed to date, with a circumference of 27 km (figure 84). That is around the length of the Circle Line of the London Tube underground train system, which surrounds inner London. The tunnels house the magnets that steer the beams around the ring and into each other at the interaction points (figure 85). The LHC has and operates up to a centre-of-mass energy of $\sqrt{s} = 13.6$ TeV, and is set for upgrades to the High-Luminosity LHC in 2026.

Collider	Lab	Beams	$\sqrt{s_{\text{max}}}$	Operational	Length	Experiments
PETRA	DESY	e^-e^+	46 GeV	1978–1986	2.3 km	JADE, MARK-J, PLUTO, TASSO
SLC	SLAC	e^-e^+	100 GeV	1989–1998	3.2 km	SLD
LEP	CERN	e^-e^+	209 GeV	1989–2000	27 km	ALEPH, DELPHI, L3, OPAL
HERA	DESY	e^-p	320 GeV	1992–2007	6.3 km	H1, HERMES, HERA-B, ZEUS
SppS	CERN	$p\bar{p}$	400 GeV	1981–1991	6.9 km	UA1, UA2
Tevatron	FNAL	$p\bar{p}$	1.96 TeV	1983–2011	6.3 km	CDF, DZero
LHC	CERN	pp	13.6 TeV	2008–2026	27 km	ALICE, ATLAS, CMS, LHCb

Table 5: **Notable high-energy particle colliders**. The full names are: Positron–Electron Tandem Ring Accelerator (PETRA), Stanford Linear Collider (SLC), Large Electron Positron Collider (LEP), Hadron–Electron Ring Accelerator (HERA), Super Proton–Antiproton Synchrotron (SppS), Large Hadron Collider (LHC).

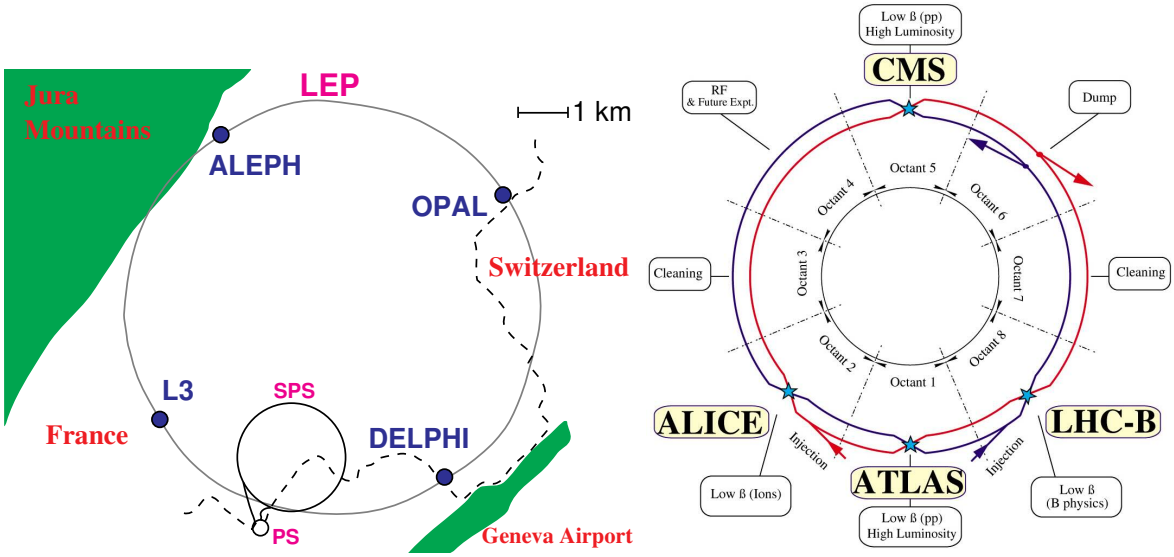

(a) Large Electron Positron Collider (b) Large Hadron Collider

Figure 84: **LEP and LHC layout at CERN**. Layout of the largest synchrotron constructed to date at 27 km circumference located at Geneva, Switzerland. Displayed are the Large Electron Positron (LEP) Collider, which was superseded by the Large Hadron Collider. Each collider has four interaction points where collisions occur and experiments are installed. The Proton Synchrotron (PS) and Super Proton Synchrotron (SPS) serve as lower-energy beam injectors into LEP and the LHC. Figures from Refs. [87, 88].

The Barr et. al. *Particle Physics in the LHC Era* textbook [1] unsurprisingly provides excellent detailed coverage of experimental aspects of collider physics, which we summarise in this section. We focus on the LHC and ATLAS as concrete examples of contemporary experiments, but the principles they illustrate readily generalise to other operational particle physics experiments.

13.2 Particle interactions with matter

We detect a particle via its interactions with matter. Detectors are thus built to fully exploit these known behaviours.

Ionisation Charged particles can liberate electrons from atoms, creating positive ions and free electrons while the incident particle loses energy. The rate of ionisation depends on the velocity $\beta\gamma$ of incident particles of charge z traversing through a material with mass density ρ, atomic number Z and atomic mass A. In 1930, Hans Bethe derived the mean rate of energy

(a) CERN LHC aerial view [89]

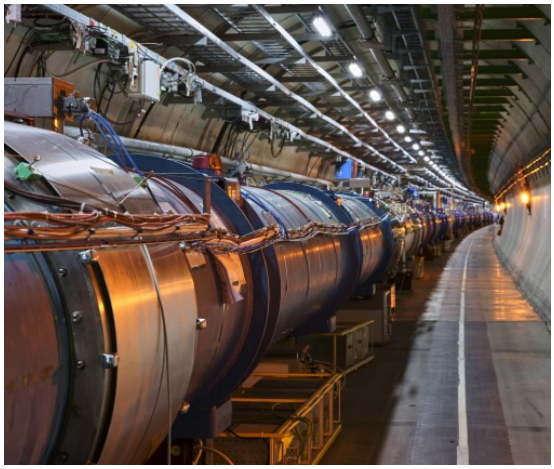

(b) LHC tunnel [90]

Figure 85: **CERN aerial view of LHC**. Photo from 2008 and tunnel of the Large Hadron Collider (LHC), which also housed the Large Electron Positron (LEP) Collider. The city of Geneva, Switzerland alongside the Alps mountain range are visible in the background.

loss per unit length $\langle \mathrm{d}E/\mathrm{d}x \rangle$ [MeV cm^{-1}] of the incident charged particle on material[58]:

$$\left\langle \frac{\mathrm{d}E}{\mathrm{d}x} \right\rangle \approx \underbrace{\left(\rho \frac{Z}{A}\right)}_{\text{target}} \left(4\pi N_A r_e^2 m_e\right) \frac{z^2}{\beta} \left[\ln\left(\frac{2m_e(\beta\gamma)^2}{I_e} \right) - \beta^2 \right]. \tag{13.1}$$

The only terms that depend on the target material properties are $\rho Z/A$, along with the effective ionisation potential I_e averaged over the electrons for the materials' atoms, given approximately by $I_e \approx 10 \cdot Z$ eV. The linear Z/A dependence is crucial for selecting materials as we want to increase the material's atomic charge Z to mass number A ratio for increased $\mathrm{d}E/\mathrm{d}x$ energy loss rate. The other proportionality constants are Avogadro's number N_A, electron mass m_e, and what is called the *classical electron radius* r_e given by

$$r_e = \frac{e^2}{4\pi\varepsilon_0 m_e c^2}. \tag{13.2}$$

Figure 86 shows this for a single charged particle traversing through liquid hydrogen, helium gas, carbon, aluminium, iron, tin, and lead. Using $\beta\gamma = \frac{p}{mc}$, we can translate the horizontal axis into the muon, pion, and proton momentum. Ionisation is strongest for low particle velocity, shown by the sharp rise at low $\beta\gamma$ and a flatter $\mathrm{d}E/\mathrm{d}x$ at high $\beta\gamma$. There is a broad minimum at around $\beta\gamma \approx 3$, and particles with such values are called **minimum**

[58] This is often called the Bethe or Bethe–Bloch formula.

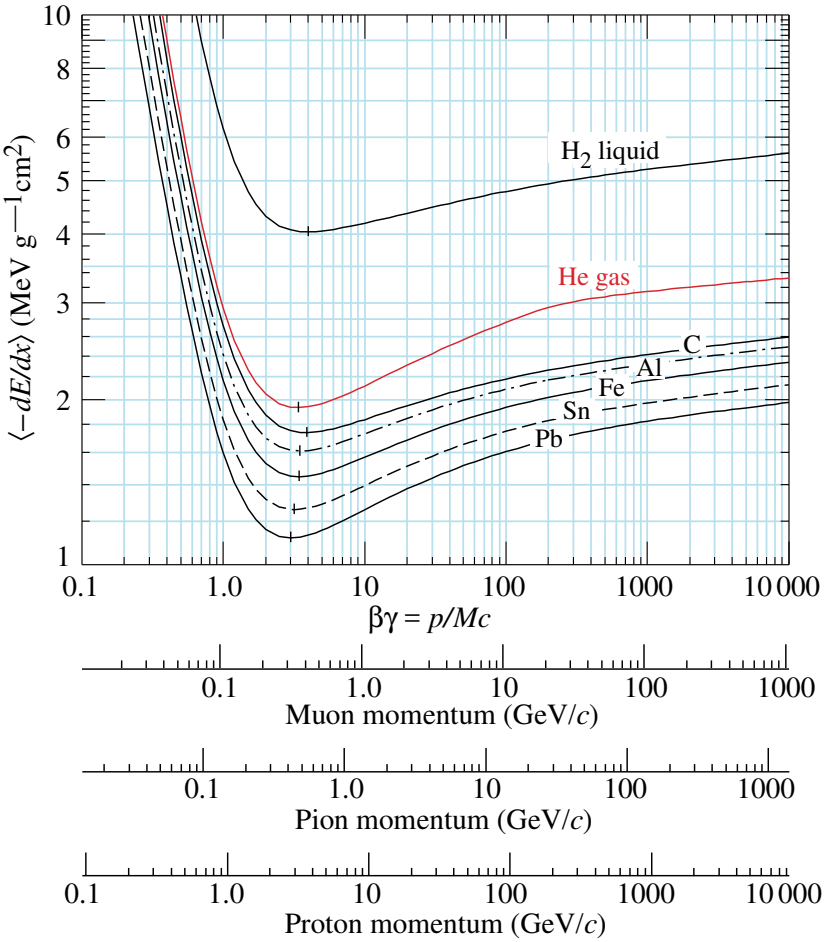

Figure 86: **Particle stopping power by material**. Stopping power $\mathrm{d}E/\mathrm{d}x$ for muon and by material from Ref. [75].

ionising particles (MIPs), which often applies to muons at colliders. At low $\beta\gamma$, the energy loss is dominated by the logarithm term and the large electromagnetic cross-section relative to the atom's ionization energy I_e. At relativistic energies, incident particles can interact with atoms deeper into the material.

Bremmstrahlung The Bethe–Bloch formula (13.1) applies to electrons and positrons at low energies. But above a critical energy E_c, the energy loss is dominated by bremsstrahlung "braking radiation", whereby the incident electron radiates a photon when bending around an atomic nucleus. This is approximately inversely proportional to the atomic number

$$E_c \approx \frac{800\ \mathrm{MeV}}{Z}. \tag{13.3}$$

At the LHC, electrons typically carry GeV-scale energies so bremsstrahlung energy losses dominate. Bremsstrahlung occurs for all charged particles but is most notable for electrons because energy loss is inversely proportional to the particle mass squared, so is a factor of $(m_e/m_\mu)^2 \approx 0.005$ rarer for muons.

When photons are radiated off, these photons can also interact electromagnetically. For energies $E_\gamma \gtrsim 1$ MeV, Compton scattering $\gamma e^- \to \gamma e^-$ becomes significant. When photon energies reach $E_\gamma \gtrsim 10$ MeV, pair creation dominates, where the photon scatters off a nucleus to undergo pair creation $\gamma N \to e^+ e^- N$.

These electron/positron/photon interactions create an **electromagnetic shower** characterised by a **radiation length** X_0. The rate of energy lost by per unit length is given by

$$\frac{\mathrm{d}E}{\mathrm{d}x} = -\frac{E}{X_0}, \quad \Rightarrow \quad E(x) = E_{\text{initial}} \mathrm{e}^{-x/X_0}. \tag{13.4}$$

The most salient features of X_0 are captured in an approximate expression

$$\frac{1}{X_0} \approx 4\alpha_{\text{EM}} n Z^2 r_e^2 \ln\left(\frac{287}{\sqrt{Z}}\right), \tag{13.5}$$

where n is the nuclei number density. Crucially, we see dependence Z^2 dependence allows short radiation lengths using high atomic number materials. Example radiation lengths for heavy materials are $X_0(\text{iron}) = 1.76$ cm and $X_0(\text{lead}) = 0.56$ cm.

13.3 Detectors for terascale physics

Detectors like ATLAS and CMS (figure 87) at the LHC contains many layers with various functions (figure 91). They typically comprise an cylindrical geometry with onion-like structures from inside to outside: (i) precision trackers with high spatial resolution surrounding the interaction point, (ii) electromagnetic (ECal) and hadronic (HCal) calorimeters for energy measurement, (iii) muon systems on the outside.

Trackers for charged-particle measurements

These measure the charge and sample the positions where charged particles pass allowing a track to be reconstructed. Bathed in a uniform magnetic field, this reconstructs the paths of muons, electrons and hadrons. More specifically, the charge to momentum ratio q/p of charged particles, whose radius of curvature $r \propto B(q/p)$ in a magnetic field strength of B. It is made from silicon pixels with strips surrounding it, designed to withstand large doses of radiation. It has a resolution of around 10μm. Long-lived particles such as B-mesons

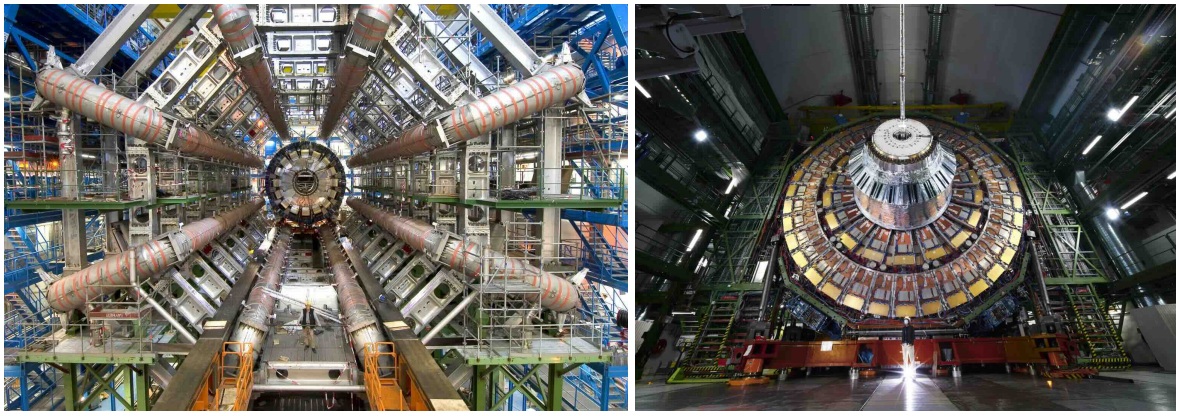

(a) ATLAS detector (b) CMS detector

Figure 87: **Photos of ATLAS and CMS detectors**. Roger Ruber is pictured standing at the bottom of the famous ATLAS photo. Images: CERN-EX-0511013 , CERN-PHOTO-202108-102.

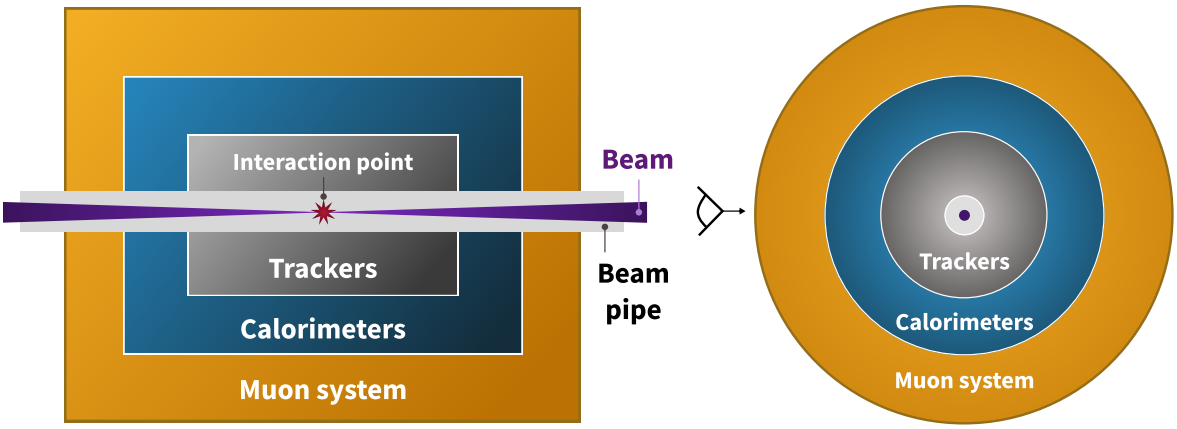

Figure 88: **Schematic of general collider detector**. The layout shows the beam interaction point, comprising the beam pipe, trackers, calorimeters, and muon chambers. The hadronic calorimeter (HCal) surrounds the electromagnetic calorimeter (ECal). Right shows the cross-section looking down the beam pipe.

containing b quarks have rest lifetimes around $\tau(B) \approx 10^{-12}$ s, leading to a finite measurable distance $c\tau(B) \approx 3 \times 10^{8}$ m s$^{-1} \times 10^{-12}$ s ≈ 0.3 mm, which increases with boost $\gamma c\tau$. So a tracker with spatial resolution of $\mathcal{O}(10\ \mu\text{m})$ can resolve the displaced tracks as the B-meson decays to tag the object as originating from a b quark.

The general principle of tracking is to measure the charge and positions of where the particles passed. This allows deduction charge to momentum ratio and radius of curvature.

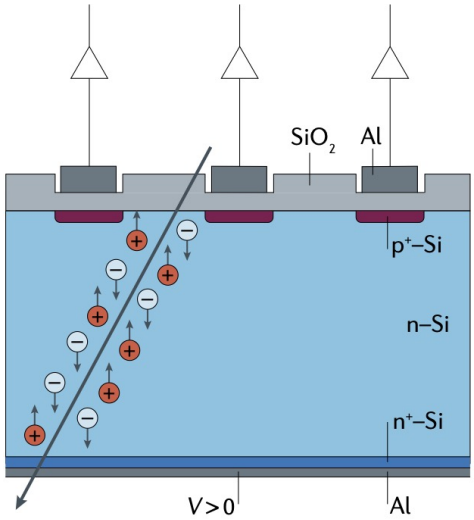

Figure 89: **Silicon sensor schematic**. This showing the principle of detection from Ref. [91].

Ideally, the tracking minimises the interactions with the charged particles it is trying to reconstruct. This allows for accurate energy momentum measurement in the calorimeter. This is primarily done through:

- **Semiconductor trackers**. Silicon can be doped to create p-n junctions (figure 89), the former with a deficit and latter with a surplus of electrons. Passing charged particles ionise the semiconductor, leaving electron–hole pairs in its path. A large reverse-bias potential difference is applied, and the holes drift with the induced electric field. These are collected at p–n junctions where an electrical signal is measured so the charge and position of the particle is determined. Two varieties of silicon trackers are used: strips and pixel detectors. Silicon strips are separated by order $\sim 25\,\mu$m while pixels give a precise position in 2 dimensional space. These can furthermore provide sensitivity to secondary vertices from delayed decays of b hadrons.

- **Gas/wire drift chambers** . This comprises array of wires, each filled with a gas such as argon-ethane. Charged particles ionise the gas and the electrons liberated from the atoms drift towards a positive anode. This is converted to an electrical signal, which is used to determine the charge of the particle and its position.

- **Muon chambers**. These are essentially large-scale tracking detectors that surround the exterior of the calorimeters. They are typically gaseous detectors, given they are more cost-effective than solid-state technology for the large required surface areas. Essentially a heavier version of the electron, muons do not interact strongly with the inner

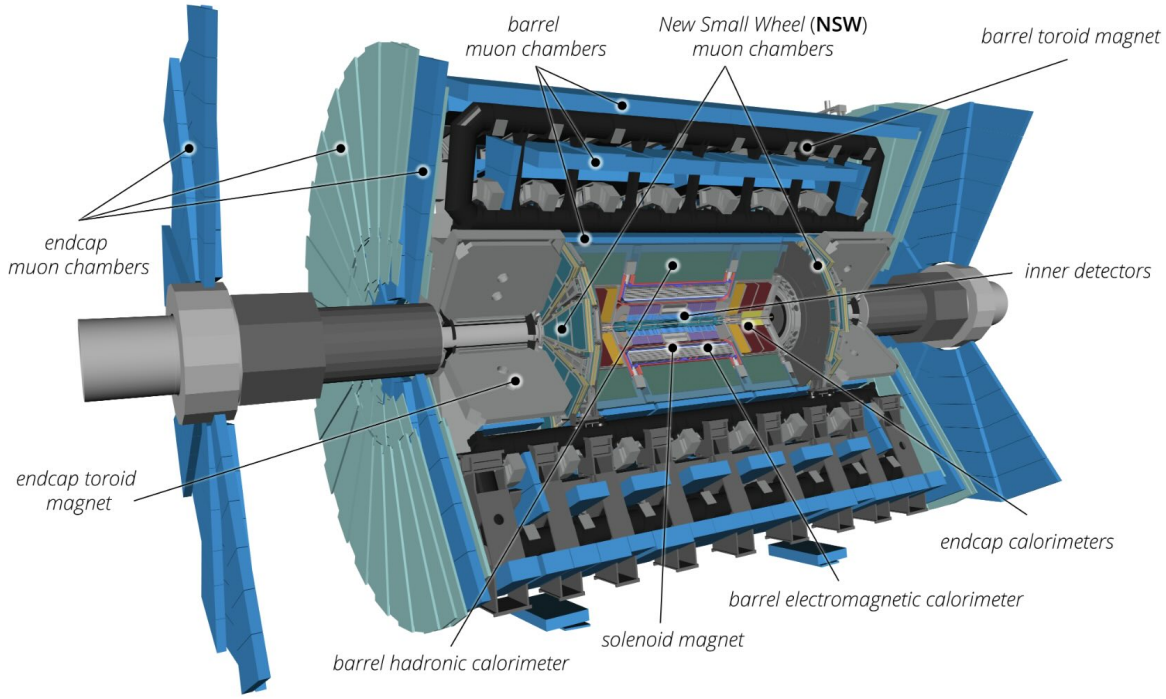

Figure 90: **ATLAS Experiment layout**. The components exemplifies a modern collider detector from Ref. [92].

calorimeters. Powerful magnets bend the muons allowing momentum measurement upon matching with trackers. New long-lived charged particles beyond the Standard Model could show up as an excess against these muons.

Calorimeters for energy measurement

These measure the kinematics of electrons and photons. These are made from crystals or liquid argon that scintillate when electrons or photons pass through. Light is emitted proportional to the particle's energy, which is converted to an electric signal for amplification.

Electromagnetic calorimeters use heavy high Z materials to stop and measure the energies of electrons and photons. In the CMS detector, they use an inorganic scintillator made of lead tungstate ($PbWO_4$) crystals, arranging 75,000 of them into a dense array. These are optically transparent and owing to a short stopping length of $X_0 = 0.83$ cm, the electromagnetic showers are contained within a compact space. Photon detectors amplify the scintillation light, which is proportional to the total energy of the incoming electron or photon. The

typical energy resolution is of the order of percent:

$$\frac{\sigma_E}{E} \sim \frac{3\% - 10\%}{\sqrt{E/\mathrm{GeV}}}. \tag{13.6}$$

Hadronic calorimeters measure kinematics of the strongly interacting hadrons, made of quarks and gluons that are emitted in collisions. Hadrons interact with dense absorbers which trigger showers into a cascade of further particles. There is also scintillators that fluoresce, whose signal is amplified by photodetectors. Many models of supersymmetry have supersymmetric particles that are coloured and hence hadronise. The comparatively larger internuclear distance of traversing hadrons usually means this calorimeter to be much larger than the electromagnetic calorimeter. A sandwich formation is typically employed: the hadronic showers develop in thick layers of highly dense absorbers, while the energies of the charged particles are measured in thinner layers of active material. The ATLAS experiment contains alternating layers of steel absorbers and plastic scintillator tiles. We then sum the signals arising from the different layers is then summed to give the total energy of the hadronic activity. Hadronic calorimeters typically have order of magnitude coarser energy resolution relative to the electromagnetic counterpart

$$\frac{\sigma_E}{E} \gtrsim \frac{50\%}{\sqrt{E/\mathrm{GeV}}}. \tag{13.7}$$

Triggering

The LHC has an operational energy of 13.6 TeV and luminosity of $10^{34}\,\mathrm{cm}^{-2}\,\mathrm{s}^{-1}$ and typical total cross-sections of 10^8 nb. The bunch spacing is 25 ns, which translates into a collision rate at the LHC is 40 MHz. Storing all events is therefore practically impossible. Modern collider experiments therefore employ a **trigger** to rapidly decide which interesting events to store permanently. In the end, only $1/40\,000$ events that occurred are actually stored for analysis. With such a high rejection ratio, it is important to understand what new physics signatures could look like in hadronic collisions. Even after this enormous rejection, the LHC records some $\approx 10^{16}$ bytes (15 000 terabytes) per year. ATLAS and CMS use a two-level trigger system:

- **First-level hardware trigger ("Level-1, L1")**: 40 MHz $\rightarrow$ 100 kHz event rate. Hardware processors seek high momentum signatures e.g. large p_T leptons and have lower resolution information from the calorimeter or muon systems to relay this to the counting room extremely quickly. The hardware trigger is fast, taking at most 2.5 microseconds to perform calculations about the event. The price for this speed is that it requires

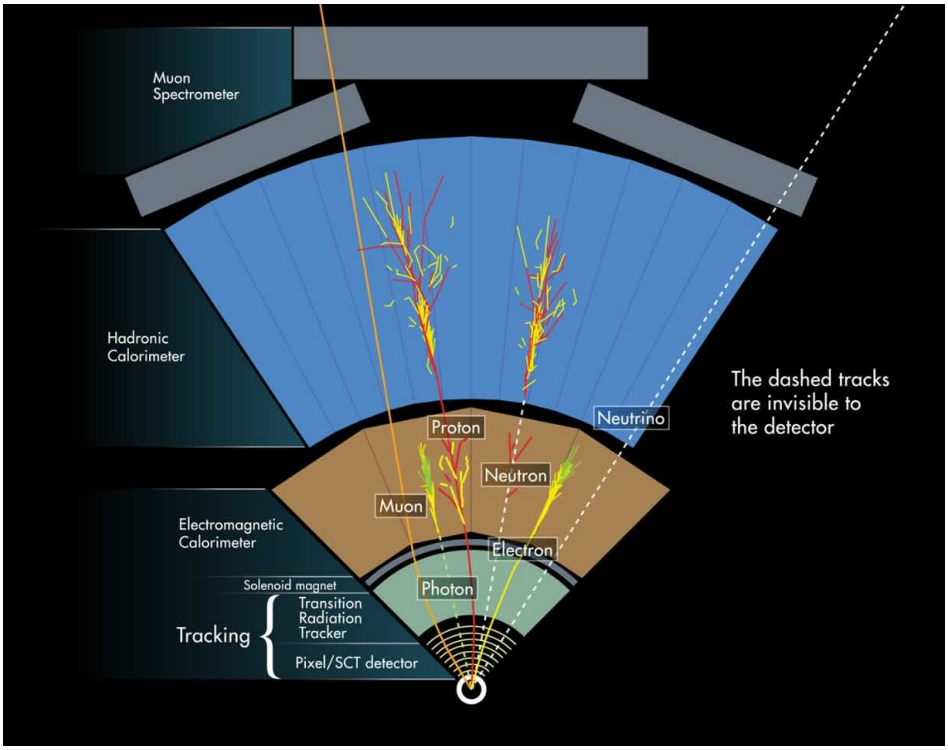

Figure 91: Particles traversing through the various subsystems of the ATLAS detector [93].

lower-level firmware programming and the event information is coarser than the software trigger.

- **Second-level software trigger ("High-level, HLT")**: 100 kHz $\rightarrow$ 1 kHz event rate. The HLT uses a large farm of 40,000 CPU cores with more configurable software code than the L1 trigger. This can utilise event information and perform basic particle reconstruction from the whole detector with higher granularity than the L1 trigger. This selects around 1000 events per second to be recorded permanently.

The trigger's primary objective is to determine if objects are *above threshold* e.g. if an electron is $p_{\mathrm{T}} > 25$ GeV rather than measuring with high precision. Events that fail to pass a trigger will never be recorded, so it is important to keep triggers as loose as possible.

13.4 Collider kinematics

At hadron colliders, the beam centre-of-mass frame does not usually coincide with the centre-of-mass frame of the interaction because protons are not fundamental particles. Only the energy and momentum $(E, \mathbf{p})$ **transverse** to the beam direction can be reliably measured. Fur-

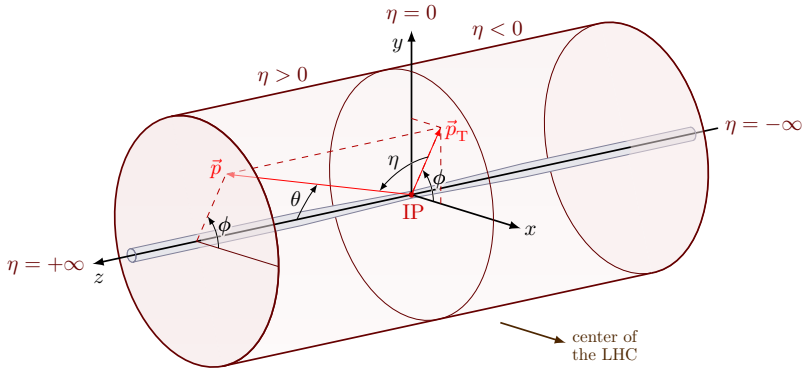

Figure 92: LHC detector coordinate system from Izaak Neutelings.

thermore, the cylindrical nature of collider detectors make cylindrical coordinates (p_T, θ, ϕ) more natural (figure 92), where θ and ϕ are the usual polar and azimuthal angles of a right-handed coordinate system. So conventionally the x direction is towards the centre of the LHC and y is towards the sky. The transverse three-momentum

$$p_{\mathrm{T}} = |\mathbf{p}| \sin\theta \tag{13.8}$$

is indeed Lorentz invariant under longitudinal boosts and has an intuitive interpretation. We can *define* the transverse energy associated with this transverse momentum

$$E_{\mathrm{T}} = E \sin\theta \tag{13.9}$$

along with the **transverse mass**

$$m_{\mathrm{T}} = \sqrt{E_{\mathrm{T}}^2 - p_{\mathrm{T}}^2}. \tag{13.10}$$

(Pseudo-)rapidity Now the polar angle θ is not boost invariant in the longitudinal direction. The reason we use the rapidity is that it is Lorentz invariant under longitudinal boosts, unlike the polar angle θ. We can define the **rapidity** y of a particle with energy E and longitudinal momentum p_z to be

$$y = \frac{1}{2} \log\left(\frac{E + p_z}{E - p_z}\right) = \tanh^{-1}\left(\frac{p_z}{E}\right). \tag{13.11}$$

For ultrarelativistic or massless particles, the rapidity limits to a quantity called the **pseudo-rapidity** η, which is still a (longitudinally) boost invariant parametrisation of the polar angle θ

$$\eta \equiv \frac{1}{2} \ln\left(\frac{1 + \cos\theta}{1 - \cos\theta}\right) = \ln\left(\cot\frac{\theta}{2}\right). \tag{13.12}$$

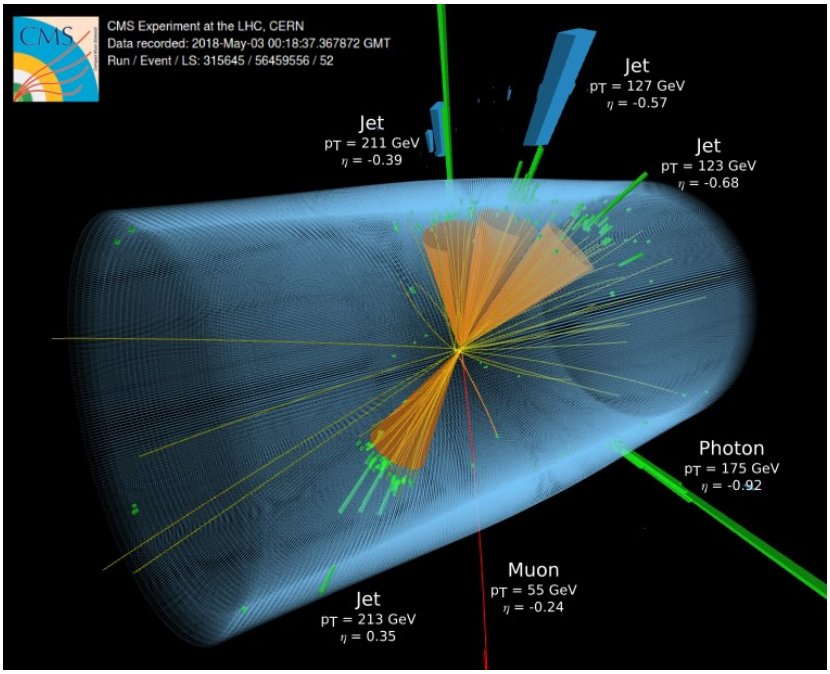

Figure 93: CMS event display where different objects are annotated by their identity, transverse momentum p_{T} and pseudorapidity η. Four hadronic jets as orange cones, one photon as a green electromagnetic calorimeter deposit, and one muon as the red line appear in this event. From CMS-PHO-EVENTS-2021-005.

We have that $\eta = 0$ is transverse to the beam while $\eta \to \pm\infty$ is parallel to the beam direction and $\theta = 45^\circ$ is about $\eta \simeq 0.88$. Lastly, ϕ is the azimuthal angle in the transverse plane to the beam.

We define η to make the detector have higher resolution in directions transverse to the beam. Interesting objects produced from hard collisions are usually ejected in the more transverse directions. The surface surrounding the detector is divided into $\Delta\eta$ and $\Delta\phi$, which coincides with how the detector components are segmented into **cells**. The region $\eta \lesssim 2.5$ is referred to as 'central' while the region $\eta \gtrsim 2.5$ towards the beam is called 'forward', which corresponds to a polar angle of $\theta \simeq 10^\circ$ from the beam direction.

We usually define the cone opening angle for objects like jets by

$$\Delta R = \sqrt{(\Delta\eta)^2 + (\Delta\phi)^2}. \tag{13.13}$$

Central jets usually have $\Delta R \sim 0.4$ Recombination algorithms used to reconstruct jets can adjust this ΔR parameter according to what kind of jets we want to analyse.

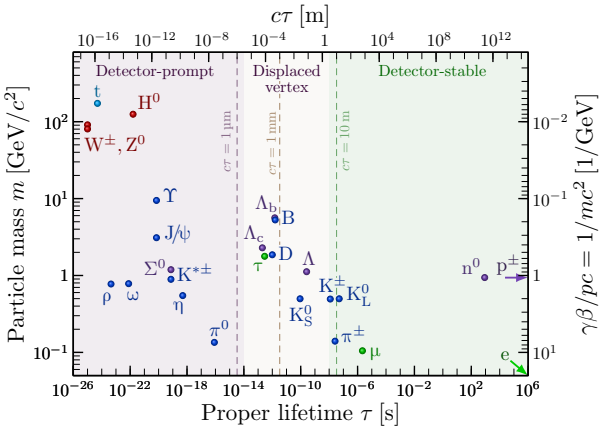

(a) SM particle proper lifetimes

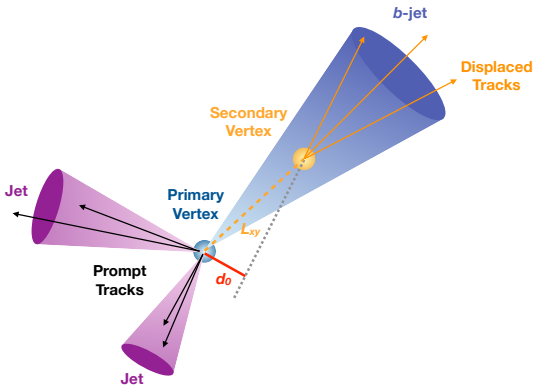

(b) Displaced vertex schematic

Figure 94: Prompt, displaced vertex, stable signatures of Standard Model particles. Proper lifetime τ and decay length $c\tau$ of particles relative to detector geometry from tikz.net. Metastable particles such as a B-hadron gives secondary vertices with finite impact parameters for heavy-flavour jet tagging from Ref. [94].

13.5 Particle identification

There are actually only a subset of the Standard Model particles we observe in modern collider detectors. Heavy states like the $W^{\pm}, Z, h$ bosons and top quark decay promptly at time scales of

$$t_W \sim \frac{1}{\Gamma} \sim \frac{1}{2\,\text{GeV}} \simeq 3.3 \times 10^{-25}\,\text{s}. \tag{13.14}$$

The lighter quarks hadronise due to QCD confinement at time scales governed by the QCD scale

$$t_{\text{QCD}} \sim \frac{1}{\Lambda_{\text{QCD}}} \simeq \frac{1}{200\,\text{MeV}} \simeq 3.3 \times 10^{-24}\,\text{s}. \tag{13.15}$$

These processes happen instantaneously relative to the capabilities of detector technologies, which are typically on the order of 0.1 to 10s of nanoseconds, depending on the detection technology. Unstable particles have a decay length of

$$d = \gamma\beta c\tau_{\text{rest}} \simeq \gamma(300\,\mu\text{m})\left(\frac{\tau_{\text{rest}}}{10^{-12}\,\text{s}}\right). \tag{13.16}$$

With these detectors in place, the signatures of standard LHC objects are illustrated in figure 91:

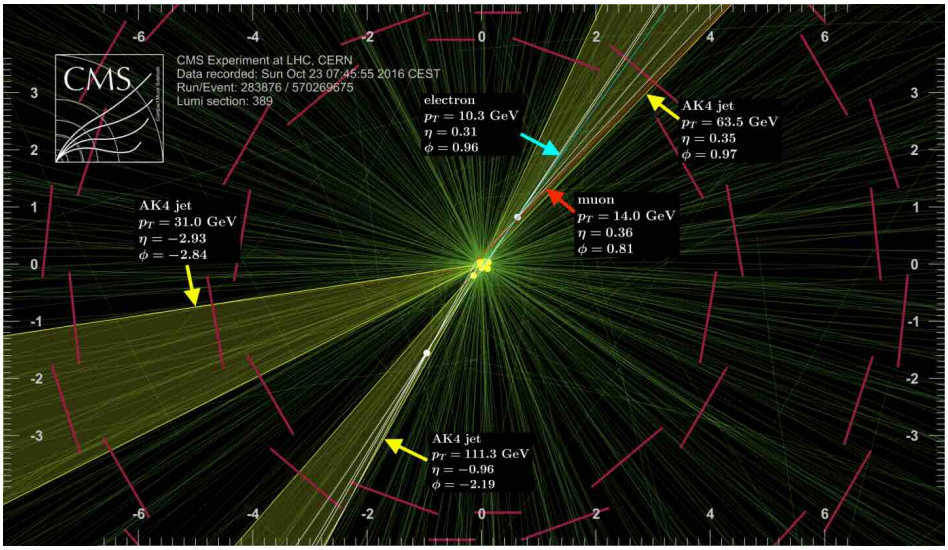

Figure 95: Event display from 2016 data collected at 13 TeV from the CMS Experiment showing displaced heavy-flavour tracks from CMS-PHO-EVENTS-2017-006. This is shown in *x*-*y* projection with the beam pipe into page. Three jets coloured yellow, one displaced muon, and one displaced electron tracks. Faint green lines show tracks with $p_{\mathrm{T}} > 0.5$ GeV. Yellow dots show the 44 primary vertices due to pileup. Displaced secondary vertices are white dots. The pink lines show the pixel detector.

- **Electrons and positrons** $e^{\pm}$: charged track with significant energy deposition in electromagnetic calorimeter and little to no hadronic activity.

- **Photons**: same as $e^{\pm}$ without corresponding hits in tracker.

- **Muons**: charged tracks in tracker, little to no deposition in calorimeters, activity in muon chambers.

- **Hadronic jets**: at ATLAS and CMS, collections of collimated hadrons are usually identified as a jet rather than individual hadrons. This allows an identification to the original hard quark or gluon that showers and hadronises. The signature is a conical spray of charged tracks left in tracker spatially correlated with significant energy deposition in both electromagnetic and hadronic calorimeters.

  Jet algorithms are employed to reconstruct the shower of particles resulting from parton hadronisation into a jet. This is done using algorithms that collect together deposits of calorimeter energy, where the preferred choice at the LHC ordered inversely to

their transverse momentum (called anti-k_T). This results in cone-shaped jets useful for experimental analysis.

- **Heavy-flavour jets**. Jets arising from a high-momentum b-quark can be identified due to the long lifetime distance $c\tau \sim 450\mu$m and relatively large mass. Figure 94 displays the hallmark signature tracks not all tracing back to the same interaction point, this being called a secondary (displaced) vertex. The impact parameter transverse to the beam line is denoted d_0.

- **Tau-lepton jets**. These have very short lifetimes $\tau_\tau \sim 10^{-13}$ s. They have a branching ratio of $\sim 49\%$ to a single charged hadron plus neutrino and $\sim 15\%$ to 3 charged hadrons plus neutrinos. These types of jets should be highly collimated. Reconstruction algorithms employ two cones to define the τ jets: 1) the signal cone is formed by surrounding the hadron shower with a cone off ΔR then 2) a larger ΔR isolation cone surrounds this first signal cone where there is little track or calorimetry activity. The signal cone requires 3 tracks and activity in the electromagnetic calorimeter. Leptonic decay channels are in principle indistinguishable from other sources of electrons and muons.

- **Neutrinos and invisibles particles**. Neutrinos are too weakly coupled to interact with conventional LHC detectors with high rate, so are classed as invisible at ATLAS and CMS. These are both the most difficult and most interesting signatures. Detectors are designed to be as hermetic as possible to impose momentum conservation in the plane transverse to the beam line:
$$\mathbf{p}_T^{\text{miss}} = -\sum_i \mathbf{p}_T^{\text{visible}}. \tag{13.17}$$
This is a two-vector in the x-y plane and its magnitude is denoted $E_T^{\text{miss}} = |\mathbf{p}_T^{\text{miss}}|$, called "missing transverse energy" or "MET". This is also the primary signature in the search for dark matter candidates.

Figure 93 shows an example annotated event display of various objects in the CMS detector. There are now interactive detector and event displays you can play with in your Internet browser[59].

[59] https://opendata.cern.ch/visualise/events/cms

14 Electroweak symmetry breaking

The city-sized colliders of LEP, Tevatron, LHC probe the fundamental dynamics of the Standard Model. At its heart is electroweak symmetry breaking via the Brout–Englert–Higgs mechanism. This generates the masses for the gauge bosons while leaving the photon massless via spontaneous symmetry breaking of a gauge theory. Direct empirical evidence of the underlying Higgs field is the experimental detection of the Higgs boson.

Let us proceed in a sequence of increasing sophistication, building up towards the Standard Model realisation of the mechanism:

- Simple illustration of spontaneous symmetry breaking.
- Abelian Higgs model: application to a gauge theory with a local U(1) symmetry.
- Standard Model: application to a chiral non-Abelian gauge theory of electroweak interactions.

14.1 Brout–Englert–Higgs mechanism

To illustrate the idea of spontaneous symmetry breaking, we can consider a very simple complex scalar field $\phi(x)$ with a quartic potential:

$$V(|\phi|^2) = \mu^2|\phi|^2 + \lambda|\phi|^4. \tag{14.1}$$

This system has a symmetry upon sign inversion $\phi \to -\phi$. We can find the minima and maxima by differentiating

$$0 = \frac{\partial V(\phi)}{\partial \phi} = (\mu^2 + 2\lambda\phi_0^2)\phi_0. \tag{14.2}$$

In the case $\mu^2 > 0$ and $\lambda > 0$, the only minimum is at $\phi_0 = 0$. Spontaneous symmetry breaking occurs when $\mu^2 < 0$, where the solutions become degenerate

$$\phi_0 = \pm\sqrt{\frac{-\mu^2}{2\lambda}}, \quad \phi_0 = 0. \tag{14.3}$$

We can visualise the shape of the potential as the sign of the quadratic term inverts in figure 96. The quartic potential $V(\phi^2)$ initially has a global minimum at $\phi^2 = 0$ when $\mu^2 > 0, \lambda > 0$. When the sign inverts $\mu^2 < 0$, the $\phi^2 = 0$ becomes unstable while the potential develops two minima. The system describing the scalar field settles into one of the two minima and the $\phi \to -\phi$ symmetry is broken.

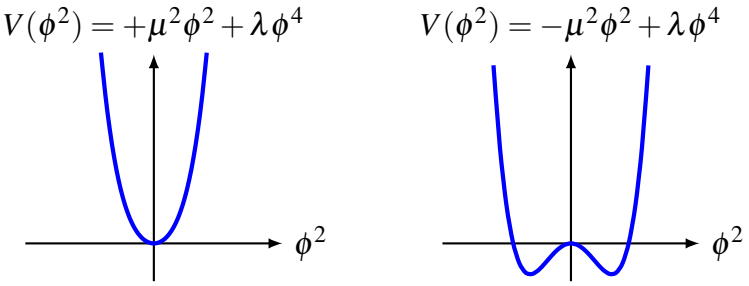

Figure 96: Simple visualisation of quartic function.

As an aside, this may seem rather contrived to the point of oversimplification. But the parameter undergoing sign inversion can be temperature dependent $\mu = \mu(T)$ and $\phi^2 \neq 0$ corresponds to a condensate when modelling superconductivity or the early universe phase transitions. We shall now illustrate its application in particle physics for mass generation in a gauge theory.

Abelian Higgs model

We now apply spontaneous symmetry breaking to the mechanism of mass generation in the simplest gauge theory: the **Abelian Higgs model**. This idea for mass generation was developed by numerous theoretical physicists in the 1960s and is now designated the Brout–Englert–Higgs mechanism. The Lagrangian comprises a massless vector A_μ interacting with a complex scalar $\phi(x)$ field

$$\mathscr{L} = -\frac{1}{4}F_{\mu\nu}F^{\mu\nu} + \frac{1}{2}(D_\mu\phi)(D^\mu\phi)^* - V(\phi^*\phi), \quad V(\phi^*\phi) = \lambda\left(\phi^*\phi - \tfrac{1}{2}v^2\right)^2, \tag{14.4}$$

where the covariant derivative is $D_\mu = \partial_\mu + \mathrm{i}eA_\mu$.

The Lagrangian is invariant under the U(1) Abelian local symmetry and gauge transformations:

$$\phi \to e^{\mathrm{i}\alpha(x)}\phi, \quad A_\mu \to A_\mu - (\partial_\mu\alpha)/e. \tag{14.5}$$

The scalar field rolls from the unstable centre $|\phi|^2 = 0$ down to the minimum of the potential at value $|\phi|^2 = v^2$, as sketched in figure 97. We assume the vev v to be real such that $\langle\phi\rangle = v$. We can expand the field $\phi(x)$ around the minimum in small perturbations $h(x)$

$$\phi(x) = \frac{\mathrm{e}^{\mathrm{i}\chi(x)}}{\sqrt{2}}(v + h(x)). \tag{14.6}$$

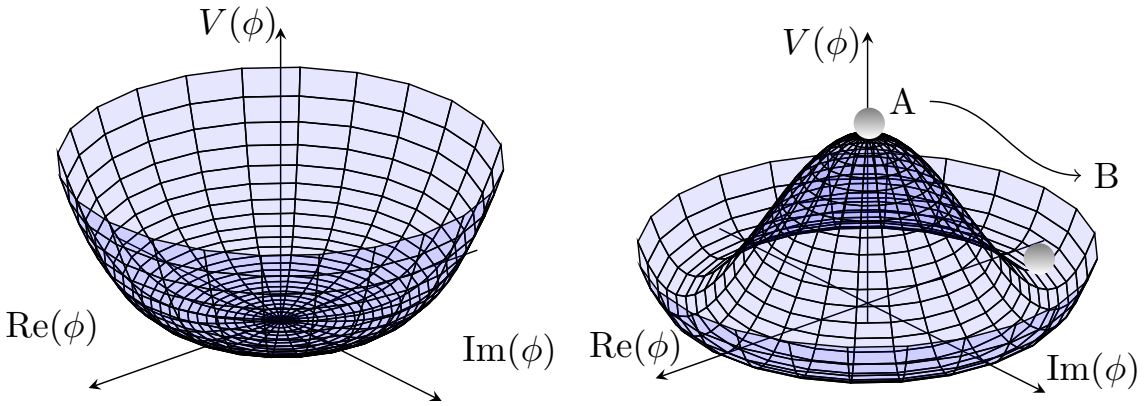

(a) Unbroken phase: "wine glass" (b) Broken phase: "wine bottle"

Figure 97: **Higgs potential visualisation**. The two-dimensional potential $V(\phi)$ starts from the characteristic "wine glass" shape. Spontaneous symmetry breaking occurs, after which into the shape becomes the base of a "wine bottle". Figures: adapted from tikz.net.

Substituting this into the kinetic and potential terms of the Lagrangian (14.4) gives

$$(D_\mu\phi)^*(D^\mu\phi) = \frac{1}{2}\left[(\partial_\mu h)^2 + (v+h)^2(\partial^\mu\chi + eA^\mu)^2\right], \tag{14.7}$$

$$V(\phi^*\phi) = \lambda\left[\frac{1}{2}(v+h)^2 - \frac{v^2}{2}\right]^2 = \lambda v^2h^2 + \lambda v^2h^3 + \frac{\lambda}{4}h^4. \tag{14.8}$$

Right now, we now see the propagating scalar degree of freedom $h(x)$ has a mass term $m_h^2/2 = \lambda v^2$; this corresponds to states oscillating up and down the radial direction of the potential in figure 97. We also see a $(\partial_\mu\chi)^2$ term that appears without any quadratic mass term; this is the **Nambu–Goldstone boson** corresponding to states rotating around the well at constant radius of the wine bottle in figure 97. To illuminate the physical vector degrees of freedom, we fix the gauge by redefining $A_\mu \to A_\mu - (\partial_\mu\chi)/e$, which is called the unitary gauge. The Lagrangian then becomes

$$\mathscr{L} = \underbrace{-\frac{1}{4}F_{\mu\nu}F^{\mu\nu} + \frac{e^2v^2}{2}A^2}_{\text{massive vector}} + \underbrace{\frac{1}{2}(\partial_\mu h)^2 - \lambda v^2h^2}_{\text{mass real scalar}} - \underbrace{\lambda v^2h^3 - \frac{\lambda}{4}h^4}_{\text{Higgs self-couplings}} + \underbrace{\frac{1}{2}(vh+h^2)A^2}_{\text{Higgs-vector couplings}}. \tag{14.9}$$

This makes manifest the **Brout–Englert–Higgs mechanism**: a non-zero vacuum expectation value of the complex scalar reshuffles the degrees of freedom (abbreviated dof.) in the theory

$$\boxed{\begin{pmatrix}\phi : 2\text{ dof.}\\ A_\mu, m_A = 0 : 2\text{ dof.}\end{pmatrix} \langle\phi\rangle \neq 0 \longrightarrow \begin{pmatrix}h : 1\text{ dof.}\\ A_\mu, m_A \neq 0 : 3\text{ dof.}\end{pmatrix}.} \tag{14.10}$$

Writing this explicitly makes it clear how the accounting of degrees of freedom are conserved. To recap on what we just saw:

- Originally, we started with two degrees of freedom in the massless vector A_μ and two in the complex scale $\phi(x) = \mathrm{Re}\phi(x) + \mathrm{iIm}\phi_(x)$ in equation (14.4).
- After symmetry breaking, the scalar acquires a vacuum expectation value $\langle\phi\rangle = v$, a massless Goldstone boson $\chi(x)$ appears and a real scalar $h(x)$ gains a mass m_h.
- By fixing the gauge choice, the massless Nambu–Goldstone boson disappears and is reassigned[60] to become the longitudinal polarisation of the massive vector A_μ. This supplements the original two transverse polarisations of a massless vector.
- At the end, we have one degree of freedom in the real scalar $h(x)$ and three degrees of freedom in the massive vector A_μ.

Applying this to chiral and non-Abelian structure of the electroweak force is slightly more complicated and is central to the Standard Model.

14.2 Glashow–Salam–Weinberg model

The Brout–Englert–Higgs mechanism applied to the Standard Model of electroweak interactions is slightly more complicated than the Abelian toy example. The SM Higgs field Φ_{SM} is exists in an SU(2) doublet of complex scalar fields, with 4 degrees of freedom. Two degrees of freedom of Φ of which are charged and the remaining two are neutral. We arrange the Higgs field into a weak isospin $\mathrm{SU(2)_L}$ doublet

$$\Phi_{\mathrm{SM}} = \begin{pmatrix} \phi^+ \\ \phi^0 \end{pmatrix} = \frac{1}{\sqrt{2}} \begin{pmatrix} \phi_1 + \mathrm{i}\phi_2 \\ \phi_3 + \mathrm{i}\phi_4 \end{pmatrix}. \tag{14.11}$$

This Higgs doublet interacts with a massless hypercharge vector B_μ and the three massless weak isospin $W_\mu^{(1,2,3)}$ vector fields. Analogous to equation (14.10), we again write out explicitly how the degrees of freedom (dof.) reshuffles to ensure our accounting adds up:

$$\begin{pmatrix} \Phi_{\mathrm{SM}} = (\phi^+, \phi^0) : 4 \text{ dof.} \\ B_\mu, m_B = 0 : 2 \text{ dof.} \\ W_\mu^{(1,2,3)}, m_W = 0 : 3 \times 2 \text{ dof.} \end{pmatrix} \underset{\longrightarrow}{\langle\Phi_{\mathrm{SM}}\rangle \neq 0} \begin{pmatrix} h : 1 \text{ dof.} \\ A_\mu, m_A = 0 : 2 \text{ dof.} \\ Z_\mu, m_Z \neq 0 : 3 \text{ dof.} \\ W_\mu^\pm, m_W \neq 0 : 2 \times 3 \text{ dof.} \end{pmatrix}. \tag{14.12}$$

[60] Textbooks often uses the technical jargon of the Nambu–Goldstone boson being "eaten".

After electroweak symmetry breaking, there is one real Higgs boson h, a massless photon, a neutral massive vector Z, and two charged massive vector $W^{\pm}$ bosons fields. Three of the degrees of freedom of the complex Higgs doublet comprise the Nambu–Goldstone bosons that are reassigned to ("eaten by") the longitudinal components of the massive vector bosons. We start with 12 physical propagating modes and also end up with 12 physical propagating modes: excellent.

The Lagrangian for the Higgs doublet of complex scalar fields is

$$\mathscr{L}_{\text{Higgs}} = (D^{\mu}\Phi)(D_{\mu}\Phi)^{\dagger} - V(\Phi^{\dagger}\Phi). \tag{14.13}$$

The Higgs field Lagrangian has the desired $\mathrm{U(1)_Y}$ and $\mathrm{SU(2)_L}$ local symmetries

$$\begin{pmatrix}\phi^{+}\\ \phi^{0}\end{pmatrix} \to \begin{pmatrix}\mathrm{e}^{\mathrm{i}g_1 Y_\phi \beta(x)/2} & 0\\ 0 & \mathrm{e}^{\mathrm{i}g_1 Y_\phi \beta(x)/2}\end{pmatrix}\begin{pmatrix}\phi^{+}\\ \phi^{0}\end{pmatrix} \qquad U(1)_Y \text{ symmetry} \tag{14.14}$$

$$\begin{pmatrix}\phi^{+}\\ \phi^{0}\end{pmatrix} \to \mathrm{e}^{\mathrm{i}g_2 I_\phi \sigma_a \alpha(x)}\begin{pmatrix}\phi^{+}\\ \phi^{0}\end{pmatrix} \qquad SU(2)_L \text{ symmetry.} \tag{14.15}$$

The Higgs field is defined to have the following weak hypercharge Y_Φ and isospin I_Φ:

$$Y_\Phi = 1, \quad I_\Phi = \frac{1}{2}. \tag{14.16}$$

Using these values, the relevant covariant derivative for the Higgs field under these local transformations is

$$D_\mu \Phi = \left(\partial_\mu - \frac{\mathrm{i}}{2}g_1 B_\mu - \frac{\mathrm{i}}{2}g_2 \sigma_a W_\mu^a\right)\Phi. \tag{14.17}$$

These covariant derivatives act on the left-handed leptons formed into $\mathrm{SU(2)_L}$ doublets

$$L_\ell = \begin{pmatrix}\nu_\ell\\ \ell\end{pmatrix}_L = \left\{\begin{pmatrix}\nu_e\\ e\end{pmatrix}_L, \begin{pmatrix}\nu_\mu\\ \mu\end{pmatrix}_L, \begin{pmatrix}\nu_\tau\\ \tau\end{pmatrix}_L\right\}. \tag{14.18}$$

Meanwhile the right-handed leptons form a singlet, comprising only of the electron flavour without neutrinos:

$$R_\ell = \ell_R = \{e_R, \mu_R, \tau_R\}. \tag{14.19}$$

The left-handed doublet experience $\mathrm{SU(2)_L}$ transformations symmetry while the right-handed leptons remain invariant:

$$\begin{pmatrix}\nu_\ell\\ \ell\end{pmatrix}_L \to \mathrm{e}^{\mathrm{i}g_2 I_L \sigma_a \alpha^a}\begin{pmatrix}\nu_\ell\\ \ell\end{pmatrix}_L, \tag{14.20}$$

$$\ell_R \to \ell_R. \tag{14.21}$$

The σ_a are the standard Pauli matrices. That $\mathrm{SU(2)_L}$ exhibits couples only to left-handed spinors and not right-handed ones is a manifestation of maximal parity violation in electroweak interactions. Consistent to this definition, the left-handed doublet and right-handed singlet take on these **weak isospin** values:

$$I_L = \frac{1}{2}, \qquad I_R = 0. \tag{14.22}$$

As the right-handed weak isospin value is zero, the nonchalance of the $\mathrm{SU(2)_L}$ is exhibited as the identity operator acting on ℓ_R. Table 6 summarise all the charges of the leptons and quarks in the Standard Model.

For the lepton fields L, ℓ_R to acquire mass after symmetry breaking, we couple them to the Higgs field via Yukawa interaction terms

$$\mathscr{L}_{\text{Yukawa}} = -y_\ell \left(\bar{L}\Phi\ell_R + \bar{\ell}_R\Phi^\dagger L \right). \tag{14.23}$$

This remain invariant under the local $\mathrm{SU(2)_L} \times \mathrm{U(1)_Y}$ symmetry. The Higgs-lepton coupling constant y_ℓ dictates the strength with which the lepton fields couple to the Higgs field. The kinetic terms for the three $\mathrm{SU(2)_L}$ weak isospin fields are W^a_μ and $\mathrm{U(1)_Y}$ hypercharge fields are B_μ:

$$\mathscr{L}_{\text{gauge}} = -\frac{1}{4} W^a_{\mu\nu} W_a^{\mu\nu} - \frac{1}{4} B_{\mu\nu} B^{\mu\nu}, \tag{14.24}$$

where the field strengths are correspondingly

$$B_{\mu\nu} = \frac{1}{\mathrm{i}g_1}[D_\mu, D_\nu] = \partial_\mu B_\nu - \partial_\nu B_\mu, \tag{14.25}$$

$$W^a_{\mu\nu} = \frac{1}{\mathrm{i}g_2}[D_\mu, D_\nu]^a = \partial_\mu W^a_\nu - \partial_\nu W^a_\mu - g_2 f^{abc} W^b_\mu W^c_\nu. \tag{14.26}$$

Putting all the ingredients together with the Dirac kinetic term describing the fermions, we arrive at the Glashow–Salam–Weinberg electroweak model of leptons before symmetry breaking

$$\begin{aligned}
\mathscr{L}_{\text{EW}} = \quad & -\frac{1}{4} W^a_{\mu\nu} W_a^{\mu\nu} - \frac{1}{4} B_{\mu\nu} B^{\mu\nu} && \text{gauge kinetic} \\
& + \mathrm{i}\bar{L}_\ell \gamma^\mu D_\mu L_\ell + \mathrm{i}\bar{\ell}_R \gamma^\mu D_\mu \ell_R && \text{Dirac leptons} \\
& - y_\ell \left(\bar{L}\Phi\ell_R + \ell_R\Phi^\dagger L \right) && \text{Yukawa couplings (14.23)} \\
& + (D^\mu\Phi)(D_\mu\Phi)^\dagger - V(\Phi^\dagger\Phi) && \text{Higgs field (14.13)}
\end{aligned} \tag{14.27}$$

This is starting to look like the Lagrangian that appears on the CERN mug of figure 6. Here the only massive field is the Higgs ϕ. The gauge $B_{\mu\nu}$, $W^a_{\mu\nu}$ and lepton fields L_l, R_l remain massless prior to symmetry breaking i.e. so long as $\mathscr{L}_{EW}$ remains invariant under the $\mathrm{SU(2)_L} \times \mathrm{U(1)_Y}$ local symmetry.

	Charge Gauge group Symbol	Colour $SU(3)_C$ C	Weak Isospin $SU(2)_L$ I_3	Hypercharge $U(1)_Y$ Y	Electric $U(1)_{EM}$ $Q = Y + \frac{I_3}{2}$
Leptons	$\begin{pmatrix}\nu_{eL}\\ e_L\end{pmatrix}, \begin{pmatrix}\nu_{\mu L}\\ \mu_L\end{pmatrix}, \begin{pmatrix}\nu_{\tau L}\\ \tau_L\end{pmatrix}$	0	$\begin{pmatrix}+\frac{1}{2}\\ -\frac{1}{2}\end{pmatrix}$	-1	$\begin{pmatrix}0\\ -1\end{pmatrix}$
	$\nu_{eR}, \nu_{\mu R}, \nu_{\tau R}$	0	0	0	0
	e_R, μ_R, τ_R	0	0	-2	-1
Quarks	$\begin{pmatrix}u_L\\ d_L\end{pmatrix}, \begin{pmatrix}c_L\\ s_L\end{pmatrix}, \begin{pmatrix}t_L\\ b_L\end{pmatrix}$	(r,g,b)	$\begin{pmatrix}+\frac{1}{2}\\ -\frac{1}{2}\end{pmatrix}$	$+\frac{1}{3}$	$\begin{pmatrix}+\frac{2}{3}\\ -\frac{1}{3}\end{pmatrix}$
	u_R, c_R, t_R	(r,g,b)	0	$+\frac{4}{3}$	$+\frac{2}{3}$
	d_R, s_R, b_R	(r,g,b)	0	$-\frac{2}{3}$	$-\frac{1}{3}$

Table 6: Charge assignment for the Standard Model matter (fermion) content. Fermions can carry colour charge C, weak isospin I_3, hypercharge Y, and electric charge $Q = Y + I_3/2$. This corresponds to the $SU(3)_C$, $SU(2)_L$, $U(1)_Y$, $U(1)_{EM}$ gauge groups, respectively. The left-handed fermions are displays as doublets **2** of $SU(2)_L$. The quarks are implicitly triplets **3** of $SU(3)_C$ with (r,g,b) colour charges. The right-handed neutrinos are greyed out given they are hypothetical singlets (uncharged) under the SM gauge groups.

14.3 Generating gauge boson masses

We now walk through the mathematical anatomy of mass generation for the fermions and gauge bosons in the Standard Model via electroweak symmetry breaking. The Higgs potential is given by (where we can define an additive constant)

$$V(\Phi^\dagger\Phi) = \lambda\left(|\Phi^\dagger\Phi|^2 - \frac{v^2}{2}\right)^2. \tag{14.28}$$

The first step is to define the electroweak vacuum expectation value and the Higgs as an excitation of this. The minimum is no longer at the origin $(\Phi)_0 = 0$ but is instead is a continuously degenerate minima satisfying

$$\frac{\partial V}{\partial \Phi} = 0 \quad \Rightarrow \quad (\Phi^\dagger\Phi)_0 = \frac{1}{2}\left(\phi_1^2 + \phi_2^2 + \phi_3^2 + \phi_4^2\right) = \frac{\mu^2}{\lambda}, \tag{14.29}$$

defining $\mu^2 = v^2\lambda/2$. Without loss of generality, we choose the ground state to be

$$(\Phi_i)_0 = \begin{cases} \sqrt{\dfrac{2\mu^2}{\lambda}} = v, & \text{if } i = 1; \\ 0, & \text{if } i = 2,3,4. \end{cases} \tag{14.30}$$

Now we find the new non-zero vacuum expectation value is

$$\langle 0|\Phi|0\rangle = \begin{pmatrix} \phi^+ \\ \phi^0 \end{pmatrix}_0 = \frac{1}{\sqrt{2}} \begin{pmatrix} 0 \\ v \end{pmatrix} \tag{14.31}$$

We can consider small perturbations $h(x) \ll v$ about the new non-zero vacuum expectation value of ϕ in the unitary gauge

$$\Phi(x) = \frac{1}{\sqrt{2}} \begin{pmatrix} 0 \\ v + h(x) \end{pmatrix}. \tag{14.32}$$

The consequences of this electroweak symmetry breaking, leading to non-zero vacuum expectation value of the Higgs field, are profound. We substitute the small field fluctuations of equation (14.32) into the kinetic term to give

$$(D_\mu \Phi)^\dagger (D_\mu \Phi) = \frac{1}{2}(\partial_\mu h)^2 + \text{terms involving gauge fields.} \tag{14.33}$$

We shall study the terms involving gauge fields below, which generates the gauge boson masses.

Generation of W boson masses

The masses of the gauge bosons after symmetry breaking are encoded in $(D_\mu\Phi)(D^\mu\Phi)^\dagger$. This is a somewhat fiddly but rewarding calculation. Using the explicit forms of the Pauli matrices and acting D_μ on the unitary gauged $H(x)$, we find

$$\begin{aligned} D_\mu \Phi &= \left[\partial_\mu - \frac{\mathrm{i}}{2} \begin{pmatrix} g_1 B_\mu + g_2 W_\mu^{(3)} & g_2 \left(W_\mu^{(1)} - \mathrm{i} W_\mu^{(2)} \right) \\ g_2 \left(W_\mu^{(1)} + \mathrm{i} W_\mu^{(2)} \right) & g_1 B_\mu - g_2 W_\mu^{(3)} \end{pmatrix} \right] \frac{1}{\sqrt{2}} \begin{pmatrix} 0 \\ v + h(x) \end{pmatrix} \\ &= \frac{1}{\sqrt{2}} \begin{pmatrix} -\frac{\mathrm{i} g_2}{2} \left(W_\mu^{(1)} - \mathrm{i} W_\mu^{(2)} \right) (v + h(x)) \\ \partial_\mu h(x) - \frac{\mathrm{i}}{2} \left(g_1 B_\mu - g_2 W_\mu^{(3)} \right) (v + h(x)) \end{pmatrix}. \end{aligned} \tag{14.34}$$

Now take the Hermitian conjugate of this to yield $(D^\mu\phi)^\dagger$ and multiplying through with a plateful of algebra to write

$$\begin{aligned}(D_\mu\Phi)(D^\mu\Phi)^\dagger = &\frac{1}{2}(\partial_\mu h)(\partial^\mu h)\\ &+\frac{g_W^2}{8}\left(W_\mu^{(1)}-\mathrm{i}W_\mu^{(2)}\right)\left(W^{(1)\mu}+\mathrm{i}W^{(2)\mu}\right)(v+h(x))^2\\ &+\frac{1}{8}\left(g_1B_\mu-g_2W_\mu^{(3)}\right)\left(g_1B^\mu-g_2W^{(3)\mu}\right)(v+h(x))^2\,.\end{aligned} \tag{14.35}$$

For now we retain only terms involving v^2 as we would like to consider how the gauge fields interact with the now non-zero expectation value of the Higgs field. Thus we have

$$\begin{aligned}(D_\mu\Phi)(D^\mu\Phi)^\dagger = &\frac{1}{2}(\partial_\mu h)(\partial^\mu h)+\underbrace{\frac{g_2^2v^2}{8}}_{\text{mass term}}\left[\left(W_\mu^{(1)}\right)^2+\left(W_\mu^{(2)}\right)^2\right]\\ &+\frac{v^2}{8}\left(g_1B_\mu-g_2W_\mu^{(3)}\right)^2+\text{terms involving } h(x).\end{aligned} \tag{14.36}$$

We can now proceed to extract the masses of the W bosons. This is encoded in the second line of (14.36) as the coefficients of the $\left(W_\mu^{(1,2)}\right)^2$ terms. There are two charged $W_\mu^\pm$ boson fields comprising linear combinations of $W_\mu^{(1,2)}$ with equal mass m_W

$$\boxed{W_\mu^\pm=\frac{W_\mu^{(1)}\mp\mathrm{i}W_\mu^{(2)}}{\sqrt{2}},\quad \frac{m_W^2}{2}=\frac{g_2^2v^2}{8}.} \tag{14.37}$$

The mass of the W bosons is determined by the coupling g_2 of the $\mathrm{SU(2)_L}$ gauge interaction and the vacuum expectation value of the Higgs field v.

Generation of photon and massive Z boson

Surreptitiously concealed in the last term of (14.36) are the massive Z boson and photon fields, which we first write as a quadratic form

$$\frac{v^2}{4}\left(g_1B_\mu-g_2W_\mu^{(3)}\right)^2=\frac{v^2}{4}\begin{pmatrix}W_\mu^{(3)} & B_\mu\end{pmatrix}\begin{pmatrix}g_2^2 & -g_1g_2\\ -g_1g_2 & g_1^2\end{pmatrix}\begin{pmatrix}W^{(3)\mu}\\ B^\mu\end{pmatrix}. \tag{14.38}$$

The off-diagonal elements in the matrix couple the $W_\mu^{(3)}$ and B_μ fields. Therefore, to find the physical independently propagating fields, we should diagonalise this matrix. Solving this

eigenvalue problem using our favourite pen-and-paper or computer method, we find (14.38) rewritten elegantly diagonal:

$$\frac{1}{2}\begin{pmatrix}A_\mu & Z_\mu\end{pmatrix}\begin{pmatrix}0 & 0\\ 0 & \frac{v^2}{2}\left(g_1^2+g_2^2\right)\end{pmatrix}\begin{pmatrix}A^\mu\\ Z^\mu\end{pmatrix}=\frac{1}{2}\begin{pmatrix}A_\mu & Z_\mu\end{pmatrix}\begin{pmatrix}m_A^2 & 0\\ 0 & m_Z^2\end{pmatrix}\begin{pmatrix}A^\mu\\ Z^\mu\end{pmatrix}. \tag{14.39}$$

From this we can read off the masses of the A_μ and Z_μ fields. Amazingly, we see a massless boson field A_μ, more affectionately known as the photon, in addition to a massive neutral boson field Z_μ. This happened as a consequence of breaking the electroweak $\mathrm{SU(2)_L}\times\mathrm{U(1)_Y}$ symmetry. These physical boson fields A_μ and Z_μ are linear combinations of the initial $W_\mu^{(3)}$ and B_μ fields:

$$\begin{pmatrix}A_\mu\\ Z_\mu\end{pmatrix}=\frac{1}{\sqrt{g_1^2+g_2^2}}\begin{pmatrix}g_2 & g_1\\ -g_1 & g_2\end{pmatrix}\begin{pmatrix}B_\mu\\ W_\mu^{(3)}\end{pmatrix}. \tag{14.40}$$

This is a rotation of basis, which we make manifest by defining the **Weinberg angle** $\tan\theta_W = g_1/g_2$ relating the ratio of $\mathrm{U(1)_Y}$ and $\mathrm{SU(2)_L}$ couplings to rewrite equation (14.40) as

$$\boxed{\begin{pmatrix}A_\mu\\ Z_\mu\end{pmatrix}=\begin{pmatrix}\cos\theta_W & \sin\theta_W\\ -\sin\theta_W & \cos\theta_W\end{pmatrix}\begin{pmatrix}B_\mu\\ W_\mu^{(3)}\end{pmatrix},\quad m_A^2=0,\quad m_Z^2=\frac{v^2}{2}\left(g_1^2+g_2^2\right).} \tag{14.41}$$

With these relations and equation (14.37), we can rewrite the Z boson mass as $m_Z=\frac{vg_2}{\sqrt{2}\cos\theta_W}$ to obtain a key prediction of electroweak symmetry breaking

$$\frac{m_W}{m_Z}=\cos\theta_W. \tag{14.42}$$

The electric charge e is then related to the $\mathrm{U(1)_Y}$ and $\mathrm{SU(2)_L}$ couplings by

$$e=g_1\sin\theta_W=g_2\cos\theta_W. \tag{14.43}$$

The relationship of electric charge with hypercharge and weak isospin couplings is usually referred to as **electroweak unification**. Knowing $e=\sqrt{4\pi\alpha_{\mathrm{EM}}}\approx 0.3$ and measuring $\cos\theta_W=m_W/m_Z$, we can determine the couplings g_1 and g_2.

Electroweak symmetry breaking results in the $\mathrm{SU(2)_L}\times\mathrm{U(1)_Y}$ gauge group being replaced by the electromagnetism $\mathrm{U(1)_{EM}}$:

$$\langle\Phi\rangle\neq 0 \quad\Rightarrow\quad \mathrm{SU(2)_L}\times\mathrm{U(1)_Y}\to\mathrm{U(1)_{EM}}. \tag{14.44}$$

In terms of the physical fields, interactions of electroweak gauge bosons to fermion currents $j^\mu = \bar{\psi}\gamma^\mu\psi$ take the form

$$-\mathscr{L}_{\rm EW}^{\rm int} = -\underbrace{eA_\mu j^\mu_{\rm EM}}_{\rm EM} + \underbrace{\frac{e}{\sqrt{2}\sin\theta_W}\left(W^+_\mu j^\mu_+ - W^-_\mu j^\mu_-\right)}_{\text{charged current}} + \underbrace{\frac{e}{\sin\theta_W\cos\theta_W}Z_\mu j^\mu_Z}_{\text{neutral current}} \tag{14.45}$$

Let us state the charged currents are (and similar for the other generations)

$$j^+_\mu = \bar{u}_L\bar{\sigma}^\mu d_L + \bar{\nu}_L\bar{\sigma}^\mu e_L, \tag{14.46}$$

$$j^-_\mu = \bar{d}_L\bar{\sigma}^\mu u_L + \bar{e}_L\bar{\sigma}^\mu \nu_L. \tag{14.47}$$

The familiar electromagnetic current and neutral current interactions look like

$$j^\mu_{\rm EM} = \sum_f Q_f(\bar{f}_L\bar{\sigma}^\mu f_L + \bar{f}_R\sigma^\mu f_R), \tag{14.48}$$

$$j^\mu_Z = \frac{1}{2}(\bar{u}_L\bar{\sigma}^\mu u_L - \bar{d}_L\bar{\sigma}^\mu d_L + \bar{\nu}_L\bar{\sigma}^\mu\nu_L - \bar{e}_L\bar{\sigma}^\mu e_L) - \sin^2\theta_W j^\mu_{\rm EM} \tag{14.49}$$

The fundamental vertex of charged-current interaction showing fermions (quarks q, charged leptons ℓ and neutrinos) coupling with the $W^\pm$ boson has the Feynman diagrams:

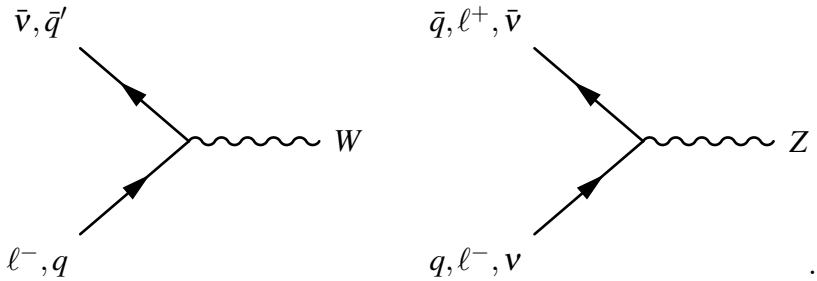

. (14.50)

Accounting for mass differences, the $W^\pm$ interact with each generation in identical ways. Consequently, the vertex of leptons and the $W^\pm$ bosons have the same weak coupling constant g_W, independent of the lepton flavour. The fundamental neutral-current interaction showing fermions (quarks q, charged leptons ℓ and neutrinos) coupling with the Z boson has this Feynman diagram.

The electrically charged leptons experience the electromagnetic and weak interactions while the neutrinos, being neutral, only experience the weak interaction. Each lepton is associated with a lepton flavour number. The electron lepton number L_e for example is given by

$$L_e = N(e^-) - N(e^+) + N(\nu_e) - N(\bar{\nu}_e), \tag{14.51}$$

where $N(X)$ denotes the number of X particles in a state. Lepton numbers for the μ and τ flavours are similarly defined by replacing e above with the flavour under discussion. In the Standard Model, the total lepton number

$$L_\ell = L_e + L_\mu + L_\tau \tag{14.52}$$

is conserved in all interactions.

Historically, the electroweak theory is due to work by Sheldon Glashow, Abdus Salam and Steven Weinberg, culminating around 1968. It made the surprising prediction that there should exist an electrically neutral massive gauge boson Z^0 which is heavier than two charged gauge bosons $W^\pm$, related by a parameter θ_W.

14.4 Discovery of W and Z bosons

The first indirect evidence for a neutral weak boson was the observation of **neutral current** interactions. At the CERN Proton Synchrotron (PS), they were able to create muon-neutrinos ν_μ from pion decays that scattered off quarks and electrons (figure 99):

$$\nu + q \to \nu + q \tag{14.53}$$

$$\nu + e^- \to \nu + e^-. \tag{14.54}$$

Such events are rather striking given a stationary electron suddenly and spontaneously gets knocked by the invisible neutrino. It is inferred that there exists a heavy neutral particle mediating these processes, which is later identified as the Z boson. These experiments were performed by the Gargamelle bubble chamber in 1973 (figure 98).

Super Proton Synchrotron

In 1983, the UA1 and UA2 collaborations[61] used events from the Super Proton Synchrotron (SPS) to directly observe the $W^\pm$ bosons in proton–antiproton $p\bar{p}$ collisions [95, 96] with centre-of-mass energies of $> 540\,\text{GeV}$. This was such that the interacting quarks carried the required $\sim 100\,\text{GeV}$ to form these heavy bosons on-shell. In 1968, the electromagnetic and weak interactions were unified into a single unified electroweak theory at high energies. One consequence of this theory is the prediction of a neutral current reactions mediated by a Z^0 boson. The $W^\pm$ and Z^0, bosons were discovered by in 1983. The masses are measured to be

$$m_W = 80.385 \pm 0.015\,\text{GeV},$$
$$m_Z = 91.1876 \pm 0.0021\,\text{GeV}.$$

[61] UA stands for Underground Area.

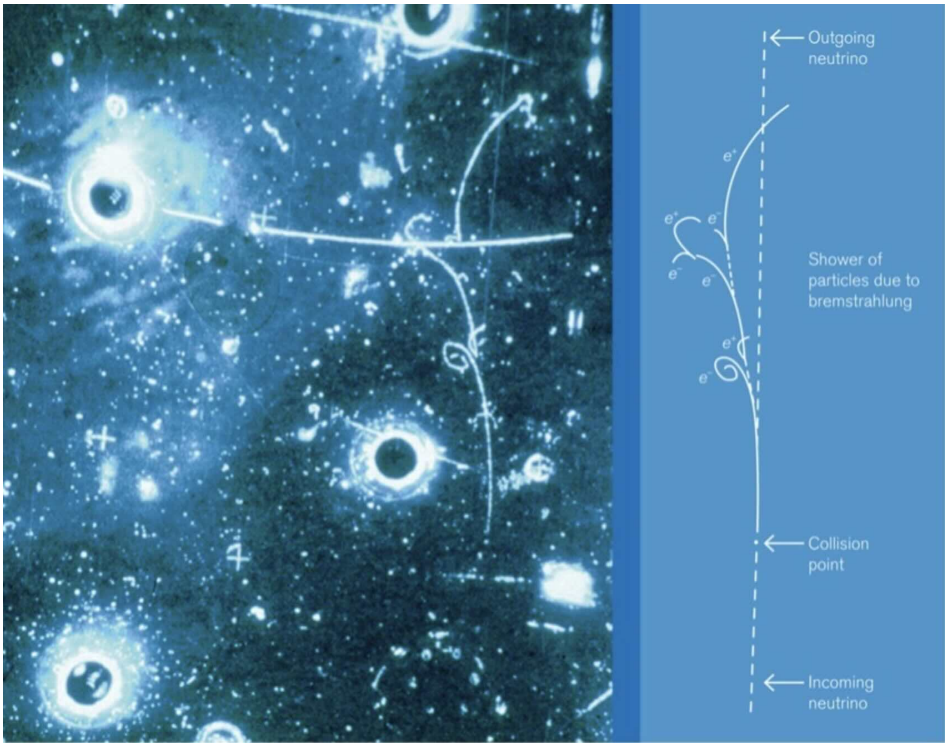

Figure 98: Neutral current by Gargemelle. Image from CERN

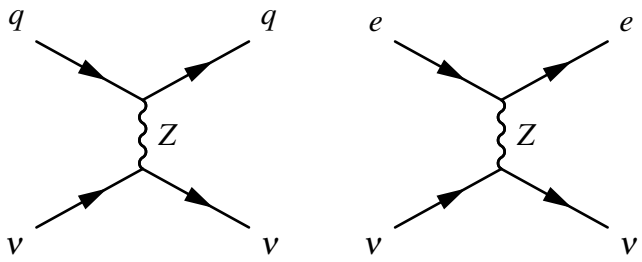

Figure 99: Neutrino-quark and neutrino-electron scattering that provided evidence for weak neutral current interactions, as indirect evidence for the existence of the Z boson.

The masses of the weak $W^{\pm}$ and Z bosons relate the mixture of the original hypercharge B_μ and weak isospin boson fields W^a_μ.

The Z boson is like the $W^{\pm}$ but is neutral and slightly more massive at $m_{Z^0} \approx 91\,\text{GeV}/c^2$. It interacts with all quarks and leptons but **conserves flavour** for any process in contrast to charged currents involving $W^{\pm}$. Thus no quark mixing occurs.

We calculate the centre-of-mass energy for production. Let each quark and antiquark carry fractions f_q and $f_{\bar{q}}$ of the proton and antiproton 4-momenta respectively. To produce a

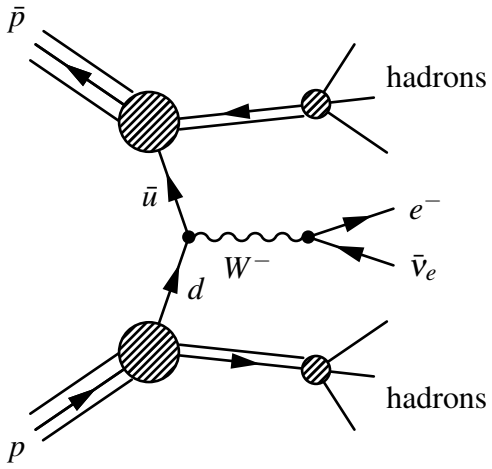

Figure 100: Production of W^- bosons via proton–antiproton collision and decay via $e^-\bar{\nu}_e$.

$W^\pm$ with mass m_W close to resonance, we conserve 4-momenta of the quarks in the centre-of-mass frame:

$$m_W^2 = (\mathsf{P}_q + \mathsf{P}_{\bar{q}})^2 = \mathsf{P}_q^2 + \mathsf{P}_{\bar{q}}^2 + 2\mathsf{P}_q \cdot \mathsf{P}_{\bar{q}} \tag{14.55}$$

The beam energies are much greater than the quark energies so $\mathsf{P}_q^2 \approx 0$ and $\mathsf{P}_{\bar{q}}^2 \approx 0$. The 4-momenta of the proton and antiproton are[62]

$$\mathsf{P}_q = f_q \begin{pmatrix} E_p \\ \mathbf{k}_p \end{pmatrix}, \qquad \mathsf{P}_{\bar{q}} = f_{\bar{q}} \begin{pmatrix} E_{\bar{p}} \\ -\mathbf{k}_{\bar{p}} \end{pmatrix}$$

Setting the magnitudes of their components to be equal, (14.55) becomes

$$m_W^2 = 4 f_q f_{\bar{q}} E_p^2. \tag{14.56}$$

Adhering to the particle physics convention of $\sqrt{s} = E_{\text{CM}}$ as the centre-of-mass energy, we obtain the condition to produce $W^\pm$ resonance:

$$\sqrt{s} = \frac{m_W}{\sqrt{f_q f_{\bar{q}}}}. \tag{14.57}$$

Figure 100 illustrates the dominant mechanism in producing W^- bosons via $p\bar{p}$ collisions. The outgoing quarks readily fragment into hadrons, generating significant background

[62] We use $\mathbf{k}$ for 3-momentum to minimise potential grief confusing it with the proton label p.

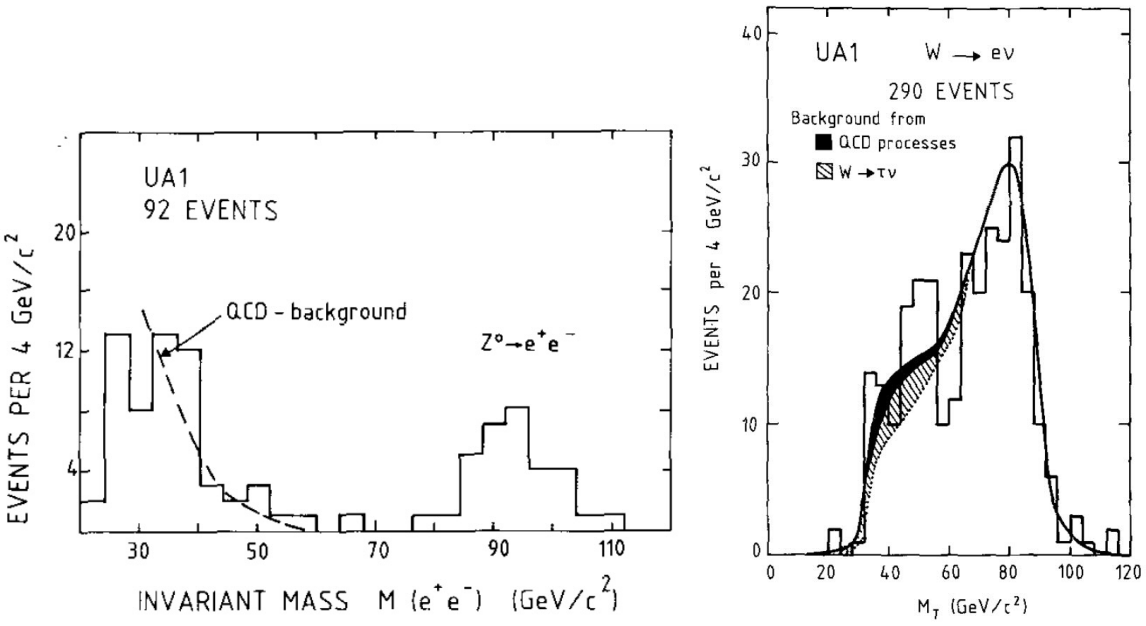

(a) Z boson (b) $W^{\pm}$ boson

Figure 101: Mass peaks of the $W^{\pm}$ and Z bosons from larger statistics samples from the UA1 Collaboration [97].

noise. Observing the W^- boson involves examining its decay modes:

$$W^- \to \begin{cases} \bar{u} + d' & (3) \\ \bar{c} + s' & (3) \\ e^- + \bar{\nu}_e & (1) \\ \mu^- + \bar{\nu}_\mu & (1) \\ \tau^- + \bar{\nu}_\tau & (1) \end{cases} \tag{14.58}$$

The $W^- \to \bar{t}b$ is kinematically forbidden as the top quark mass $> m_W$. The brackets show the relative weight of the decay channel. The hadronic ones are weighted by 3 due to quarks having a choice of existing in three colour states.

Observing the W^- boson decaying via a leptonic channel $W^- \to e^- + \bar{\nu}_e$ was key. Ignoring quark flavour mixing and assuming each decay mode in (14.58) are equally likely (given ultrarelativistic limit of outgoing particles and universality of weak coupling), we can estimate its branching ratio:

$$\mathrm{B}\left(W^- \to e^- + \bar{\nu}_e\right) \approx \frac{1}{3+3+1+1+1} = \frac{1}{9}. \tag{14.59}$$

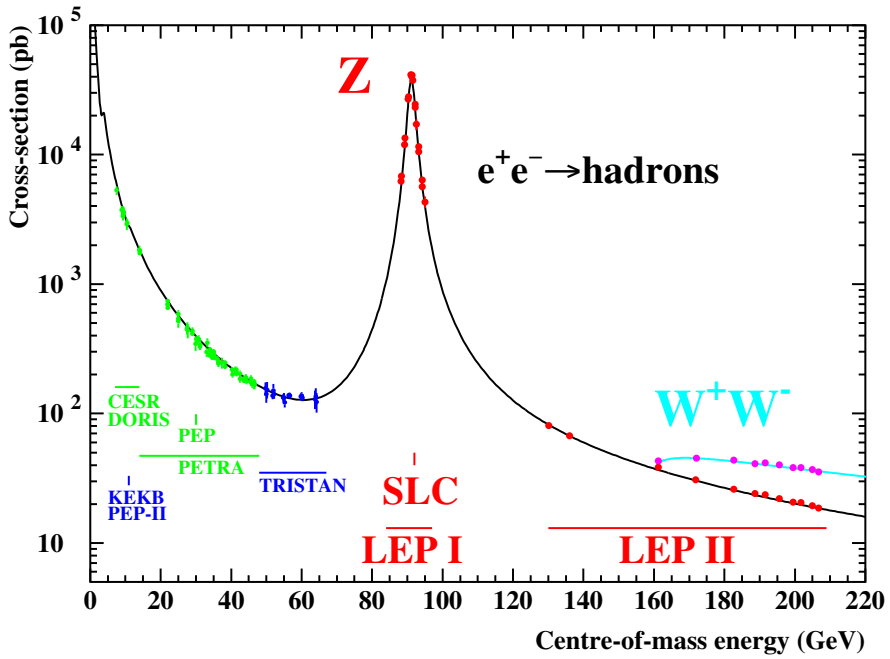

Figure 102: Measurements of e^-e^+ annihilation through LEP energies, from Ref. [87]

This decay produces a signature asymmetric track: the electrically charged e^- is easily detected but the antineutrino carrying the remaining momentum is very weakly interacting and does not leave a track.

With no QCD hadronic backgrounds to contend with, electron-positron collisions allow us to measure properties of the $W^\pm$ and Z^0 boson are most precisely. The reactions that take place are

$$e^+ + e^- \to X \to W^+ + W^-, \tag{14.60}$$

mediated by X, which can be a Z boson, photon γ or neutrino ν_e. This threshold is shown at high energies in figure 102.

14.5 Invisible width of Z boson

We exploit the fact all Standard Model fermions couple to the Z^0 boson equally to reveal an upper bound of only three neutrino types with masses below $< m_{Z^0}/2$. Considering the decay of Z^0 in its rest frame, we have the following observed states:

$$Z \to q\bar{q}, \quad q = u,d,s,c,b, \quad \text{(top too heavy)} \tag{14.61}$$

$$Z \to \ell\bar{\ell}, \quad \ell = e^-, \mu^-, \tau^-. \tag{14.62}$$

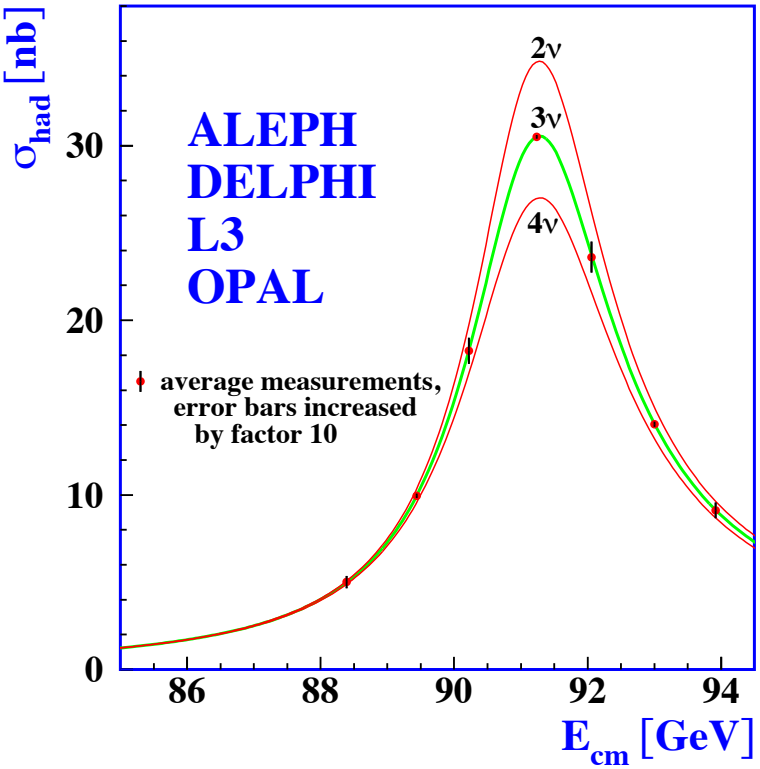

Figure 103: Invisible width of Z boson and number of neutrinos. The data are a combination of the four LEP experiments at CERN, where the measurement error bars are inflated by a factor of ten for visibility. Reproduced from the final LEP Z boson properties report [87].

The Breit–Wigner resonance gives:

$$\sigma = \frac{12\pi}{m_Z^2}\frac{\Gamma_e\Gamma_f}{\Gamma_Z^2}\frac{s\Gamma_Z}{(s-m_Z^2)^2+m_Z^2\Gamma_Z^2}. \tag{14.63}$$

It is found in experiments that the sum of the partial widths (observed decay channels) does not equal the full width (all possible decay channels):

$$\sum_{\text{observed}\,i}\Gamma_i \neq \Gamma_{\text{FWHM}}. \tag{14.64}$$

where i refers to all the observed states of (14.61) and (14.62).

This implies is some "invisible width" from which we infer the existence of further decay channels to neutrinos. We can measure the decay width of each decay channel to each type of neutrino pair $\Gamma_{\nu\bar{\nu}} = \Gamma(Z \to \nu\bar{\nu})$ via neutral current elastic scattering reactions such as:

$$\nu + q \to \nu + q.$$

These measurements can be cross-checked using electroweak theory to calculate the fermion branching width is given by

$$\Gamma_f = \Gamma(Z \to f\bar{f}) = \frac{G_F\sqrt{2}}{12\pi} m_Z^3 (c_V^2 + c_A^2) N_{\text{colours}}, \tag{14.65}$$

where the vector electroweak coupling is $c_V = I_3 - 2Q\sin^2\theta_W$ and $c_A = I_3$, with $I_3, (Q)$ being the weak isospin (electromagnetic) charges for the fermions. Making measurements of all these widths in e^+e^- collisions, we can count the number n_ν of neutrino species:

$$\Gamma_{\text{FWHM}} = \sum_{\text{observed}\, i} \Gamma_i + n_\nu \Gamma_{\nu\bar{\nu}} \tag{14.66}$$

$$= \Gamma_{\text{hadrons}} + \Gamma_{ee} + \Gamma_{\mu\mu} + \Gamma_{\tau\tau} + n_\nu \Gamma_{\nu\nu} \tag{14.67}$$

The best value for the number of light neutrino species is

$$n_\nu = 2.984(8). \tag{14.68}$$

We infer there are three types of neutrinos with mass $< m_Z/2$. Figure 103 shows the data from the four LEP experiments compared with different hypotheses considered, where the data unambiguously favours the three-neutrino hypothesis. This rules out there being more than three generations of leptons in the Standard Model, but it does not preclude the existence of neutrinos heavier than $m_Z/2$.

15 Higgs boson discovery

The Standard Model does not predict the Higgs boson mass. Substituting the small perturbations around the electroweak vacuum $\Phi(x) = \frac{1}{\sqrt{2}}\begin{pmatrix} 0 \\ v+h(x) \end{pmatrix}$ (14.32) into the Higgs potential (14.28) gives

$$V(\Phi^\dagger\Phi) = \lambda\left[\frac{1}{2}(v+h)^2 - \frac{v^2}{2}\right]^2 = \underbrace{\lambda v^2 h^2}_{\text{mass}} + \underbrace{\lambda v h^3 + \frac{1}{4}\lambda h^4}_{\text{self-interactions}}. \tag{15.1}$$

We find the Higgs boson mass is identified as $m_h^2 = 2\lambda v^2$ along with cubic and quartic terms defining Higgs boson self-interactions. Nonetheless, there were several indications for the Higgs boson mass before the direct LHC observation (figure 104).

15.1 Higgs boson searches

The W boson mass receives radiative corrections parametrised by Δr

$$m_W^2 = \frac{\pi\alpha}{\sqrt{2}G_F \sin^2\theta_W}\frac{1}{1-\Delta r}, \tag{15.2}$$

where the dominant contributions are from

$$\Delta r = \Delta r_{\text{QED}} + \Delta r_{\text{Higgs}} + \Delta r_{\text{top}}. \tag{15.3}$$

Here the contributions $\Delta r_{\text{QED}} = 1 - \alpha/\alpha(m_Z)$ is due to the running of the fine structure constant, while the Higgs and top loop contribute:

$$\Delta r_{\text{Higgs}} = \frac{11G_F^2}{24\pi^2\sqrt{2}} m_Z^2 \cos^2\theta_W \ln\left(\frac{m_h^2}{m_Z^2}\right) \propto \ln m_h, \tag{15.4}$$

$$\Delta r_{\text{top}} = \frac{3G_F^2}{8\pi^2\sqrt{2}}\frac{\cos^2\theta_W}{\sin^2\theta_W} m_t^2 \propto m_t^2. \tag{15.5}$$

Note the top loop contributes large corrections due to its quadratic mass dependence compared to the Higgs boson's logarithmic corrections. Therefore, precision measurements of the electroweak couplings $G_F, \sin\theta_W$ together with the masses m_W, m_Z, m_t can indirectly constrain the Higgs boson mass m_h.

Direct LEP searches exclude a light Higgs boson $m_h > 114.5$ GeV, while precision electroweak combinations disfavour one that is too heavy $m_h < 285$ GeV at 95% CL. The best fit value from the LEP 2005 combination is $m_h = 129^{+74}_{-49}$ GeV [87]. In 2011, Tevatron direct searches excluded of around Higgs boson 160–170 GeV.

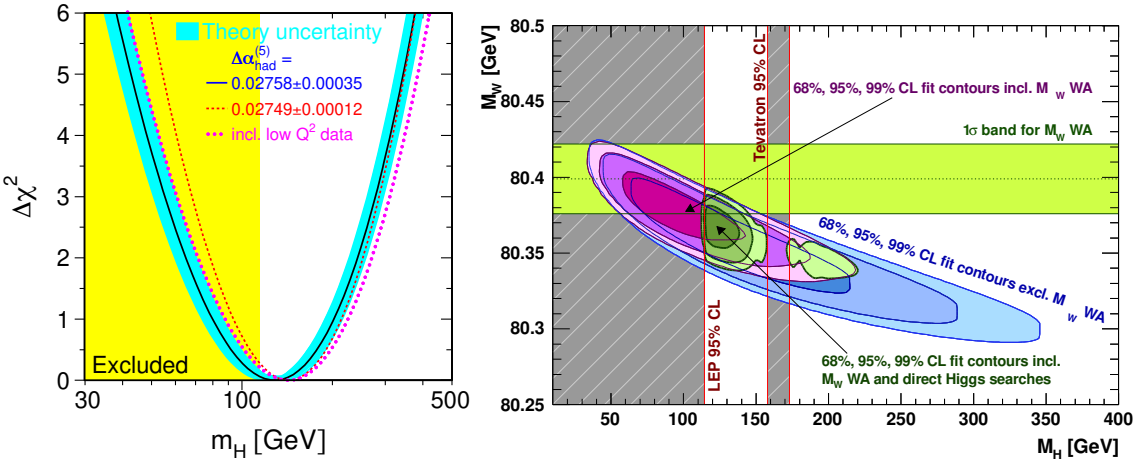

(a) LEP+SLD 2005 global fits [87] (b) Global fits 2011 with Tevatron exclusion [98]

Figure 104: Constraints on the Higgs boson mass from global electroweak data just after LEP finished in 2005. best fit Higgs boson mass of around 115 GeV, favouring masses $m_h <$ 285 GeV at 95% CL. In 2011, Tevatron direct searches excluded masses around 160 GeV.

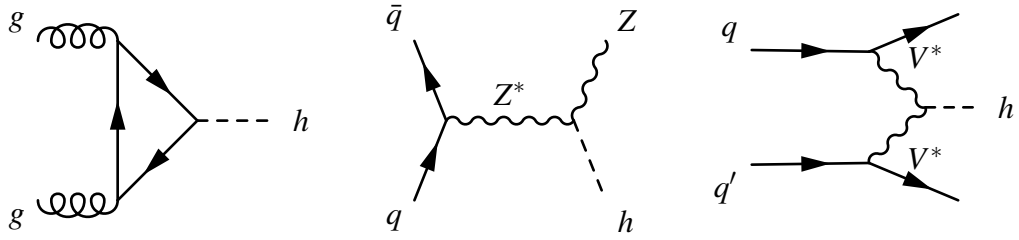

(a) Gluon-gluon fusion (b) Higgs-strahlung (c) Vector boson fusion

Figure 105: **Higgs boson production diagrams**. These show the important production mechanisms for the Higgs boson at the LHC.

Toward the end of 2011, ATLAS and CMS were analysing the first 7 TeV proton-proton collisions recorded at the LHC. There are a few different production modes of the Higgs boson:

- **Gluon-gluon fusion**: $gg \to h$ (figure 105a). A gluon from each of the protons fuse via a top quark loop. This has the highest cross-section at the LHC of all the production modes. At the LHC, the gluon parton distribution function from the protons dominate over the quarks. The top Yukawa coupling is the largest of all the quark loops, which dominates.

- **Higgs-strahlung**: $qq \to V^* \to Vh$, where $V = W/Z$ (figure 105b). This is also called **associated production**, where a Higgs boson in association with a gauge boson.

- **Vector boson fusion**: $qq \to q'(V^*V^* \to h)q'$ (figure 105c). Here quarks from each proton emit a virtual gauge boson W^*/Z^* that fuse into a Higgs boson. Two outgoing quarks form two additional jets, which are usually boosted in the forward direction.

The cross-sections for these are displayed in figure 107a, which steadily decrease with Higgs boson mass. The Higgs bosons decays depend strongly on the mass (figure 107b), but the primary channels used for the discovery were:

- **Diboson four-lepton** $h \to Z^*Z \to 4\ell$ (figure 106a). The small branching fraction is compensated by the relatively low background rate. The four-lepton invariant mass $m_{4\ell}$ distribution and a recent event display are shown in figure 108. In particular, the four leptons can either be electrons or muons, which are grouped into pairs of same-flavour opposite-sign pairs $(\ell^+\ell^-, \ell'^+\ell'^-)$, one of which satisfies an on-shell Z boson mass constraint $m_{\ell\ell} \in (m_Z \pm \Delta m)$.

- **Di-photon** $h \to \gamma\gamma$ (figure 106b). The branching fraction is only around 0.2%, but the excellent di-photon mass resolution of the ATLAS and CMS detectors means the signal-to-background rates are reasonable for discovery. The invariant mass distribution $m_{\gamma\gamma}$ and a recent event display are shown in figure 109.

- **Diboson semi-leptonic** $h \to W^*W \to \ell\nu_\ell\ell\nu_\ell$. This has a much higher branching fraction than the 4ℓ final state, but the two neutrinos makes reconstruction challenging.

- **Di-fermion** $h \to b\bar{b}, \tau^+\tau^-$ (figure 106c). Given the coupling is proportional to the fermion mass, these have large branching fractions. However, these hadronic signatures especially $b\bar{b}$ have very large backgrounds from QCD initiated processes such as gluon splitting $g \to b\bar{b}$. These channels do not contribute substantially to the discovery, but their later observation during 13 TeV runs play a pivotal role in testing the Yukawa structure of fermion couplings. Post-discovery, the branching ratios of $\mathscr{B}(h \to b\bar{b}) \approx 58\%$ and $\mathscr{B}(h \to \tau^+\tau^-) \approx 6.3\%$.

15.2 Discovery statistics

In data analysis or statistics classes, we first learn to fit data to some model expectation and quantify the goodness of fit. Among the simplest approaches is the method of *least*

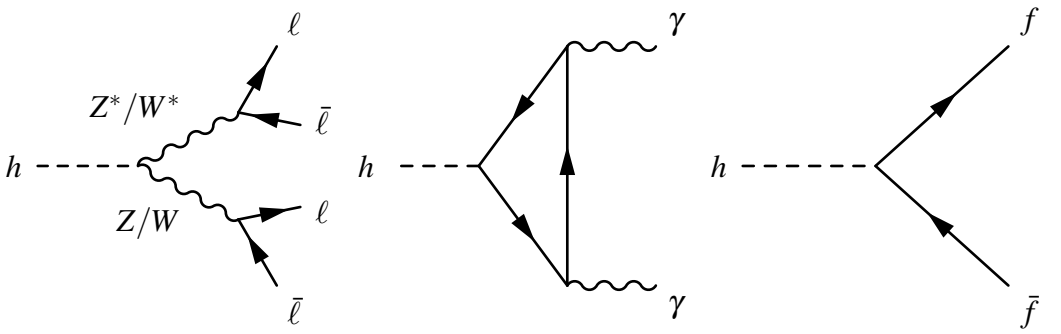

(a) Diboson (to four lepton) (b) Di-photon (c) Di-fermion

Figure 106: **Feynman diagrams of Higgs boson decays**. These are the key decay modes for discovering and characterising the Higgs boson.

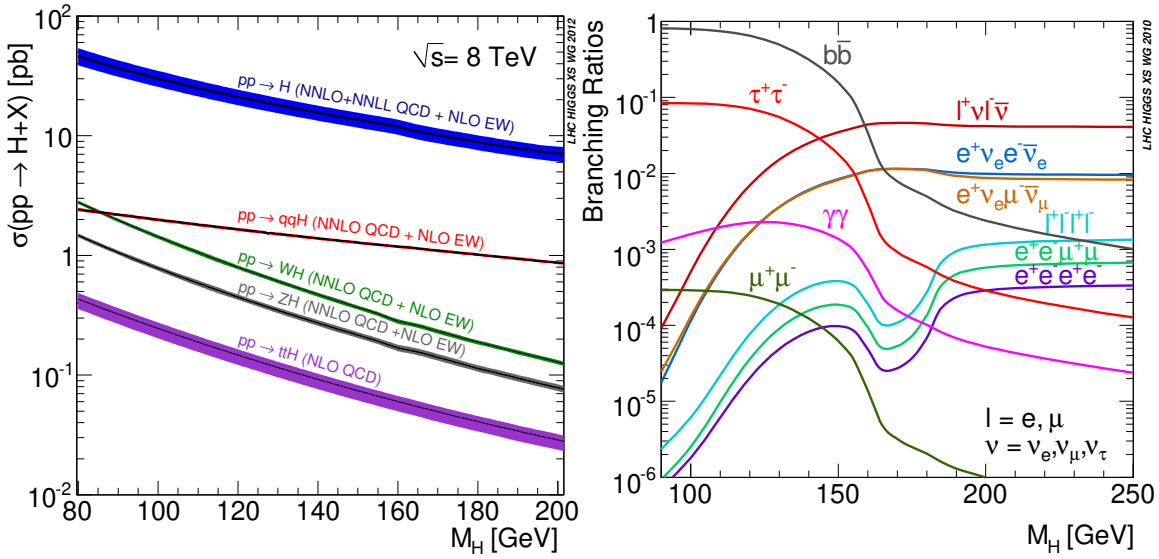

(a) LHC 8 TeV cross-section (b) Higgs branching fractions

Figure 107: **Higgs boson cross-sections and decays**. Standard Model Higgs boson production cross-section at 8 TeV vs mass and branching fraction with gauge boson decays into the observed lepton final states, from LHC Higgs Working Group.

squares, which minimises the sum of the square differences between the observed and model expectation given its uncertainties for each data point or bin i:

$$\chi^2 = \sum_i \frac{(\text{observed}_i - \text{expected}_i)^2}{(\text{uncertainty on expected})_i^2} = \sum_i \frac{(N^i_{\text{data}} - N^i_{\text{bkg}})^2}{\sigma^2_{\text{bkg},i}}. \tag{15.6}$$

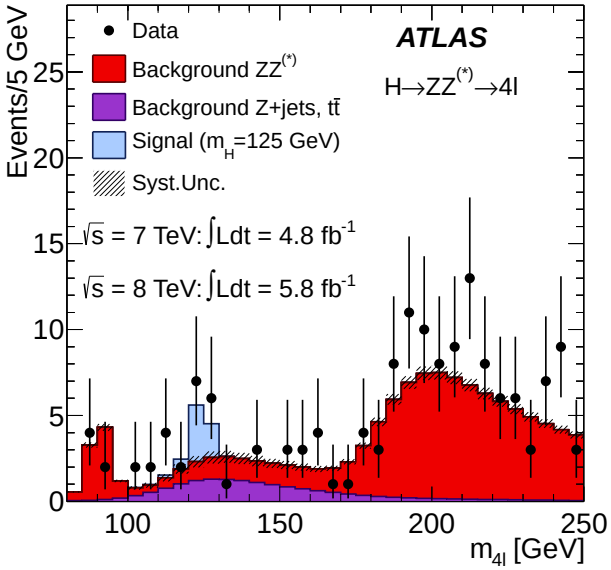

(a) ATLAS $h \to 4\ell$ 2011–12

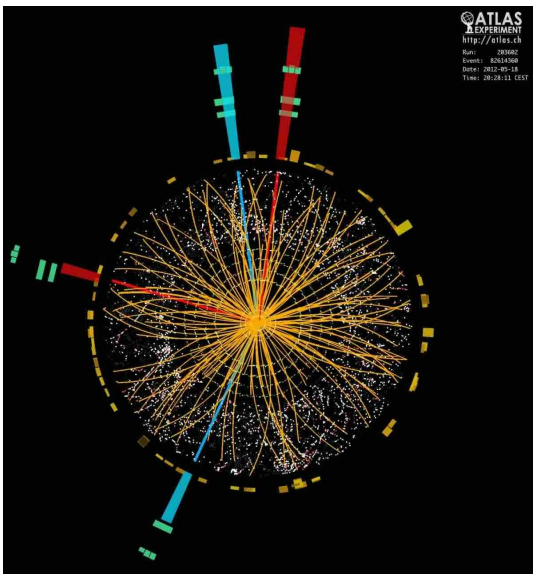

(b) Event display of $2e2\mu$

Figure 108: **ATLAS Higgs boson discovery: four-lepton channel**. The Higgs 4 lepton observed at the ATLAS Experiment in the $h \to 4\ell$ decay mode, which is the blue resonance peak centred at its 125 GeV mass. Images: Ref. [99], ATLAS-PHO-COLLAB-2012-007.

Not only is this intuitive, it is grounded in the statistics of the chi-square distribution. To discover new particles like the Higgs boson, we test the goodness of fit between two hypotheses: the background-only (null H_0) hypothesis with no Higgs boson and the background-plus-signal (alternative H_1) with a Higgs boson. As a rule of thumb (due to the central limit theorem), you will often see statistical significance Z formulas like

$$Z_{\text{stat}} \approx \frac{S}{\sqrt{B}}, \quad Z_{\text{stat+syst}} \approx \frac{S}{\sqrt{B + (\zeta_{\text{syst}} B)^2}} \tag{15.7}$$

as rough approximations of the signal significance for signal counts $S = N_{\text{obs}} - B$ above background counts B with uncertainties from only statistical fluctuations $\sigma_{\text{stat}} = \sqrt{B}$ or including systematic uncertainties $\sigma_{\text{syst}} = \zeta_{\text{syst}} B$. These apply in the limit where the background uncertainties follow a Gaussian distribution and the signal is small relative to the background.

For consistency between experiments, the LHC adopts community standards in presenting statistical analyses, detailed in Ref. [101, 102] with prominent NYU history spearheaded by Kyle Cranmer. These use the likelihood $L(\mu)$ function as a product of probabilities for observing event i

$$L(\mu) = \prod_i \text{Poisson}(i|\mu), \tag{15.8}$$

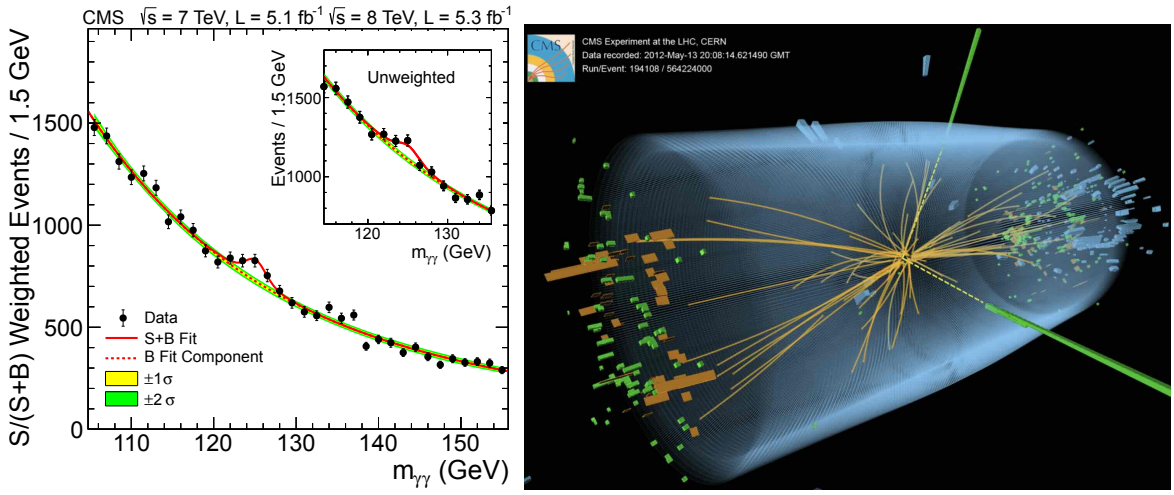

(a) CMS $h \to \gamma\gamma$ 2011–12 (b) Event display of $\gamma\gamma$

Figure 109: **CMS Higgs boson discovery: diphoton channel**. The original diphoton discovery data observed at the CMS Experiment using 2011–12 LHC data. Images: Ref. [100], CMS-PHO-EVENTS-2013-003.

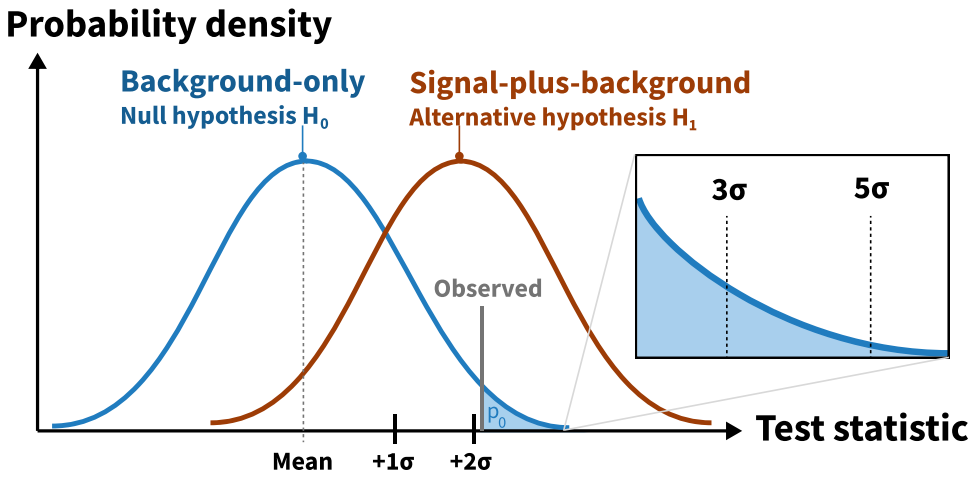

Figure 110: Sketch of probability distributions for test statistics and p-values for background-only and signal-plus-background hypotheses.

given a parameter μ characterising the presence of a signal, which follows a Poissonian distribution for random particle counts

$$\text{Poisson}(n|\lambda) = \frac{\lambda^n e^{-\lambda}}{n!}. \tag{15.9}$$

Figure 111: Selected photos from the 4th July 2012 event at the CERN main auditorium announcing the discovery of the Higgs boson. Centre shows Fabiola Gianotti announcing the ATLAS discovery. Right shows François Englert and Peter Higgs at the event. Images: CERN-HI-1207136-58.

For the scope of these lectures, we neglect systematic uncertainties in the likelihood. We then construct a test statistic called the **profile-likelihood ratio**[63] λ and the negative logarithm is taken (to turn products into summations) to give the profile log-likelihood q_μ:

$$q_\mu = -2\ln\lambda, \quad \lambda = \frac{L(\mu)}{L(\hat{\mu})}, \tag{15.10}$$

where $\hat{\mu}$ is the value of the signal parameter that maximises the likelihood L. You will often see the signal strength as the ratio of the fitted vs predicted $\mu = N_{\text{fit}}^{\text{signal}}/N_{\text{pred}}^{\text{signal}}$.

As we learn in statistics classes, we conduct statistical tests via two hypotheses:

- **Background-only hypothesis** (null hypothesis H_0) that sets signal $\mu = 0$ set to zero. We compute the probability that the test statistic is greater than that the data is compatible with the background-only hypothesis called the p-value

$$p_0 = 1 - p_b = \int_{q_0^{\text{obs}}}^{\infty} f(q_0|\mu = 0)\mathrm{d}q_0, \tag{15.11}$$

  where f is the probability density function of the test statistic, where Ref. [101] details asymptotic formulas for its determination.

- **Signal-plus-background hypothesis** (alternative hypothesis H_1) that is the scenario with a non-zero signal $\mu \neq 0$. We compute an analogous p-value for this hypothesis:

$$p_{s+b} = \int_{q_\mu^{\text{obs}}}^{\infty} f(q_\mu|\mu)\mathrm{d}q_\mu. \tag{15.12}$$

[63] For enthusiasts, the Neyman–Pearson lemma ensures the likelihood ratio is the most powerful test statistic.

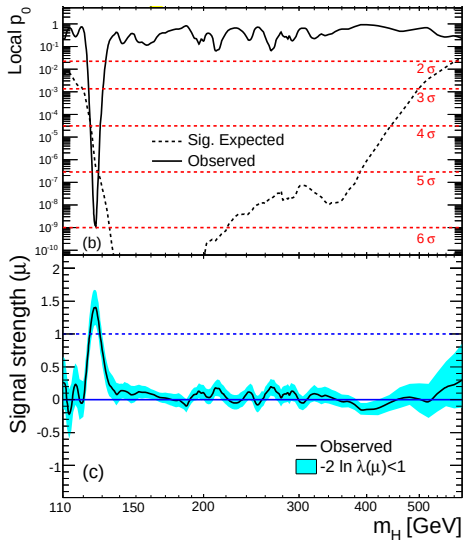

(a) ATLAS p-values [103]

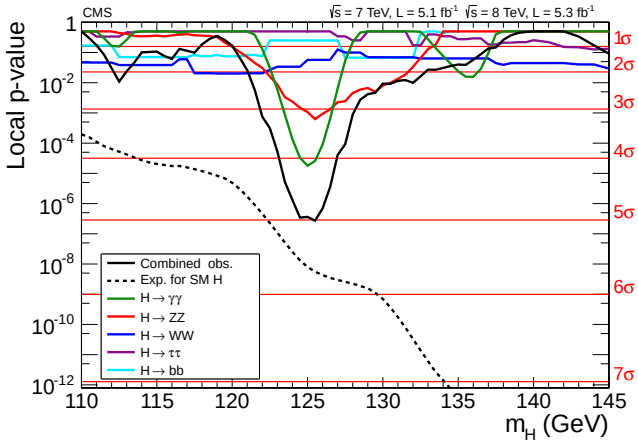

(b) CMS p-values by channel [100]

Figure 112: Statistical analysis combining the different production and decay modes during the SM Higgs boson searches during the initial years of the LHC.

The statistical significance is computed by

$$Z = \Phi^{-1}(1 - p_0), \tag{15.13}$$

where Φ is the inverse cumulative probability distribution. A statistical significance of 5 standard deviations (5σ) corresponds to a p-value $p_0 = 2.87 \times 10^{-7}$. Therefore, 5σ implies less 3 in 10 million chance an excess is due to statistical fluctuations alone. To exclude the presence of a signal, the LHC experiments uses a conservative $\mathrm{CL_s}$ value defined by

$$\mathrm{CL_s} = \frac{p_{s+b}}{1 - p_b}. \tag{15.14}$$

Injected signals with a μ parameter that causes $\mathrm{CL_s} < 0.05$ are excluded at 95% CL.

The ATLAS and CMS statistical analyses feature greater complexity, given they combine different Higgs boson production and decay channels, and account for systematic uncertainties. Figure 112a shows background-only p-values p_0 and the signal strength μ by the ATLAS combination for different Higgs boson masses m_h. Figure 112b shows the CMS p-value plot for different m_h separated by the different Higgs boson decay modes, showing the di-photon $\gamma\gamma$ and four-lepton $Z^*Z \to 4\ell$ channels dominate the discovery sensitivity. A new boson consistent with this Standard Model Higgs boson was announced in 2012 by the ATLAS [103] and CMS [100] Collaborations. This was promptly recognised by the 2013

Nobel prize in physics[64]. The mass of the Higgs boson was initially measured in 2012 to be

$$m_h(\text{ATLAS}) = 126.0 \pm 0.4\,(\text{stat}) \pm 0.4\,(\text{syst})\ \text{GeV}, \tag{15.15}$$

$$m_h(\text{CMS}) = 125.3 \pm 0.4(\text{stat}) \pm 0.5(\text{syst})\ \text{GeV}. \tag{15.16}$$

The statistical compatibility between the two independent collaborations and experimental apparatus is a gold standard of scientific reproducibility. The signal significance and statistical precision has since been improved with the large LHC dataset collected since.

15.3 Higgs–Yukawa interaction

A hallmark of the Higgs boson is that its interaction strength is characterised by the Yukawa coupling y_{hff} to fermions. The mass of the fermion is given by its coupling to the Higgs and the electroweak vacuum expectation value (v_{EW}):

$$m_f = \frac{y_f}{\sqrt{2}} v_{\text{EW}}. \tag{15.17}$$

Figure 113 shows a recent ATLAS measurements of Higgs coupling strengths to massive fermions and bosons. This provides a direct test of the dynamical structure of the Standard Model.

From the fermion-lepton Yukawa part of the electroweak Lagrangian (14.23), we have explicitly

$$\mathscr{L}_{\text{Yukawa}} = -y_\ell \left[\begin{pmatrix} \bar{\nu}_\ell & \bar{\ell} \end{pmatrix}_L \begin{pmatrix} \phi^+ \\ \phi_0 \end{pmatrix} \ell_R + \bar{\ell}_R \begin{pmatrix} \phi^{+\dagger} & \phi^{0\dagger} \end{pmatrix} \begin{pmatrix} \nu_\ell \\ \ell \end{pmatrix}_L \right] \tag{15.18}$$

Now recall from (14.32) that after symmetry breaking, the scalar fields in the unitary gauge become

$$\begin{pmatrix} \phi^+ \\ \phi^0 \end{pmatrix} = \frac{1}{\sqrt{2}} \begin{pmatrix} 0 \\ v + h(x) \end{pmatrix}. \tag{15.19}$$

Substituting this into (15.18) we obtain the Lagrangian after symmetry breaking

$$\mathscr{L} = -\frac{y_\ell v}{\sqrt{2}} \left(\bar{\ell}_L \ell_R + \bar{\ell}_R \ell_L \right) - \frac{y_\ell h(x)}{\sqrt{2}} \left(\bar{\ell}_L \ell_R + \bar{\ell}_R \ell_L \right) \tag{15.20}$$

We recognise the first set of terms are precisely the form of a Dirac fermion mass term:

$$\boxed{\mathscr{L} = \underbrace{-m_\ell \left(\bar{\ell}_L \ell_R + \bar{\ell}_R \ell_L \right)}_{\text{lepton mass term}} \underbrace{- \frac{m_\ell}{v} h(x) \left(\bar{\ell}_L \ell_R + \bar{\ell}_R \ell_L \right)}_{\text{lepton-Higgs interaction}}, \quad \text{where} \quad m_\ell = \frac{y_\ell v}{\sqrt{2}}.} \tag{15.21}$$

[64] https://www.nobelprize.org/prizes/physics/2013/summary/

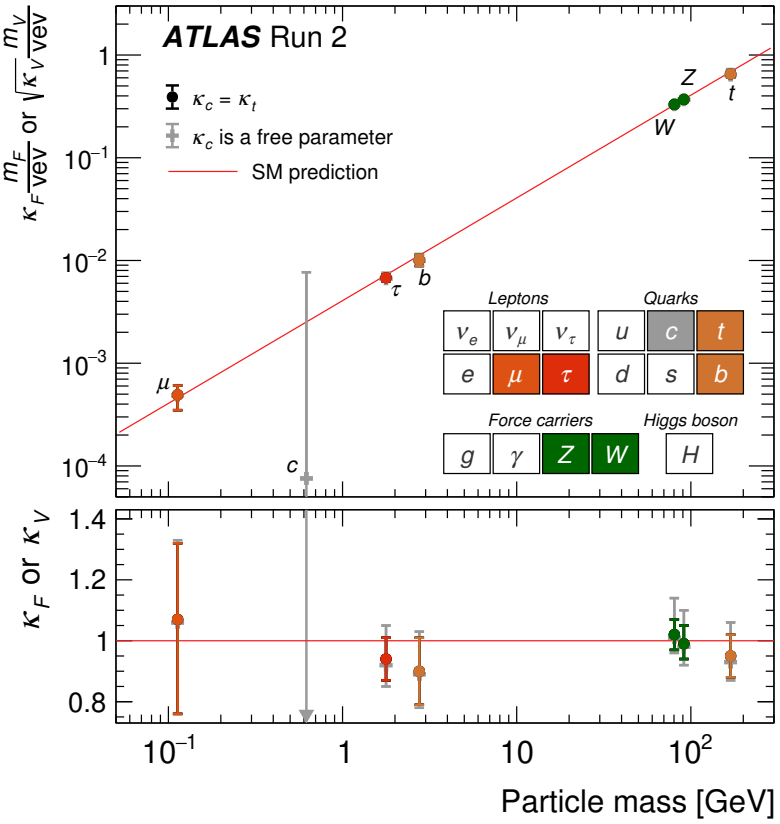

Figure 113: Higgs couplings measured relative to the Standard Model prediction from ATLAS [104] with similar measurements by CMS [105]. These measurements are from 2022, based on the full Run 2 LHC results. The red line shows the Standard Model expectation where the Higgs coupling is proportional to the mass of the particle.

The second term is the lepton-Higgs interaction term which gives the amplitude for leptons to emit a Higgs boson, with coupling m_ℓ/v. Originally, the Glashow–Salam–Weinberg model was developed to describe only leptons given quarks remained speculative in the 1960s and evidence for non-trivial neutrino masses was lacking. Remarkably, the quarks follow a similar construction with quark–Higgs mass generation mechanism analogous but slightly enlarged. We place the left-handed quarks into SU(2) doublets as

$$Q_L = \begin{pmatrix} q_u \\ q_d \end{pmatrix}_L \in \left\{ \begin{pmatrix} u_L \\ d_L \end{pmatrix}, \begin{pmatrix} c_L \\ s_L \end{pmatrix}, \begin{pmatrix} t_L \\ b_L \end{pmatrix} \right\}. \tag{15.22}$$

Quark	m_q [GeV]	$y_q = m_q(\sqrt{2}/v$
Up	$\approx 2.3 \times 10^{-3}$	$\approx 1.3 \times 10^{-5}$
Down	$\approx 4.8 \times 10^{-3}$	$\approx 2.8 \times 10^{-5}$
Strange	0.0958	5.51×10^{-4}
Charm	1.28	7.36×10^{-3}
Bottom	4.7	0.027
Top	173.2	0.996

Table 7: **Quark masses and Yukawa couplings**. Masses taken from reading off figure 5.

The right-handed quarks just exist as SU(2) singlets in their up and down types:

$$u_R^i = \{u_R, c_R, t_R\}, \quad d_R^i = \{d_R, s_R, b_R\}. \tag{15.23}$$

Then construct the Yukawa interactions analogously

$$\mathscr{L}_{\text{quark-Yukawa}} = -Y_u^{ij} \bar{Q}_L^i \tilde{\Phi} u_R^j - Y_d^{ij} \bar{Q}_L^i \Phi d_R^j, \tag{15.24}$$

where $\tilde{\phi} = \mathrm{i}\sigma_2 \phi^*$ with σ_2 being the second Pauli matrix. The i, j indices run over generations.

To reach the physical mass basis, we can rotate the quark fields in the flavour basis via a set of 3×3 unitary matrices $\mathbb{V}_d, \mathbb{V}_u$, conventionally:

$$d_L \to \mathbb{V}_d \cdot d_L, \quad u_L \to \mathbb{V}_u \cdot u_L, \tag{15.25}$$

$$d_R \to \mathbb{U}_d \cdot d_R, \quad u_R \to \mathbb{U}_u \cdot u_R. \tag{15.26}$$

This allows the reach the basis that is diagonal in masses for the Yukawa couplings

$$Y_d \to \mathbb{V}_d^\dagger \cdot Y_d \cdot \mathbb{U}_d = \begin{pmatrix} y_d & & \\ & y_s & \\ & & y_b \end{pmatrix}, \quad Y_u \to \mathbb{V}_u^\dagger \cdot Y_u \cdot \mathbb{U}_u = \begin{pmatrix} y_u & & \\ & y_c & \\ & & y_t \end{pmatrix}. \tag{15.27}$$

From the quark masses the mass, we can divide by $\sqrt{2}/(246\ \text{GeV})$ as predicted by the Standard Model to obtain the expected Yukawa couplings. These are displayed in table 7. We can then test this hypothesis by measuring the Yukawa couplings directly via events with e.g. tth processes for y_t. It is possible to performa similar exercise for the charged leptons. Figure 113 displays recent status of these measurements by the ATLAS Collaboration. Why is the top quark Yukawa coupling nearly unity and others span five orders of magnitude? We currently do not know.

15.4 Cabibbo–Kobayashi–Maskawa matrix

We see six degrees of freedom in the Yukawa matrices are for the six quark masses. There are actually four further independent degrees of freedom corresponding to angles and a complex phase. During the diagonalisation of the Higgs–Yukawa matrices, the quark fields in the charged-current interaction with the $W^{\pm}$ bosons (14.47) are also rotated:

$$j_{+}^{\mu} = \bar{u}_L \bar{\sigma}^{\mu} d_L \to \bar{u}_L \bar{\sigma}^{\mu} (\mathbb{V}_u^{\dagger} \mathbb{V}_d) d_L, \tag{15.28}$$

$$j_{-}^{\mu} = \bar{d}_L \bar{\sigma}^{\mu} u_L \to \bar{d}_L \bar{\sigma}^{\mu} (\mathbb{V}_u^{\dagger} \mathbb{V}_d)^{\dagger} u_L. \tag{15.29}$$

The combination $\mathbb{V}_u^{\dagger}\mathbb{V}_d$ is not the identity matrix but rather the **Cabibbo-Kobayashi-Maskawa (CKM) matrix**:

$$V_{\mathrm{CKM}} = \mathbb{V}_u^{\dagger} \mathbb{V}_d. \tag{15.30}$$

The discovery of a third generation of quarks, namely the bottom and top quark, naturally extends the Cabibbo mixing matrix into a 3×3 mixing matrix. Now we see the origin of quark flavour mixing proposed by Cabibbo: it actually comes from diagonalising the Higgs–Yukawa matrices to reach the mass basis! One conventional way to write the CKM matrix is via an equation for quark flavour mixing:

$$\begin{pmatrix} d' \\ s' \\ b' \end{pmatrix} = \begin{pmatrix} V_{ud} & V_{us} & V_{ub} \\ V_{cd} & V_{cs} & V_{cb} \\ V_{td} & V_{ts} & V_{tb} \end{pmatrix} \begin{pmatrix} d \\ s \\ b \end{pmatrix}, \tag{15.31}$$

$$(\text{mass basis}) = \quad V_{\mathrm{CKM}} \quad \times \quad (\text{flavour basis}). \tag{15.32}$$

We see that the upper left 2×2 part of the matrix is exactly the Cabibbo matrix. The mass basis comprises the states coupling to the Higgs boson while the flavour basis are the states coupling to the weak gauge bosons. This describes how each up-type quark mixes with the other three generations. The standard parametrisation of the CKM matrix [75] is to write it in terms of three Euler angles $\theta_{12}, \theta_{13}, \theta_{23}$, where $s_{ij} = \sin\theta_{ij}, c_{ij} = \cos\theta_{ij}$ and one irreducible complex phase δ

$$V_{\mathrm{CKM}} = \begin{pmatrix} 1 & 0 & 0 \\ 0 & c_{23} & s_{23} \\ 0 & -s_{23} & c_{23} \end{pmatrix} \begin{pmatrix} c_{13} & 0 & s_{13} e^{-\mathrm{i}\delta} \\ 0 & 1 & 0 \\ s_{13} e^{-\mathrm{i}\delta} & 0 & c_{13} \end{pmatrix} \begin{pmatrix} c_{12} & s_{12} & 0 \\ -s_{12} & c_{12} & 0 \\ 0 & 0 & 1 \end{pmatrix}. \tag{15.33}$$

The values of the four independent parameters comprising three angles and the complex phase are, as taken from the PDG 2024 update [75]:

$$\sin\theta_{12} = 0.22501 \pm 0.00068, \quad \sin\theta_{13} = 0.003732^{+0.000090}_{-0.000085} \tag{15.34}$$

$$\sin\theta_{23} = 0.04183^{+0.00079}_{-0.00069}, \qquad \delta \qquad = 1.147 \pm 0.026. \tag{15.35}$$

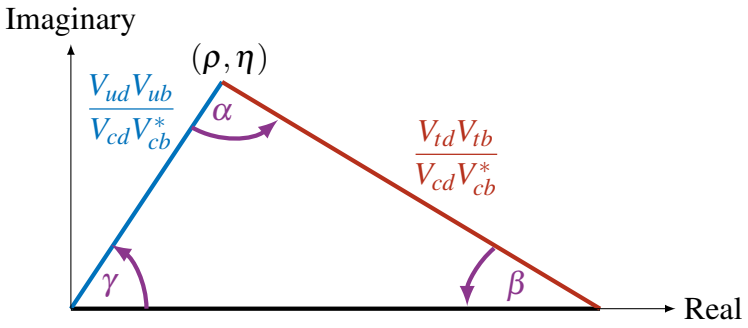

Figure 114: Sketch of CKM matrix unitarity triangle in the complex plane, with the angle names following the α, β, γ convention and base of triangle being unit normalised.

Interestingly, the values of the CKM matrix are nearly diagonal [75]:

$$\begin{pmatrix} |V_{ud}| & |V_{us}| & |V_{ub}| \\ |V_{cd}| & |V_{cs}| & |V_{cb}| \\ |V_{td}| & |V_{ts}| & |V_{tb}| \end{pmatrix} = \begin{pmatrix} 0.97435\,(16) & 0.22501\,(68) & 0.003732^{+0.000090}_{-0.000085} \\ 0.22487\,(68) & 0.97349\,(16) & 0.04183^{+0.00079}_{-0.00069} \\ 0.00858^{+0.00019}_{-0.00017} & 0.04111^{+0.00077}_{-0.00068} & 0.999118^{+0.000029}_{-0.000034} \end{pmatrix}. \quad (15.36)$$

We see the near-diagonal structure of the CKM matrix means quarks interactions via the weak force that stay within its own generation have the highest probability. This is strongest for the third generation, where we see $V_{tb} \approx 0.999$ being close to unity means a top-quark decays via the weak force predominantly to a bottom-quark, and very rarely to a down or strange quark due to the smallness of $V_{td} \approx 0.009$ and $V_{ts} \approx 0.04$, respectively. We can visualise the relative sizes of the CKM matrix elements to see the hierarchy of quark flavour mixing more clearly:

$$V_{\text{CKM}} \approx$$

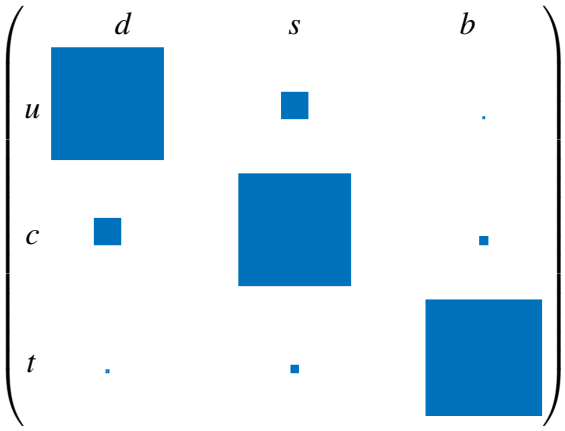

. (15.37)

Motivated by the near-diagonal structure in the CKM matrix elements, this is often re-

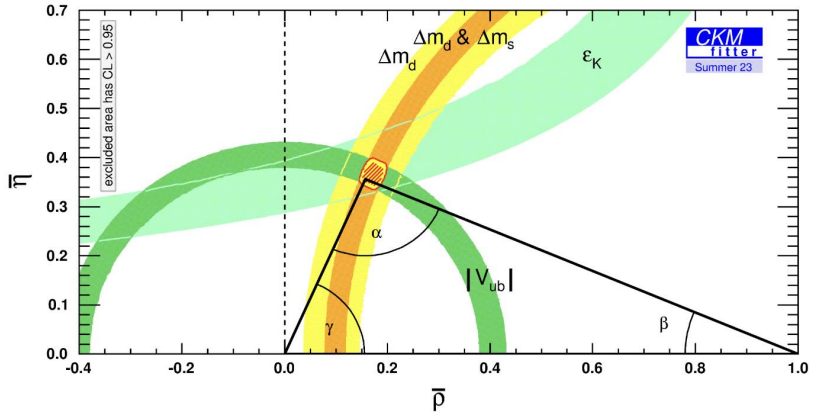

(a) Non-angle measurements

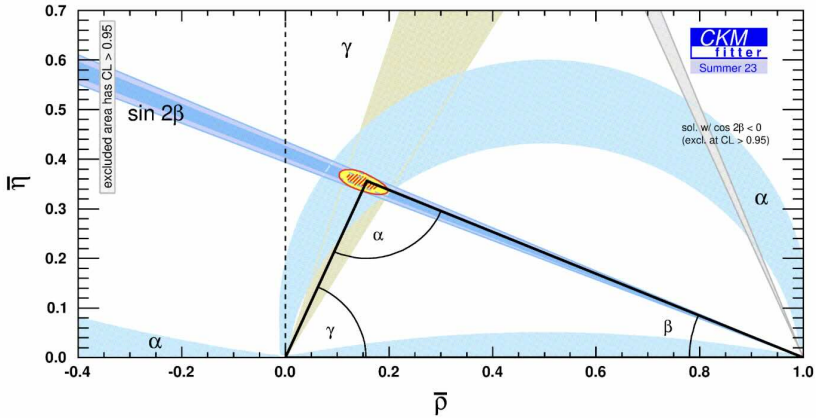

(b) Only angle measurements

Figure 115: Experimental constraints from the CKMFitter collaboration and the best fit values divided into measurements of the unitarity triangle lengths and angles.

casted into what is called the Wolfenstein parametrisation as an expansion in small λ:

$$V_{\text{CKM}} = \begin{pmatrix} 1 & 0 & 0 \\ 0 & 1 & 0 \\ 0 & 0 & 1 \end{pmatrix} + \lambda \begin{pmatrix} -\frac{\lambda}{2} & 1 & A\lambda^2(\rho - \mathrm{i}\eta) \\ -1 & -\frac{\lambda}{2} & A\lambda \\ A\lambda^2(\rho - \mathrm{i}\eta) & -A\lambda & 0 \end{pmatrix} + \dots$$
$$\approx \begin{pmatrix} 1 - \frac{\lambda^2}{2} & \lambda & A\lambda^3(\rho - \mathrm{i}\eta) \\ -\lambda & 1 - \frac{\lambda^2}{2} & A\lambda^2 \\ A\lambda^3(1 - \rho - \mathrm{i}\eta) & -A\lambda^2 & 1 \end{pmatrix}. \tag{15.38}$$

With this, λ, A, ρ, η are the four parameters mapped to the original three Euler angles and one phase, with the correspondence to the Cabibbo angle $\lambda \approx \sin\theta_{12}$. This approximation

is phenomenologically motivated and makes the hierarchical structure of the CKM matrix more manifest.

The CKM matrix is unitary in the Standard Model, where the unitarity conditions are $\sum_i V_{ij}V_{ik}* = \delta_{ij}, \sum_j V_{ij}V^*_{kj} = \delta_{ik}$. This leads to the CKM triangle constraints, where the standard choice for experimental tests is

$$1 + \frac{V_{ud}V^*_{ub}}{V_{cd}V^*_{cb}} + \frac{V_{td}V^*_{tb}}{V_{cd}V^*_{cb}} = 0 \tag{15.39}$$

As the right two terms are in general complex, we can plot this as a triangle, know as the **unitarity triangle**. Cecilia Jarlskog introduced an invariant J [106] to parametrise the amount of CP-violation, which is twice the area of the unitarity triangle using the cross product

$$J = \mathrm{Im}\,(V_{us}V_{cb}V^*_{ub}V^*_{cs}) = c_{12}s_{12}s_{13}s_{23}c^2_{13}\sin\delta = (2.96 \pm 0.20) \times 10^{-5}. \tag{15.40}$$

Measuring $J \neq 0$ implies the existence of CP violation and is equivalent to half the area of the unitarity triangle.

Figure 114 shows a sketch of this triangle in the complex plane adopting widely used convention. Figure 115 displays recent experimental constraints on the triangle.

Let us see how this relates to CP violation first observed in kaon mixing we introduced in section 12.5. Consider this matrix element for a kaon transitioning into its antiparticle:

$$\mathscr{M}(K \to \bar{K}) = \quad \propto V_{ud}V^*_{cs}V_{us}V^*_{cd}. \tag{15.41}$$

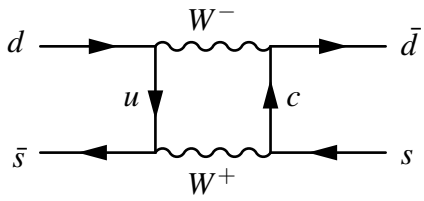

The *CP* conjugate process is

$$\mathscr{M}(\bar{K} \to K) \propto \quad \propto V^*_{ud}V_{cs}V^*_{us}V_{cd}. \tag{15.42}$$

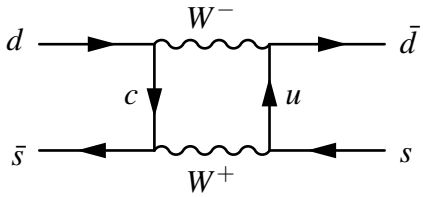

This is equivalent to the conjugating the matrix element $\mathscr{M}^*(K \to \bar{K})$. Because the CKM elements in such combinations have a non-zero imaginary part, CP violation is encapsulated by $\mathscr{M}(K \to \bar{K}) - \mathscr{M}(\bar{K} \to K) \neq 0$ being non-vanishing by an amount

$$\mathscr{M}(\bar{K} \to K) - \mathscr{M}(K \to \bar{K}) \propto \mathrm{Im}(V^*_{ud}V_{cs}V^*_{us}V_{cd}). \tag{15.43}$$

Together with other diagrams in the box loop, this sets the value of ε in equation (12.75).

The underlying origin of the three angles plus one complex phase, which appear to have non-random structure is unknown. It is an open question in particle physics. This is reminiscent of the periodic table first being constructed in the nineteenth century before quantum mechanics and atomic nuclei were discovered. It is similar to the particle zoo of hadrons in the 1950s, where the particle zoo of newly discovered hadrons motivated detailed measurement of mass, spin, lifetime properties before motivating a deeper explanation of the quark model and the strong force. This motivates significant research effort to measure and explain these values of the CKM matrix. This is **the problem of flavour**.

16 Massive neutrinos

The 2015 Nobel prize in physics[65] recognised the experimental evidence for atmospheric and solar neutrino oscillations, which were subsequently confirmed by laboratory and reactor neutrinos. This requires extending the conventional Standard Model to include neutrinos with non-zero mass differences.

16.1 Two-flavour oscillation model

The behaviour is elucidated using non-relativistic quantum mechanics. For algebraic simplicity, we consider the possibility of two flavours of neutrinos $\{\nu_e, \nu_\mu\}$ mixing. We assume their non-zero masses are not well-defined states, but are instead superpositions of mass eigenstates $\{i, j\}$. We write the electron-neutrino and muon-neutrino states as a mixed state, similar to quark flavour mixing:

$$\begin{pmatrix} |\nu_e\rangle \\ |\nu_\mu\rangle \end{pmatrix} = \begin{pmatrix} \cos\theta & -\sin\theta \\ \sin\theta & \cos\theta \end{pmatrix} \begin{pmatrix} |i\rangle \\ |j\rangle \end{pmatrix} \tag{16.1}$$

We suppose an electron-neutrino was produced at time $t = 0$ with well-defined momentum[66] $\mathbf{p}$. So the initial state of the electron-neutrino is

$$|\nu_e, \mathbf{p}\rangle = \cos\theta |i, \mathbf{p}\rangle - \sin\theta |j, \mathbf{p}\rangle \tag{16.2}$$

i.e. simply multiplying the top row of the matrix in (16.1).

Solving the time-dependent Schrödinger equation in stationary states, each term in the initial state (16.2) acquires a phase related to the energy of the corresponding mass eigenstate:

$$|\psi(t)\rangle = \exp(-\mathrm{i}E_i t)\cos\theta |i\rangle - \exp\big(-\mathrm{i}E_j t\big)\sin\theta |j\rangle \tag{16.3}$$

where we drop the $\mathbf{p}$ label in the kets. We now seek the amplitude for measuring $|\nu_\mu\rangle$ at some arbitrary time by using the linear combinations formed from the lower row of (16.1):

$$\langle\nu_\mu|\psi(t)\rangle = (\sin\theta|i\rangle + \cos\theta|j\rangle)\left(\mathrm{e}^{-\mathrm{i}E_i t}\cos\theta|i\rangle - \mathrm{e}^{-\mathrm{i}E_j t}\sin\theta|j\rangle\right). \tag{16.4}$$

Using orthogonality of the mass eigenstates, this becomes

$$\langle\nu_\mu|\psi(t)\rangle = \sin\theta\cos\theta\left(\mathrm{e}^{-\mathrm{i}E_i t} - \mathrm{e}^{-\mathrm{i}E_j t}\right). \tag{16.5}$$

[65] https://www.nobelprize.org/prizes/physics/2015/summary/

[66] We assume the momenta of both mass eigenstates are equal $\mathbf{p}_i = \mathbf{p}_j$ from the outset. This is a questionable assumption textbooks usually make, but this simplification turns out to agree with experiment rather well.

Extracting a factor of $e^{-i(E_i+E_j)/2}$ and taking the modulus square $|\langle \nu_\mu | \psi(t) \rangle|^2$ gives the probability of finding the neutrino in the muon type state:

$$P(\nu_e \to \nu_\mu, t) = \sin^2(2\theta) \sin^2 \left[\frac{(E_j - E_i)t}{2} \right] \tag{16.6}$$

Neutrinos are ultra-relativistic so we can make the binomial approximations

$$E_j - E_i = p\sqrt{1 + \left(\frac{m_j}{p}\right)^2} - p\sqrt{1 + \left(\frac{m_i}{p}\right)^2} \approx \frac{m_j^2 - m_i^2}{2p} \tag{16.7}$$

Then taking $E \approx p$, we see neutrinos travel a distance x in time t given by $x \approx ct$. With these approximations, we rewrite (16.6) as

$$\boxed{P(\nu_e \to \nu_\mu, x) \approx \sin^2(2\theta) \sin^2 \left(\frac{x}{L_{\text{osc}}} \right)} \tag{16.8}$$

where the characteristic oscillation length L_{osc} is

$$L_{\text{osc}} = \frac{4E}{\Delta m_{ij}^2}, \quad \Delta m_{ij}^2 = m_i^2 - m_j^2. \tag{16.9}$$

16.2 Atmospheric neutrinos

Atmospheric neutrinos provide evidence for neutrino oscillations. Energetic cosmic-rays striking the Earth's atmosphere produce showers of charge pions, which decays to muons with 99.988% probability (due to helicity suppression of weak decays):

$$\begin{aligned} \pi^+ &\to \mu^+ + \nu_\mu, \\ &\downarrow \\ &\mu^+ \to e^+ + \bar{\nu}_\mu + \nu_e \end{aligned} \tag{16.10}$$

and its charge conjugate for antiparticles. We therefore expect a 2 : 1 ratio of muon : electron type neutrinos.

$$R = \frac{N(\nu_\mu) + N(\bar{\nu}_\mu)}{N(\nu_e) + N(\bar{\nu}_e)} \approx 2 \tag{16.11}$$

This ratio allows the correlated systematic uncertainties related to the atmospheric neutrino flux to partly cancel. The Kamiokande and its upgrade Super-Kamiokande (Super-K) experiments[67] are located 1000 m underground in the Mozumi Mine of Kamioka, Japan. Super-K

[67] Originally, these experiments were constructed to look for proton decay $p \to e^+ + \pi^0$.

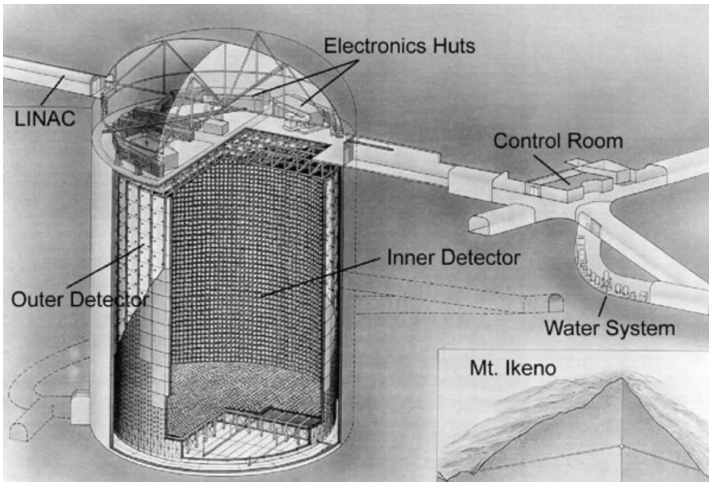

Figure 116: Super-Kamiokande detector situated in Mount Ikenoyama, Japan. Image: Ref. [107]

uses a large 40 m $\times$ 40 m vessel containing 50 kilotonnes of ultra-pure water surrounded by photomultiplier tubes to detect Cerenkov light from the neutrinos turning back into electrons or muons to identify its flavour. The electrons produce fuzzier rings due to electromagnetic showers in contrast to muons which are heavier. Experimental results present the double ratio $R' = R_{\text{obs}}/R^{\text{no-osc}}_{\text{model}}$, which should be unity if the no-oscillation model predicts the observed data.

The decisive experimental results came from Super-Kamiokande in 1998. They used a very large 535-day dataset comprising 33 kilotonne-years of exposure to report a significant overall deficit [108]:

$$\frac{R_{\text{obs}}}{R^{\text{no-osc}}_{\text{model}}} = 0.63 \pm 0.03\,(\text{stat.}) \pm 0.05\,(\text{syst.}) \tag{16.12}$$

This rejects the no-oscillation hypothesis $R_{\text{expectation}}/R^{\text{no-oscillation}}_{\text{model}} \simeq 1$ with high statistical significance.

Further evidence is available by measuring the rates as a function of propagation distance. Down-going and up-going atmospheric neutrinos traverse vastly different distances of the Earth's atmosphere vs diameter. Super-K can measure the zenith asymmetry of up-vs-down arrival of neutrinos $A = (N_{\text{up}} - N_{\text{down}})/(N_{\text{up}} + N_{\text{down}})$, where they define N_{up} for $-1 < \cos\Theta_Z < -0.2$ otherwise they are assigned to N_{down}. In no-oscillation models, the expectation should be zero. Instead they measure a significant deficit for muon-type neutrinos with GeV momenta:

$$A_{\text{osc}} = -0.296 \pm 0.048\,(\text{stat.}) \pm 0.01\,(\text{syst.}), \tag{16.13}$$

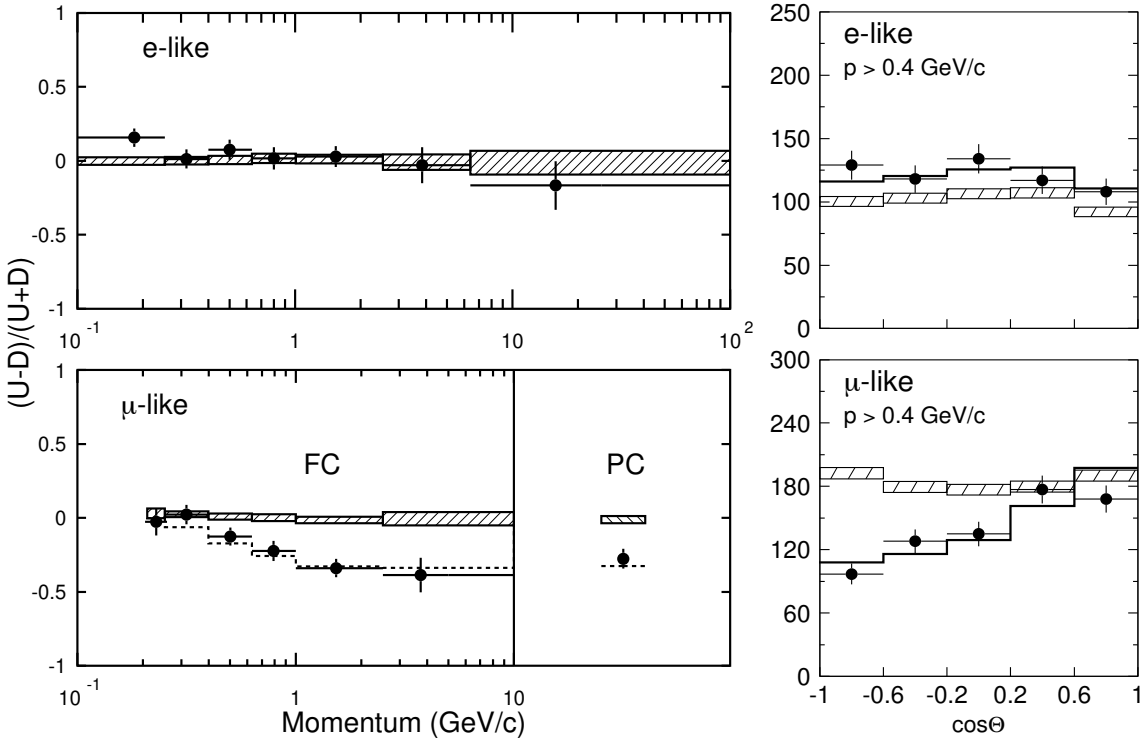

(a) Zenith asymmetry vs momentum

(b) Counts vs zenith angle

Figure 117: Atmospheric neutrino measurements from the 1998 Super-Kamiokande paper [108]. Hatched boxes show the simulated prediction from the no-oscillation model; lines (dotted on left, solid on right) show the best-fit to a $\nu_\mu \to \nu_\tau$ oscillation model. Upper (lower) panels show electron-like (muon-like) candidates. A zenith angle of $\cos\Theta_Z$ corresponds to directly overhead, $\cos\Theta_Z < 0$ is up-going and $\cos\Theta_Z > 0$ is down-going.

which alone rejects the no-oscillation hypothesis $A^{\text{no-osc}}_{\text{model}} \approx 0$ by over 6 standard deviations. Figure 117a shows this for electron-type and muon-type neutrinos as a function of momentum. Figure 117b shows this as a function of zenith angle for momenta $p > 0.4$ GeV. In both cases, there is a significant deficit for muon-type neutrinos, whereas electrons see no deficit. shows a significant deficit for muon-neutrinos arriving from below compared with above, consistent with $\nu_\mu \to \nu_\tau$ oscillations:

$$\text{Down-going} : \cos\Theta_Z > 0, \quad L^{\oplus}_{\text{atmosphere}} \approx 10\,\text{km}, \quad \nu_e, \nu_\mu \text{ little change}, \tag{16.14}$$

$$\text{Up-going} : \cos\Theta_Z < 0, \quad L^{\oplus}_{\text{diameter}} \approx 10\,000\,\text{km}, \quad \nu_\mu \to \nu_\tau \text{ inferred}. \tag{16.15}$$

These data represent the observation of atmospheric neutrino oscillations. Meanwhile, electron-neutrinos show no oscillations.

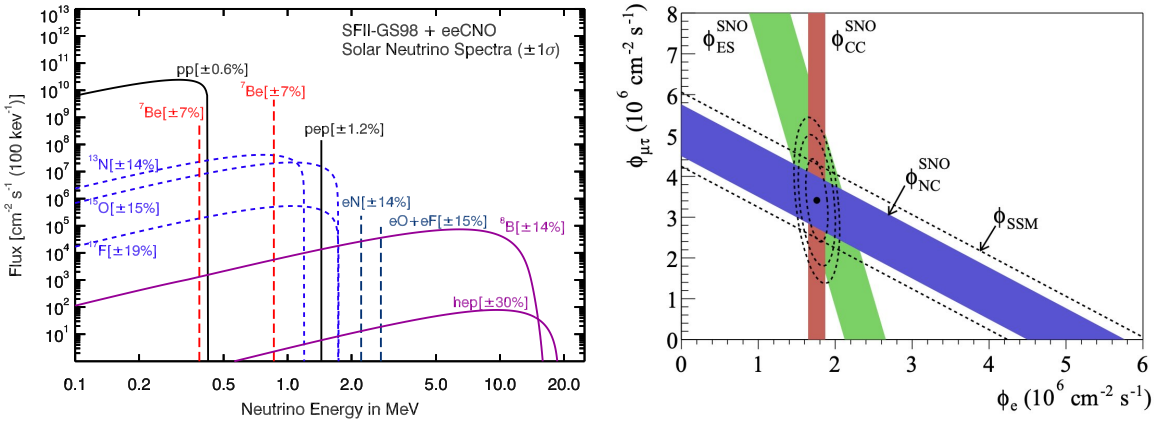

(a) Standard Solar Model neutrinos [109] (b) Measured fluxes by SNO [110]

Figure 118: Solar neutrino flux. The Standard Solar Model (SSM) shows the nuclear reactions in the Sun and the corresponding neutrino energy spectra, which only has sufficient energy to produce electron-type neutrinos ν_e. The SNO flux measurements for electron-type neutrinos ϕ_e and a significant combined muon-type and tau-type flux $\phi_{\mu\tau}$.

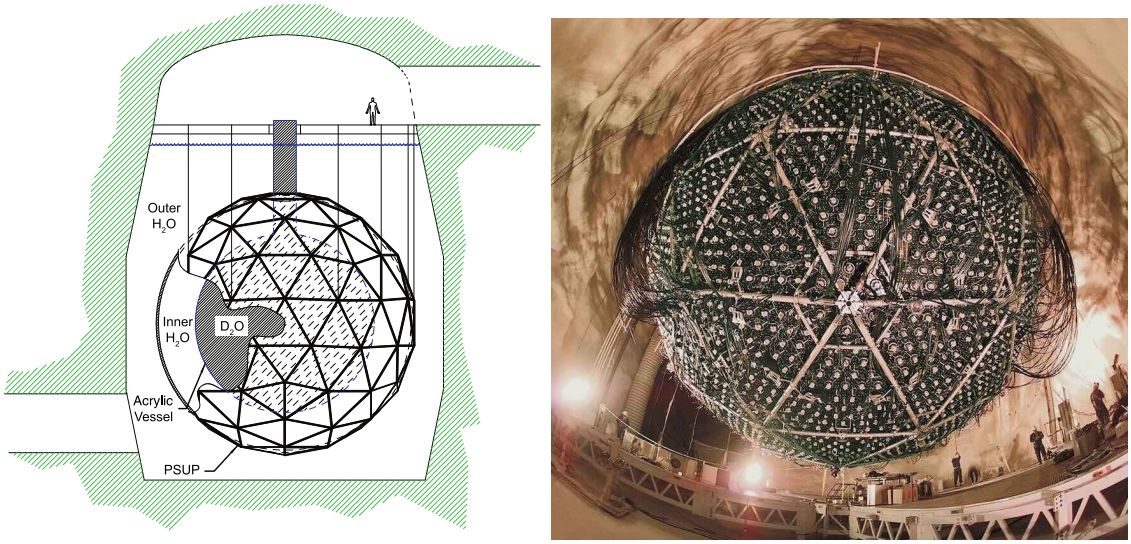

(a) Detector schematic (b) Detector photo

Figure 119: Sudbury Neutrino Observatory situated at Sudbury, Ontario, Canada. Images: Ref. [111], LBNL/R. Kaltschmidt

16.3 Solar neutrinos

Independent evidence of neutrino oscillations were observed with solar neutrinos. Undergoing nuclear fusion processes, the Sun only emits electron-type neutrinos under the reactions.

The pp cycle fusion reaction entails

$$4p \rightarrow {}^{4}_{2}\mathrm{He} + 2e^{+} + 2\nu_e + 26.73 \text{ MeV} \tag{16.16}$$

with the initial fusion being

$$p + p \rightarrow {}^{2}_{1}\mathrm{H} + e^{+} + \nu_e. \tag{16.17}$$

The photons carry most of the energy, with a small amount imparted into the neutrino kinetic energy $\langle E_{2\nu_e} \rangle = 0.59$ MeV. There are several other production mechanisms for solar neutrinos shown in figure 118a and understood from the Standard Solar Model:

$$^{7}\mathrm{Be} + e^{-} \rightarrow {}^{7}\mathrm{Li} + \nu_e + \gamma, \tag{16.18}$$

$$^{8}\mathrm{B} \rightarrow {}^{8}\mathrm{Be} + e^{+} + \nu_e. \tag{16.19}$$

We subsequently detect and identify electron-neutrinos through reactions involving the reaction

$$\nu_e + {}^{37}\mathrm{Cl} \rightarrow e^{-} + {}^{37}\mathrm{Ar} \tag{16.20}$$

To obtain a large source of chlorine atoms, 630 tonnes of C_2Cl_4 (perchloroethylene) often used for dry cleaning was procured and placed inside a vessel. Non-electron-type neutrinos cannot trigger this reaction. Therefore, any deficit in the measured amount of ^{37}Ar indicates neutrinos having oscillated to other flavours. This was first measured by Davis et al. in 1968. The Standard Solar Model of nuclear reactions without oscillations had a calculated capture rate of 7.6 solar neutrino units (SNU $\approx 10^{-36}$ captures per second). The observed result was 2.56 SNU, a third of the calculated rate. This suggests the ν_e has oscillated to equal amounts of ν_μ and ν_τ over its 149 million kilometre journey from the Sun to Earth.

More decisive evidence came from the Sudbury Neutrino Observatory (SNO) experiment. This comprises heavy water D_2O and detects three types of neutrino reactions

$$\nu_e + \mathrm{D} \rightarrow p + p + e^{-} \quad \text{charged current} \quad \text{(electron-neutrino only)}, \tag{16.21}$$

$$\nu_x + \mathrm{D} \rightarrow p + n + e^{-} \quad \text{neutral current} \quad \text{(all neutrino flavours)}, \tag{16.22}$$

$$\nu_x + e^{-} \rightarrow \nu_x + e^{-} \quad \text{elastic scattering} \quad \text{(all neutrino flavours)}. \tag{16.23}$$

These have the following reaction rates:

- Charged-current interaction can only produce electron type neutrinos because Solar neutrinos are produced via nuclear processes and have energies below the muon and tau-lepton mass threshold.

- Neutral current interaction via Z boson exchange occurs for all three neutrino flavours and can be tagged by its neutron emission compared to the charged current.
- Elastic scattering also occurs for all flavours with a signature of isolated electron recoil. This has a cross-section six times larger than for the neutral current case.

By carefully measuring these three rates, it is possible to determine the $\nu_e + \nu_\mu + \nu_\tau$ rate and fit for the flux from electron-type only vs muon-type plus tau-type neutrinos (figure 118b). The measured rates are [110]:

$$\phi_{\text{charged}} = 1.68 \pm 0.06\,(\text{stat.})^{+0.08}_{-0.09}\ (\text{syst.}), \tag{16.24}$$

$$\phi_{\text{neutral}} = 4.94 \pm 0.21\,(\text{stat.})^{+0.38}_{-0.24}\ (\text{syst.}), \tag{16.25}$$

$$\phi_{\text{elastic}} = 2.35 \pm 0.22\,(\text{stat.}) \pm 0.15\,(\text{syst.}) \tag{16.26}$$

This allowed SNO measured the flux ϕ of muon-type and tau-type neutrinos to be

$$\phi(\nu_\mu) + \phi(\nu_\tau) = 3.26 \pm 0.25\,(\text{stat.})^{+0.40}_{-0.35}\,(\text{syst.}) \tag{16.27}$$

This provides evidence that Solar electron-type neutrinos are oscillating into muon-type and tau-type neutrinos during its journey to Earth.

16.4 Neutrino mass determination

Determination of the neutrino mass hierarchy is a major research effort, and the following discussion is subject to be updated in the coming years. Global fits to oscillation data give the following measurements [75, 113]:

$$\Delta m^2_{21} = 7.50^{+0.22}_{-0.20} \times 10^{-5}\ \text{eV}^2, \tag{16.28}$$

$$|\Delta m^2_{32}| = 2.47^{+0.02}_{-0.03} \times 10^{-3}\ \text{eV}^2. \tag{16.29}$$

The sign of Δm^2_{32} being positive (negative) value is referred to **normal (inverted) ordering**. Combining recent oscillation with cosmological data give mild $\sim 2.5\sigma$ preference for normal ordering [75, 113].

The main absolute mass constraints come from kinematic endpoint measurements of tritium decay

$$^3\text{H} \rightarrow\ ^3\text{He} + e^- + \bar{\nu}_e. \tag{16.30}$$

Massive neutrinos distort the endpoint as illustrated in figure 120. The most recent limit for the electron-neutrino is from the Karlsruhe Tritium Neutrino (KATRIN) experiment [112]

$$m_{\nu_e} < 0.8\ \text{eV}, \quad 90\%\ \text{CL}. \tag{16.31}$$

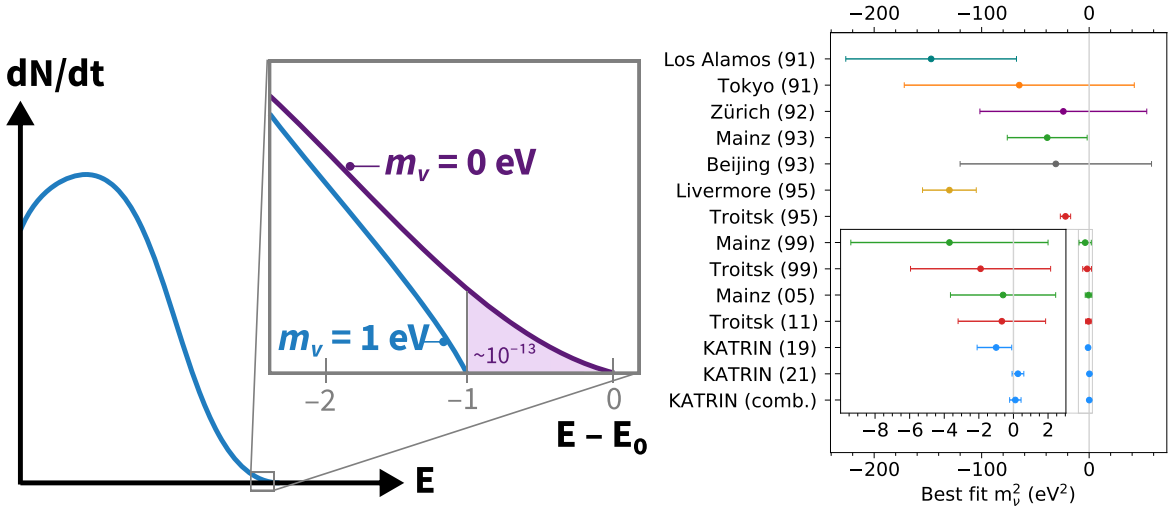

(a) Beta decay endpoint

(b) KATRIN constraints

Figure 120: **Beta decay spectrum for massless vs massive neutrinos**. Only around 2×10^{-13} of all decays reside in the last 1 eV. Right image: Ref. [112].

The value is still consistent with zero but the KATRIN experiment is expected to improve sensitivity to 0.2 eV:

$$m_\nu^2 = (0.26 \pm 0.34)\ \text{eV}^2. \tag{16.32}$$

The muon and tau neutrino masses have poorer laboratory constraints and arise from kinematic endpoint analyses of pion π^- and tau-lepton τ^- decays at 95% CL:

$$m_{\nu_\mu} < 190\ \text{keV}, \qquad \pi^- \to \mu^- + \bar{\nu}_\mu \quad [114], \tag{16.33}$$

$$m_{\nu_\tau} < 18.2\ \text{MeV}, \qquad \tau^- \to n\pi + \nu_\tau \quad [115]. \tag{16.34}$$

In a three-neutrino mixing scenario, distortions to tritium beta decay spectra lead to a lower bound on one of the neutrino species. This depends on the mass ordering scheme with the following bounds at 95% CL [75]:

$$m_{\nu_e} > 0.048\ \text{eV}, \qquad \text{normal ordering}, \tag{16.35}$$

$$m_{\nu_e} > 0.0085\ \text{eV}, \qquad \text{inverted ordering}. \tag{16.36}$$

Neutrinos on early universe cosmology leave their imprints the spectrum of the cosmic microwave background provide limits on the total mass of neutrino species being [75, 113]:

$$\sum_i \nu_i < 0.12\ (0.15)\ \text{eV} \qquad \text{normal (inverted) ordering}. \tag{16.37}$$

References

[1] G. Barr, R. Devenish, R. Walczak and T. Weidberg, "Particle Physics in the LHC Era." Oxford University Press, 978–0–19–874855–7, Open Access sponsored by SCOAP3 https://library.oapen.org/handle/20.500.12657/59108.

[2] X. Fan, T. G. Myers, B. A. D. Sukra and G. Gabrielse, *Measurement of the electron magnetic moment*, *Phys. Rev. Lett.* **130** (2023) 071801.

[3] L. Morel, Z. Yao, P. Cladé and S. Guellati-Khélifa, *Determination of the fine-structure constant with an accuracy of 81 parts per trillion*, *Nature* **588** (2020) 61.

[4] D. Clowe, M. Bradac, A. H. Gonzalez, M. Markevitch, S. W. Randall, C. Jones et al., *A direct empirical proof of the existence of dark matter*, *Astrophys. J. Lett.* **648** (2006) L109 [astro-ph/0608407].

[5] CERN, "History of the Universe." https://cds.cern.ch/record/39397, 1991.

[6] PLANCK collaboration, N. Aghanim et al., *Planck 2018 results. VI. Cosmological parameters*, *Astron. Astrophys.* **641** (2020) A6 [1807.06209].

[7] T. J. Berners-Lee, "Information Management: A Proposal." https://cds.cern.ch/record/369245, CERN-DD-89-001-OC (1989).

[8] A. Rao, "Screenshot of the recreated page of the first website." https://cds.cern.ch/record/2665153, 2019.

[9] M. Brice, "CERN Member State flags on the Esplanade des Particules." https://cds.cern.ch/record/2857083, 2023.

[10] A. Lasocki and R. J. Hicks, *How we read: the combined use of mri and novel pet tracers for the characterisation and treatment planning of masses in neuro-oncology*, *Cancer Imaging* **19** (2019) 57.

[11] S. Procureur et al., *Precise characterization of a corridor-shaped structure in Khufu's Pyramid by observation of cosmic-ray muons*, *Nature Commun.* **14** (2023) 1144.

[12] K. Morishima et al., *Discovery of a big void in Khufu's Pyramid by observation of cosmic-ray muons*, *Nature* **552** (2017) 386 [1711.01576].

[13] MURAVES collaboration, A. Giammanco et al., *Simulation Tools, First Results, and Experimental Status of the MURAVES Experiment*, *JAIS* **2024** (2024) 501 [2311.13663].

[14] R. Van Noorden, *Open-access deal for particle physics*, *Nature* **489** (2012) 486.

[15] S. Banerjee et al., *Environmental sustainability in basic research: a perspective from HECAP+*, 2306.02837.

[16] CERN, *Environment report 2021–22*, *CERN e-publishing* **3** (2023) .

[17] C. Burgard and S. Kottwitz, "Tikz Example: Standard model of physics." https://texample.net/tikz/examples/model-physics/.

[18] J. Woithe, G. J. Wiener and F. F. Van der Veken, *Let's have a coffee with the Standard Model of particle physics!*, *Phys. Educ.* **52** (2017) 034001.

[19] ATLAS Collaboration, "Standard Model Summary Plots June 2024." https://cds.cern.ch/record/2903866, 2024.

[20] C. T. R. Wilson, *On an expansion apparatus for making visible the tracks of ionising particles in gases and some results obtained by its use*, *Proc. R. Soc. Lond. A* **87** (1912) 277.

[21] E. Rutherford and H. Geiger, *An electrical method of counting the number of α-particles from radio-active substances*, *Proc. R. Soc. Lond. A* **81** (1908) 141.

[22] C. T. R. Wilson, *On a method of making visible the paths of ionising particles through a gas*, *Proc. R. Soc. Lond. A* **85** (1911) 285.

[23] N. G. J., *The β-ray spectrum of radium e*, *Proc. R. Soc. Lond. A* **17** (1940) 87.

[24] H. Geiger and E. Marsden, *Lxi. the laws of deflexion of a particles through large angles*, *The London, Edinburgh, and Dublin Philosophical Magazine and Journal of Science* **25** (1913) 604.

[25] E. Rutherford, *Lxxix. the scattering of α and β particles by matter and the structure of the atom*, *The London, Edinburgh, and Dublin Philosophical Magazine and Journal of Science* **21** (1911) 669.

[26] V. Nesvizhevsky and J. Villain, *The discovery of the neutron and its consequences (1930–1940)*, *Comptes Rendus Physique* **18** (2017) 592.

[27] I. Curie and F. Joliot, *Émission de protons de grande vitesse par les substances hydrogénées sous l'influence des rayons tres pénétrants*, .

[28] J. Chadwick, *Possible Existence of a Neutron*, *Nature* **129** (1932) 312.

[29] P. Carlson and A. De Angelis, *Nationalism and internationalism in science: the case of the discovery of cosmic rays*, *Eur. Phys. J. H* **35** (2010) 309 [1012.5068].

[30] "Domenico Pacini and the origin of cosmic rays." https://cds.cern.ch/record/1734821, 2012.

[31] V. F. Hess, *Über Beobachtungen der durchdringenden Strahlung bei sieben Freiballonfahrten (On the Observations of the Penetrating Radiation during Seven Balloon Flights)*, *Phys. Z.* **13** (1912) 1084.

[32] C. D. Anderson, *The positive electron*, *Phys. Rev.* **43** (1933) 491.

[33] P. M. S. Blackett and G. P. S. Occhialini, *Some Photographs of the Tracks of Penetrating Radiation*, *Proc. Roy. Soc. Lond. A* **139** (1933) 699.

[34] J. C. Street and E. C. Stevenson, *New evidence for the existence of a particle of mass intermediate between the proton and electron*, *Phys. Rev.* **52** (1937) 1003.

[35] PARTICLE DATA GROUP collaboration, R. L. Workman et al., *Review of Particle Physics*, *PTEP* **2022** (2022) 083C01.

[36] S. H. Neddermeyer and C. D. Anderson, *Note on the nature of cosmic-ray particles*, *Phys. Rev.* **51** (1937) 884.

[37] N. Nereson and B. Rossi, *Further measurements on the disintegration curve of mesotrons*, *Phys. Rev.* **64** (1943) 199.

[38] M. Conversi, E. Pancini and O. Piccioni, *On the disintegration of negative mesons*, *Phys. Rev.* **71** (1947) 209.

[39] C. Evoli, *The cosmic-ray energy spectrum*, .

[40] EAS-MSU, ICECUBE, KASCADE-GRANDE, NEVOD-DECOR, PIERRE AUGER, SUGAR, TELESCOPE ARRAY, YAKUTSK EAS ARRAY collaboration, H. P. Dembinski et al., *Report on Tests and Measurements of Hadronic Interaction Properties with Air Showers*, *EPJ Web Conf.* **210** (2019) 02004 [1902.08124].

[41] PIERRE AUGER collaboration, A. Aab et al., *Observation of a Large-scale Anisotropy in the Arrival Directions of Cosmic Rays above* 8×10^{18} *eV*, *Science* **357** (2017) 1266 [1709.07321].

[42] A. A. Michelson and E. W. Morley, *On the Relative Motion of the Earth and the Luminiferous Ether*, *Am. J. Sci.* **34** (1887) 333.

[43] G. Breit and J. A. Wheeler, *Collision of two light quanta*, *Phys. Rev.* **46** (1934) 1087.

[44] J. D. Cockcroft and E. T. S. Walton, *Experiments with high velocity positive ions. II. -The disintegration of elements by high velocity protons*, *Proc. Roy. Soc. Lond. A* **137** (1932) 229.

[45] "The Cockcroft-Walton Column." https://cds.cern.ch/record/39553, 1975, CERN-HI-7504054.

[46] B. Bell, H. Friedsam, W. Oren and R. E. Ruland, "Datum definition problems in accelerator alignment." https://cds.cern.ch/record/209215, 1990, SLAC-PUB-5226.

[47] S. Bethke and A. Wagner, *The JADE Experiment at the PETRA* e^+e^- *collider – history, achievements and revival*, *Eur. Phys. J. H* **47** (2022) 16 [2208.11076].

[48] W. E. Lamb and R. C. Retherford, *Fine structure of the hydrogen atom by a microwave method*, *Phys. Rev.* **72** (1947) 241.

[49] P. Kusch and H. M. Foley, *Precision measurement of the ratio of the atomic 'g values' in the* ${}^2p_{\frac{3}{2}}$ *and* ${}^2p_{\frac{1}{2}}$ *states of gallium*, *Phys. Rev.* **72** (1947) 1256.

[50] P. Kusch and H. M. Foley, *The magnetic moment of the electron*, *Phys. Rev.* **74** (1948) 250.

[51] J. S. Schwinger, *On Quantum electrodynamics and the magnetic moment of the electron*, *Phys. Rev.* **73** (1948) 416.

[52] R. H. Parker, C. Yu, W. Zhong, B. Estey and H. Müller, *Measurement of the fine-structure constant as a test of the Standard Model*, *Science* **360** (2018) 191 [1812.04130].

[53] T. Aoyama, T. Kinoshita and M. Nio, *Theory of the Anomalous Magnetic Moment of the Electron*, *Atoms* **7** (2019) 28.

[54] T. Aoyama, M. Hayakawa, T. Kinoshita and M. Nio, *Tenth-order qed contribution to the electron* $g-2$ *and an improved value of the fine structure constant*, *Phys. Rev. Lett.* **109** (2012) 111807.

[55] E. Tiesinga, P. J. Mohr, D. B. Newell and B. N. Taylor, *Codata recommended values of the fundamental physical constants: 2018*, *Rev. Mod. Phys.* **93** (2021) 025010.

[56] L3 collaboration, L3 Collaboration, *Measurement of the running of the electromagnetic coupling at large momentum-transfer at LEP*, *Phys. Lett. B* **623** (2005) 26 [hep-ex/0507078].

[57] I. Neutelings, A. Tsagkaropolulos and S. Kottwitz, "History timeline and energy scale of particle physics." https://tikz.net/timeline/.

[58] I. I. Rabi, J. M. B. Kellogg and J. R. Zacharias, *The magnetic moment of the proton*, *Phys. Rev.* **46** (1934) 157.

[59] I. I. Rabi, J. M. B. Kellogg and J. R. Zacharias, *The magnetic moment of the deuton*, *Phys. Rev.* **46** (1934) 163.

[60] L. W. Alvarez and F. Bloch, *A quantitative determination of the neutron moment in absolute nuclear magnetons*, *Phys. Rev.* **57** (1940) 111.

[61] R. Brown, U. Camerini, P. H. Fowler, H. Muirhead, C. F. Powell and D. M. Ritson, *Observations With Electron Sensitive Plates Exposed to Cosmic Radiation*, *Nature* **163** (1949) 82.

[62] G. D. Rochester and C. C. Butler, *Evidence for the Existence of New Unstable Elementary Particles*, *Nature* **160** (1947) 855.

[63] V. E. Barnes, P. L. Connolly et al., *Observation of a hyperon with strangeness minus three*, *Phys. Rev. Lett.* **12** (1964) 204.

[64] R. Hofstadter, *Electron scattering and nuclear structure*, *Rev. Mod. Phys.* **28** (1956) 214.

[65] B. Hahn, D. G. Ravenhall and R. Hofstadter, *High-Energy Electron Scattering and the Charge Distributions of Selected Nuclei*, *Phys. Rev.* **101** (1956) 1131.

[66] R. Hofstadter and R. W. McAllister, *Electron Scattering From the Proton*, *Phys. Rev.* **98** (1955) 217.

[67] D. R. Yennie, D. G. Ravenhall and R. N. Wilson, *Phase-Shift Calculation of High-Energy Electron Scattering*, *Phys. Rev.* **95** (1954) 500.

[68] M. Breidenbach, J. I. Friedman, H. W. Kendall, E. D. Bloom, D. H. Coward, H. DeStaebler et al., *Observed behavior of highly inelastic electron-proton scattering*, *Phys. Rev. Lett.* **23** (1969) 935.

[69] J. I. Friedman and H. W. Kendall, *Deep inelastic electron scattering*, *Ann. Rev. Nucl. Part. Sci.* **22** (1972) 203.

[70] C. G. Callan and D. J. Gross, *High-energy electroproduction and the constitution of the electric current*, *Phys. Rev. Lett.* **22** (1969) 156.

[71] GARGAMELLE NEUTRINO collaboration, H. Deden et al., *Experimental Study of Structure Functions and Sum Rules in Charge Changing Interactions of Neutrinos and anti-neutrinos on Nucleons*, *Nucl. Phys. B* **85** (1975) 269.

[72] J. J. Aubert, U. Becker, P. J. Biggs, J. Burger, M. Chen, G. Everhart et al., *Experimental observation of a heavy particle J*, *Phys. Rev. Lett.* **33** (1974) 1404.

[73] J. E. Augustin, A. M. Boyarski, M. Breidenbach, F. Bulos, J. T. Dakin, G. J. Feldman et al., *Discovery of a narrow resonance in e^+e^- annihilation*, *Phys. Rev. Lett.* **33** (1974) 1406.

[74] G. S. Abrams, D. D. Briggs, W. Chinowsky, C. E. Friedberg, G. Goldhaber, J. A. Kadyk et al., *Decay of $\psi(3684)$ into $\psi(3095)$*, *Phys. Rev. Lett.* **34** (1975) 1181.

[75] PARTICLE DATA GROUP collaboration, S. Navas et al., *Review of particle physics*, *Phys. Rev. D* **110** (2024) 030001.

[76] P. Soding, *On the discovery of the gluon*, *Eur. Phys. J. H* **35** (2010) 3.

[77] JADE collaboration, W. Bartel et al., *Observation of Planar Three Jet Events in e+ e- Annihilation and Evidence for Gluon Bremsstrahlung*, *Phys. Lett. B* **91** (1980) 142.

[78] CMS collaboration, S. Chatrchyan et al., *Measurement of the Ratio of the Inclusive 3-Jet Cross Section to the Inclusive 2-Jet Cross Section in pp Collisions at $\sqrt{s}$ = 7 TeV and First Determination of the Strong Coupling Constant in the TeV Range*, *Eur. Phys. J. C* **73** (2013) 2604 [1304.7498].

[79] M. L. Perl et al., *Evidence for anomalous lepton production in $e^+ - e^-$ annihilation*, *Phys. Rev. Lett.* **35** (1975) 1489.

[80] C. L. Cowan, F. Reines, F. B. Harrison, H. W. Kruse and A. D. McGuire, *Detection of the Free Neutrino: a Confirmation*, *Science* **124** (1956) 103.

[81] H. Bethe and R. Peierls, *The 'neutrino'*, *Nature* **133** (1934) 532.

[82] Christine Sutton, "Ghosts in the machine." https://cds.cern.ch/record/2232603, 2016.

[83] C. S. Wu, E. Ambler, R. W. Hayward, D. D. Hoppes and R. P. Hudson, *Experimental Test of Parity Conservation in β Decay*, *Phys. Rev.* **105** (1957) 1413.

[84] R. L. Garwin, L. M. Lederman and M. Weinrich, *Observations of the failure of conservation of parity and charge conjugation in meson decays: the magnetic moment of the free muon*, *Phys. Rev.* **105** (1957) 1415.

[85] M. Gell-Mann and A. Pais, *Behavior of neutral particles under charge conjugation*, *Phys. Rev.* **97** (1955) 1387.

[86] J. H. Christenson, J. W. Cronin, V. L. Fitch and R. Turlay, *Evidence for the 2π Decay of the K_2^0 Meson*, *Phys. Rev. Lett.* **13** (1964) 138.

[87] ALEPH, DELPHI, L3, OPAL, SLD, LEP Electroweak Working Group, SLD Electroweak Group, SLD Heavy Flavour Group, *Precision electroweak measurements on the Z resonance*, *Phys. Rept.* **427** (2006) 257 [hep-ex/0509008].

[88] J.-L. Caron, "LHC layout. Schema general du LHC." https://cds.cern.ch/record/841573, 1997.

[89] M. Brice, "Aerial View of the CERN taken in 2008." https://cds.cern.ch/record/1295244, 2008, CERN-MI-0807031.

[90] M. Brice and J. M. Ordan, "LHC tunnel point 1 various angles." https://cds.cern.ch/record/2302977, CERN-PHOTO-201802-030.

[91] P. Allport, *Applications of silicon strip and pixel-based particle tracking detectors*, *Nature Rev. Phys.* **1** (2019) 567.

[92] ATLAS Collaboration, *The ATLAS experiment at the CERN Large Hadron Collider: a description of the detector configuration for Run 3*, *JINST* **19** (2024) P05063 [2305.16623].

[93] ATLAS collaboration, S. Mehlhase, "ATLAS detector slice (and particle visualisations)." https://cds.cern.ch/record/2770815, 2021.

[94] ATLAS Collaboration, *Configuration and performance of the ATLAS b-jet triggers in Run 2*, *Eur. Phys. J. C* **81** (2021) 1087 [2106.03584].

[95] UA1 collaboration, G. Arnison et al., *Experimental Observation of Isolated Large Transverse Energy Electrons with Associated Missing Energy at $\sqrt{s} = 540$ GeV*, *Phys. Lett. B* **122** (1983) 103.

[96] UA2 collaboration, M. Banner et al., *Observation of Single Isolated Electrons of High Transverse Momentum in Events with Missing Transverse Energy at the CERN anti-p p Collider*, *Phys. Lett. B* **122** (1983) 476.

[97] UA1 collaboration, C. Albajar et al., *Studies of Intermediate Vector Boson Production and Decay in UA1 at the CERN Proton - Antiproton Collider*, *Z. Phys. C* **44** (1989) 15.

[98] GFITTER collaboration, M. Baak, M. Goebel, J. Haller, A. Hoecker, D. Kennedy, K. Moenig et al., *Updated Status of the Global Electroweak Fit and Constraints on New Physics*, *Eur. Phys. J. C* **72** (2012) 2003 [1107.0975].

[99] ATLAS Collaboration, *Measurements of the Higgs boson inclusive and differential fiducial cross sections in the 4ℓ decay channel at $\sqrt{s}$ = 13 TeV*, *Eur. Phys. J. C* **80** (2020) 942 [2004.03969].

[100] CMS Collaboration, *Observation of a New Boson at a Mass of 125 GeV with the CMS Experiment at the LHC*, *Phys. Lett. B* **716** (2012) 30 [1207.7235].

[101] G. Cowan, K. Cranmer, E. Gross and O. Vitells, *Asymptotic formulae for likelihood-based tests of new physics*, *Eur. Phys. J. C* **71** (2011) 1554 [1007.1727].

[102] ROOT collaboration, K. Cranmer, G. Lewis, L. Moneta, A. Shibata and W. Verkerke, *HistFactory: A tool for creating statistical models for use with RooFit and RooStats*, .

[103] ATLAS Collaboration, *Observation of a new particle in the search for the Standard Model Higgs boson with the ATLAS detector at the LHC*, *Phys. Lett. B* **716** (2012) 1 [1207.7214].

[104] ATLAS Collaboration, *A detailed map of Higgs boson interactions by the ATLAS experiment ten years after the discovery*, *Nature* **607** (2022) 52 [2207.00092].

[105] CMS collaboration, A. Tumasyan et al., *A portrait of the Higgs boson by the CMS experiment ten years after the discovery.*, *Nature* **607** (2022) 60 [2207.00043].

[106] C. Jarlskog, *Commutator of the quark mass matrices in the standard electroweak model and a measure of maximal* CP *nonconservation*, *Phys. Rev. Lett.* **55** (1985) 1039.

[107] SUPER-KAMIOKANDE collaboration, Y. Fukuda et al., *The Super-Kamiokande detector*, *Nucl. Instrum. Meth. A* **501** (2003) 418.

[108] SUPER-KAMIOKANDE collaboration, Y. Fukuda et al., *Evidence for oscillation of atmospheric neutrinos*, *Phys. Rev. Lett.* **81** (1998) 1562 [hep-ex/9807003].

[109] A. Serenelli, *Alive and well: a short review about standard solar models*, *Eur. Phys. J. A* **52** (2016) 78 [1601.07179].

[110] SNO collaboration, Q. R. Ahmad et al., *Direct evidence for neutrino flavor transformation from neutral current interactions in the Sudbury Neutrino Observatory*, *Phys. Rev. Lett.* **89** (2002) 011301 [nucl-ex/0204008].

[111] SNO Collaboration, *Constraints on neutrino lifetime from the sudbury neutrino observatory*, *Phys. Rev. D* **99** (2019) 032013.

[112] KATRIN collaboration, M. Aker et al., *Direct neutrino-mass measurement with sub-electronvolt sensitivity*, *Nature Phys.* **18** (2022) 160 [2105.08533].

[113] P. F. de Salas, D. V. Forero, S. Gariazzo, P. Martínez-Miravé, O. Mena, C. A. Ternes et al., *2020 global reassessment of the neutrino oscillation picture*, *JHEP* **02** (2021) 071 [2006.11237].

[114] K. Assamagan et al., *Upper limit of the muon-neutrino mass and charged pion mass from momentum analysis of a surface muon beam*, *Phys. Rev. D* **53** (1996) 6065.

[115] ALEPH collaboration, R. Barate et al., *An Upper limit on the tau-neutrino mass from three-prong and five-prong tau decays*, *Eur. Phys. J. C* **2** (1998) 395.